Trinity College Dublin
Coláiste na Tríonóide, Baile Átha Cliath
The University of Dublin

Optimal Real-Time Predictive Control for Maximising the Power-Take-Off Efficiency of the WaveRAM Wave Energy Converter

Author:
Christopher Daniel SIGNORELLI

Supervisor:
Prof. Biswajit BASU

Thesis submitted to the University of Dublin, Trinity College for the degree of Doctor of Philosophy

August, 2018

Declaration of Authorship

I, Christopher Daniel SIGNORELLI, declare that this thesis titled, "Optimal Real-Time Predictive Control for Maximising the Power-Take-Off Efficiency of the WaveRAM Wave Energy Converter" has not been submitted as an exercise for a degree at this or any other university and it is entirely my own work.

I agree to deposit this thesis in the University's open access institutional repository or allow the library to do so on my behalf, subject to Irish Copyright Legislation and Trinity College Library conditions of use and acknowledgement.

Signed:

_____

Date:

_____

Abstract

The aim of this thesis is to develop a control strategy for optimising the power-take-off (PTO) efficiency of the newly developed WaveRAM (WRAM) wave energy converter. The three main research streams established to satisfy these requirements have been: 1) the development of a wave-to-wire numerical model of the WRAM and its PTO system; 2) the implementation of a real-time model predictive control (RT MPC) algorithm; and 3) the construction of a laboratory test rig, capable of emulating the behaviour of a sea-going device. Given that the WRAM is intended for deployment at sea in the near future, the control algorithm must be capable of operating in real-time. This has been the primary motivation of the second research stream, where portions of the model created in the first stream were used as the controlled plant. In order to verify the algorithm's performance prior to sea-deployment, the laboratory test facility from the third stream ensures that the algorithm can operate successfully within practical constraints.

With regards to the first research stream, many parts of the numerical model for WRAM were derived based on well-accepted fundamental physics in the literature. For the subsystems where the fundamental physics were not well-known, or parameters were captured more accurately with physical equipment, new models were derived. The well-accepted components include the WRAM's hydrodynamics, air chamber pneumatics and the turbine's characteristics. The unknown components were within the turbo-generator system, where not all parameter values were available at design. As such, system identification was adopted to identify the unknown values from laboratory experiments. Results of the system identification process showed a closeness-of-fit of 96% between the experimental results and theoretical model. The WRAM's wave-to-wire model was then completed, with the turbine-to-wire portion being controlled by the RT MPC algorithm.

The real-time control algorithm, adopted in the second research stream, follows an approach in the literature that implements fast constrained MPC using Laguerre networks. This has been applied to the WRAM's PTO, with focus placed on maximising the turbine's operating efficiency. Motivation for this algorithm was based on its ability to perform optimal control with practical constraints and fast execution speeds. Results from this research have shown that speeds in the order of tens of μs are possible for this application, much

faster than what has been reported in the literature for wave energy applications. The high speed of the algorithm makes it possible for real-time implementation on standard industrial control systems. Another component of the research was to investigate the performance of alternative cost functions in the optimal control problem. Results showed that care is needed in choosing an appropriate cost function, depending on the type of wave energy converter being controlled. Further questions were raised as to whether the closed-form method of RT MPC is appropriate for both cost functions used.

Lastly, in the third stream, an emulation platform has been produced, allowing for advanced control algorithms to be tested on realistic hardware, prior to implementation at sea. The platform has been integrated into an existing real-time hybrid test (RTHT) facility, such that aspects of the WRAM model, not implemented on the emulator platform, can be simulated within a real-time feedback loop. The RTHT approach helps bridge the gap between academic and industrial partners, where advanced theoretical algorithms can be tested in a safe laboratory environment. Industrial partners can then draw confidence in the technology before bearing the financial risk of failure at sea. The emulation platform developed in this research is the first of its kind, as it is capable of emulating the bidirectional, irregular flow conditions typical of oscillating water columns. Furthermore, it can do so within a RTHT framework. Other similar test facilities offer only a subset of these features.

The main contributions of the research include: a complete wave-to-wire model of the WRAM that incorporates existing well-accepted fundamental principles with newly formulated models of standard industry equipment; the demonstration of execution speeds for RT MPC in the order of μs; and a novel WRAM emulation platform, capable of generating air flow conditions typical for oscillating water columns. Several new research opportunities have surfaced, including: implementation of the control approach within the RTHT framework; further investigation into alternative cost functions of the optimal control problem; exploration into alternative methods for solving quadratic programming problems in real-time; further investigation of the control tuning parameters; consideration of alternative electrical generators; and examination of electrical power quality for grids.

Acknowledgements

Prof. Biswajit Basu. I would like to sincerely thank my supervisor, Professor Biswajit Basu, both on a personal and professional level for granting me the opportunity to undertake this Ph.D. In addition to his mathematical expertise, I'm grateful for his flexibility in allowing me to work at my own pace, which during some periods would have appeared much more industrial than academic when developing the elaborate test rig. This has allowed a very well developed test rig to be built with the potential for significant future research that links academic research and off-the-shelf industrial technology. Finally I would like to acknowledge his financial support in the early stages of the Ph.D.

William Dick. Special thanks also to William Dick, founder of Swirl Generators Limited (SGL), who was the key inspiration for taking on the Ph.D. As with most opportunities the timing was perfect, given that at the time I was eager to take on work that was more academically stimulating. William has also been very flexible and generous in granting me the time to focus on my research when needed. Since late 2015, his contribution through Enterprise Ireland's Innovation Partnership Programme (IPP) and subsequently directly from SGL, has provided the financial support to sustain myself and my family while completing the Ph.D. I look forward to further applying what I have learned throughout the Ph.D. to William's WaveRAM invention.

Other Funding Sources. Thanks to Enterprise Ireland who granted 80% of the funds for developing the WRAM emulation platform in this research. The platform is a valuable asset to the Civil Engineering department at Trinity and will hopefully prove useful to many students over the years to come. The IPP Project number is: IP/2015/0396. The funding from European Commission Marie-Slodowska-Curie Actions under the H2020 European Industrial Doctorate project ICONN (Grant No. 675659) is also gratefully acknowledged

University College Cork, Electrical & Electronic Engineering. Thanks to Prof. William Wright and his team at the Electrical & Electronic Engineering department in UCC for loaning their replica turbine for use on the test rig. The help came when time was quickly running out on the IPP project, however thanks to speedy refurbishment and delivery, project delays were avoided and significant value has been added to the research outcomes.

Civil Engineering Technical Team. The outstanding efforts of Civil Engineering's technicians deserve special mention, especially Dr. Kevin Ryan and Dave McAulay. In addition to their willingness to assist under constantly strained resources, and needless to say their technical expertise, their openness in bouncing implementation ideas back and forth was greatly welcomed. This particularly helped the creative process in the early design stages and some retrofitting towards the end.

Family and Friends. Last but not least to my family and friends. Thanks to my parents who continually offer their love and support from the southern hemisphere, who are both very proud that I have completed this Ph.D. Also, I have made some great friends here at Trinity who have made the experience all the more rewarding. Thanks to Christy Kollmar, who proof read the thesis, and despite the topic not being related in any way to her field of expertise, provided insightful constructive criticism that ultimately led to a higher quality of work. Finally, to say thank you to my daughter Sofía for coming into the world during the second half of the Ph.D. Over the years to come I'll utilise it to guide you, inspire you, and ensure you have everything you need.

Contents

List of Figures

List of Tables

List of Abbreviations

BEM	**B**oundary **E**lement **M**ethod
BS	**B**ret**S**chneider
CCW	**C**ounter **C**lock**W**ise
CW	**C**lock**W**ise
cRIO	**C**ompact **R**econfigurable **I**nput **O**utput (controller)
DAQ	**D**ata **A**c**Q**uisition
DLQR	**D**iscrete **L**inear **Q**uadratic **R**egulator
DoF	**D**egree **o**f **F**reedom
FD	**F**requency **D**omain
FDI	**F**requency **D**omain **I**dentification
FPGA	**F**ield **P**rogrammable **G**ate **A**rray
FSS	**F**ull-**S**cale **S**pan
FTC	**F**ault-**T**olerant **C**ontrol
GPC	**G**eneralised **P**redictive **C**ontrol
HIL	**H**ardware **I**n (the) **L**oop
HRCF	**H**alf-**R**ange **C**hebyshev **F**ourier
IO	**I**nput **O**utput
IP	**I**ntellectual **P**roperty
LCOE	**L**evelised **C**ost **O**f **E**nergy
LMFD	**L**eft **M**atrix **F**raction **D**escription
LQR	**L**inear **Q**uadratic **R**regulator
LTI	**L**inear **T**ime-**I**nvariant
LUT	**L**ook **U**p **T**able
MIMO	**M**ulti-**I**nput **M**ulti-**O**utput

MPC	**M**odel **P**redictive **C**ontrol
MTS	**MTS** (Systems Corporation)
NLP	**N**on**L**inear **P**rogram
NMSS	**N**on-**M**inimal **S**tate **S**pace
NRMSE	**N**ormalised **R**oot-**M**ean-**S**quared **E**rror
OWC	**O**scillating **W**ater **C**olumn
P2P	**P**eer-**2**-**P**eer
PI	**P**roportional-**I**ntegral
PID	**P**roportional-**I**ntegral-**D**erivative
PLC	**P**rogrammable **L**ogic **C**ontroller
PMP	**P**ontryagin's **M**aximum **P**rinciple
PTO	**P**ower-**T**ake-**O**ff
QP	**Q**uadratic **P**rogramming
RHPSC	**R**eceding **H**orizon **P**seudospectral (optimal) **C**ontrol
RL	**R**einforcement **L**earning
RMS	**R**oot-**M**ean-**S**quared
RT MPC	**R**eal-**T**ime **M**odel **P**redictive **C**ontrol
RTHT	**R**eal-**T**ime **H**ybrid **T**est
SCFM	**S**tandard **C**ubic **F**eet (per) **M**inute
SCRAMNET	**S**hared **C**ommon **R**andom **A**ccess **M**emory **NET**work
SISO	**S**ingle-**I**nput **S**ingle-**O**utput
STS	**S**tructural **T**est **S**ystem
TD	**T**ime **D**omain
TPMLG	**T**ubular **P**ermanent **M**agnet **L**inear **G**enerator
WEC	**W**ave **E**nergy **C**onverter
WRAM	**W**ave**RAM**

List of Symbols

Symbol	Unit	Description
a		Laguerre network pole
$a_{\infty_{33}}$	kg	Added mass at infinite frequency for 3-3 coupling
$a_{\infty_{39}}$	kg	Added mass at infinite frequency for 3-9 coupling
$a_{\infty_{93}}$	kg	Added mass at infinite frequency for 9-3 coupling
$a_{\infty_{99}}$	kg	Added mass at infinite frequency for 9-9 coupling
$\mathbf{A}$		Augmented state matrix for $\mathbf{A}_m$
$\mathbf{A}_{33}$		State matrix for the state space approximation of $f_{rad_{33}}(t)$
$\mathbf{A}_{39}$		State matrix for the state space approximation of $f_{rad_{39}}(t)$
$\mathbf{A}_{93}$		State matrix for the state space approximation of $f_{rad_{93}}(t)$
$\mathbf{A}_{99}$		State matrix for the state space approximation of $f_{rad_{99}}(t)$
$\mathbf{A}_c$		State matrix for continuous wave-to-relative motion model
$\mathbf{A}_d$		State matrix for discrete wave-to-relative motion model
$\mathbf{A}_g$		State matrix for MIMO generator model
$\mathbf{A}_m$		State matrix for a generic LTI model
$\mathbf{A}_\Omega$		State matrix for non-augmented NMSS MIMO generator model
$\hat{\mathbf{A}}_\Omega$		State matrix for augmented NMSS MIMO generator model
b_t	N m s	Generator viscous friction constant (rotor and turbine)
$B(t)$	psi	Barometric pressure
$\mathbf{B}$		Augmented input matrix for $\mathbf{B}_m$
$\mathbf{B}_{33}$		Input matrix for the state space approximation of $f_{rad_{33}}(t)$
$\mathbf{B}_{39}$		Input matrix for the state space approximation of $f_{rad_{39}}(t)$
$\mathbf{B}_{93}$		Input matrix for the state space approximation of $f_{rad_{93}}(t)$
$\mathbf{B}_{99}$		Input matrix for the state space approximation of $f_{rad_{99}}(t)$

$\mathbf{B}_c$		Input matrix for continuous wave-to-relative motion model
$\mathbf{B}_d$		Input matrix for discrete wave-to-relative motion model
$\mathbf{B}_g$		Input matrix for MIMO generator model
$\mathbf{B}_m$		Input matrix for a generic LTI model
$\mathbf{B}_\Omega$		Input matrix for non-augmented NMSS MIMO generator model
$\hat{\mathbf{B}}_\Omega$		Input matrix for augmented NMSS MIMO generator model
c_3	$\mathrm{N\,m^{-1}}$	Hydrostatic restoring coefficient of WRAM body
c_9	$\mathrm{N\,m^{-1}}$	Hydrostatic restoring coefficient of water column
c_i		i^{th} Laguerre coefficient
$\mathbf{C}$		Augmented output matrix for $\mathbf{C}_m$
$\mathbf{C}_{33}$		Output matrix for the state space approximation of $f_{rad_{33}}(t)$
$\mathbf{C}_{39}$		Output matrix for the state space approximation of $f_{rad_{39}}(t)$
$\mathbf{C}_{93}$		Output matrix for the state space approximation of $f_{rad_{93}}(t)$
$\mathbf{C}_{99}$		Output matrix for the state space approximation of $f_{rad_{99}}(t)$
$\mathbf{C}_B$	$\mathrm{N\,m^{-1}}$	Hydrostatic restoring coefficient matrix
$\mathbf{C}_c$		Output matrix for continuous wave-to-relative motion model
$\mathbf{C}_d$		Output matrix for discrete wave-to-relative motion model
$\mathbf{C}_g$		Output matrix for MIMO generator model
$\mathbf{C}_m$		Output matrix for a generic LTI model
$\mathbf{C}_\Omega$		Output matrix for non-augmented NMSS MIMO generator model
$\hat{\mathbf{C}}_\Omega$		Output matrix for augmented NMSS MIMO generator model
d_i	inches	Internal duct diameter
$dP(t)$	inches H_2O	Differential pressure
$D(s)$		Generic feedback model disturbance signal
D_t	m	Turbine rotor diameter
$\mathbf{D}_c$		Feedthrough matrix for continuous wave-to-relative motion model
$\mathbf{D}_d$		Feedthrough matrix for discrete wave-to-relative motion model
$\mathbf{D}_m(z)$		Partial LMFD decomposition of $\mathbf{G}_m(z)$
$e_\Delta(t)$		Error between displacement setpoint and output for generic loop
$e_v(t)$		Error between velocity setpoint and output for generic loop

$E(t)$	V	Generator winding voltage
$\mathbf{E}_\lambda$		Equality constraint matrix
f	Hz	Frequency of sea state spectra
$f_c(t)$	$\mathrm{N\,m^{-1}}$	Generic excitation force impulse response function
$f_e(t)$	N	Excitation force on a general body
$f_{e_3}(t)$	N	Excitation force on WRAM body
$f_{e_9}(t)$	N	Excitation force on water column
$f_{PTO}(t)$	N	PTO force
$f_{rad_{33}}(t)$	N	Radiation damping force for 3-3 coupling
$f_{rad_{39}}(t)$	N	Radiation damping force for 3-9 coupling
$f_{rad_{93}}(t)$	N	Radiation damping force for 9-3 coupling
$f_{rad_{99}}(t)$	N	Radiation damping force for 9-9 coupling
$\mathbf{F}$		State matrix block for MPC
$\mathbf{F}_{rad}(t)$	N	Radiation damping forces for the wave-to-relative motion model
$F_c(\omega)$	$\mathrm{N\,m^{-1}}$	FD excitation force coefficient
$F_{e_i}(\omega)$		i^{th} frequency response function component of the excitation force
$\angle F_{e_i}(\omega)$	rad	Phase of $F_{e_i}(\omega)$
$\lvert F_{e_i}(\omega)\rvert$	$\mathrm{N\,m^{-1}}$	Magnitude $F_{e_i}(\omega)$
$\mathbf{F}_i$		Coefficients of like-orders from $\mathbf{D}_m(z)$
$\mathbf{F}_\lambda$		Equality constraint vector
$G(s)$		Generic feedback model open-loop transfer function
$G_{drive}(s)$		Servo-drive transfer function including generator
$\mathbf{G}_g(s)$		MIMO generator transfer function
$G_{g_{11}}(s)$		SISO transfer function relating T_t and Ω_t
$G_{g_{12}}(s)$		SISO transfer function relating E and Ω_t
$G_{g_{21}}(s)$		SISO transfer function relating T_t and I
$G_{g_{22}}(s)$		SISO transfer function relating E and I
$\mathbf{G}_i(s)$		MIMO current loop transfer function
$G_{i_{12}}(s)$		SISO transfer function relating I_{SP} and Ω_t
$G_{i_{21}}(s)$		SISO transfer function relating T_t and I

$G_{i_{22}}(s)$		SISO transfer function relating I_{SP} and I
$\mathbf{G}_m(z)$		Generic second order discrete model
$G_{pd}(s)$		Displacement loop PD-gains
$G_{pi}(s)$		Equivalent velocity loop PI-gains
$\mathbf{G}_\Omega(s)$		MIMO velocity loop transfer function
$\hat{\mathbf{G}}_\Omega(s)$		Parametrised version of $\mathbf{G}_\Omega(s)$
$\hat{\mathbf{G}}_{\Omega_d}(z)$		Discretised version of $\hat{\mathbf{G}}_\Omega(s)$
$H(k)$		Generic discrete impulse response function
$H(s)$		Generic feedback model feedback transfer function
$\mathbf{H}_i$		Coefficients of like-orders from $\mathbf{N}_m(z)$
H_p	m	Paddle height
H_s	m	Significant waveheight
$I(t)$	A	Generator current
$I_{SP}(t)$	A	Setpoint current
J		Cost function
J_c		Cost function for use with equality constraints
J_P		Cost function for direct power maximisation
J_{SP}		Cost function for setpoint tracking
J_t	$\mathrm{kg\,m^2}$	Generator moment of inertia (rotor and turbine)
k		Discrete time iteration number
K		Pitot tube coefficient
k_{d_Δ}		D-gain for generic displacement loop
k_{d_v}		D-gain for generic velocity loop
K_{dac}		Digital to analog gain
k_{i_Δ}		I-gain for generic displacement loop
k_{i_v}		I-gain for generic velocity loop
K_{i_Ω}		I-gain for the velocity loop
K_{p_i}		Current loop P-gain
k_{p_Δ}		P-gain for generic displacement loop
k_{p_v}		P-gain for generic velocity loop

K_{p_Ω}		P-gain for the velocity loop
K_a	$\mathrm{A\,V^{-1}}$	Servo-drive input signal gain
K_e	$\mathrm{V\,s\,rad^{-1}}$	Generator electromotive force constant
$\mathbf{K}_{mpc}$		State feedback control gain vector
$\mathbf{K}_{ob}$		Observer gain matrix
K_t	$\mathrm{N\,m\,A^{-1}}$	Generator torque constant
K_y		Setpoint gain within $\mathbf{\Delta U}(k)$
K_Ω		Angular velocity scaling factor
L	H	Generator electric inductance
$\mathbf{L}(k)$		Vector of discrete time Laguerre functions at time instant k
$L_{33}(t)$	$\mathrm{N\,m\,s^{-1}}$	Radiation damping impulse response function for 3-3 coupling
$L_{39}(t)$	$\mathrm{N\,m\,s^{-1}}$	Radiation damping impulse response function for 3-9 coupling
$L_{93}(t)$	$\mathrm{N\,m\,s^{-1}}$	Radiation damping impulse response function for 9-3 coupling
$L_{99}(t)$	$\mathrm{N\,m\,s^{-1}}$	Radiation damping impulse response function for 9-9 coupling
m_3	kg	Mass of WRAM body
m_9	kg	Mass of water column
m_n	$\mathrm{m^2Hz^{n-1}}$	n^{th} spectral moment
$\dot{m}_t(t)$	$\mathrm{kg\,s^{-1}}$	Turbine mass flow rate
$\mathbf{M}$	kg	Mass matrix for the continuous wave-to-relative motion model
$\mathbf{M}_c$		Inequality constraint matrix
$\mathbf{M}_{c_{act}}$		Inequality constraint matrix with active constraints only
N		Number of Laguerre functions (network order)
N_c		Control horizon length
N_f		Number of frequencies in sea state spectra
N_p		Prediction window length
$\mathbf{N}_m(z)$		Partial LMFD decomposition of $\mathbf{G}_m(z)$
$p(t)$	Pa	Absolute chamber pressure
$p^*(t)$		Dimensionless chamber pressure
$p_{at}(t)$	Pa	Atmospheric pressure
p_{max}	Pa	Pressure upper range limit

p_{min}	Pa	Pressure lower range limit
$p_{out}(t)$	Pa	Measured pressure
$P(t)$	psig	Static line pressure
$P_g(t)$	W	Generator power
$P_t(t)$	W	Turbine power
$P_{WEC}(t)$	W	WEC absorber power
$\mathbf{Q}$		Quadratic optimisation matrix in RT MPC cost function
$\mathbf{Q}_P$		Quadratic optimisation matrix for direct power maximisation
Q_{pad}	$m^3\,s^{-1}$	Volumetric flow swept by paddle
Q_{rel}	$m^3\,s^{-1}$	Volumetric flow from WRAM model
Q_{scfm}	SCFM	Volumetric flow at Pitot tube
$\mathbf{Q}_{SP}$		Quadratic optimisation matrix for setpoint tracking
r	m	Paddle radial width
r_s		Setpoint amplitude at beginning of prediction window
r_w		Control action tuning parameter amplitude
R	Ω	Generator electric resistance
$R(s)$		Generic feedback model setpoint signal
$\overline{\mathbf{R}}$		Control action tuning matrix
$\mathbf{R}_L$		Control action tuning matrix in RT MPC cost function
$\mathbf{R}_s$		Setpoint signal over prediction window
s		Complex variable for FD transfer functions
$S(f)$	$m^2\,Hz^{-1}$	Spectral density
$S(\omega)$	$m^2\,s\,rad^{-1}$	Spectral density
S_s		Specific gravity at 60 °F
$T(t)$	°F	Temperature
T_e	s	Energy period
$T_g(t)$	N m	Generator torque
T_p	s	Peak period
T_s	s	Sample period for discretising the wave-to-relative motion model
$T_t(t)$	N m	Turbine torque

T_z	s	Zero-crossing period
$u(k)$		Discrete control signal for a generic SISO LTI model
$u_\Delta(t)$		Control output variable for generic displacement loop
$u_v(t)$		Control output variable for generic velocity loop
$\mathbf{U}^{max}$		Upper constraint limits on the control signal
$\mathbf{U}^{min}$		Lower constraint limits on the control signal
$\mathbf{U}_c(t)$	N	Wave-to-relative motion continuous model input
$\mathbf{U}_d(k)$	N	Wave-to-relative motion discrete model input
$\mathbf{U}_g(t)$		MIMO generator inputs
$\mathbf{U}_i(t)$		Current loop inputs
$\mathbf{U}_m(k)$		Inputs for $\mathbf{G}_m(z)$
$\mathbf{U}_\Omega(k)$		Inputs for non-augmented NMSS MIMO generator model
$\mathbf{U}_\Omega(s)$		Velocity loop inputs to $\mathbf{G}_g(s)$
$\mathbf{\Delta}\hat{\mathbf{U}}_\Omega$		Input for augmented NMSS MIMO generator model
$\mathbf{\Delta U}(k)$		Differential control signal vector over control horizon
$\mathbf{\Delta U}^{max}$		Upper constraint limits on the differential control signal
$\mathbf{\Delta U}^{min}$		Lower constraint limits on the differential control signal
$\mathbf{\Delta U}_{opt}(k)$		Optimal differential control vector over the control horizon
$\Delta u(k)$		Differential control signal for $u(k)$
V_0	m^3	Chamber volume at rest
$V_c(t)$	m^3	Chamber volume
$V_{out}(t)$	V	Measured pressure sensor voltage
$V_{pad}(t)$	m^3	Volume of a cylindrical sector swept by the paddle
V_s	V	Supply voltage for pressure sensors
x_{r_i}		i^{th} state of the radiation damping approximations
$\mathbf{X}(k)$		Augmented state variable for $\mathbf{X}_m$
$\mathbf{X}_c(t)$		State variable for continuous wave-to-relative motion model
$\mathbf{X}_d(k)$		State variable for discrete wave-to-relative motion model
$\mathbf{X}_g(t)$		MIMO generator state variable
$\mathbf{X}_m(k)$		State variable of a generic LTI model

$\hat{\mathbf{X}}_m(k)$		Estimated state variable for $\mathbf{X}_m(k)$
$\mathbf{X}_P(k)$		Augmented state variable for direct power maximisation
$\mathbf{X}_{SP}(k)$		Augmented state variable for setpoint tracking
$\mathbf{X}_\Omega(k)$		State variable for non-augmented NMSS MIMO generator model
$\mathbf{\Delta X}_m(k)$		Differential state variable for $\mathbf{X}_m(k)$
$\mathbf{\Delta}\hat{\mathbf{X}}_\Omega(k)$		Differential state variable for $\hat{\mathbf{X}}_\Omega(k)$
$y(k)$		Discrete output signal for a generic SISO LTI model
$y_{33}(t)$		State space approximation of $f_{rad_{33}}(t)$
$y_{39}(t)$		State space approximation of $f_{rad_{39}}(t)$
$y_{93}(t)$		State space approximation of $f_{rad_{93}}(t)$
$y_{99}(t)$		State space approximation of $f_{rad_{99}}(t)$
$Y(s)$		Generic feedback model output signal
$\mathbf{Y}(k)$		Outputs over prediction window
$\mathbf{Y}_c(t)$		Outputs for continuous wave-to-relative motion model
$\mathbf{Y}_d(k)$		Outputs for discrete wave-to-relative motion model
$\mathbf{Y}_g(t)$		MIMO generator outputs
$\mathbf{Y}_i(s)$		Current loop outputs from $\mathbf{G}_i(s)$
$\mathbf{Y}_m(k)$		Output vector for $\mathbf{G}_m(z)$
$\mathbf{Y}^{max}$		Upper constraint limits on the output
$\mathbf{Y}^{min}$		Lower constraint limits on the output
$\mathbf{Y}_\Omega(k)$		Output vector for non-augmented NMSS MIMO generator model
$\mathbf{Y}_\Omega(s)$		Velocity loop outputs from $\mathbf{G}_\Omega(s)$
$\hat{\mathbf{Y}}_\Omega(k)$		Output for augmented NMSS MIMO generator model
$z_3(t)$	m	Heave displacement of WRAM body
$z_9(t)$	m	Heave displacement of water column
$\dot{z}_Y$	$\mathrm{m\,s^{-1}}$	Velocity input to state space approximation of $f_{rad_{XY}}(t)$
γ_a		Specific heat ratio for air
γ		Inequality constraint vector
γ_{act}		Inequality constraint vector with active constraints only
$\Gamma_N(z)$		N^{th} function in the Laguerre network

$\zeta(t)$	m	Wave elevation
ζ_i	m	Wave amplitude of the i^{th} sea state spectral component
η_t		Turbine efficiency
$\boldsymbol{\eta}$		Laguerre coefficient vector
$\boldsymbol{\eta}_{opt}$		Optimal Laguerre coefficient vector
$\boldsymbol{\eta}_{opt_P}$		Optimal Laguerre coefficient vector for direct power maximisation
$\boldsymbol{\eta}_{opt_{SP}}$		Optimal Laguerre coefficient vector for setpoint tracking
$\theta(t)$	rad	Output shaft displacement
$\theta_r(t)$	rad	Paddle angle of rotation
$\theta_{SP}(t)$	rad	Setpoint shaft displacement
$\boldsymbol{\lambda_e}$		Closed-loop system eigenvalues
ξ		Turbine hub-to-tip ratio
Π_t		Turbine dimensionless power coefficient
$\rho(t)$	$\mathrm{kg\,m^{-3}}$	Chamber air density
$\rho_{at}(t)$	$\mathrm{kg\,m^{-3}}$	Atmospheric air density
$\rho_{in}(t)$	$\mathrm{kg\,m^{-3}}$	Inlet density at stagnation conditions
ϕ_i	rad	Random phase of the i^{th} sea state spectral component
$\boldsymbol{\phi}$		Discrete convolution sum for RT MPC formulation
Φ_t		Turbine dimensionless flow coefficient
$\boldsymbol{\Phi}$		Current prediction matrix for MPC
Ψ_t		Turbine dimensionless pressure coefficient
$\boldsymbol{\Psi}$		Linear Laguerre cost matrix
$\boldsymbol{\Psi}_P$		Linear Laguerre cost matrix for direct power maximisation
$\boldsymbol{\Psi}_{SP}$		Linear Laguerre cost matrix for setpoint tracking
ω	$\mathrm{rad\,s^{-1}}$	Angular frequency of sea state spectra
ω_i	$\mathrm{rad\,s^{-1}}$	Angular frequency of the i^{th} sea state spectral component
ω_p	$\mathrm{rad\,s^{-1}}$	Peak angular frequency of sea state spectra
$\Omega_t(t)$	$\mathrm{rad\,s^{-1}}$	Turbine angular velocity
$\boldsymbol{\Omega}$		Quadratic Laguerre cost matrix
$\Omega_{opt}(t)$	$\mathrm{rad\,s^{-1}}$	Optimal turbine setpoint velocity

$\Omega_{rev}(t)$	rev s^{-1}	Output velocity
$\Omega_{rev_{SP}}(t)$	rev s^{-1}	Setpoint velocity
$\mathbf{\Omega}_P$		Quadratic Laguerre cost matrix for direct power maximisation
$\mathbf{\Omega}_{SP}$		Quadratic Laguerre cost matrix for setpoint tracking

Dedicated to Christy and Sofía

Chapter 1

Introduction

1.1 Motivation

Maximising the power capture of wave energy converters (WEC) is crucial for reducing their levelised cost of energy (LCOE), which in turn contributes to economic viability. The control of wave energy devices has been extensively studied over the last several decades, however there is still a lack of convergence to a proven strategy or subset of strategies, suitable for deployment at sea. This is partly due to the lack of convergence towards a single WEC type, and partly due to the hesitation of wave energy developers to implement advanced control strategies.

The WEC under consideration in this research is the WRAM, fully described in Chapter 4. The fundamental physics of the WRAM are very similar to those of a floating point absorber with an oscillating water column (OWC). As such the control related issues are directly relevant to the WRAM. All WECs have several stages of power conversion from the wave-to-wire. In the case of OWC-like devices, the first controllable stage is the air plenum in the OWC chamber, where the pressure or volumetric flow rate are controlled. The next controllable stage is the turbine-generator set, where the turbine velocity or torque are controlled through the generator. It is important to control both of these stages, since both of their efficiencies can significantly affect the WEC's overall power output. Furthermore, each stage needs to be controlled within practical engineering constraints, such as maximum torques, velocity and power ratings.

Practical challenges are faced when implementing advanced control algorithms on sea-going WECs, for example some control algorithms are computationally intensive. This can

be challenging for systems with fast dynamics, such as electrical generators, whose industrial control systems cannot execute commands at the rates required by demanding control algorithms. Therefore, real-time computation is a vital requirement for any control algorithm, if it is to be implementable on a sea-going WEC. Other control challenges that exist for sea-going WECs include: power capture sensitivity to hydrodynamic model assumptions; PTO constraints and efficiencies; algorithm suitability for OWCs; and whether or not the WEC has multiple bodies.

Advanced control techniques can significantly contribute to the increase of power capture through active control of the PTO force. This force reacts against the WEC's motion, and when controlled optimally, leads to near resonant conditions where power capture is maximised. In order to achieve this the control tuning parameters need to be optimised, which are not always possible to determine analytically. Sensitivity analysis can be used to help identify the most important parameters, and subsequently their optimum values.

A reocurring theme with the advanced control of wave energy converters is the use of predictive control or wave climate prediction. While predictive techniques offer significant potential, not all of them are suitable for real-time implementation. Recent research has been conducted in wave energy regarding model predictive control (MPC), a constrained optimal control technique where PTO limits have typically been used as the constraints. A large barrier to achieving real-time computation with traditional MPC is the quadratic programming problem that can be very computationally intensive. This is especially true when controlling the PTO, which has much faster dynamics than that of the WEC absorber. This thesis investigates the fast MPC technique described in [1] by applying it to the WRAM's PTO, thereby addressing the issue of real-time MPC computation.

One reason that industrial-based wave energy developers hesitate to implement advanced control algorithms on sea-going WECs, is that there is often a large gap in the knowledge between design engineers and academic researchers. Effort needs to be made to bridge this gap and minimise the risk of sea-going failure. Real-time hybrid testing (RTHT) is a laboratory based testing approach that merges real-world technology with advanced control algorithms. Part of the research in this thesis is concerned with designing and building a RTHT rig for the WRAM, such that the risk associated with implementing advanced control

algorithms at sea can be reduced.

1.2 Research Aims

The current research is ultimately focussed on optimising the PTO efficiency of the WRAM wave energy converter. Furthermore, it is intended that the control algorithms formulated in this research will be capable of real-time execution on a sea-going prototype. The high level research aims are therefore defined as follows:

1. Devise control strategies for the WRAM, suitable for implementation on a sea-going prototype.

2. Bridge the gap between theory and practice, ensuring that control algorithms can be tested in the laboratory in real-time, prior to implementation on the sea-going prototype.

1.3 Research Questions

The following research questions were established at the outset as being key issues to address in the research: 1) What modelling approaches are best suited for each stage of the WRAM?; 2) Assuming the WRAM's absorber and PTO have different control requirements, what are the main features that a control algorithm should have for the WRAM's absorber?; 3) What are the sea-going challenges for controlling the WRAM's PTO, and hence what control algorithm should be adopted in this research?; 4) During the development of WEC control algorithms at the design stage, how can the financial risk for technology developers be reduced?; 5) In regards to real-time hybrid testing, which of the WRAM's conversion processes should be emulated on the emulation platform versus being numerically simulated on the RTHT system?

1.4 Research Objectives

In order to answer the above research questions, the following objectives were set: 1) Design a test facility, suitable for testing WEC control algorithms within a real-time hybrid

test framework; 2) Derive a wave-to-turbine model of the WRAM that combines standard practices in the wave energy community; 3) Develop a controllable plant model that encapsulates the generator-drive dynamics, installed on a WRAM emulation platform, that can be utilised to assess advanced control algorithms; 4) Formulate advanced control strategy(ies) based on existing approaches found in the literature; 5) Demonstrate the performance of a PTO control algorithm, with focus on real-time execution and sensitivity of the control tuning parameters for power capture.

1.5 Research Streams

Figure 1.1 shows the various streams undertaken in this research, which can be split into three main categories: 1) the WRAM model; 2) RT MPC applied to the PTO; and 3) the WRAM emulator. The WRAM model (wave-to-turbine) feeds into the PTO generator model, controlled by the RT MPC control algorithm. The WRAM emulator has been designed such that the control algorithm can, in the future, be tested on industrial hardware in a RTHT framework.

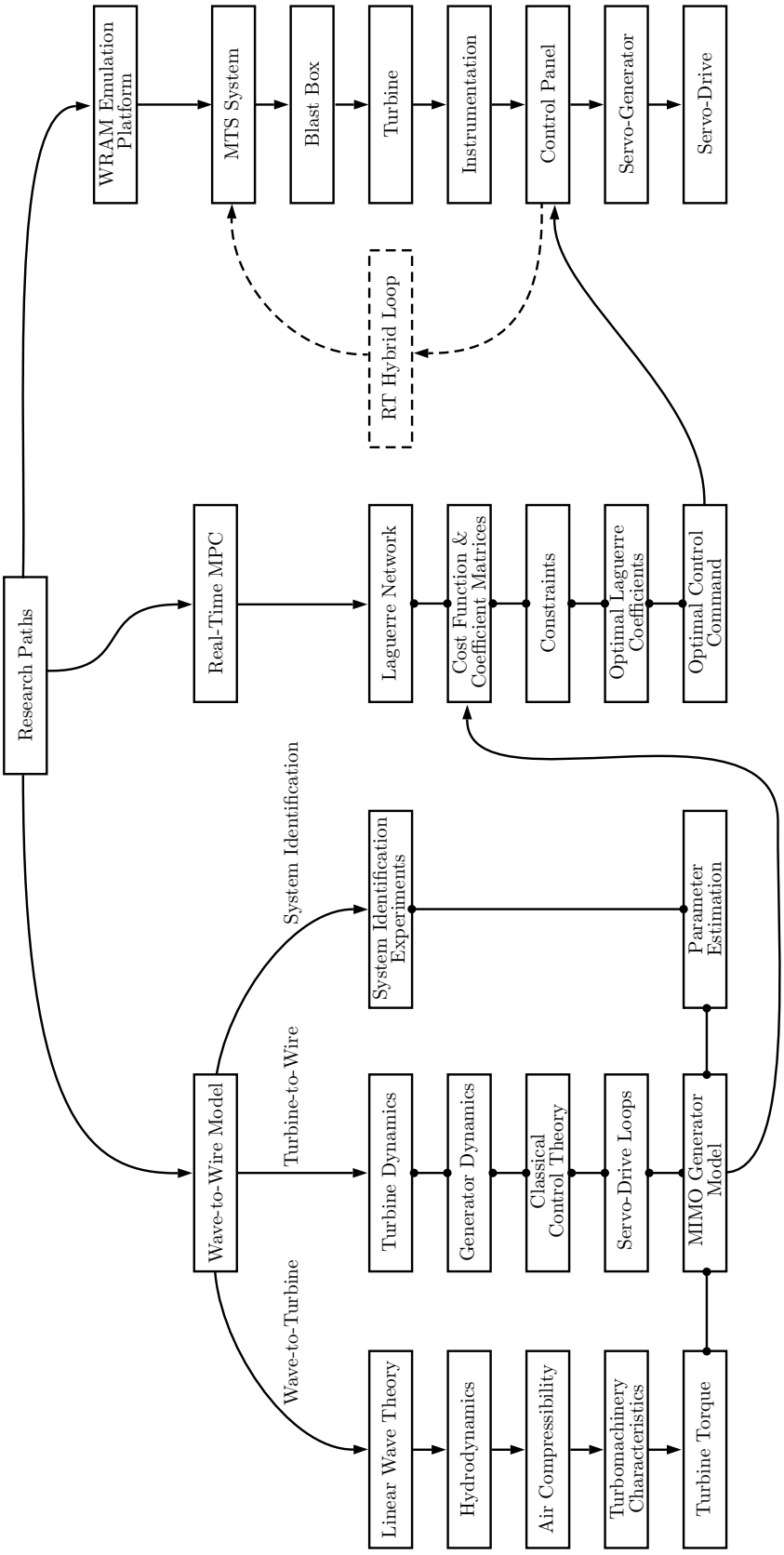

Figure 1.1: Research Streams.

1.6 Chapter Outline

Firstly, a review of the literature is provided in Chapter 2, aimed at identifying which of the widely studied optimal control strategies should be applied to the WRAM in the first instance. Historical context is established for the wave energy sector, highlighting the goals, challenges, and examples of some approaches. The chapter concludes with a discussion of key issues relating to the challenges faced when implementing control algorithms on sea-going WECs.

Chapter 3 provides the background into the fast MPC algorithm in [1], referred to as real-time MPC in this thesis. The chapter is split into two sections, where the first section presents the theory behind traditional MPC, and the second presents the theory behind the RT MPC algorithm. In contrast to traditional MPC, it is shown how Laguerre networks can be formulated into a closed-form MPC solution, thereby avoiding the necessity to solve the quadratic programming (QP) problem, the main bottleneck in traditional MPC problems.

An analytical model of the WRAM has been derived in Chapter 4, forming a core part of the thesis. The first part of the model includes the conversion process from the wave-to-turbine, where the model inputs are derived from an irregular sea state, assuming linear wave theory. The conversion stages include mechanical oscillation of the WEC absorber, hydrodynamics, pneumatics, and turbomachinery. The second part of the model is the turbine-to-wire model that represents the controlled plant, composed of the electrical generator and servo-drive. The adoption of system identification for estimating some of the model parameters is presented along with the resulting values. The model is then discretised and formulated into a non-minimal state space structure for subsequent use with the control algorithm.

Chapter 5 describes the concept and design of the WRAM emulator, beginning with a general overview of its functionality and architecture. This is followed by a breakdown of the conversion subsystems, with details provided for the instrumentation setup, calibration, data synchronisation and experimental results. Real-time hybrid testing is then discussed in terms of its concept, historical development and applications. Finally, the design details of the real-time hybrid test system are presented.

Chapter 6 provides the details of how control has been applied to the WRAM, with a distinction being made between control of the WRAM absorber and the PTO. This is followed by a high level control algorithm for the WRAM absorber being proposed for implementation on the first sea-going WRAM prototype. The algorithm concept is presented without further simulation or analysis, since the primary focus of this research is control of the PTO. Traditional MPC is then discussed in the context of controlling the PTO, highlighting some of the salient implementation challenges. It is then explained how the real-time MPC principles, described in Chapter 3, are applied to the WRAM. Two alternative optimisation cost functions are formulated, and the real-time algorithm steps are listed.

Chapter 7 presents the results of the modelling and control efforts conducted in this research. Section 7.1 to Section 7.3 show simulation results of the the wave-to-wire WRAM model described in Chapter 4. Section 7.4 shows the results from the RT MPC algorithm, with details provided for the performance assessment and sensitivity of the control tuning parameters. Comparisons are made for the two cost functions described in Chapter 6, and the algorithm's execution speed is benchmarked. Finally, Chapter 8 provides conclusions of the research.

1.7 Novelty of the Research

The novelty and contributions to the research community of this work can be summarised as follows:

- A new wave-to-wire model has been derived for an OWC-like wave energy converter, specifically the WRAM device. The various energy conversion stages are based on the fundamental physics associated with linear wave theory, oscillating systems, hydrodynamics, pneumatics, turbomachinery, electrical generation and classical feedback control.

- A test rig, described as the WRAM emulator, has been designed and built to emulate the bidirectional and irregular air flow of an OWC. The rig has also been integrated into a real-time hybrid test loop for the purpose of combining the installed PTO equipment and the simulated hydrodynamic WRAM model. This test rig is the first of its kind in the sense that it can emulate both oscillating and irregular air flow within a real-time hybrid testing framework.

- A real-time model predictive control technique, from [1], has been simulated for the installed PTO turbo-generator, which is treated as the controlled plant, where system identification has been used to determine its unknown empirical values based on measured open-loop responses. Control simulations show that real-time execution rates of faster than a millisecond are possible, by virtue of the fact that these rates have been achieved on a standard non-real-time PC. New branches of future research are opened up including: the effect of alternative cost functions on power capture; robust RT MPC for solving the WEC absorber control problem; fast QP solutions using Hildreth's algorithm on real-time microprocessors; ultra-fast execution using field programmable gate array (FPGA) computing; and real-time execution performance with industry standard programmable logic controllers (PLC).

Chapter 2

Literature Review

2.1 WEC Control Strategies

The vast majority of research into control for wave energy conversion has taken place since the 1970's. Initially, focus was placed on pure optimal control however it was soon realised that non-causality and practical constraints presented a problem for realisation. Suboptimal approaches then followed in the area of phase control, most of which still required prediction of the incident waves or excitation forces. See [2] for an example of this. Further details on these early research methods can be seen in [3]. Optimal command theory has also been applied to phase control since the 1980's [4] and continued to be used to the current day [5]–[8]. However these approaches are non-causal as they rely on future wave prediction, which is still an open research topic for realistic sea waves.

More recently there has been an increasing trend to develop causal strategies that can operate in real-time, or close to it. Some causal reactive control methods have been investigated in [9]–[15] and examples of causal phase control can be seen in [16], [17]. Many of these causal approaches, directly or indirectly, replace the non-causality with a stochastic measure while also removing computational complexities.

Other control approaches reviewed involve MPC [18], nonlinear programming [19], model-free reinforcement learning (RL) [20] and fault-tolerant control (FTC) [21]. The reader is also referred to a comprehensive review of WEC control in [22]. The following sections briefly describe the above mentioned control approaches after which a discussion is provided on their merits and pitfalls in the context of being applied to the WRAM device.

2.1.1 Optimal Control

A logical starting point when searching for an optimal energy extraction approach is to consider the theoretical optimum. Unfortunately, strict optimal control is not possible for real sea states due to the need for prediction, which is imperfect [3]. On the other hand, optimal control for regular waves can be achieved provided the two following conditions can be met [3]:

1. Phase control: the oscillating WEC's velocity is brought into phase with the excitation force. In the case of an OWC, this corresponds to the air pressure being in phase with the exciting volumetric flow.

2. Unconstrained amplitude control: the amplitude of oscillation is optimal when the power absorbed is equal to the power re-radiated away from the oscillating system with the most destructive interference.

Mathematically the above conditions can be represented by a complex mechanical 'source' impedance consisting of the oscillator's mechanical impedance, radiation impedance and a resistive loss [3]. Optimal absorption occurs when the PTO's 'load' impedance is equal to the complex-conjugate of the 'source' impedance [3]. It can be seen that non-causality comes from the non-causality of the optimum load impulse-response function [3].
Deviation from the above optimal conditions (towards more realistic sea states) necessarily results in suboptimal control. And while true optimal control is not realisable in practice it serves as a useful measuring stick against which we can assess the effectiveness of other suboptimal implementations.

2.1.2 Non-Causal Discrete Control

Discrete control in the current context refers to variations of bang-bang control where the control command can be switched between two discrete states. In wave energy this is usually labelled as either latching or declutching. The principal aim of the approach is to bring two quantities into phase with each other, for example the excitation force and absorber velocity in the case of a heaving point absorber, or alternatively the air pressure and volumetric flow of an OWC.

The first example presented here is a spherical OWC point absorber, described in [23]. The buoy is attached to the seabed via a mooring strut through which a latching mechanism operates. Submerged pressure measurements represent the excitation force, and a Kalman filter is used for wave prediction and determination of the unlatching instants.

In [5], latching control is applied to the SEAREV device [24] using optimal command theory based on Pontryagin's Maximum Principle (PMP). It is reported that assuming accurate excitation force predictions can be obtained, this control method offers significant energy capture gains. The authors of [5] claim however that real-time implementation of the optimal command method on a full scale device at sea is unrealistic, since approximately 100 seconds of predicted wave excitation are needed.

Declutching was subsequently applied to the SEAREV device in [6] using the same PMP control approach. Declutching is similar to latching in that it is a type of discrete bang-bang control, however instead of locking the device to prevent motion it allows the WEC to freewheel, during which times the energy transfer is bypassed around the PTO. The performance of declutching is compared to that of a pseudo-continuous scheme with positive results. While the control algorithm shows good theoretical performance the authors again reiterate that it is not suitable as implemented, for use in the real world due its need for excitation force prediction. Instead, it is proposed that future research efforts should focus more on causal algorithms.

Latching control is once again applied in the same manner to the SEAREV device in [8] however this time investigating how an actuation time constant, applied to the latching brake affects power performance. The sensitivity of latching performance to the timing of latching / unlatching instants was demonstrated to be significant.

Latching control was applied to the OWC spar-buoy in [7] using PMP, using receding horizon to limit the length of predicted control commands. Hardware-in-the-loop (HIL) testing was conducted, and wave prediction was acknowledged as still being an open problem for floating OWC spar-buoys.

2.1.3 Causal Reactive Control

In [11] it is investigated how control strategies and PTO constraints affect the power capture of a direct-drive spherical point absorber. The two control strategies considered are passive damping and causal reactive control for irregular waves. In the latter case a constant load impedance was used such that its reactance would be optimal for a regular wave with a frequency corresponding to the peak frequency of a Bretschneider spectrum. Considered also, were the effects of the PTO power rating, power saturation and non-ideal PTO efficiencies. It was found that applying power saturation in the control command can facilitate derating the PTO without significant reduction in overall performance. It was also found that non-ideal PTO characteristics could make passive control perform better than optimal reactive control.

A causal reactive control method is devised in [12] for a bottom-referenced point absorber, where the non-causal relationship between excitation force and velocity is replaced with a coefficient of proportionality. This is achieved through the process of model reduction of the WEC to a second order model based on the WEC's dominant second order dynamics. Radiation damping then becomes frequency independent, leading to causal control. A low-level velocity following control loop for the WEC can then be constructed using standard proportional-integral-derivative (PID) control.

An optimal causal feedback controller is devised in [9] for a single degree-of-freedom (DoF) bottom-referenced point absorber, where the main idea is to force the absorber's velocity into phase with the excitation force. The optimal control law works on the basis of creating a constant control gain to replace the non-causal integral in the optimal control force. The optimal gain factor is calculated as the integral of the excitation force's auto-correlation coefficient multiplied by the impulse response function for the radiation force. Furthermore, it is assumed that the PTO can provide a control force without significant time delay or saturation problems. Hence it must operate in both generation and motoring modes. A closed-loop feedback controller for the control force relies on measurements of the present displacement, acceleration and all past velocities of the absorber.

A suboptimal approximation of reactive control is applied to a bottom-referenced point

absorber in [10] using a simple method for dealing with the non-causality and PTO constraint problems. Once again the frequency dependent transfer function between excitation force and velocity is replaced with a constant gain and is based on the peak frequency of the excitation force. Hence the approach is similar to that in [11] and comes with the assumption that the irregular sea spectrum is narrow-banded. A velocity constraint is included in the algorithm such that the control gain becomes piecewise variable depending on whether the constraint is to be prioritised.

The effect of non-ideal PTOs on the performance of reactive control is also investigated in [15]. Partial reactive control is used, as in [11], on a single DoF bottom-referenced point absorber with two actuators linking it to the reference. The first is a passive linear damper and the second is for reactive control. An efficiency factor is applied to the control force representing the PTO efficiency.

2.1.4 Causal Discrete Control

Latching is applied to a fixed OWC in [17] where the unlatching instants are determined using an 'unlatching threshold' of the excitation force. This follows on from previous work by Falcão [25] which used the hydraulic piston pump pressure of the PTO rather than the excitation force. The latching mechanism was a shut-off valve at the top of the chamber. In [17] the control decision for latching / unlatching is as follows: the valve closes when the inner velocity goes through a zero-crossing; and opens when the excitation force crosses a threshold. The wave elevation just outside the chamber is used for determining when the threshold is crossed and assumes negligible phase difference with the excitation force.

Latching is applied to a bottom-referenced point absorber in [16], where rather than using wave prediction to decide the latching duration, a statistical method is used to simplify its implementation. This causal control approach uses an irregular sea state's characteristic period, for determining the latching duration defined to be either the peak period, T_p, energy period, T_e, or zero-crossing period, T_z. Results showed that energy maximisation was best when T_e was used, and also that latching provided significant power gains. It was found that optimal damping is somewhat insensitive to the characteristic period, suggesting

that once the optimal value is found for one sea state, it is also found for several. Interestingly, optimal damping as calculated in regular waves led to sensitivity problems with the latching duration when applied to irregular waves. Further, optimal damping did not provide maximum energy capture for irregular waves, with the examples showing that larger damping values were preferable.

2.1.5 Other Control Strategies

An optimal control method is devised in [19] for maximising the energy capture of a two-body self-reacting point absorber subject to amplitude restriction. The PTO is assumed to be continuously variable with typical excursion constraints similar to those of linear generators and hydraulic rams. The constrained optimisation problem is transformed into a Nonlinear Program (NLP) through the discretisation of the PTO force and motion of the bodies. Discretisation is approximated with linear combinations of basis functions that govern the properties of the cost function and constraint. An orthogonal basis was formed using a Fourier series, leading to a quadratic and concave cost function, guaranteeing convergence and quick execution. The method does however rely on excitation force prediction.

A causal reinforcment learning strategy is adopted in [20] to optimise a point absorber's mean power capture on a sea state-by-sea state basis. A model-free Q-learning algorithm is used to decide the optimal PTO damping, and is held fixed over the duration of a sea state. The control algorithm reacts to the WEC motion in a passive manner, where displacement and force constraints are also included in the formulation. The optimisation loop does not rely on an identified model, but rather uses states, actions and rewards to determine the optimal control command in real-time. In combination with the environment, this results in a change in the WEC's mean power capture, where a newly calculated state is fed back into the Q-learning algorithm, thus closing the loop. An important benefit of the algorithm is that it can adapt to physical WEC changes over time, for example marine growth, that affects the WEC's hydrodynamics. The model-free approach is therefore immune to such physical changes, demonstrating itself as a good example of model-insensitive control. The results show the RL algorithm converging to the optimal control case in reasonable time, and factors are also discussed regarding the algorithm's convergence properties.

Adaptive impedance tuning control has been implemented and tested in a wave flume, on a simple bottom-referenced point absorber [13] with a tubular permanent magnet linear generator (TPMLG) PTO. It is controlled with the objective of maintaining a small phase shift between the estimated wave excitation and WEC velocity, thereby maximising power capture. The mechanism through which the PTO is controlled is to continuously vary the electrical load impedance with a variable resistor-inductor-capacitor. The control method is reported to achieve acceptable power conversion and motion limitations, in addition to maintaining good performance of the position and electrical current tracking for the TPMLG.

Fault-tolerant control (FTC) is an area that has not received significant attention in wave energy, as it has in wind energy [26], and could prove to be quite beneficial for real sea-going technology. Potential benefits of FTC, presented in [21], include: the potential cost savings through preventative maintenance; analytical redundancy for excitation force estimation; fault estimation and compensation for improved power efficiency; and the ability of handling system faults on-line through active FTC.

Model predictive control has been applied in [18] to a bottom-referenced point absorber with idealised PTO. The MPC formulation is set up to reward energy maximisation while penalising reactive flow back into the WEC due to the control function. Observability of the system allows estimation of the wave-excitation force by soft sensing. The algorithm can also handle displacement and velocity constraints. It is intended that the approach remedies some shortcomings of other algorithms such as reactive control and latching. The issues highlighted for latching include the lack of assessment with electrical PTOs and potential inadequacy in large arrays.

Constrained pseudospectral control is presented in [27] as an alternative to MPC, addressing its real-time computational burden. The algorithm differs from prior pseudospectral techniques by using half-range Chebyshev Fourier (HRCF) basis functions to circumvent the Gibbs phenomenon that occurs due to discontinuities at the boundaries of the receding horizon. Through the case study of a flap-type WEC, results showed that the controller could operate in real-time, with energy capture rates approaching the theoretical optimum. As part of the study, a comparison was made with other basis function sets, demonstrating that an appropriate basis function is needed to allow for transient and steady

state signals. It was concluded that the HRCF basis function set is well suited to the wave energy control problem, since the excitation forces and system variables can be modelled well with harmonic signals [27].

2.1.6 Model Predictive Control in Wave Energy

Model predictive control is a powerful tool that provides an optimal control framework, where solutions can be found within specified operational constraints. See [1], [28] for explanations of the fundamental principles. In traditional MPC a quadratic cost function is used for optimal setpoint tracking, where relative weighting is applied between the optimisation goal and control signal. Prediction and control horizons are built-in to the formulation, such that the plant's behaviour is predicted over a *prediction window*, in response to the algorithm's calculated control command over a *control horizon*. Within the receding horizon framework, only the control command at the next time step is actuated before the prediction is re-calculated, after which the algorithm advances to the next step. With constrained optimal control, the control command is calculated while attempting to ensure that the defined constraints are satisfied. Depending on how the constraints are defined, it may not be possible to satisfy them all simultaneously. This can occur spuriously and unpredictably, at times when competing constraints are active.

MPC has been researched in the wave energy field only very recently, where initially traditional MPC was adopted. An example of this can be seen in [29], where the technique was applied to a point absorber to optimally track the WEC velocity, subject to velocity and displacement constraints. This preliminary study proposed MPC to be very attractive for wave energy applications, however it focussed simply on its benefits without real consideration of the challenges, including the difficulty with reliable excitation force prediction, and the computational demands of the algorithm.

In spite of the potentially high gains for the WEC absorber's power capture, challenges exist with the implementation of MPC at a practical level, as is indeed the case with other control techniques. This can partly be explained by a reluctance of WEC developers to trial what they perceive to be complicated algorithms on expensive sea-going machinery. It is also the case that most mathematical approximations of the absorber significantly differ

from real world physics. In this regard, MPC has been shown to be particularly sensitive to the quality of approximation of the WEC radiation damping [30], [31]. Also, early implementations of MPC in wave energy were particularly hindered by the challenges associated with excitation force prediction. In part, this was due to the lack of reliability in the prediction technology. It was also due to uncertainties introduced by irregular waves, prediction error and model inaccuracy, making the implementations susceptible to infeasibility and instability problems [32].

The results from physical tank tests of a 20th scale point absorber, reported in [33], corroborate the stipulations in [32], where the challenge of implementing MPC on real WECs was clearly demonstrated. It is reported that the MPC algorithm captured 10% less power than a simple PI control strategy. While there is uncertainty regarding the exact cause of the poor performance, attention is drawn in [33] towards imperfect modelling and excitation force prediction inaccuracies, when the control algorithm is used in real life environments. Concerns were also raised regarding the high amounts of unaccounted friction in the physical model, and also the time delay associated with estimating the excitation force. It should be noted that the frictional forces are likely to be much higher as a percentage of the operational PTO forces on the 20th scale model, compared with the full scale WEC. Also, the dynamics of the 20th scale model are much faster than those of a full scale device. For both of these issues, it can be expected that the challenges experienced in the tank testing campaign would not be as prominent at full scale.

One of the main barriers for the real-time control of many systems is the computational burden associated with calculating the optimal control command, while satisfying constraints in the solution. Quadratic programming is often utilised to solve these calculations. Some early examples of WEC applications that use this approach can be seen in [29] and [18]. It should be noted that the MPC algorithm in [18] was reported in [31] to be executable in real-time at full scale in a particular WEC case study. Another approach in [34] introduced nonlinear moorings into a previously linear WEC model, leading a to nonlinear MPC implementation. This resulted in computation times that were deemed unsuitable for real-time application.

Other research has sought to speed up MPC in WEC applications, for example [30],

which implemented a move-blocking technique that reduces the number of free variables in the control horizon. The resulting solve times in [30] were, on average, approximately 50 ms for unconstrained simulations, even for large control horizons. For constrained systems it was much higher, ranging from approximately 90 ms to 740 ms. Also, there was a steep trend between the lower and upper values, indicating a strong motivation to keep the length of the control horizon very low. A caveat was provided however, that care was needed with low control horizons. It was found that low horizons could affect the control signal damping to the point that the risk of constraint violation would be heightened, leading to potential damage. This was concluded to be an issue when considering the effects of mismatched systems, where 'mismatched' refers to a discrepancy between the actual WEC physics and the WEC model incorporated into the MPC formulation.

The well-known challenge of real-time computation with MPC was the main focus in [31], that compared the performance of MPC in [18] with the receding horizon pseudospectral optimal control (RHPSC) in [27]. In that study, both algorithms are applied to a heave-only WEC for both constrained and unconstrained cases. It was shown that the computation time for MPC was three times slower than that of RHPSC, where MPC computation times ranged from 15 ms to 100 ms depending on the wave period, and those for RHPSC ranged from 5 ms to 25 ms. It was concluded that both algorithms would be capable of executing in real-time on sea-going WECs, given the relatively slow dynamics. It was also found that the performance of both algorithms was very sensitive to the approximation quality of the radiation force, such as when state space approximations are used. Also, the robustness of highly tuned numerical optimal WEC controllers was reported to still be an open research area [31].

The topic of fast MPC has been researched in [35], where the focus was to speed up the online QP optimisation computation. The approach taken was to formulate an approximate primal barrier method by varying the basic infeasible-start primal barrier method. The fundamental principle of the speed increase was to not compute the QP problem to full accuracy. Interestingly, the reduced accuracy did not cause a significant deterioration in the quality of the MPC control, while at the same time drastically speeding up the computation. The reported computation times for three very different example cases were 5 ms, 12 ms and

25 ms.

From the literature we can see that the application of MPC is relatively new in wave energy, and is ideally suited to the slow dynamics of WEC absorbers. Key issues in the literature include MPC's computational burden, excitation force prediction, numerical modelling sensitivities for MPC when used in real life environments, numerical robustness, and comparisons with other optimal control techniques.

The vast majority of MPC research in wave energy has been associated with controlling the WEC absorber, rather than the PTO. Most of the literature implies that real-time MPC is only possible when controlling the absorber. The outcomes of [35] suggest that it could also be possible for the PTO, given the fast computational speeds achieved in that study. Another technique for implementing fast MPC, described in [1], is the main focus of PTO control in this thesis. Simulation results in this research have shown that computation times at fractions of a millisecond, executed in MATLAB®, are achievable. Chapter 3 explains the theory behind the approach.

2.2 Control Challenges for Sea-Going WECs

The following section provides a discussion of the pertinent issues for selecting a suitable control strategy for the WRAM. Given the wide variety of WEC-PTO combinations there is no one-strategy-fits-all approach and so the various issues need to be assessed in the context of the particular WEC being considered, in this case WRAM.

2.2.1 Model Sensitivity

Model accuracy is crucial for model-based control strategies, which is used in the vast majority of applications in the literature. Example strategies include reactive control, optimal command theory (used for some bang-bang implementations) and MPC. With bang-bang control, it has been shown that power performance can be highly sensitive to the timing instants of switching [8],[16]. Prediction strategies based on linear wave theory produce wave elevations significantly different to what is observed in real sea waves. Model inaccuracies can be compounded by prediction errors even when bounded by confidence intervals as in [36]. One possible way to reduce the impact of model-sensitive strategies for model-based

control is to use adaptive approaches that update model parameters over time per sea state. Such strategies could use observer models that operate on measured quantities, thus leading to more robust implementations for real sea applications. It is reasonable to expect that the real-time computational efforts would significantly decrease over time as the parameters become better adapted to the sea conditions [20].

2.2.2 PTO Constraints and Efficiencies

The effects of non-ideal system imperfections have shown also to have a significant effect on power production [8],[11],[15]. Not only do these imperfections further add to inaccuracies if not modelled correctly but they also increase the risk of device failure. Hence it is vital that sea-going WECs include these non-ideal properties in their optimisation algorithms.

2.2.3 Real-Time Capability

Often, non-causal control techniques rely on wave or excitation force prediction, for example optimal command theory that is structured around Pontryagin's maximum principle. This type of approach results in a large computational burden for real-time systems [5], [6], and has been reported to be unrealistic for sea-going WECs [5], [6]. It is worth noting however that the longer time frame associated with average wave periods at full scale is likely to be more forgiving for computationally intensive algorithms. Also, fast computing resources are continually improving and indeed FPGA technology can certainly already deal with the fast real-time calculations, albeit at the cost of more complicated programming style and compilation methods. Therefore computationally intensive control strategies should not necessarily be ruled out from that viewpoint alone but should be considered among the engineering design trade-offs. From a testing perspective, real-time hybrid testing provides an elegant way of confirming the control approach in the safe and economic environment of the laboratory.

2.2.4 Suitability for OWCs

Since the WRAM's PTO is similar to other floating OWC point absorbers the choice of algorithm must obviously be suitable for OWCs. This rules out approaches designed for direct-drive PTOs while reactive control is also unsuitable [7]. Furthermore, air compressibility [7] and large air pressure fluctuations [16] where bang-bang control is used need to be dealt with.

2.2.5 Multiple Bodies

Multibody WECs can increase the control challenge for several reasons. The relative forces between each degree-of-freedom can become mutually restrictive, frictional energy can be wasted through the linkages, and the control algorithm can become less effective. For example, a two-body heaving point absorber will have mechanical bearings that align each body in relative heave. When the device simultaneously experiences heave and pitch motion, the frictional forces will be high, leading to the abovementioned inefficiencies. In contrast, the WRAM is somewhat immune to this problem, firstly because it is a single body WEC without large bearings, but also because the air chamber pressure is omnidirectional, and therefore the air is not directionally inhibited from travelling through the PTO. Air compressibility does however pose a control challenge due to the phase delay introduced between the absorber's motion and air flow. It is important that this issue is addressed [7].

2.2.6 Algorithm Complexity

Complex control algorithms can place a significant burden on real-time control systems. However, if they can provide achievable and robust solutions, then they should be weighted highly in the design trade-off process, since they have the potential to maximise energy capture quite well. It is considered here that a complex algorithm is one that requires a high number of calculations within the sample time of a real-time control system. For example, some algorithms that use optimal command theory converge to a solution by simulating several iterations of a predicted model over a relatively long time window. This results in a high number of calculations, placing a high computational load on the real-time control system. As such, algorithm complexity needs to be treated with caution, and this perhaps

explains why there have been increased research efforts into causal strategies, such as those mentioned in Sections 2.1.3 and 2.1.4.

Chapter 3

Real-Time MPC Background

While MPC has been described above as having potential for the PTO control problem, the main obstacle is overcoming the computational burden. The current research applies the fast MPC framework in [1] to WRAM's PTO control problem. The principles are explained in this chapter and its application for WRAM are presented in Chapter 6. The main features can be summarised as follows.

Firstly, discrete linear time-invariant (LTI) models of the plant are used in the optimisation problem, which immediately provides a time cost saving since integration in real-time is avoided. For cases where the QP problem must be solved, Hildreth's algorithm can be used to quickly eliminate inactive constraints, thus reducing the required number of calculations. The most significant time savings however are made through the use of discrete Laguerre functions in the MPC formulation [37] that drastically reduce the computational effort in the prediction calculations. Additional time savings can be made by using a non-minimal state space (NMSS) representation of the system where the inputs and outputs are used as the state variables. This eliminates the need for an observer since the states variables are measurable. Further time savings can be made from the avoidance of solving the QP problem altogether if the constraints can be reduced to a single control signal. This is made possible through the use of a closed-form solution to the constrained control problem. The closed-form solution has another trade-off in that only one active constraint can be active at a time, where multiple active constraints need to be prioritised. This framework allows up to three constraints, namely, the control command, change of control or output.

The basic theory behind the real-time MPC formulation used in this research is now

presented. The motivation for deviating from the traditional approach is to be able to implement MPC on real-time microprocessors. In the context of the WRAM, RT MPC is being applied to the electrial generator, mechanically coupled to the turbine where the angular velocity is the controlled variable. Since constrained optimisation of the generated power is desired, MPC provides an ideal solution if it can be made to run in real-time. Most of the theory in this chapter comes from [1] which should be referred to for further detail, derivations and examples.

3.1 Traditional MPC

To begin with, traditional MPC is briefly discussed such that the deviation of the RT MPC approach can be seen. Also, the context is limited here to discrete-time models since they naturally execute faster.

3.1.1 Plant Model

Traditional MPC is typically concerned with controlling a plant such that the output tracks a given setpoint with minimal error. A SISO plant may be described by the following state space equations:

$$\begin{aligned} \mathbf{X}_m(k+1) &= \mathbf{A}_m\mathbf{X}_m(k) + \mathbf{B}_m u(k) \\ y(k) &= \mathbf{C}_m\mathbf{X}_m(k) \end{aligned} \tag{3.1}$$

where:

k:	Discrete time iteration number.
$u(k)$:	Current input.
$y(k)$:	Current output.
$\mathbf{A}_m$:	State matrix.
$\mathbf{B}_m$:	Input matrix.
$\mathbf{C}_m$:	Output matrix.
$\mathbf{X}_m(k)$:	State variable for the current iteration.
$\mathbf{X}_m(k+1)$:	State variable for the next iteration.

It should be noted that the $\mathbf{D}_m$ term from the plant model has been set to zero. This is based on the principle that with receding horizon control, the current plant information is required for prediction and control, and therefore the input cannot directly affect the output at the same time [1]. To achieve setpoint tracking an integrator is embedded into the plant where the states and input are modified to become state and input changes. The state variable is augmented with the output to become:

$$\mathbf{X}(k) = [\Delta\mathbf{X}_m(k)^T \quad y(k)]^T \tag{3.2}$$

$$\mathbf{X}(k+1) = [\Delta\mathbf{X}_m(k+1)^T \quad y(k+1)]^T \tag{3.3}$$

where:

$\Delta\mathbf{X}_m(k)$: Differential state variable for $\mathbf{X}_m(k)$.

$\mathbf{X}(k)$: Augmented state variable for $\mathbf{X}_m(k)$.

The augmented state space equations then become:

$$\begin{aligned} \mathbf{X}(k+1) &= \mathbf{A}\mathbf{X}(k) + \mathbf{B}\Delta u(k) \\ y(k) &= \mathbf{C}\mathbf{X}(k) \end{aligned} \tag{3.4}$$

where:

$\Delta u(k)$: Differential input signal for $u(k)$.

A: Augmented state matrix.

B: Augmented input matrix.

C: Augmented output matrix.

$$\mathbf{A} = \begin{bmatrix} \mathbf{A}_m & \mathbf{O}_m^T \\ \mathbf{C}_m\mathbf{A}_m & \mathbf{I} \end{bmatrix}, \quad \mathbf{B} = \begin{bmatrix} \mathbf{B}_m \\ \mathbf{C}_m\mathbf{B}_m \end{bmatrix}, \quad \mathbf{C} = \begin{bmatrix} \mathbf{O}_m & \mathbf{I} \end{bmatrix}, \quad \mathbf{O}_m = [0 \dots 0] \tag{3.5}$$

3.1.2 Prediction Window

At each time step MPC calculates the next control signal to apply for optimising the predicted plant output over a specified time window. The output is predicted over N_p samples and is a function of the current state, $\mathbf{X}(k)$, and the future control trajectory, $\mathbf{\Delta U}$, in response

to a specified number of control signals, N_c. From the augmented system matrices in (3.5), the predicted state variable at time instant $k + N_p$, given the value at the current instant k is:

$$\begin{aligned}\mathbf{X}(k+N_p|k) &= \mathbf{A}^{N_p}\mathbf{X}(k) + \mathbf{A}^{N_p-1}\mathbf{B}\Delta u(k) + \mathbf{A}^{N_p-2}\mathbf{B}\Delta u(k+1) \\ &+ \cdots + \mathbf{A}^{N_p-N_c}\mathbf{B}\Delta u(k+N_c-1)\end{aligned} \tag{3.6}$$

The predicted output variable at instant $k + N_p$ are:

$$\begin{aligned}y(k+N_p|k) &= \mathbf{C}\mathbf{A}^{N_p}\mathbf{X}(k) + \mathbf{C}\mathbf{A}^{N_p-1}\mathbf{B}\Delta u(k) + \mathbf{C}\mathbf{A}^{N_p-2}\mathbf{B}\Delta u(k+1) \\ &+ \cdots + \mathbf{C}\mathbf{A}^{N_p-N_c}\mathbf{B}\Delta u(k+N_c-1)\end{aligned} \tag{3.7}$$

By defining the predicted output and control vectors as:

$$\mathbf{Y} = [y(k+1|k), \quad y(k+2|k), \quad \ldots \quad , y(k+N_p|k)]^T \tag{3.8}$$

$$\mathbf{\Delta U} = [\Delta u(k), \quad \Delta u(k+1), \quad \ldots \quad , \Delta u(k+N_c-1)]^T \tag{3.9}$$

the output prediction matrix can be expressed as:

$$\mathbf{Y} = \mathbf{F}\mathbf{X}(k) + \mathbf{\Phi}\mathbf{\Delta U} \tag{3.10}$$

where:

- $\mathbf{Y}$: Output signal vector over the prediction window.
- $\mathbf{\Delta U}$: Differential control vector over the control horizon.
- $\mathbf{F}$: State matrix block for MPC.
- $\mathbf{\Phi}$: Input matrix block for MPC.

$$\mathbf{F} = \begin{bmatrix} \mathbf{C}\mathbf{A} \\ \mathbf{C}\mathbf{A}^2 \\ \mathbf{C}\mathbf{A}^3 \\ \vdots \\ \mathbf{C}\mathbf{A}^{N_p} \end{bmatrix}, \quad \mathbf{\Phi} = \begin{bmatrix} \mathbf{C}\mathbf{B} & \mathbf{0} & \mathbf{0} & \ldots & \mathbf{0} \\ \mathbf{C}\mathbf{A}\mathbf{B} & \mathbf{C}\mathbf{B} & \mathbf{0} & \ldots & \mathbf{0} \\ \mathbf{C}\mathbf{A}^2\mathbf{B} & \mathbf{C}\mathbf{A}\mathbf{B} & \mathbf{C}\mathbf{B} & \ldots & \mathbf{0} \\ \vdots & \vdots & \vdots & & \vdots \\ \mathbf{C}\mathbf{A}^{N_p-1}\mathbf{B} & \mathbf{C}\mathbf{A}^{N_p-2}\mathbf{B} & \mathbf{C}\mathbf{A}^{N_p-3}\mathbf{B} & \ldots & \mathbf{C}\mathbf{A}^{N_p-N_c}\mathbf{B} \end{bmatrix} \tag{3.11}$$

3.1.3 Unconstrained Optimal Control

When the optimisation goal is to achieve setpoint tracking, the cost function, J, is defined as:

$$J = (\mathbf{R}_s - \mathbf{Y})^T(\mathbf{R}_s - \mathbf{Y}) + \mathbf{\Delta U}^T\overline{\mathbf{R}}\mathbf{\Delta U} \tag{3.12}$$

where $\mathbf{R}_s$ represents the setpoint signal over the whole prediction window, using the setpoint value at the beginning of the prediction window, $r_s(k)$. $\mathbf{R}_s$ is defined as:

$$\mathbf{R}_s = r_s(k)[1 \quad 1 \quad \dots \quad 1]^T \tag{3.13}$$

The diagonal matrix $\overline{\mathbf{R}} = r_w\mathbf{I}_{N_c \times N_c}$ acts as a tuning parameter where a high value of r_w has the effect of penalising fast changes in the control signal rather than simply reducing the tracking error as much as possible. The optimal control sequence is found by minimising J with respect to $\mathbf{\Delta U}$ such that:

$$\frac{\partial J}{\partial \mathbf{\Delta U}} = 0 \tag{3.14}$$

After substituting (3.10) into (3.12) minimisation leads to:

$$\mathbf{\Delta U}_{opt} = (\mathbf{\Phi}^T\mathbf{\Phi} - \overline{\mathbf{R}})^{-1}\mathbf{\Phi}^T(\mathbf{R}_s - \mathbf{F}\mathbf{X}(k)) \tag{3.15}$$

where:

$\mathbf{\Delta U}_{opt}$: Optimal control vector over the control horizon.

3.1.4 Closed-Loop Feedback

Considering that the approach of receding horizon control only implements the first value of $\mathbf{\Delta U}_{opt}$ at each time step, equation (3.15) can be revised to be:

$$\mathbf{\Delta U}(k) = \overbrace{[1\ 0\ \dots\ 0]}^{N_c}\mathbf{\Delta U}_{opt} \tag{3.16}$$

This can be manipulated into the standard form of LTI state feedback control in terms of the current setpoint, $r_s(k)$, and augmented state variable, $\mathbf{X}(k)$, such that:

$$\mathbf{\Delta U}(k) = K_y r_s(k) - \mathbf{K}_{mpc}\mathbf{X}(k) \tag{3.17}$$

where K_y is the setpoint gain within $\mathbf{\Delta U}(k)$. The state feedback control gain vector, $\mathbf{K}_{mpc}$, is therefore:

$$\mathbf{K}_{mpc} = \overbrace{[1\ 0\ \dots\ 0]}^{N_c}(\mathbf{\Phi}^T\mathbf{\Phi} - \overline{\mathbf{R}})^{-1}\mathbf{\Phi}^T\mathbf{F} \tag{3.18}$$

Substituting (3.17) into (3.4) gives the closed-loop system equation:

$$\mathbf{X}(k+1) = (\mathbf{A} - \mathbf{B}\mathbf{K}_{mpc})\mathbf{X}(k) + \mathbf{B}K_y r_s(k) \tag{3.19}$$

and the eigenvalues, $\boldsymbol{\lambda_e}$, can be found from the closed-loop characteristic equation:

$$\det[\boldsymbol{\lambda_e}\mathbf{I} - (\mathbf{A} - \mathbf{B}\mathbf{K}_{mpc})] = \mathbf{0} \tag{3.20}$$

3.1.5 State Estimation

As can be seen from equation (3.15) predictive control depends on the state variable. Since the states are not always measurable, observers can be used to estimate them from the control signals and outputs. The estimated state equation is composed of an expression for the model and an expression to correct for the estimation error. The difference equation for the estimated state variable, $\hat{\mathbf{X}}_m$, is:

$$\hat{\mathbf{X}}_m(k+1) = \overbrace{\mathbf{A}_m\hat{\mathbf{X}}_m(k) + \mathbf{B}_m u(k)}^{model} + \overbrace{\mathbf{K}_{ob}(y(k) - \mathbf{C}_m\hat{\mathbf{X}}_m(k))}^{correction\ term} \tag{3.21}$$

The observer gain, $\mathbf{K}_{ob}$, controls the convergence rate of the error. Assuming the system is observable, for a single-output system $\mathbf{K}_{ob}$ can be found with the pole-placement method using the characteristic equation of the closed-loop error equation:

$$\det[\lambda_e\mathbf{I} - (\mathbf{A}_m - \mathbf{K}_{ob}\mathbf{C}_m)] = \mathbf{0} \tag{3.22}$$

For a multi-output system, $\mathbf{K}_{ob}$ can be calculated recursively using a Kalman filter. While observers can provide very good state estimation they have some disadvantages such as the additional computational load, and for unobservable systems, the fact that not all states can be estimated.

3.1.6 Constrained Control

Incorporating constraints into the control problem is important for constricting key system variables to stay within predefined limits. It is often desirable to base these on actuator saturation limits, or perhaps safety limits within the plant's environment. Should a mismatch occur between the plant's numerical model and the physically constrained plant, instability could also be a problem when the constraints become active. In traditional MPC, constraints are typically considered for upper and lower limits on control amplitude, $\mathbf{U}$, change of control, $\mathbf{\Delta U}$ and output, $\mathbf{Y}$. They are built into the MPC formulation as a set of linear inequalities, which are traditionally applied to the set of all future instants in terms of $\mathbf{\Delta U}$ such that:

$$\mathbf{\Delta U}^{min} \leq \mathbf{\Delta U} \leq \mathbf{\Delta U}^{max} \tag{3.23}$$

$$\mathbf{U}^{min} \leq \mathbf{C}_a u(k-1) + \mathbf{C}_b \mathbf{\Delta U} \leq \mathbf{U}^{max} \tag{3.24}$$

$$\mathbf{Y}^{min} \leq \mathbf{F}\mathbf{X}(k) + \mathbf{\Phi}\mathbf{\Delta U} \leq \mathbf{Y}^{max} \tag{3.25}$$

where:

$\mathbf{\Delta U}^{min}$: Lower constraint limits on the differential control signal.

$\mathbf{\Delta U}^{max}$: Upper constraint limits on the differential control signal.

$\mathbf{U}^{min}$: Lower constraint limits on the control signal.

$\mathbf{U}^{max}$: Upper constraint limits on the control signal.

$\mathbf{Y}^{min}$: Lower constraint limits on the output.

$\mathbf{Y}^{max}$: Upper constraint limits on the output.

$$\mathbf{C}_a = \begin{bmatrix} 1 \\ 1 \\ 1 \\ \vdots \\ 1 \end{bmatrix}, \quad \mathbf{C}_b = \begin{bmatrix} 1 & 0 & 0 & \dots & 0 \\ 1 & 1 & 0 & \dots & 0 \\ 1 & 1 & 1 & \dots & 0 \\ \vdots & \vdots & \ddots & \ddots & \vdots \\ 1 & 1 & \dots & 1 & 1 \end{bmatrix} \tag{3.26}$$

The constrained optimisation problem is defined by the following cost function and set of inequality constraints:

$$J_c = \frac{1}{2}\mathbf{\Delta U}^T\mathbf{E}_\lambda\mathbf{\Delta U} + \mathbf{\Delta U}^T\mathbf{F}_\lambda \tag{3.27}$$

$$\mathbf{M}_c\mathbf{\Delta U} \leq \boldsymbol{\gamma} \tag{3.28}$$

where:

J_c: Cost function with equality constraints.

$\mathbf{E}_\lambda$: Quadratic equality constraint matrix.

$\mathbf{F}_\lambda$: Linear equality constraint vector.

$\mathbf{M}_c$: Inequality constraint matrix.

$\boldsymbol{\gamma}$: Inequality constraint vector.

Note that the expressions in (3.23) to (3.26) have been condensed into matrix inequality, (3.28), where the i^{th} row of $\mathbf{M}_c$, and the i^{th} element of $\boldsymbol{\gamma}$, form the i^{th} inequality constraint. Each constraint is said to be active if $\mathbf{M}_{c_i}\mathbf{\Delta U} = \gamma_i$ and inactive if $\mathbf{M}_{c_i}\mathbf{\Delta U} < \gamma_i$. When solving the cost function, J_c, for the optimal control command, $\mathbf{\Delta U}_{opt}$, it is possible that both active and inactive constraints will exist in (3.28), however a feasible solution requires that only active constraints are included. The process of identifying and eliminating inactive constraints can be performed using a dual method, where the following QP problem is solved using the Lagrange multiplier vector, $\boldsymbol{\lambda}$, as the decision variable:

$$J_c = \frac{1}{2}\boldsymbol{\lambda}^T\mathbf{H}\boldsymbol{\lambda} + \boldsymbol{\lambda}^T\mathbf{K} + \frac{1}{2}\boldsymbol{\gamma}^T\mathbf{E}_\lambda^{-1}\boldsymbol{\gamma} \tag{3.29}$$

where:

$$\mathbf{H} = \mathbf{M}_c\mathbf{E}_\lambda^{-1}\mathbf{M}_c^T \tag{3.30}$$

$$\mathbf{K} = \boldsymbol{\gamma} + \mathbf{M}_c \mathbf{E}_\lambda^{-1} \mathbf{F}_\lambda \tag{3.31}$$

The set of Lagrange multipliers, $\boldsymbol{\lambda}_{act}$ that minimise (3.29) correspond to the set of active constraints defined by $\mathbf{M}_{c_{act}}$ and $\boldsymbol{\gamma}_{act}$. Hildreth's QP algorithm is an efficient method of finding $\boldsymbol{\lambda}_{act}$, since it is a one dimensional element-by-element search method with no matrix inversions. As such, the procedure executes without interruption, vital for real-time applications. Once $\boldsymbol{\lambda}_{act}$ is obtained, the constrained optimal control can then be calculated from:

$$\boldsymbol{\Delta}\mathbf{U}_{opt} = -\mathbf{E}_\lambda^{-1}\mathbf{F}_\lambda - \mathbf{E}_\lambda^{-1}\mathbf{M}_{c_{act}}^T \boldsymbol{\lambda}_{act} \tag{3.32}$$

Again, the above theory on traditional MPC has been taken from [1]. The reader is directed there for more detailed descriptions and examples.

3.2 MPC using Laguerre Functions

This section briefly covers the material in [1], related to how Laguerre functions can be used in an alternative formulation of MPC, drastically improving the algorithm's speed.

3.2.1 Main Concept

Laguerre functions have been mostly used in system identification. They form a set of orthonormal basis functions called a Laguerre network that efficiently combine to approximate impulse response functions. The quality of approximation improves with the number of basis functions. The z-transform of N^{th} function in the network is defined as:

$$\begin{aligned} \Gamma_N(z) &= \Gamma_{N-1}(z)\frac{z^{-1}-a}{1-az^{-1}} \\ \Gamma_1(z) &= \frac{\sqrt{1-a^2}}{1-az^{-1}} \end{aligned} \tag{3.33}$$

where a is the pole of the network. The discrete-time Laguerre functions in vector form are expressed in shorthand as:

$$\mathbf{L}(k) = [l_1(k)\ ,\ l_2(k)\ ,\ \ldots\ ,\ l_N(k)]^T \tag{3.34}$$

and satisfy the difference equation:

$$\mathbf{L}(k+1) = \mathbf{A}_l \mathbf{L}(k) \tag{3.35}$$

where:

$$\mathbf{L}(0)^T = \sqrt{\beta}[1\ ,\ -a\ ,\ a^2\ ,\ -a^3\ ,\ \ldots\ ,\ (-a)^{N-1}]\ , \quad \beta = 1 - a^2 \tag{3.36}$$

$$\mathbf{A}_l = \begin{bmatrix} a & 0 & 0 & 0 & 0 \\ \beta & a & 0 & 0 & 0 \\ -a\beta & \beta & a & 0 & 0 \\ \vdots & \ddots & \ddots & \ddots & 0 \\ (-a)^{N-2}\beta & \ldots & -a\beta & \beta & a \end{bmatrix} \tag{3.37}$$

$\mathbf{L}(k)$ is the vector of all Laguerre function values at time instant k. When constructing the network, the goodness of fit can be assessed by checking how close the functions are to being orthonormal. The following summation, $\mathbf{S}$, converges to an identity matrix as the prediction window length $N_p \to \infty$.

$$\mathbf{S} = \sum_{i}^{N_p} \mathbf{L}(k)\mathbf{L}(k)^T \tag{3.38}$$

It happens that only a small number of Laguerre functions are needed to achieve a good approximation. This means that in the context of receding horizon control, Laguerre functions allow for long control horizons with a small number of parameters, resulting in a much reduced computational load. With discrete MPC (DMPC) the future control trajectory, $\Delta u(k)$, is approximated as an impulse response function with a set of Laguerre functions and Laguerre coefficients. For example, if the impulse response function is defined as $H(k)$ then it is approximated with N Laguerre functions and coefficients as:

$$H(k) = c_1 l_1(k) + \ \ldots\ + \ c_N l_N(k) \tag{3.39}$$

Based on the orthonormal property, the i^{th} coefficient is calculated as:

$$c_i = \sum_{k=0}^{\infty} H(k) l_i(k) \tag{3.40}$$

The coefficients are grouped into the following Laguerre coefficient vector:

$$\boldsymbol{\eta} = [c_1 \ , \ \dots \ , \ c_N]^T \tag{3.41}$$

An arbitrary future control sample at instant k, given the current sample, k_i, is then:

$$\Delta u(k_i + k) = \mathbf{L}(k)^T \boldsymbol{\eta} \tag{3.42}$$

An important feature of using Laguerre functions in DMPC is that the control horizon length, N_c, no longer exists in the mathematical formulation but is instead replaced with N that now describes the future control trajectory, along with a.

3.2.2 State and Output Prediction

Equation (3.42) is then substituted into (3.6) and (3.7) to produce the following Laguerre versions of the state and output predictions respectively:

$$\mathbf{X}(k+m|k) = \mathbf{A}^m \mathbf{X}(k) + \sum_{i=0}^{m-1} \mathbf{A}^{m-i-1} \mathbf{B} \mathbf{L}(i)^T \boldsymbol{\eta} \tag{3.43}$$

$$y(k+m|k) = \mathbf{C}\mathbf{A}^m \mathbf{X}(k) + \sum_{i=0}^{m-1} \mathbf{C}\mathbf{A}^{m-i-1} \mathbf{B} \mathbf{L}(i)^T \boldsymbol{\eta} \tag{3.44}$$

It can be seen that the predictions are now expressed in terms of the Laguerre coefficient vector, $\boldsymbol{\eta}$, rather than $\boldsymbol{\Delta U}$ and so the optimisation problem becomes a case of solving for optimal $\boldsymbol{\eta}$.

3.2.3 Minimising the Cost Function

Considering equation (3.42), the $\boldsymbol{\Delta U}^T \overline{\mathbf{R}} \boldsymbol{\Delta U}$ term of the cost function in (3.12) can be reformulated as:

$$\boldsymbol{\Delta U}^T \overline{\mathbf{R}} \boldsymbol{\Delta U} = \sum_{m=0}^{N_p} \left[\mathbf{L}(m)^T \boldsymbol{\eta} \right]^T r_w \mathbf{L}(m)^T \boldsymbol{\eta} \tag{3.45}$$

Based on the orthonormal property of the Laguerre network, for sufficiently large N_p, the following summation should result in an identity matrix as $N_p \to \infty$:

$$\sum_{m=0}^{N_p} \mathbf{L}(m)\mathbf{L}(m)^T = \mathbf{I}_{N\times N} \tag{3.46}$$

It is also desired to formulate the cost function in such a way that allows solving for the optimal $\boldsymbol{\eta}$ when implementing setpoint tracking. The new cost function is:

$$J = \sum_{m=1}^{N_p} \mathbf{X}(k+m|k)^T \mathbf{Q}\mathbf{X}(k+m|k) + \boldsymbol{\eta}^T \mathbf{R}_L \boldsymbol{\eta} \tag{3.47}$$

Note that $\mathbf{R}_L = r_w \mathbf{I}_{N\times N}$ has replaced $\overline{\mathbf{R}}$ from the traditional MPC approach. To incorporate the setpoint tracking feature, $\mathbf{Q}$ is defined as $\mathbf{Q} = \mathbf{C}^T\mathbf{C}$ and the augmented state variable from (3.2) is modified to subtract the setpoint signal from the output, leading to:

$$\mathbf{X}(k+m|k) = \begin{bmatrix} \Delta\mathbf{X}_m(k+m|k)^T & y(k+m|k) - r_s(k) \end{bmatrix}^T \tag{3.48}$$

Considering equations (3.43) and (3.44), the following convolution sum is defined as:

$$\boldsymbol{\phi}(m) = \sum_{i=0}^{m-1} \mathbf{A}^{m-i-1}\mathbf{B}\mathbf{L}(i)^T \tag{3.49}$$

This can be calculated recursively through the use of the difference equation (3.35), such that:

$$\begin{aligned} \boldsymbol{\phi}(m) &= \mathbf{A}\boldsymbol{\phi}(m-1) + \boldsymbol{\phi}(1)\left(\mathbf{A}_l^{m-1}\right)^T \\ \boldsymbol{\phi}(1) &= \mathbf{B}\mathbf{L}(0)^T \end{aligned} \tag{3.50}$$

Combining (3.49) and (3.43), and then substituting into (3.47) transforms the cost function into:

$$J = \boldsymbol{\eta}^T\boldsymbol{\Omega}\boldsymbol{\eta} + 2\boldsymbol{\eta}^T\boldsymbol{\Psi}\mathbf{X}(k) + \sum_{m=1}^{N_p} \mathbf{X}(k)^T(\mathbf{A}^T)^m\mathbf{Q}\mathbf{A}^m\mathbf{X}(k) \tag{3.51}$$

where:

$$\boldsymbol{\Omega} = \sum_{m=1}^{N_p} \boldsymbol{\phi}(m)\mathbf{Q}\boldsymbol{\phi}(m)^T + \mathbf{R}_L \tag{3.52}$$

$$\boldsymbol{\Psi} = \sum_{m=1}^{N_p} \boldsymbol{\phi}(m)\mathbf{Q}\mathbf{A}^m \tag{3.53}$$

The unconstrained optimal Laguerre coefficient vector is found by minimisation of $\frac{\partial J}{\partial \boldsymbol{\eta}} = 0$, leading to:

$$\boldsymbol{\eta}_{opt} = -\boldsymbol{\Omega}^{-1}\boldsymbol{\Psi}\mathbf{X}(k) \tag{3.54}$$

3.2.4 Receding Horizon Control and Closed-Loop Stability

The receding horizon control law applies only the first value of the optimal control trajectory. Once $\boldsymbol{\eta}_{opt}$ is found, $\Delta u(k)$ is calculated from:

$$\Delta u(k) = \mathbf{L}(0)^T \boldsymbol{\eta}_{opt} \tag{3.55}$$

In the case of unconstrained control, equation (3.55) can also be expressed in the form of state feedback control where:

$$\Delta u(k) = -\mathbf{K}_{mpc}\mathbf{X}(k) \tag{3.56}$$

Combining (3.54), (3.55) and (3.56) leads to the state feedback gain matrix:

$$\mathbf{K}_{mpc} = \mathbf{L}(0)^T \boldsymbol{\Omega}^{-1}\boldsymbol{\Psi} \tag{3.57}$$

The closed-loop stability for unconstrained predictive control systems can be evaluated from the eigenvalues of $(\mathbf{A} - \mathbf{B}\mathbf{K}_{mpc})$, which for discrete LTI systems must be within the unit circle to be stable. However with constrained control, if the constraints are activated, the control problem becomes nonlinear and therefore the stability properties of LTI systems no longer apply. Refer to [1] for a discussion on ascertaining stability in this case, with regards to combining dual mode control and a terminal constraint set. The main idea is that different control laws are selected, during execution to guarantee stability, depending on whether the constraints become active.

3.2.5 Laguerre Tuning Parameters

The features of a well-performing RT MPC formulation using Laguerre networks are orthonormality of the basis functions, minimal network order, and a suitable response time for the application. This is achieved by careful selection of the parameters, a, N, r_w and N_p.

For cases where $N > 1$, true orthonormality can only be achieved in the limit with an infinite prediction window, that is when $N_p \to \infty$. However in practice, the Laguerre network can be tuned such that, with very small values of N_p, a fast decaying impulse response function of the Laguerre network can be achieved depending on the values of a and N.

In regards to the control action tuning parameter r_w, it has been shown in [1] how the optimal control trajectory converges very quickly to the discrete linear quadratic regulator (DLQR) solution using the algebraic Riccati equation. It has also been shown that a reduction in r_w increases the error with respect to the DLQR solution. Hence the DLQR approach provides a good benchmark with which to compare the Laguerre solution, and thus tune the control parameters. Some features of the tuning parameters include [1]:

- When r_w is reduced, the closed loop poles move towards the origin of the discrete complex plane, leading to a faster response.
- The value of N determines the order of the response. For example, $N = 1$ would produce a first order response of the control system.
- A large value of a can be used to achieve a long control horizon with a small N.
- If $a = 0$ and $N = N_c$ the design is equivalent to traditional MPC.
- When N is large the performance converges to the DLQR solution. In this case the effect of tuning a is small.
- When N is small a can be used to tune the controller which may offer an improved performance over DLQR [1].

3.2.6 Closed-Form Constrained Control

When the constraint set is limited to $\pm u$, $\pm \Delta u$ and $\pm y$ (a total of 6) for a single control it is possible to find a closed-form analytical solution to the constrained problem. Also, by using a NMSS formulation the observer can also be omitted for an extra computation saving. When there are a large number of constraints, such as in MIMO systems or the traditional MPC approach, QP is still the preferred method. However fast implementations such as Hildreth's algorithm can be used to speed up the process. A closed-form constrained

control approach, presented in [1], simplifies the constraint problem by only considering the above constraints in the first sample of the receding horizon. Firstly, the cost function to be minimised is:

$$J = \boldsymbol{\eta}^T \boldsymbol{\Omega} \boldsymbol{\eta} + 2\boldsymbol{\eta}^T \boldsymbol{\Psi} \mathbf{X}(k) \tag{3.58}$$

Note, this is a truncated version of (3.51), resulting in the same minimisation of the cost function, J, since the truncated term is independent to $\boldsymbol{\eta}$. Given that $\Delta u(k) = \mathbf{L}(0)^T \boldsymbol{\eta}$, three cases exist for each of the constraint variables:

Constraint 1:

$$\Delta u^{min} < \mathbf{L}(0)^T \boldsymbol{\eta} < \Delta u^{max} \tag{3.59}$$

1. If (3.59) is satisfied then: $\boldsymbol{\eta}_{opt} = -\boldsymbol{\Omega}^{-1} \boldsymbol{\Psi} \mathbf{X}(k)$
2. Otherwise if $\mathbf{L}(0)^T \boldsymbol{\eta} \leq \Delta u^{min}$, for $\boldsymbol{\eta} = -\boldsymbol{\Omega}^{-1} \boldsymbol{\Psi} \mathbf{X}(k)$, then $\Delta u(k) = \Delta u^{min}$
3. Otherwise if $\mathbf{L}(0)^T \boldsymbol{\eta} \geq \Delta u^{max}$, for $\boldsymbol{\eta} = -\boldsymbol{\Omega}^{-1} \boldsymbol{\Psi} \mathbf{X}(k)$, then $\Delta u(k) = \Delta u^{max}$
4. The control amplitude is then calculated as $u(k) = u(k-1) + \Delta u(k)$

Constraint 2:

$$u^{min} < u(k-1) + \mathbf{L}(0)^T \boldsymbol{\eta} < u^{max} \tag{3.60}$$

1. If (3.60) is satisfied then: $\boldsymbol{\eta}_{opt} = -\boldsymbol{\Omega}^{-1} \boldsymbol{\Psi} \mathbf{X}(k)$
2. Otherwise if $u(k-1) + \mathbf{L}(0)^T \boldsymbol{\eta} \leq u^{min}$, for $\boldsymbol{\eta} = -\boldsymbol{\Omega}^{-1} \boldsymbol{\Psi} \mathbf{X}(k)$, then:

$$u(k) = u^{min} \text{ and } \Delta u(k) = u^{min} - u(k-1)$$

3. Otherwise if $u(k-1) + \mathbf{L}(0)^T \boldsymbol{\eta} \geq u^{max}$, for $\boldsymbol{\eta} = -\boldsymbol{\Omega}^{-1} \boldsymbol{\Psi} \mathbf{X}(k)$, then:

$$u(k) = u^{max} \text{ and } \Delta u(k) = u^{max} - u(k-1)$$

Constraint 3:

$$y^{min} < y(k) < y^{max} \tag{3.61}$$

Given that the next predicted output is:

$$y(k+1|k) = \mathbf{CAX}(k) + \mathbf{CBL}(0)^T \boldsymbol{\eta} \tag{3.62}$$

then:

$$y^{min} < \mathbf{CAX}(k) + \mathbf{CBL}(0)^T \boldsymbol{\eta} < y^{max} \tag{3.63}$$

1. If (3.63) is satisfied then: $\boldsymbol{\eta}_{opt} = -\boldsymbol{\Omega}^{-1}\boldsymbol{\Psi}\mathbf{X}(k)$

2. Otherwise if $\mathbf{CAX}(k) + \mathbf{CBL}(0)^T\boldsymbol{\eta} \leq y^{min}$, for $\boldsymbol{\eta} = -\boldsymbol{\Omega}^{-1}\boldsymbol{\Psi}\mathbf{X}(k)$, then the analytical solution is found using equality constraints such that J is minimised with:

$$-\mathbf{CBL}(0)^T\boldsymbol{\eta} \leq -y^{min} + \mathbf{CAX}(k) \tag{3.64}$$

Defining $\mathbf{M}_{c_{act}} = -\mathbf{CBL}(0)^T$, the solution for the Lagrange multipliers is:

$$\boldsymbol{\lambda}_{act} = -\left(\mathbf{M}_{c_{act}}\boldsymbol{\Omega}^{-1}\mathbf{M}_{c_{act}}^T\right)^{-1}\left(-y^{min} + \mathbf{CAX}(k) + \mathbf{M}_{c_{act}}\boldsymbol{\Omega}^{-1}\boldsymbol{\Psi}\mathbf{X}(k)\right) \tag{3.65}$$

and then:

$$\boldsymbol{\eta}_{opt} = -\boldsymbol{\Omega}^{-1}\left(\boldsymbol{\Psi}\mathbf{X}(k) + \mathbf{M}_{c_{act}}^T\boldsymbol{\lambda}_{act}\right) \tag{3.66}$$

will satisfy (3.63).

3. Otherwise if $\mathbf{CAX}(k) + \mathbf{CBL}(0)^T\boldsymbol{\eta} \geq y^{max}$, for $\boldsymbol{\eta} = -\boldsymbol{\Omega}^{-1}\boldsymbol{\Psi}\mathbf{X}(k)$, then the analytical solution is found through the inequality:

$$\mathbf{CBL}(0)^T\boldsymbol{\eta} \leq y^{max} - \mathbf{CAX}(k) \tag{3.67}$$

With $\mathbf{M}_{c_{act}} = \mathbf{CBL}(0)^T$, the solution for the Lagrange multipliers is:

$$\boldsymbol{\lambda}_{act} = -\left(\mathbf{M}_{c_{act}}\boldsymbol{\Omega}^{-1}\mathbf{M}_{c_{act}}^T\right)^{-1}\left(y^{max} - \mathbf{CAX}(k) + \mathbf{M}_{c_{act}}\boldsymbol{\Omega}^{-1}\boldsymbol{\Psi}\mathbf{X}(k)\right) \tag{3.68}$$

and again $\boldsymbol{\eta}_{opt}$ is calculated from (3.66), thereby satisfying (3.63).

It should be noted that all of these constraints are linearly dependent through $\mathbf{L}(0)^T$, and therefore they can not all be satisfied if they become active simultaneously. Attempting to calculate $\boldsymbol{\lambda}_{act}$ in this scenario would result in a zero result since the determinant of $\left(\mathbf{M}_{c_{act}}\boldsymbol{\Omega}^{-1}\mathbf{M}_{c_{act}}^T\right)$ is zero. As such, the constraints need to be ranked in terms of priority.

Since the output depends on model accuracy, it makes sense to treat the control amplitude and control change as being more important.

3.2.7 Justification of Laguerre Functions in the Current Research

A brief justification is provided here on choosing a Laguerre network as the orthonormal set of basis functions for the real-time MPC used in this thesis. It is possible to use other basis functions for optimal control, for example, Kautz functions [38], as used in [39], and half range Chebyshev functions [40], as used in [27]. Both these alternative basis function sets are best suited to harmonic signals, and in the case of [27] it is certainly justified to use HRCF, since the controlled variable is an oscillatory PTO force. Also, in contrast to using a Laguerre network, the Kautz approach requires its poles to be placed based on *a priori* knowledge of the linear–quadratic regulator (LQR) solution to the optimal control problem [1]. In this research, the PTO reaction torque is not oscillatory due to the air flow rectification at the turbine stage (see Chapters 4 and 5), thus making the Laguerre approach more suitable.

Chapter 4

Modelling of the WRAM

This chapter describes the numerical wave-to-wire model of the WRAM, developed for simulating the real-time MPC control algorithm in this thesis.

4.1 WRAM Concept

The WRAM device (IP protected by world patents) is a heaving buoy that reacts against the sea-surface via a partially enclosed air plenum inside the float. An illustration of the WEC is provided in Figure 4.1. The WRAM is a sea-worthy, single-bodied, axisymmetric device on compliant moorings with at least two separate turbine / generator power trains within the PTO. Unlike other point absorbers, the WRAM is an oscillating system with up to four resonant frequencies depending on the tunable setting of its submerged tank, rigidly coupled to the float through the neck. The tank's tunability is a significant advantage for the WRAM with respect to the changing weather patterns of the North Atlantic. The ballast, located at the bottom of the tank, is primarily designed to assist pitch stability, however it also slightly contributes to the WEC's resonant tuning.

At first glance, the WRAM appears similar to other WECs such as the OWC spar-buoy in [41]. However the WRAM is not categorised as an OWC device since its predominant power-absorbing mass comes from its submerged inertial tanks rather than the water column. This relates to the fact that the WRAM is designed to have its structure, rather than the water column tuned to the incident waves. It can then be considered that the WRAM rams against the internal water surface, hence its name. Despite these distinctions, the fundamental physics of both WEC types is essentially the same, and therefore the WRAM has

been modelled in this research based on the fundamental physics of an OWC spar-buoy.

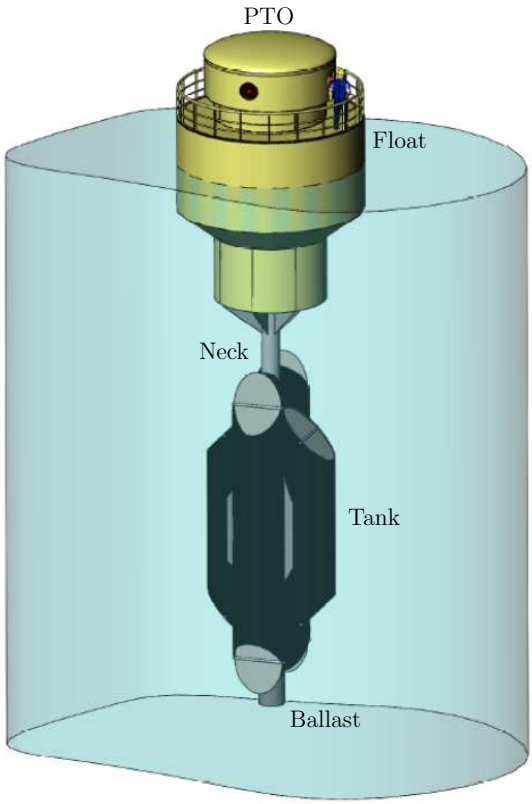

Figure 4.1: WRAM Illustration, Courtesy of SGL.

4.2 Broad Description of the Numerical Model

The model can be thought of as being split into two linked sections, the wave-to-turbine model, and the turbine-to-wire model. The formulation of the wave-to-turbine model follows standard and well-established practices in the wave energy community. The conversion stages include the fundamental physics of the WEC hydrodynamics, mechanical oscillating bodies, air chamber dynamics, and turbomachinery dimensional analysis. The inputs to the wave-to-turbine model are the hydrodynamic excitation forces, simulated from irregular spectral sea states. The output is the torque applied to the turbine due to the air flow from the water column chamber.

The turbine-to-wire model has been developed in this research to accurately represent the dynamics of the PTO installed on the WRAM emulator test rig (see Chapter 5). Note that

the 'wire' portion of the model refers to the point of connection at the electrical generator's windings. The model has been derived based on the fundamental principles of the DC generator and classical feedback control theory, related to the servo-drive's internal control loops. In order to completely specify all of the numerical parameter values of the model, some of the parameters have been approximated using system identification, discussed in Section 4.6.2.

4.3 Wave-to-Turbine Model

4.3.1 Mechanical Oscillator

The WRAM is represented as a two-body mechanical oscillator where the first DoF is associated with the heave displacement of the WEC structure, z_3, and the second represents that of the water column, z_9. Figure 4.2(a) provides a schematic diagram of the WRAM, showing the main components including the float, neck, tank and ballast. As is commonly done for OWC spar-buoys, the WEC structure and internal water column are modelled with boundary element method (BEM) software, where each body is treated independently when finding the hydrodynamic coefficients. This results in various cross-coupling terms that account for radiation damping and added mass. Other reaction terms exist for the body masses and buoyancy. Buoyancy is treated as linear, under the assumption that negligible pitch motion occurs and that the internal free surface area of the water column remains constant during the WEC's motion.

The input driving forces are the hydrodynamic excitation forces that include both Froude-Krylov and diffraction force components. The Froude-Krylov component is the force that would result on the body from undisturbed waves, and the diffraction component is associated with the floating body disturbing the waves with its own motion. See [42] for an in-depth study on the topic. The PTO is modelled as a coupling force between the two bodies, where both are treated as rigid. The reaction terms, excitation forces and PTO force can be seen on the free-body diagram in Figure 4.2(b).

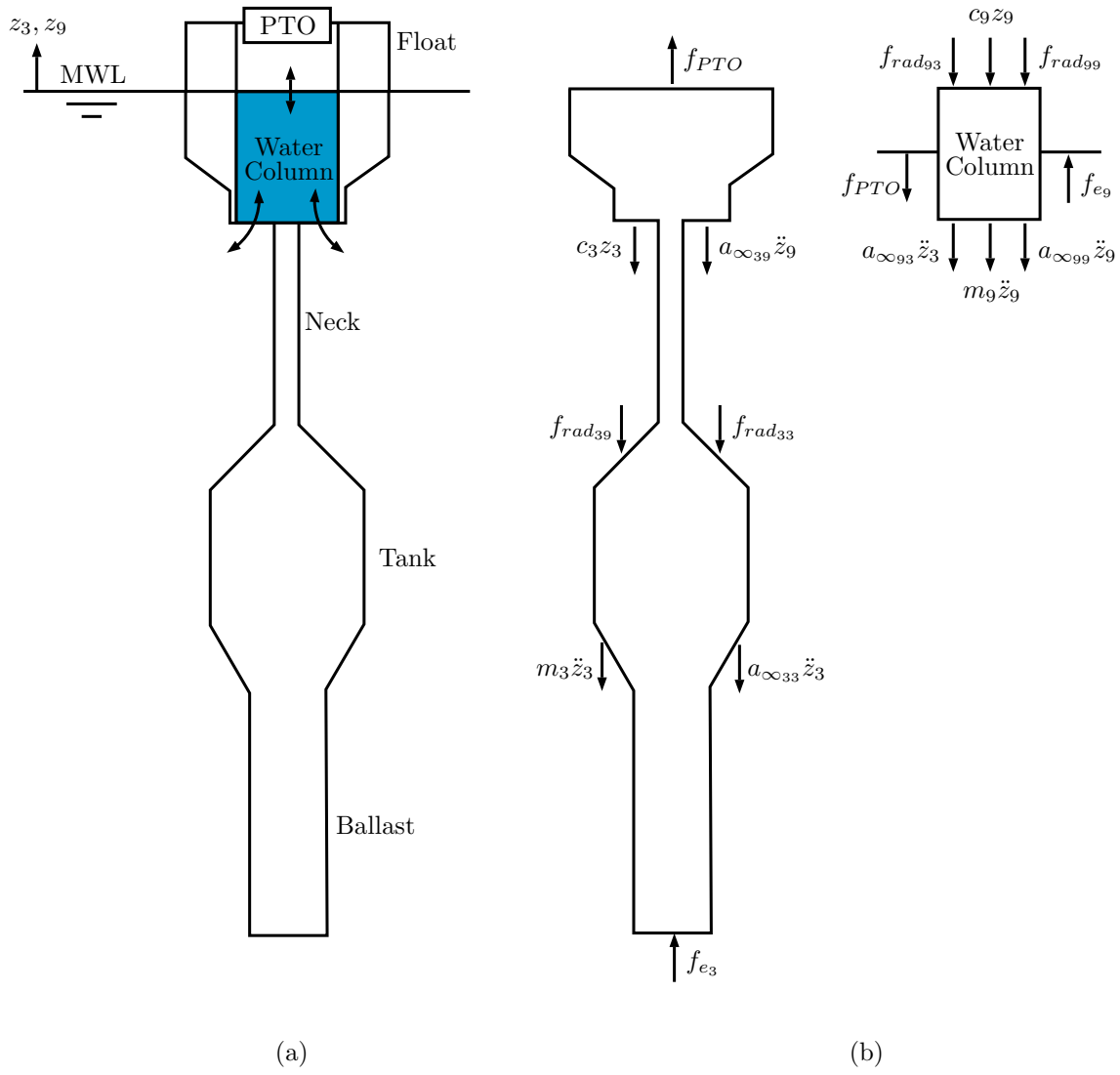

Figure 4.2: (a) WRAM Schematic Diagram (b) WRAM Free-Body Diagram.

4.3.2 Equations of Motion

The equations of motion for the two-body system are:

$$(m_3 + a_{\infty_{33}})\ddot{z}_3 + a_{\infty_{39}}\ddot{z}_9 + \int_{-\infty}^{t} L_{33}(t-\tau)\dot{z}_3 d\tau + \int_{-\infty}^{t} L_{39}(t-\tau)\dot{z}_9 d\tau + c_3 z_3 = f_{e_3} + f_{PTO} \tag{4.1}$$

$$(m_9 + a_{\infty_{99}})\ddot{z}_9 + a_{\infty_{93}}\ddot{z}_3 + \int_{-\infty}^{t} L_{93}(t-\tau)\dot{z}_3 d\tau + \int_{-\infty}^{t} L_{99}(t-\tau)\dot{z}_9 d\tau + c_9 z_9 = f_{e_9} - f_{PTO} \tag{4.2}$$

where:

z_3 and z_9:	Heave displacement	(m)
m_3 and m_9:	Body mass	(kg)
c_3 and c_9:	Hydrostatic restoring coefficient	($\mathrm{N\,m^{-1}}$)
$a_{\infty_{XY}}$:	Added mass at infinite frequency	(kg)
f_{e_3} and f_{e_9}:	Excitation force	(N)
f_{PTO}:	PTO force	(N)

$L_{XY}(t)$ are the impulse response functions of the radiation damping impedance with the units of $\mathrm{N\,m\,s^{-1}}$. The subscripts 3 and 9 refer to the WRAM structure and water column bodies, taken from the convention in Nemoh boundary element method (BEM) software [43]. The double subscript indices, X and Y in all radiation terms, relate to cross-coupling effects that can be considered to be 'the force on body X due to the motion of body Y'.

4.3.3 Water Column Representation

There has been some discussion in the literature regarding the best way to numerically model oscillating water columns. A recent study [44] has investigated the treatment of the OWC as a massless piston, comparing various piston lengths, with analysis being conducted in both frequency and time domains. The time domain results for irregular waves show higher accuracy when using a piston length equal to the full depth of the OWC. Based on these results, the approach adopted in this research has been to model the water column as a solid oscillating cylinder with a density equal to that of sea water.

4.3.4 Hydrodynamic Coefficients

The radiation damping, added mass and excitation force terms in the equations of motion, (4.1) and (4.2), come from frequency domain (FD) hydrodynamic coefficients obtained from BEM software. The equations of motion are expressed in the time domain (TD) such that the WRAM can be simulated with irregular waveforms. Also, the TD model is needed for benchmarking the real-time computation times of the control simulations. For this reason, the FD coefficients are converted to TD equivalents for use in the TD model.

4.3.5 Boundary Element Method

Boundary element method software is commonly used in the naval architecture and wave energy analysis for determining frequency domain coefficients of the hydrodynamic forces acting on submerged bodies. Fundamentally, the wetted surface of the submerged body is divided into a multifaceted mesh, where for each panel, the Laplace equation is solved for the velocity potential. From this, the hydrodynamic coefficients are obtained. The process is computationally very intensive and is typically done offline. Possibly the most established and well known BEM software is WAMIT [45], however another open-source alternative called Nemoh [43] is available. Nemoh has been used in this research since it is freely accessible, user friendly and easy to interface directly with MATLAB®. Figures 4.3 and 4.4 show the meshes created for the WRAM and water column bodies respectively using Nemoh's *axisym* function.

An undesirable feature in the resulting coefficients is often the occurrence of irregular sharp spikes at certain frequencies. This is a known issue to the Nemoh developers and is addressed in [43]. The discontinuity is attributed to the relationship between mesh size and wavelength. One approach for removing the irregularities is to refine the mesh at the problem points, or alternatively to simply filter out the spikes.

4.3.6 Approximation of the Radiation Damping

The convolution integral terms in the equations of motion, $f_{rad_{XY}} = \int_{-\infty}^{t} L_{XY}(t-\tau)\dot{z}_Y d\tau$, are slow to compute, and it has become commonplace to replace them with low-order LTI state space models. Orders of between 2 and 4 have shown to work well with good accuracy [46].

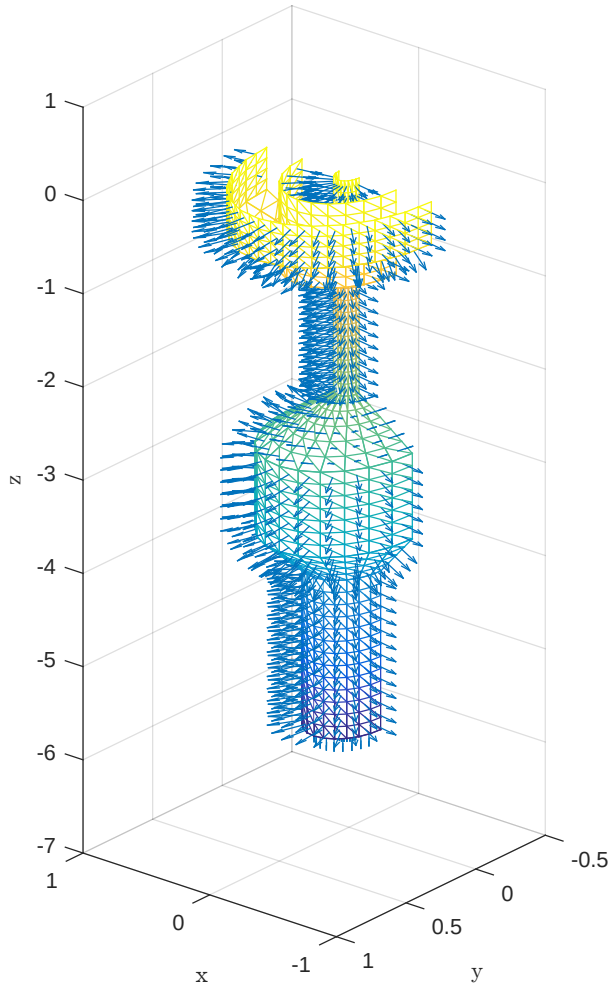

Figure 4.3: Nemoh Mesh for WRAM Body.

The general approach is to first approximate the FD coefficients with transfer functions. One of various techniques can then be applied for converting them to the time domain, including Prony's method and frequency domain identification (FDI). In this research the FDI Toolbox for MATLAB® [47] has been used, which also allows the removal of the irregular spikes through a graphical user interface. The final state space approximations take the form:

$$\begin{aligned} \dot{\mathbf{X}}_{XY} &= \mathbf{A}_{XY}\mathbf{X}_{XY} + \mathbf{B}_{XY}\dot{z}_Y \\ f_{rad_{XY}} &\approx y_{XY} = \mathbf{C}_{XY}\mathbf{X}_{XY} \end{aligned} \tag{4.3}$$

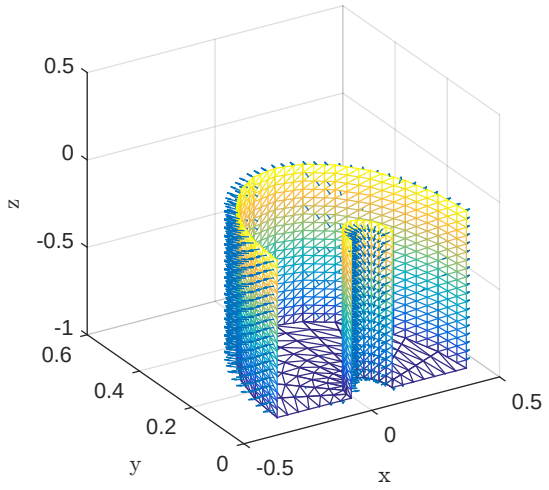

Figure 4.4: Nemoh Mesh for Water Column.

4.3.7 Excitation Forces

The hydrodynamic excitation forces, $f_{e_3}(t)$ and $f_{e_9}(t)$, acting on the WRAM body and water column respectively, are described analytically by the time domain convolution integral between the wave elevation and the impulse response function of the excitation force coefficient [42]. In general, $f_e(t)$ is calculated from:

$$f_e(t) = \int_{-\infty}^{\infty} f_c(\tau)\zeta(t-\tau)d\tau \tag{4.4}$$

$$f_c(t) = \frac{1}{2\pi}\int_{-\infty}^{\infty} F_c(\omega)e^{i\omega t}d\omega \tag{4.5}$$

where:

$F_c(\omega)$:	FD excitation force coefficient	$(\mathrm{N\,m^{-1}})$
$f_c(t)$:	Impulse response function of the excitation force	$(\mathrm{N\,m^{-1}})$
$\zeta(t)$:	Wave elevation	(m)

In the frequency domain, the convolution integral is equivalent to the multiplication of frequency response functions of the excitation force coefficient, $F_c(\omega)$, and wave elevation, $Z_c(\omega)$. Nemoh provides the excitation force coefficient, $F_c(\omega)$, from which the frequency

response function of the excitation force, $F_e(\omega)$ can be calculated from:

$$F_e(\omega) = F_c(\omega)Z_c(\omega) \tag{4.6}$$

Also, $f_e(t)$ is non-causal since future information about the wave elevation is needed. To avoid the problem of predicting future excitation forces during online WEC simulations, it is common to calculate the excitation force offline. When constructing an irregular excitation force waveform for $f_e(t)$, the frequency response functions, $F_c(\omega)$ and $Z_c(\omega)$ are used to construct each harmonic component. They are then superimposed to produce the final waveform. The details of this are explained further in Section 4.4.

4.3.8 Wave-to-Relative Motion

The LTI model described by equations (4.1) and (4.2) defines the relationship between the excitation forces and relative motion between the WRAM body and the water column. The outputs of this portion of the model are the relative displacement and velocity of the water column's internal free surface. These outputs feed into the chamber pneumatics portion of the model, in Section 4.3.9, that calculates the air chamber pressure. The PTO force is then calculated from the pressure and fed back into the LTI model. In this research, it has been decided to represent the wave-to-relative motion part of the model as a state space structure, expressed as:

$$\begin{aligned} \dot{\mathbf{X}}_c &= \mathbf{A}_c\mathbf{X}_c + \mathbf{B}_c\mathbf{U}_c \\ \mathbf{Y}_c &= \mathbf{C}_c\mathbf{X}_c + \mathbf{D}_c\mathbf{U}_c \end{aligned} \tag{4.7}$$

where the state variable, $\mathbf{X}_c$, is defined as:

$$\mathbf{X}_c = [x_1 \quad x_2 \quad x_3 \quad x_4 \quad x_{r_1} \quad \dots \quad x_{r_n}]^T \tag{4.8}$$

The states x_1 to x_4 are defined as:

$x_1 = z_3$

$x_2 = z_9$

$x_3 = \dot{x}_1 = \dot{z}_3$

$x_4 = \dot{x}_2 = \dot{z}_9$

The states, x_{r_1} to x_{r_n} correspond to the states of the radiation damping subsystems from equation (4.3). Equations (4.1) and (4.2) can be written succinctly in matrix format as:

$$\mathbf{M}\begin{bmatrix}\dot{x}_3\\ \dot{x}_4\end{bmatrix} + \mathbf{F}_{rad} + \mathbf{C}_B\begin{bmatrix}x_1\\ x_2\end{bmatrix} = \mathbf{U}_c \tag{4.9}$$

where:

$$\mathbf{M} = \begin{bmatrix} m_3 + a_{\infty_{33}} & a_{\infty_{39}} \\ a_{\infty_{93}} & m_9 + a_{\infty_{99}}\end{bmatrix}, \quad \mathbf{C}_B = \begin{bmatrix} c_3 & 0 \\ 0 & c_9\end{bmatrix}, \quad \mathbf{I} = \begin{bmatrix} 1 & 0 \\ 0 & 1\end{bmatrix} \tag{4.10}$$

$$\mathbf{F}_{rad} = \begin{bmatrix} f_{rad_{33}} + f_{rad_{39}} \\ f_{rad_{93}} + f_{rad_{99}}\end{bmatrix} \mathbf{U}_c = \begin{bmatrix} f_{e_3} + f_{PTO} \\ f_{e_9} - f_{PTO}\end{bmatrix} \tag{4.11}$$

$$\therefore \begin{bmatrix}\dot{x}_3\\ \dot{x}_4\end{bmatrix} = -\mathbf{M}^{-1}\mathbf{F}_{rad} - \mathbf{M}^{-1}\mathbf{C}_B\begin{bmatrix}x_1\\ x_2\end{bmatrix} + \mathbf{M}^{-1}\mathbf{U}_c \tag{4.12}$$

The continuous LTI state space matrices for the WRAM's wave-to-relative motion model are constructed as:

$$\mathbf{A}_c = \begin{bmatrix} \mathbf{0} & \mathbf{I} & \mathbf{0} & \mathbf{0} & \mathbf{0} & \mathbf{0} \\ -\mathbf{M}^{-1}\mathbf{C}_B & \mathbf{0} & -\mathbf{M}^{-1}\begin{bmatrix}\mathbf{C}_{33} & \mathbf{C}_{39} & \mathbf{0} & \mathbf{0} \\ \mathbf{0} & \mathbf{0} & \mathbf{C}_{93} & \mathbf{C}_{99}\end{bmatrix} & & & \\ \mathbf{0} & \begin{bmatrix}\mathbf{B}_{33} & \mathbf{0} \\ \mathbf{0} & \mathbf{B}_{39}\end{bmatrix} & \mathbf{A}_{33} & \mathbf{0} & \mathbf{0} & \mathbf{0} \\ \mathbf{0} & & \mathbf{0} & \mathbf{A}_{39} & \mathbf{0} & \mathbf{0} \\ \mathbf{0} & \begin{bmatrix}\mathbf{B}_{93} & \mathbf{0} \\ \mathbf{0} & \mathbf{B}_{99}\end{bmatrix} & \mathbf{0} & \mathbf{0} & \mathbf{A}_{93} & \mathbf{0} \\ \mathbf{0} & & \mathbf{0} & \mathbf{0} & \mathbf{0} & \mathbf{A}_{99} \end{bmatrix} \tag{4.13}$$

$$\mathbf{B}_c = \begin{bmatrix} \mathbf{0} \\ \mathbf{M}^{-1} \\ \mathbf{0} \\ \mathbf{0} \\ \mathbf{0} \\ \mathbf{0} \end{bmatrix}, \quad \mathbf{C}_c = \begin{bmatrix} -1 & 1 & 0 & 0 & \mathbf{0} & \mathbf{0} & \mathbf{0} & \mathbf{0} \\ 0 & 0 & -1 & 1 & \mathbf{0} & \mathbf{0} & \mathbf{0} & \mathbf{0} \end{bmatrix}, \quad \mathbf{D}_c = \mathbf{0} \tag{4.14}$$

Note the two outputs, defined by $\mathbf{C}_c$, are the relative displacement and velocity between the water column and the WRAM body. The sign convention corresponds to air being exhaled from the water column chamber. For future work with real-time hybrid testing, a discrete version of the model has been formulated that combines the linear WEC with the nonlinear PTO. This is important such that the model can be solved in real-time and be compatible with the control algorithm. The LTI state space part of the model is discretised using the zero-order-hold method, as described in [48], with a sample period of T_s. The discrete state space model is described by:

$$\begin{aligned} \mathbf{X}_d(k+1) &= \mathbf{A}_d\mathbf{X}_d(k) + \mathbf{B}_d\mathbf{U}_d(k) \\ \mathbf{Y}_d(k) &= \mathbf{C}_d\mathbf{X}_d(k) + \mathbf{D}_d\mathbf{U}_d(k) \end{aligned} \tag{4.15}$$

where:

$$\mathbf{A}_d = e^{\mathbf{A}_c T_s}, \quad \mathbf{B}_d = \left(\int_0^{T_s} e^{\mathbf{A}_c \tau} d\tau \right) \mathbf{B}_c, \quad \mathbf{C}_d = \mathbf{C}_c, \quad \mathbf{D}_d = \mathbf{D}_c \tag{4.16}$$

MATLAB's® *c2d* function can easily be used to perform the discretisation. Incorporating the PTO force is achieved by feeding back the WRAM LTI and PTO models into each other.

4.3.9 Air Chamber Pneumatics

The basic principle of the OWC is that as the water column oscillates, the chamber air contracts and expands while passing through the turbine to and from atmosphere. Here, the air is considered compressible and it is assumed that the process is isentropic, therefore adiabatic and reversible. The air is considered an ideal gas that mixes instantaneously with the

incoming air from atmosphere, and it should be noted that these assumptions are commonplace in the field. For example, see [49]–[51]. Closely following the work in [7] and [52] the mass flow rate through the turbine is:

$$\dot{m}_t = \rho \dot{V}_c + V_c \dot{\rho} \tag{4.17}$$

where:

$\dot{m}_t$:	Turbine mass flow rate	$(\mathrm{kg\,s^{-1}})$
ρ :	Chamber air density	$(\mathrm{kg\,m^{-3}})$
V_c :	Chamber volume	$(\mathrm{m^3})$

V_c is a function of the relative displacement of the water column, z_9, and WRAM body, z_3, defined to be positive when exhaling, such that:

$$V_c = V_0 + A_{wc}(z_9 - z_3) \tag{4.18}$$

$$\dot{V}_c = A_{wc}(\dot{z}_9 - \dot{z}_3) \tag{4.19}$$

where:

V_0 :	Chamber volume at rest	$(\mathrm{m^3})$
A_{wc} :	Water column cross-sectional area	$(\mathrm{m^2})$

From the isentropic assumption:

$$\frac{p}{\rho^{\gamma_a}} = \frac{p_{at}}{\rho_{at}^{\gamma_a}} = \text{constant} \tag{4.20}$$

where:

p :	Absolute chamber pressure	(Pa)
p_{at} :	Atmospheric pressure	(Pa)
ρ_{at} :	Atmospheric air density	$(\mathrm{kg\,m^{-3}})$
$\gamma_a = 1.4$:	Specific heat ratio for air	

It is helpful to use a dimensionless chamber pressure for simulation robustness, defined as [52]:

$$p^* = \frac{p}{p_{at}} - 1 \tag{4.21}$$

With this definition, equation (4.20) is equivalent to:

$$\rho = \rho_{at}(p^* + 1)^{1/\gamma_a} \tag{4.22}$$

Taking the logarithm of both sides gives:

$$\ln(\rho) = \ln(\rho_{at}) + \frac{1}{\gamma_a}\ln(p^* + 1) \tag{4.23}$$

which is then differentiated to give:

$$\frac{\dot{\rho}}{\rho} = \frac{1}{\gamma_a}\frac{\dot{p}^*}{p^* + 1} \tag{4.24}$$

Substituting (4.22) into (4.24) leads to:

$$\dot{\rho} = \frac{\rho_{at}}{\gamma_a}(p^* + 1)^{\left(\frac{1}{\gamma_a} - 1\right)}\dot{p}^* \tag{4.25}$$

Finally, substituting (4.22) and (4.25) into (4.17) leads to a nonlinear ordinary differential equation for dimensionless pressure:

$$\dot{p}^* = -\gamma_a(p^* + 1)\frac{\dot{V}_c}{V_c} - \gamma_a(p^* + 1)^{\beta}\frac{\dot{m}_t}{\rho_{at}V_c} \tag{4.26}$$

where:

$$\beta = \frac{\gamma_a - 1}{\gamma_a} \tag{4.27}$$

4.3.10 Turbine Torque and PTO Force

The characteristics of the turbine used in this research are very well understood, having been extensively studied as part of the CORES project [53] and elsewhere [54]–[56]. Different authors use either turbine dimensions, e.g. [57] or dimensional analysis, [58] to describe the turbine characteristics. Dimensional analysis is useful where the Mach and Reynolds

No. effects are negligible, which can be considered valid in the case of OWC's [58]. Each have their benefits depending on the information available and the analysis requirements. A relationship has been established in [55] that allows conversion between the flow coefficients of the two approaches. With dimensional analysis the turbine's characteristics are described by [59]:

$$\Phi_t = \frac{\dot{m}_t}{\rho_{in}\Omega_t D_t^3} \tag{4.28}$$

$$\Psi_t = \frac{p_{at}p^*}{\rho_{in}\Omega_t^2 D_t^2} \tag{4.29}$$

$$\Pi_t = \frac{P_t}{\rho_{in}\Omega_t^3 D_t^5} \tag{4.30}$$

$$\eta_t = \frac{\Pi_t}{\Phi_t \Psi_t} \tag{4.31}$$

where:

Φ_t :	Turbine dimensionless flow coefficient	
Ψ_t :	Turbine dimensionless pressure coefficient	
Π_t :	Turbine dimensionless power coefficient	
η_t :	Turbine efficiency	
ρ_{in} :	Inlet density at stagnation conditions	($\mathrm{kg\,m^{-3}}$)
Ω_t :	Turbine angular velocity	($\mathrm{rad\,s^{-1}}$)
D_t :	Turbine rotor diameter	(m)
P_t :	Turbine power	(W)

The turbine torque, T_t, is the main output of the wave-to-turbine model, and is calculated using the power coefficient relation as:

$$T_t = \rho_{in}\Omega_t^2 D_t^5 \Pi_t \tag{4.32}$$

The turbine's inlet density, ρ_{in}, changes depending on the sign of the pressure such that:

$$\rho_{in} = \begin{cases} \rho_{at} & \text{if } p^* < 0 \\ \rho & \text{if } p^* \geq 0 \end{cases} \tag{4.33}$$

This can be expressed more compactly as:

$$\rho_{in} = \rho_{at} \max(p^* + 1, 1)^{1/\gamma_a} \tag{4.34}$$

It is advantageous to express the turbine coefficients as a function of the pressure coefficient such that the flow, power and efficiency become functions of the chamber pressure. This is helpful with regards to simulations since the pressure is one of the differential equations being solved. Another practical reason is that on real PTOs the pressure is more accurately measured than the flow. This is due to the fact that most flow sensors are calibrated for steady state conditions which is in direct contrast to the behavour of OWCs. Figure 4.5 to shows Φ_t as a function of Ψ_t which has been created by inverting the pressure versus flow coefficient relationship in [56]. The power versus flow coefficient in [56] is in Figure 4.6. A curve has been fitted to the Φ_t versus Ψ_t data in the form:

$$\Phi_t(\Psi_t) = a\Psi_t^b + c \tag{4.35}$$

where the parameter values have been identified as:

$a = 0.2751$

$b = 0.4666$

$c = -0.07211$

The fitted curve for Π_t versus Ψ_t is:

$$\Pi_t(\Phi_t) = p_1\Phi_t^2 + p_2\Phi_t + p_3 \tag{4.36}$$

where the parameter values have been identified as:

$p_1 = 3.138$

$p_2 = -0.1379$

$p_3 = -0.0023$

Equations (4.28), (4.29) and (4.35) combine to give:

$$\dot{m}_t = \text{sign}(p^*)\rho_{in}\Omega_t D_t^3 \left[a \left(\frac{p_{at}\,|p^*|}{\rho_{in}\Omega_t^2 D_t^2} \right)^b + c \right] \tag{4.37}$$

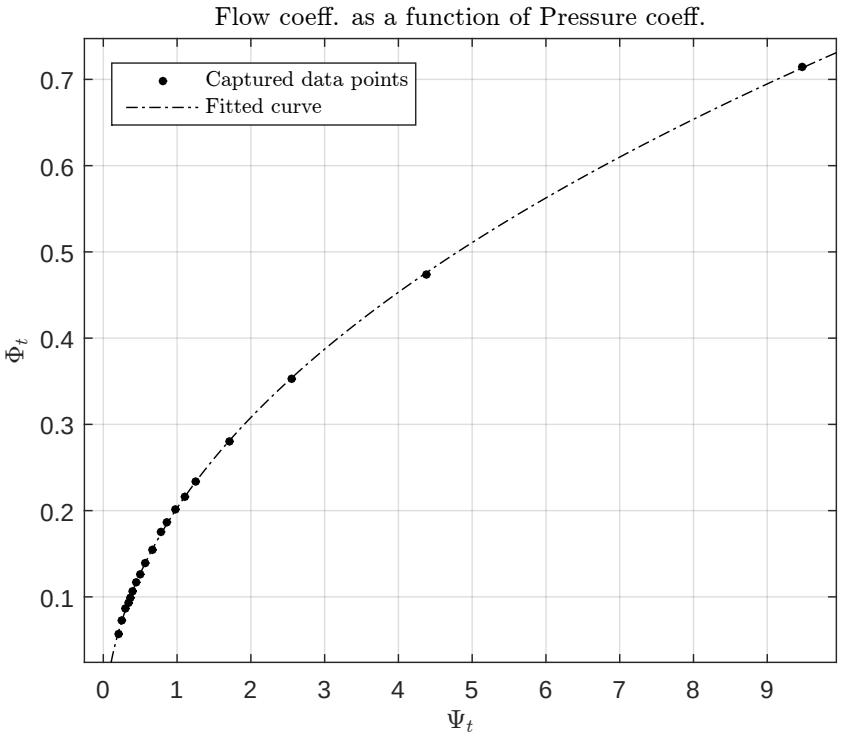

Figure 4.5: Flow Coefficient versus Pressure Coefficient.

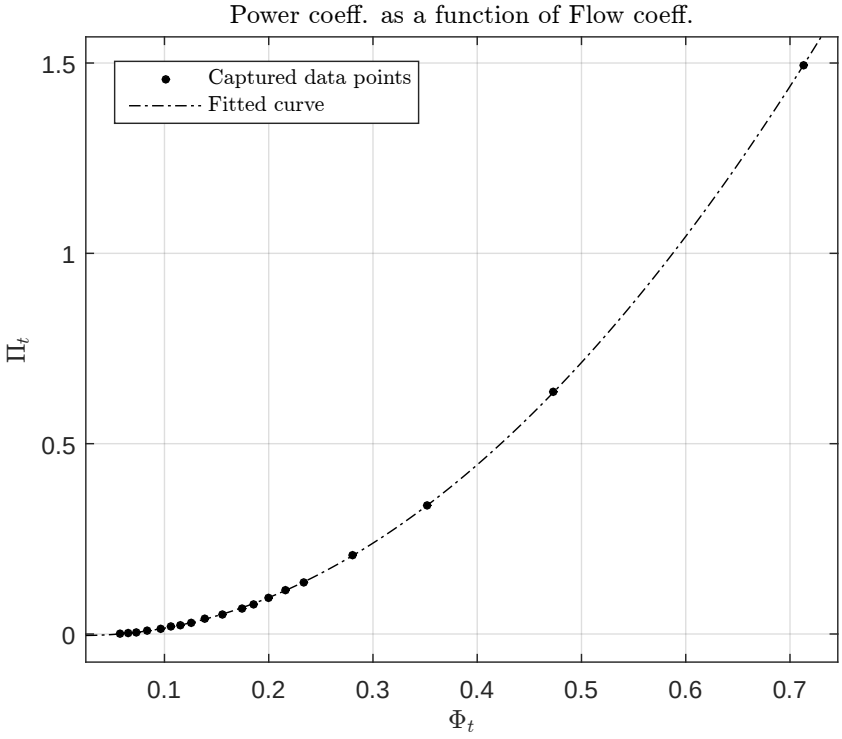

Figure 4.6: Power Coefficient versus Flow Coefficient.

The *sign* operator is used to correct for the *absolute* operator. Equation (4.37) is then substituted into (4.26) to obtain the coupled nonlinear pressure, that relates the air chamber and turbine:

$$\dot{p}^* = -\gamma_a(p^*+1)\frac{\dot{V}_c}{V_c} - \gamma_a(p^*+1)^\beta \frac{1}{\rho_{at}V_c}\left\{\text{sign}(p^*)\rho_{in}\Omega_t D_t^3\left[a\left(\frac{p_{at}\,|p^*|}{\rho_{in}\Omega_t^2 D_t^2}\right)^b + c\right]\right\} \quad (4.38)$$

The nonlinear ODE for the chamber pressure in (4.38) has been solved in this research with the Runge-Kutta 4th order method [60] using:

$$p^*(k) = p^*(k-1) + \frac{1}{6}(k_1 + 2k_2 + 2k_3 + k_4)T_s \quad (4.39)$$

where:

$$\begin{aligned} k_1 &= f_p\left\{p^*(k-1), \quad \dot{V}_c(k), \quad V_c(k)\right\} \\ k_2 &= f_p\left\{p^*(k-1) + 0.5T_s k_1, \quad \dot{V}_c(k), \quad V_c(k)\right\} \\ k_3 &= f_p\left\{p^*(k-1) + 0.5T_s k_2, \quad \dot{V}_c(k), \quad V_c(k)\right\} \\ k_4 &= f_p\left\{p^*(k-1) + k_3 T_s, \quad \dot{V}_c(k), \quad V_c(k)\right\} \end{aligned} \quad (4.40)$$

Note: $f_p\left\{p^*(k-1), \quad \dot{V}_c(k), \quad V_c(k)\right\}$ is used as shorthand here for equation (4.38). Also:

$$V_c(k) = V_o + A_{wc}(z_9(k-1) - z_3(k-1)) \quad (4.41)$$

$$\dot{V}_c(k) = A_{wc}(\dot{z}_9(k-1) - \dot{z}_3(k-1)) \quad (4.42)$$

Once the solution to p^* is found, the PTO force is calculated from:

$$f_{PTO}(k) = A_{wc}p_{at}p^*(k) \quad (4.43)$$

The PTO force and WEC's absorbed power are calculated as:

$$f_{PTO} = A_{wc}p_{at}p^* \quad (4.44)$$

$$P_{WEC} = f_{PTO}(\dot{z}_9 - \dot{z}_3) \quad (4.45)$$

The turbine torque applied to the MIMO generator model in Section 4.5 is calculated

by combining equations (4.28), (4.32), (4.35), (4.36), and (4.37). This leads to T_t becoming a function of p^*, Ω_t and ρ_{in}, which is relatively straightforward to calculate in simulations or measure in the field.

The optimal efficiency of the turbine can be found from the efficiency characteristic, in [57], to be $\Phi_{t_{opt}} = 1.05$. In order to use it with the dimensionless characteristics it can be transformed using the following relationship that relates the two coefficients through the hub-to-tip ratio, ξ [55]:

$$\Phi_t = \phi \left\{ \frac{\pi(1+\xi)^2(1-\xi)}{16} \right\} \tag{4.46}$$

The optimal dimensionless flow coefficient is then found to be $\Phi_{t_{opt}} = 0.18$. Substituting it into (4.28) allows calculation of the optimal turbine velocity, $\Omega_{t_{opt}}$. Also, the air flow needs to be rectified when using the turbine characteristics. It should be noted that the modelling approach adopted in this research decouples the model at the point of the turbine torque. The torque then becomes an input into the turbine-to-wire model, which is the plant being controlled by the control algorithm.

Currently, the control algorithm does not include online optimisation of the turbine velocity, however future research could modify the approach such that the optimal velocity setpoint is calculated online from the turbine's optimal efficiency characteristic. One approach would be to calculate the root-mean-squared (RMS) value of $\dot{m}_t$ over a historic window, and then substitute it into (4.28), obtaining the optimal velocity setpoint as:

$$\Omega_{t_{opt}} = \frac{\text{RMS}(\dot{m}_t)}{\rho_{in}\Phi_{t_{opt}}D_t^3} \tag{4.47}$$

4.4 Sea States

One of the locations being considered for testing a full scale WRAM is the AMETS test site. Comparisons between idealised and measured sea conditions are summarised in [61] with more detail provided in [62]. Given the good agreement between the Bretschneider (BS) spectrum and measured spectra at AMETS, the BS spectrum is used in the current research. This also comes with the assumption that linear wave theory is reasonable, meaning that the fluid layer is assumed to have a uniform mean depth, and that the fluid flow is inviscid,

incompressible and irrotational. Mathematically, the BS spectrum is described by [62]:

$$S(f) = Af^{-5}e^{-Bf^{-4}} \tag{4.48}$$

where:

$$A = 0.25B(H_s^2) \tag{4.49}$$

$$B = (0.751)^4 T_z^{-4} \tag{4.50}$$

T_z and H_s are the zero-crossing period and significant waveheight respectively. It is often the case that T_e is known rather than T_z, in which case for the BS spectrum it is valid to use $T_e = 1.206T_z$ [61]. In the scenario where the reverse calculation is desired, for example when calculating the spectral parameters from measured waverider data, spectral moment analysis can be used. The n^{th} spectral moment is defined as:

$$m_n = \int_0^\infty f^n S(f) df \tag{4.51}$$

From the n^{th} spectral moment the following parameters can be found:

$$H_s = 4\sqrt{m_0} \tag{4.52}$$

$$T_e = m_{-1}/m_0 \tag{4.53}$$

$$T_z = \sqrt{m_0/m_2} \tag{4.54}$$

Another common parameter is the peak period, T_p, defined simply as the period corresponding to the peak of the spectrum. Some software packages such as the MATLAB® WAFO toolbox [63] use T_p rather than T_z to calculate the spectral density. In this case, the BS spectrum is created from the JONSWAP spectrum defined as [64]:

$$S(\omega) = \frac{\alpha g^2}{\omega^5} \exp\left(-\frac{5}{4}\left(\frac{\omega_p}{\omega}\right)^4\right) \gamma_{js}^{\exp\left(\frac{-(\omega/\omega_p - 1)^2}{2\sigma^2}\right)} \tag{4.55}$$

where:

$$\sigma = \begin{cases} 0.07 & \text{if } \omega < \omega_p \\ 0.09 & \text{if } \omega \geq \omega_p \end{cases}$$

$$\alpha \approx 5.061 \frac{H_s^2}{T_p^4} \left\{1 - 0.287 \ln(\gamma_{js})\right\}$$

JONSWAP and Bretschneider are equivalent when $\gamma_{js} = 1$. After converting ω to f, ω_p to T_p and substituting in $\gamma_{js} = 1$, equation (4.55) takes the form of (4.48) such that:

$$S(f) = A' f^{-5} e^{-B' f^{-4}} \tag{4.56}$$

where:

$$A' = \frac{5.061 g^2 H_s^2}{(2\pi)^5 T_p^4} \tag{4.57}$$

$$B' = \frac{5}{4} T_p^{-4} \tag{4.58}$$

Figure 4.7 shows the Bretschneider spectrum for the sea state simulated in Chapter 7. Irregular sea states are usually simulated in the time domain by linearly superimposing the harmonic components of the spectrum, applying a random phase to each component. The wave elevation time series is expressed as:

$$\zeta(t) = \sum_{i=1}^{N_f} \zeta_i \cos(\omega_i t + \phi_i) \tag{4.59}$$

where:

ζ_i :	Wave amplitude of the i^{th} spectral component	(m)
ω_i :	Angular frequency of the i^{th} spectral component	(rad s^{-1})
ϕ_i :	Random phase of the i^{th} spectral component	(rad)
N_f :	Number of frequencies	

The i^{th} wave elevation amplitude component is found from the spectrum:

$$\zeta_i = \sqrt{2S(f)df} \tag{4.60}$$

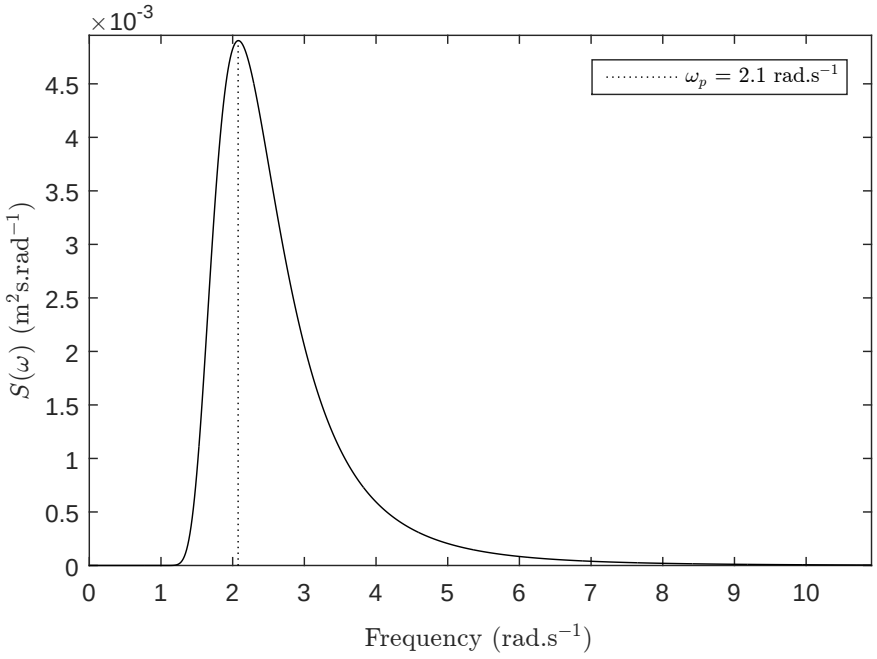

Figure 4.7: Bretschneider Spectrum, scaled down from Full Scale: $H_s = 6.75$ m, $T_e = 11.5$s.

The excitation force is calculated as an extension of the wave elevation:

$$f_e(t) = \sum_{i=1}^{N_f} |F_{e_i}(\omega)|\, \zeta_i \cos(\omega_i t + \phi_i + \angle F_{e_i}(\omega)) \tag{4.61}$$

where:

$|F_{e_i}(\omega)|$: Magnitude $F_{e_i}(\omega)$ $(\mathrm{N\,m^{-1}})$

$\angle F_{e_i}(\omega)$: Phase of $F_{e_i}(\omega)$ (rad)

$F_{e_i}(\omega)$ is the i^{th} component of the excitation force frequency response function.

4.5 Turbine-to-Wire Model

4.5.1 Generator

The focus of this research is to apply real-time MPC to the maximise power capture of the WRAM's PTO. Firstly, an appropriate model is needed for the generator and its electrical drive system. Also, it is usual for these drives to have low level PID loops, around which

optimal control algorithms must operate. Therefore, this low level control needs to be incorporated into the generator model and furthermore, the practical implementation challenges with the embedded control system need to dealt with. An example is when the low level control loops are distributed across different third party vendors. The generator and control systems used on the WRAM emulation platform are no exception, and developing a real-time optimal control application for it has required taking all of these issues into account, sometimes with limited access to the necessary supplier data. Nevertheless, a suitable generator model has been successfully developed and used within the framework of real-time MPC. This section describes the details of the generator model and how the underlying low level PID control has been incorporated into it. In explaining the complete generator model it makes sense to start with the innermost component and work outwards though the different control loops. Eventually, this leads to a MIMO system with two inputs and two outputs.

4.5.2 Fundamental Generator Model

The innermost component is the generator installed on the WRAM emulation platform. It is an off-the-shelf Kollmorgen AKM23F brushless DC servo-generator (see Figure 4.8), that can operate in all four quadrants, meaning that it can motor as well as generate. Conveniently, this type of generator has enough similarities with a simple brushed DC generator to be able to utilise its well-established linear model. Also, the AKM23F datasheet gives lumped parameter specifications that can be substituted directly into the model. It should be noted that while a DC generator model is used in this research, the modelling approach is modular. Therefore alternative generator models can be used in future research without loss of generality of the control approach.

Fundamentally, the generator model is a two DoF LTI system, where the two DoF's are coupled through the shaft's angular velocity, Ω_t, and winding current, I. The two inputs to the system are the turbine torque, T_t, and winding voltage, E, and the two outputs are Ω_t and I. This MIMO system is encapsulated in the sections that follow by the internal servo-drive control loops. For the coupled turbine-generator, the ordinary differential equations

Figure 4.8: Kollmorgen AKM23F Servo-Generator.

are:

$$J_t \frac{d\Omega_t}{dt} - b_t \Omega_t - K_t I = T_t \tag{4.62}$$

$$L \frac{dI}{dt} + RI + K_e \Omega_t = E \tag{4.63}$$

The state space equivalent is:

$$\begin{aligned} \dot{\mathbf{X}}_g &= \mathbf{A}_g \mathbf{X}_g + \mathbf{B}_g \mathbf{U}_g \\ \mathbf{Y}_g &= \mathbf{C}_g \mathbf{X}_g \end{aligned} \tag{4.64}$$

where:

$$\mathbf{A}_g = \begin{bmatrix} \frac{b_t}{J_t} & \frac{K_t}{J_t} \\ -\frac{K_e}{L} & -\frac{R}{L} \end{bmatrix}, \mathbf{B}_g = \begin{bmatrix} \frac{1}{J_t} & 0 \\ 0 & \frac{1}{L} \end{bmatrix}, \mathbf{C}_g = \begin{bmatrix} 1 & 0 \\ 0 & 1 \end{bmatrix}, \mathbf{X}_g = \begin{bmatrix} \Omega_t \\ I \end{bmatrix}, \mathbf{U}_g = \begin{bmatrix} T_t \\ E \end{bmatrix} \tag{4.65}$$

I:	Current	(A)
Ω_t:	Turbine angular velocity	(rad s^{-1})
J_t:	Moment of inertia (rotor and turbine)	(kg m^2)
b_t:	Generator viscous friction constant (rotor and turbine)	(N m s)
K_t:	Generator torque constant	(N m A^{-1})
E:	Winding voltage	(V)
R:	Electric resistance	(Ω)
L:	Electric inductance	(H)
K_e:	Electromotive force constant	(V s rad^{-1})

To simplify the model formulation, it is helpful to recast the state space formulation in (4.65) into the following MIMO, frequency domain transfer function:

$$\mathbf{G}_g(s) = \mathbf{C}_g(s\mathbf{I} - \mathbf{A}_g)^{-1}\mathbf{B}_g \triangleq \begin{bmatrix} G_{g_{11}}(s) & G_{g_{12}}(s) \\ G_{g_{21}}(s) & G_{g_{22}}(s) \end{bmatrix} \tag{4.66}$$

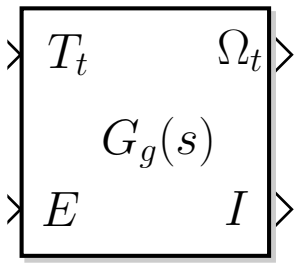

Figure 4.9: MIMO Generator Block.

It can be seen that (4.66) contains the following SISO relationships between each input and output:

$G_{g_{11}}(s)$ relates T_t and Ω_t.

$G_{g_{12}}(s)$ relates E and Ω_t.

$G_{g_{21}}(s)$ relates T_t and I.

$G_{g_{22}}(s)$ relates E and I.

4.5.3 Drive Loops

The generator is directly controlled by a Kollmorgen AKD servo-drive, shown in Figure 4.10, that energises the generator's windings in response to its internal control loop and power electronics. This operates on an internal PID control loop that accepts an externally

Figure 4.10: Kollmorgen AKD Servo-Drive.

provided setpoint to control either the velocity, torque or displacement, depending on the configuration. In this application, the drive's control loop is coupled with the real-time embedded controller (cRIO) on the emulation platform that uses a specific software module, called NI SoftMotion, to configure and connect to the servo-drive. Section 5.4.3 shows how Labview's P- and D-gains in the displacement loop can be used to tune the system response to behave like a PI-controlled velocity loop. Figure 4.11 shows the actual PD-control loop.

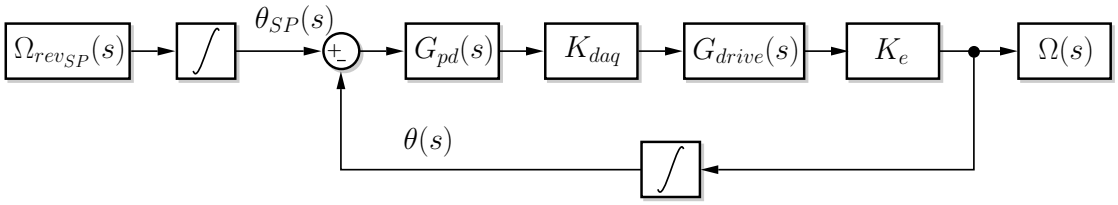

Figure 4.11: Actual PD-Control Loop for Servo-Drive.

Figure 4.12 shows the equivalent simpler PI-control loop used in the formulation of the MIMO plant model derived in this chapter. Note the following variable definitions for Figure 4.11 and Figure 4.12:

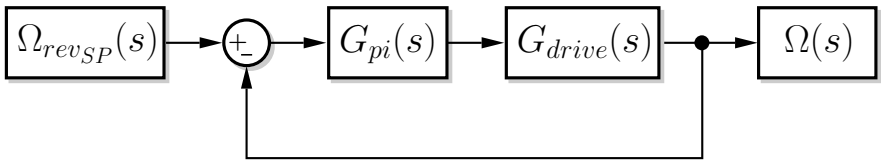

Figure 4.12: Simplified Equivalent PI-Control Loop.

K_{dac}:	Digital to analog gain.	
$G_{pd}(s)$:	Displacement loop PD-gains.	
$G_{pi}(s)$:	Equivalent velocity loop PI-gains.	
$G_{drive}(s)$:	Servo-drive transfer function including generator.	
$\theta_{SP}(s)$:	Setpoint shaft displacement	(rad).
$\theta(s)$:	Output shaft displacement	(rad).

4.5.4 Current Loop

Figure 4.13 shows how the generator is incorporated into the servo-drive's innermost current loop, where the setpoint current is provided by the cRIO's PI-control output. Note that K_{p_i} is the current loop's P-gain. After block simplification, the current loop is represented by the MIMO block shown in Figure 4.14.

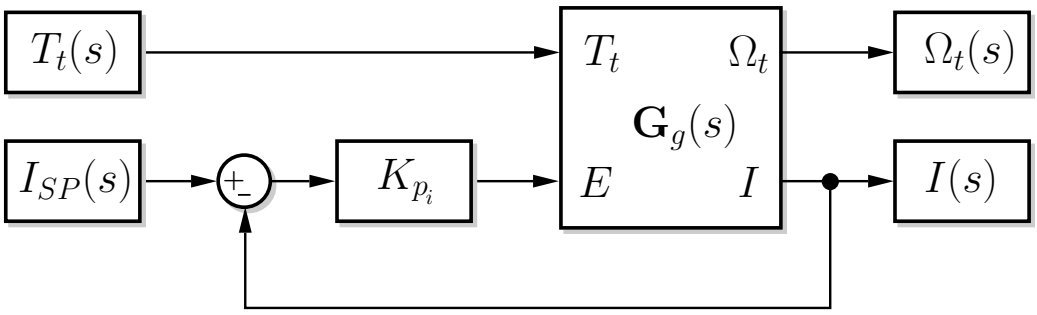

Figure 4.13: Current Loop with MIMO Generator.

The current loop MIMO block has been structured such that the link between T_t and Ω_t is removed, and then re-established into the velocity loop. This was necessary in order to correctly implement the disturbance rejection of T_t. As such, $G_{i_{11}}$ has been set to zero. The

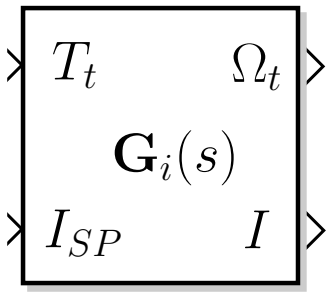

Figure 4.14: Current Loop MIMO Block.

inputs, outputs and internal SISO transfer functions for $\mathbf{G}_i(s)$ are:

$$\mathbf{Y}_i(s) = \begin{bmatrix} \Omega_t(s) \\ I(s) \end{bmatrix}, \quad \mathbf{G}_i(s) = \begin{bmatrix} 0 & G_{i_{12}}(s) \\ G_{i_{21}}(s) & G_{i_{22}}(s) \end{bmatrix}, \quad \mathbf{U}_i(s) = \begin{bmatrix} T_t(s) \\ I_{SP}(s) \end{bmatrix} \tag{4.67}$$

where:

$\mathbf{U}_i(s)$:	Current loop inputs	
$\mathbf{Y}_i(s)$:	Current loop outputs	
$I_{SP}(s)$:	Setpoint current	(A)
$I(s)$:	Generator current	(A)

From classical control theory, a general feedback model with input, $R(s)$, output, $Y(s)$, and disturbance, $D(s)$ is shown in Figure 4.15.

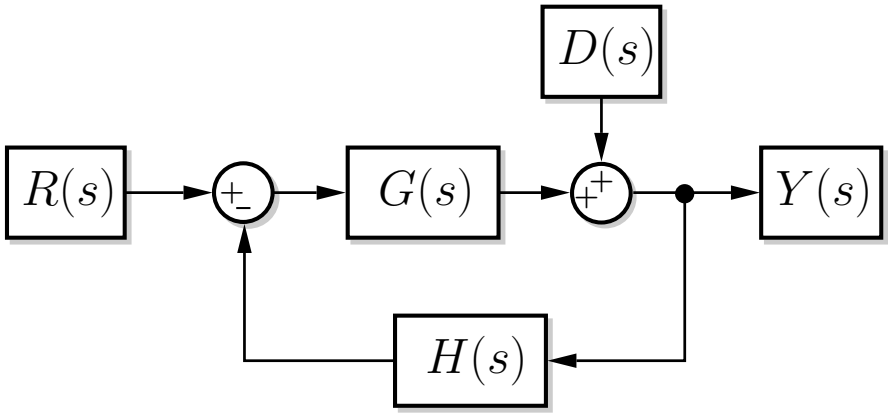

Figure 4.15: Classical Feedback Loop Model.

The relationship between the input and output can be represented by the transfer function:

$$\frac{Y(s)}{R(s)} = \frac{G(s)}{1 + G(s)H(s)} \tag{4.68}$$

The relationship between the disturbance and output is represented by:

$$\frac{Y(s)}{D(s)} = \frac{1}{1 + G(s)H(s)} \tag{4.69}$$

Based on the block simplification approach, using (4.68), the SISO transfer function for I_{SP} to I in equation (4.67) is:

$$G_{i_{22}}(s) = \frac{I(s)}{I_{SP}(s)} = \frac{K_{p_i} G_{g_{22}}(s)}{1 + K_{p_i} G_{g_{22}}(s)} \tag{4.70}$$

The current feedback loop poses some difficulty in determining the transfer function from I_{SP} to Ω_t. However, the relationships between E to Ω_t and E to I are defined by $G_{g_{12}}(s)$ and $G_{g_{22}}(s)$ respectively, in equation (4.66). Combining these with $G_{i_{22}}(s)$, in equation (4.70), and also:

$$E(s) = G_{i_{22}}^{-1}(s) I(s) \tag{4.71}$$

leads to the following transfer function for I_{SP} to Ω_t:

$$G_{i_{12}}(s) = \frac{\Omega_t(s)}{I_{SP}(s)} = \frac{K_{p_i} G_{g_{12}}(s)}{1 + K_{p_i} G_{g_{22}}(s)} \tag{4.72}$$

The transfer function, $G_{i_{21}}(s)$, that relates T_t to I, is the same as $G_{g_{21}}(s)$. The complete current loop MIMO transfer function is:

$$\mathbf{G}_i(s) = \begin{bmatrix} 0 & \frac{K_{p_i} G_{g_{12}}(s)}{1 + K_{p_i} G_{g_{22}}(s)} \\ G_{g_{21}}(s) & \frac{K_{p_i} G_{g_{22}}(s)}{1 + K_{p_i} G_{g_{22}}(s)} \end{bmatrix} \tag{4.73}$$

4.5.5 Velocity Loop

The MIMO transfer function for the velocity loop, $\mathbf{G}_\Omega(s)$, has been defined to have the following the inputs, outputs and internal SISO transfer functions:

$$\mathbf{Y}_\Omega(s) = \begin{bmatrix} \Omega_{rev}(s) \\ T_g(s) \end{bmatrix}, \mathbf{G}_\Omega(s) = \begin{bmatrix} G_{\Omega_{11}}(s) & G_{\Omega_{12}}(s) \\ G_{\Omega_{21}}(s) & G_{\Omega_{22}}(s) \end{bmatrix}, \mathbf{U}_\Omega(s) = \begin{bmatrix} T_t(s) \\ \Omega_{rev_{SP}}(s) \end{bmatrix} \tag{4.74}$$

where:

$\mathbf{U}_\Omega(s)$:	Velocity loop inputs	
$\mathbf{Y}_\Omega(s)$:	Velocity loop outputs	
$\Omega_{rev_{SP}}(s)$:	Setpoint velocity	(rev s^{-1})
$\Omega_{rev}(s)$:	Output velocity	(rev s^{-1})
$T_g(s)$:	Generator torque	(Nm)

Note that $\Omega_{rev_{SP}}(s)$ and $\Omega_{rev}(s)$ are in the units of rev.s^{-1}, rather than rad.s^{-1}, to suit the code implementation on the cRIO. The block diagram for the velocity loop is shown in Figure 4.16, where:

$G_{pi}(s)$:	PI-controller transfer function	
K_a:	Servo-drive input signal gain	(A V^{-1})
$K_\Omega = (2\pi)^{-1}$:	Angular velocity scaling factor	(rad.s^{-1} to rev.s^{-1})

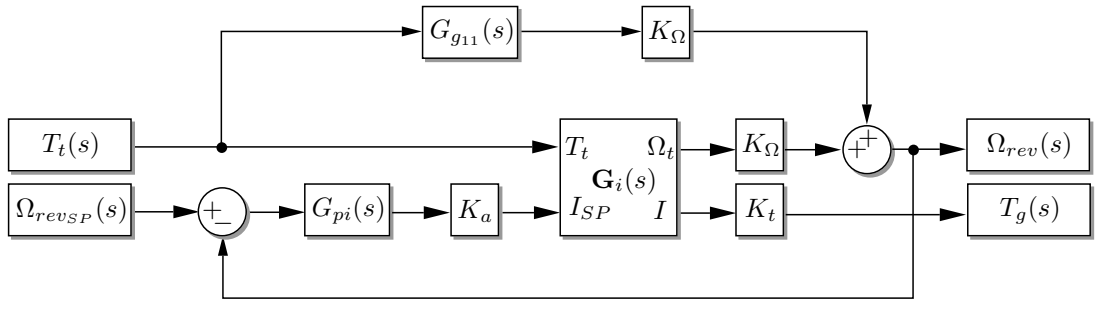

Figure 4.16: Velocity Loop Block Diagram.

The proportional-integral (PI) controller is represented by the transfer function:

$$G_{pi}(s) = K_{p_\Omega} + \frac{K_{i_\Omega}}{s} \tag{4.75}$$

where:

K_{p_Ω}: P-gain for the velocity loop.

K_{i_Ω}: I-gain for the velocity loop.

For the velocity loop, the turbine torque is treated as a disturbance to the velocity output. In order to simplify the block diagram, the terms $G_{pi}(s)$, K_a, $G_{i_{12}}(s)$, and K_Ω, in the velocity feedback loop need to be incorporated into a disturbance model. Using equation (4.69) and a disturbance signal equal to $T_t(s)K_\Omega G_{g_{11}}(s)$ leads to:

$$G_{\Omega_{11}}(s) = \frac{K_\Omega G_{g_{11}}(s)}{1 + K_a K_\Omega G_{pi}(s) G_{i_{12}}(s)} \tag{4.76}$$

The transfer function for T_t to I is taken from the open-loop generator transfer function, $G_{g_{21}}(s)$, and then multiplied by K_t to obtain the generator torque, T_g. The resulting transfer function is:

$$G_{\Omega_{21}}(s) = G_{g_{21}}(s) K_t \tag{4.77}$$

The transfer function for $\Omega_{rev_{SP}}$ to Ω_{rev} is formulated by considering only the components in the feedback loop, excluding the torque input and disturbance signal which have already be accounted for. The resulting transfer function is:

$$G_{\Omega_{12}}(s) = \frac{K_a K_\Omega G_{pi}(s) G_{i_{12}}(s)}{1 + K_a K_\Omega G_{pi}(s) G_{i_{12}}(s)} \tag{4.78}$$

The transfer function for $\Omega_{rev_{SP}}$ to T_g is constructed by working backwards from Ω_{rev} by applying the inverse of $G_{i_{12}}(s)$ to get I_{SP}, and then applying the transfer function $G_{i_{22}}(s)$ to obtain I. The output is then multiplied by K_t to obtain the final transfer function:

$$G_{\Omega_{22}}(s) = \frac{K_t K_a K_\Omega G_{pi}(s) G_{i_{22}}(s)}{1 + K_a K_\Omega G_{pi}(s) G_{i_{12}}(s)} \tag{4.79}$$

The overall velocity loop MIMO transfer function is finally formulated as:

$$\mathbf{G}_\Omega(s) = \begin{bmatrix} \dfrac{K_\Omega G_{g_{11}}(s)}{1 + K_a K_\Omega G_{pi}(s) G_{i_{12}}(s)} & \dfrac{K_a K_\Omega G_{pi}(s) G_{i_{12}}(s)}{1 + K_a K_\Omega G_{pi}(s) G_{i_{12}}(s)} \\ G_{g_{21}}(s) K_t & \dfrac{K_t K_a K_\Omega G_{pi}(s) G_{i_{22}}(s)}{1 + K_a K_\Omega G_{pi}(s) G_{i_{12}}(s)} \end{bmatrix} \tag{4.80}$$

The MIMO transfer function in (4.80) provides a very compact representation of the generator, turbine, servo-drive and low level velocity PI-controller.

4.6 System Identification

4.6.1 Model Parametrisation

Seven of the eleven parameters embedded within the MIMO model in equation (4.80) were known from specification datasheets, however the remaining four needed to be estimated. Two of these, J_t and b_t, were partially found from the datasheets for the generator. However, portions of these parameters have been derived from the effect of the coupled turbine. The other two unknown parameters are the P- and I-gains of the velocity loop, K_{p_Ω} and K_{i_Ω}. Given that the transfer function, $\mathbf{G}_\Omega(s)$, is well defined, grey-box identification is an ideal tool for estimating the unknown parameters. Prior to identification, and through the use of Mathematica®, the model was fully expanded and grouped by coefficients of the Laplace operator, 's'. Manipulating the transfer function in this way was simply done to suit the MATLAB® implementation requirements. The resulting parametrised model is compactly expressed here, to ease readability, as:

$$\hat{\mathbf{G}}_\Omega(s) = \begin{bmatrix} \dfrac{\epsilon_1 s^3 + \cdots + \epsilon_3 s}{\zeta_1 s^5 + \cdots + \zeta_5 s + \zeta_6} & \dfrac{\mu_1 s + \mu_2}{\nu_1 s^3 + \cdots + \nu_3 s + \nu_4} \\ \dfrac{\sigma_1}{v_1 s^2 + v_2 s + v_3} & \dfrac{\chi_1 s^2 + \chi_2 s + \chi_3}{\omega_1 s^3 + \cdots + \omega_3 s + \omega_4} \end{bmatrix} \tag{4.81}$$

where:

$$\epsilon_1 = K_\Omega(J_t K_{p_i} L - b_t L^2 + 2J_t LR)$$

$$\epsilon_2 = K_\Omega(-b_t K_{p_i} L + K_e K_t L + J_t K_{p_i} R - 2b_t LR + J_t R^2)$$

$$\epsilon_3 = K_\Omega(-b_t K_{p_i} R + K_e K_t R - b_t R^2)$$

$$\zeta_1 = J_t^2 L^2$$

$$\zeta_2 = J_t^2 K_{p_i} L - 2b_t J_t L^2 + 2J_t^2 LR$$

$$\zeta_3 = -2b_t J_t K_{p_i} L + 2J_t K_e K_t L + J_t K_a K_{p_i} K_{p_\Omega} K_\Omega K_t L + b_t^2 L^2 + J_t^2 K_{p_i} R$$
$$-4b_t J_t LR + J_t^2 R^2$$

$$\zeta_4 = J_t K_e K_{p_i} K_t + b_t^2 K_{p_i} L - 2b_t K_e K_t L + J_t K_a K_{i_\Omega} K_{p_i} K_\Omega K_t L - b_t K_a K_{p_i} K_{p_\Omega} K_\Omega K_t L$$
$$-2b_t J_t K_{p_i} R + 2J_t K_e K_t R + J_t K_a K_{p_i} K_{p_\Omega} K_\Omega K_t R + 2b_t^2 LR - 2b_t J_t R^2$$

$$\zeta_5 = -b_t K_e K_{p_i} K_t + K_e^2 K_t^2 + K_a K_e K_{p_i} K_{p_\Omega} K_\Omega K_t^2 - b_t K_a K_{i_\Omega} K_{p_i} K_\Omega K_t L + b_t^2 K_{p_i} R$$
$$-2b_t K_e K_t R + J_t K_a K_{i_\Omega} K_{p_i} K_\Omega K_t R - b_t K_a K_{p_i} K_{p_\Omega} K_\Omega K_t R + b_t^2 R^2$$

$$\zeta_6 = K_a K_e K_{i_\Omega} K_{p_i} K_\Omega K_t^2 - b_t K_a K_{i_\Omega} K_{p_i} K_\Omega K_t R$$

$$\mu_1 = K_a K_{p_i} K_{p_\Omega} K_\Omega K_t$$

$$\mu_2 = K_a K_{i_\Omega} K_{p_i} K_\Omega K_t$$

$$\nu_1 = J_t L$$

$$\nu_2 = J_t K_{p_i} - b_t L + J_t R$$

$$\nu_3 = -b_t K_{p_i} + K_e K_t + K_a K_{p_i} K_{p_\Omega} K_\Omega K_t - b_t R$$

$$\nu_4 = K_a K_{i_\Omega} K_{p_i} K_\Omega K_t$$

$$\sigma_1 = -K_e K_t$$

$$v_1 = J_t L$$

$$v_2 = -b_t L + J_t R$$

$$v_3 = K_e K_t - b_t R$$

$$\chi_1 = J_t K_a K_{p_i} K_{p_\Omega} K_\Omega K_t$$

$$\chi_2 = -K_a K_{p_i}(-J_t K_{i_\Omega} + b_t K_{p_\Omega}) K_\Omega K_t$$

$$\chi_3 = -b_t K_a K_{i_\Omega} K_{p_i} K_\Omega K_t$$

$$\omega_1 = J_t L$$

$$\omega_2 = J_t K_{p_i} - b_t L + J_t R$$

$$\omega_3 = -b_t K_{p_i} + K_e K_t + K_a K_{p_i} K_{p_\Omega} K_\Omega K_t - b_t R$$

$$\omega_4 = K_a K_{i_\Omega} K_{p_i} K_\Omega K_t$$

Note that the grey-box estimation problem is solved with all of the above parameters substituted into (4.81), thus distinguishing the approach as grey-box identification from black-box identification.

4.6.2 System Identification Experiments

In order to utilise grey-box identification, experiments were conducted to obtain measured output responses to known input commands of the coupled turbine and generator. The input and output were the generator's setpoint and measured angular velocities respectively, where the input consisted of random setpoint changes of varying amplitudes. These signals can be seen in Figure 4.17.

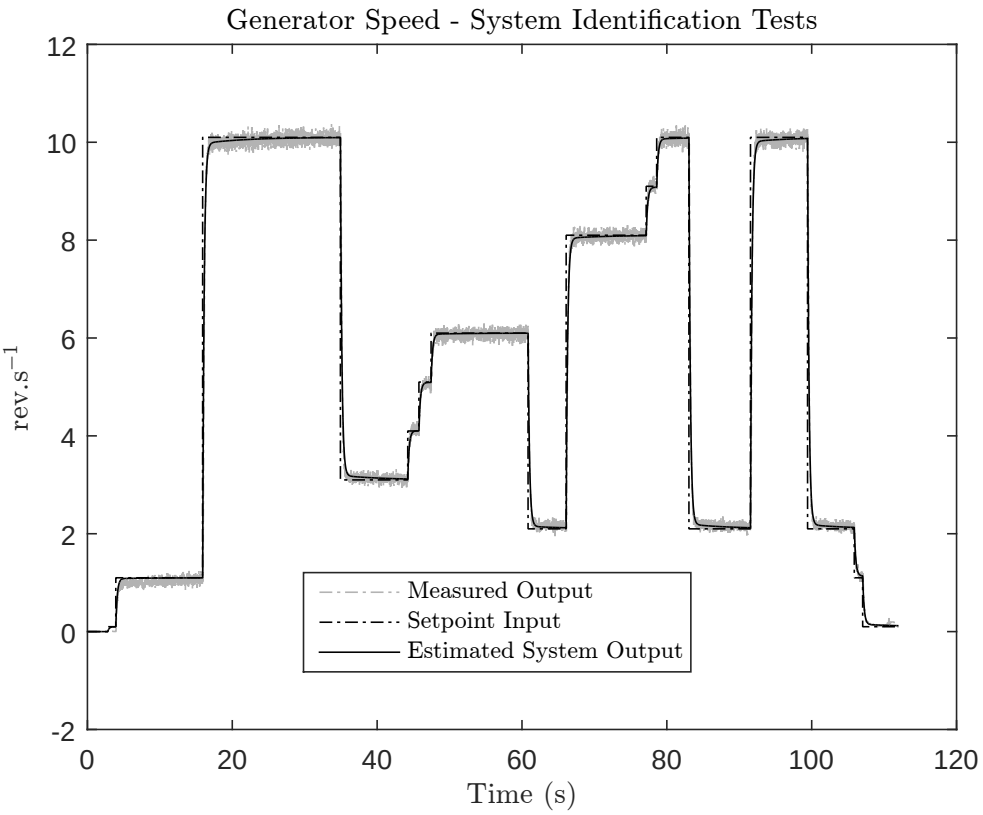

Figure 4.17: System Identification of the Generator Parameters.

Table 4.1: Identified Parameters of the MIMO Generator.

Parameter	Initial Estimate	Final Value
J_t	$5.79(10)^{-3}$	$5.82(10)^{-3}$
b_t	$6.21(10)^{-5}$	$4.191(10)^{-5}$
K_{p_Ω}	8000	1.693
K_{i_Ω}	0.1	0.2932

4.6.3 Grey-Box System Identification

Based on measured responses, the MATLAB® function, *greyest*, from the System Identification Toolbox® was used to identify the unknown parameters, J_t, b_t, K_{p_Ω} and K_{i_Ω}. The initial value of J_t was based on the sum of inertias of the generator rotor, from the supplier datasheet, and the turbine inertia calculated in the software package Solidworks®. The initial value of b_t was taken directly from the generator specification sheet, ignoring the contribution of turbine viscous friction. Following execution of the grey-box identification algorithm, the output response of the system can be seen in Figure 4.17. A goodness-of-fit of 95.97% has been calculated using the normalised root-mean-square error (NRMSE), indicating a very close fit. Table 4.1 shows the converged parameter values for J_t, b_t, K_{p_Ω} and K_{i_Ω}.

4.6.4 Reduced Order Discrete Model

In addition to parametrising the model, Mathematica® was used to reduce the model order through the cancellation of terms in the transfer functions. Equation (4.81) shows the highest order of all the transfer functions after simplification to be five, whereas the highest order of the original transfer function, (4.80), when expanded in MATLAB®, was sixteen. Following reduction of the model, it was discretised for subsequent use in the RT MPC formulation

(Chapter 6) that uses an augmented NMSS structure. The discretised version of (4.81) is:

$$\hat{\mathbf{G}}_{\Omega_d}(z) = \begin{bmatrix} \dfrac{\epsilon_{d_1}z^{-1} + \cdots + \epsilon_{d_5}z^{-5}}{1 + \zeta_{d_1}z^{-1} + \cdots + \zeta_{d_4}z^{-4}} & \dfrac{\mu_{d_1}z^{-1} + \cdots + \mu_{d_3}z^{-3}}{1 + \nu_{d_1}z^{-1} + \cdots + \nu_{d_3}z^{-3}} \\ \dfrac{\sigma_{d_1}z^{-1} + \sigma_{d_2}z^{-2}}{1 + \upsilon_{d_1}z^{-1} + \upsilon_{d_2}z^{-2}} & \dfrac{\chi_{d_1}z^{-1} + \cdots + \chi_{d_3}z^{-3}}{1 + \omega_{d_1}z^{-1} + \cdots + \omega_{d_3}z^{-3}} \end{bmatrix} \tag{4.82}$$

4.7 NMSS Plant Formulation

4.7.1 MIMO Plant Model

It is possible to formulate the plant model such that the use of an observer can be avoided. This is one of the goals in classical predictive control, for example generalised predictive control (GPC). The observers are avoided through direct use of the plant's inputs and outputs in the closed-loop feedback control. A modified approach, presented in [1], transforms the plant from a discrete transfer function into a NMSS model. A key point is that the state variable includes differential inputs and outputs of the system, thus simplifying the implementation compared to GPC. Also, the coefficients of the state space model are the same as those in the original transfer function. The NMSS model also allows the closed-loop controller to be formulated into a transfer function directly from the coefficients in the control feedback matrix, $\mathbf{K}_{mpc}$. This assists in the analysis of frequency response data such as gain and phase margins. Of course, the state space formulation also allows the system eigenvalues to be easily calculated. The procedure in [1], for formulating the NMSS model for a MIMO system with two inputs and outputs is presented here, which is identical to the structure of the controlled plant in this research. It should be noted however that the approach is valid for any sized MIMO system.

4.7.2 Matrix Fraction Description

The first step in creating the NMSS model is to reformulate the MIMO transfer function such that (4.83) can be expressed as a matrix difference equation. This can be achieved with a left matrix fraction description (LMFD) as outlined in [1], [65]. Consider the example of a

generic second order discrete MIMO transfer function, defined by:

$$\begin{bmatrix} y_1(k) \\ y_2(k) \end{bmatrix} = \mathbf{G}_m(z) \begin{bmatrix} u_1(k) \\ u_2(k) \end{bmatrix} \tag{4.83}$$

where:

$$\mathbf{Y}_m(k) = \begin{bmatrix} y_1(k) \\ y_2(k) \end{bmatrix}, \mathbf{U}_m(k) = \begin{bmatrix} u_1(k) \\ u_2(k) \end{bmatrix} \tag{4.84}$$

$$\mathbf{G}_m(z) = \begin{bmatrix} \dfrac{N_{11}(z)}{D_{11}(z)} & \dfrac{N_{12}(z)}{D_{12}(z)} \\ \dfrac{N_{21}(z)}{D_{21}(z)} & \dfrac{N_{22}(z)}{D_{22}(z)} \end{bmatrix} \tag{4.85}$$

and $N_{ij}(z)$ and $D_{ij}(z)$, $(i,j) = (1,2)$, are in the form:

$$N_{ij}(z) = n_{1_{ij}} z^{-1} + \cdots + n_{p_{ij}} z^{-p} \tag{4.86}$$

$$D_{ij}(z) = 1 + d_{1_{ij}} z^{-1} + \cdots + d_{p_{ij}} z^{-p} \tag{4.87}$$

Note that each element of $\mathbf{G}_m(z)$ contains a SISO transfer function that describes the relationship between a particular input and output. From the equation (4.85), $\mathbf{G}_m(z)$ is decomposed as:

$$\mathbf{G}_m(z) = \mathbf{D}_m^{-1}(z)\mathbf{N}_m(z) \tag{4.88}$$

where:

$$\mathbf{D}_m(z) = \begin{bmatrix} D_{11}(z)D_{12}(z) & 0 \\ 0 & D_{21}(z)D_{22}(z) \end{bmatrix} \tag{4.89}$$

$$\mathbf{N}_m(z) = \begin{bmatrix} N_{11}(z)D_{12}(z) & N_{12}(z)D_{11}(z) \\ N_{21}(z)D_{22}(z) & N_{22}(z)D_{21}(z) \end{bmatrix} \tag{4.90}$$

Coefficients of like-orders are then grouped to create the following matrices:

$$\mathbf{F}_i = \begin{bmatrix} \mathbf{D}_m(11)_i & 0 \\ 0 & \mathbf{D}_m(22)_i \end{bmatrix}, \quad \mathbf{H}_i = \begin{bmatrix} \mathbf{N}_m(11)_i & \mathbf{N}_m(12)_i \\ \mathbf{N}_m(21)_i & \mathbf{N}_m(22)_i \end{bmatrix} \tag{4.91}$$

where the notation is defined such that, for example, $\mathbf{N}_m(21)_i$ refers to the i^{th} coefficient of the polynomial in element-21 of $\mathbf{N}_m(z)$. Through the use of (4.88), equation (4.83) is manipulated into the form:

$$\mathbf{D}_m(z)\mathbf{Y}_m(z) = \mathbf{N}_m(z)\mathbf{U}_m(z) \tag{4.92}$$

The difference equation representing the MIMO system is created by combining equations (4.89) to (4.92), and taking the inverse Z-transform to obtain:

$$\begin{aligned} \mathbf{Y}_m(k+1) &= -\mathbf{F}_1\mathbf{Y}_m(k) - \mathbf{F}_2\mathbf{Y}_m(k-1) - \cdots - \mathbf{F}_P\mathbf{Y}_m(k-P+1) \\ &+ \mathbf{H}_1\mathbf{U}_m(k) + \mathbf{H}_2\mathbf{U}_m(k-1) + \cdots + \mathbf{H}_Q\mathbf{U}_m(k-Q+1) \end{aligned} \tag{4.93}$$

where P and Q are the highest polynomial orders in $\mathbf{D}_m(z)$ and $\mathbf{N}_m(z)$ respectively. The LMFD approach has been applied in this research to the discrete plant model, $\hat{\mathbf{G}}_{\Omega_d}(z)$, in (4.82). Expressing $\hat{\mathbf{G}}_{\Omega_d}(z)$ in the compact form of:

$$\hat{\mathbf{G}}_{\Omega_d}(z) = \begin{bmatrix} \dfrac{\epsilon(z)}{\zeta(z)} & \dfrac{\mu(z)}{\nu(z)} \\ \dfrac{\sigma(z)}{\upsilon(z)} & \dfrac{\chi(z)}{\omega(z)} \end{bmatrix} \tag{4.94}$$

leads to the following LMFD matrices:

$$\mathbf{D}_\Omega(z) = \begin{bmatrix} \zeta(z)\nu(z) & 0 \\ 0 & \upsilon(z)\omega(z) \end{bmatrix}, \quad \mathbf{N}_\Omega(z) = \begin{bmatrix} \epsilon(z)\nu(z) & \zeta(z)\mu(z) \\ \sigma(z)\omega(z) & \upsilon(z)\chi(z) \end{bmatrix} \tag{4.95}$$

$\mathbf{D}_\Omega(z)$ and $\mathbf{N}_\Omega(z)$ are then decomposed into their coefficient orders to form:

$$\mathbf{F}_i(z) = \begin{bmatrix} \zeta\nu_i & 0 \\ 0 & \upsilon\omega_i \end{bmatrix}, \quad \mathbf{H}_i(z) = \begin{bmatrix} \epsilon\nu_j & \zeta\mu_j \\ \sigma\omega_j & \upsilon\chi_j \end{bmatrix} \tag{4.96}$$

defining the following nomenclature, to ease readability:

$\zeta\nu_i \triangleq \mathrm{i}^{th}$ coefficient of $\zeta(z)\nu(z)$.

$\upsilon\omega_i \triangleq \mathrm{i}^{th}$ coefficient of $\upsilon(z)\omega(z)$.

$\epsilon\nu_j \triangleq \mathrm{j}^{th}$ coefficient of $\epsilon(z)\nu(z)$.

$\zeta\mu_j \triangleq \mathrm{j}^{th}$ coefficient of $\zeta(z)\mu(z)$.

$\sigma\omega_j \triangleq \mathrm{j}^{th}$ coefficient of $\sigma(z)\omega(z)$.

$\upsilon\chi_j \triangleq \mathrm{j}^{th}$ coefficient of $\upsilon(z)\chi(z)$.

For this model the highest coefficient in $\mathbf{D}_\Omega(z)$ was seven and that of $\mathbf{N}_\Omega(z)$ was eight. However the values of the coefficients for these terms were less than $(10)^{-18}$ and so they were truncated for a slight reduction in model order. Hence there are six $\mathbf{F}_i$ matrices and seven $\mathbf{H}_i$ matrices.

4.7.3 NMSS Formulation

When all of the matrices in (4.96) are defined, the non-augmented NMSS model can be constructed. Firstly, the state variable is defined to be a combination of the inputs and outputs in the form:

$$\mathbf{X}_m(k)^T = [\mathbf{Y}_m(k)^T, \ \dots \ , \mathbf{Y}_m(k-P+1)^T, \mathbf{U}_m(k-1)^T, \ \dots \ , \mathbf{U}_m(k-Q+1)^T] \tag{4.97}$$

for which, the non-augmented NMSS system is:

$$\begin{aligned} \mathbf{X}_m(k+1) &= \mathbf{A}_m\mathbf{X}_m(k) + \mathbf{B}_m\mathbf{U}_m(k) \\ \mathbf{Y}_m(k) &= \mathbf{C}_m\mathbf{X}_m(k) \end{aligned} \tag{4.98}$$

where:

$$\mathbf{A}_m = \begin{bmatrix} \mathbf{A}_1 & \mathbf{A}_2 \\ \mathbf{A}_3 & \mathbf{A}_4 \end{bmatrix}, \quad \mathbf{B}_m = \begin{bmatrix} \mathbf{B}_1 \\ \mathbf{B}_2 \end{bmatrix}, \quad \mathbf{C}_m = \begin{bmatrix} \mathbf{C}_1 & \mathbf{C}_2 \end{bmatrix} \tag{4.99}$$

$$\mathbf{A}_1 = \begin{bmatrix} -\mathbf{F}_1 & -\mathbf{F}_2 & \dots & -\mathbf{F}_{P-1} & -\mathbf{F}_P \\ \mathbf{I} & \mathbf{0} & \dots & \dots & \mathbf{0} \\ \mathbf{0} & \mathbf{I} & \ddots & \ddots & \vdots \\ \vdots & \ddots & \mathbf{I} & \ddots & \vdots \\ \mathbf{0} & \dots & \mathbf{0} & \mathbf{I} & \mathbf{0} \end{bmatrix}, \quad \mathbf{A}_2 = \begin{bmatrix} \mathbf{H}_2 & \mathbf{H}_3 & \dots & \mathbf{H}_{Q-1} & \mathbf{H}_Q \\ \mathbf{0} & \dots & \dots & \dots & \mathbf{0} \\ \vdots & \vdots & \vdots & \vdots & \vdots \\ \vdots & \vdots & \vdots & \vdots & \vdots \\ \mathbf{0} & \dots & \dots & \dots & \mathbf{0} \end{bmatrix} \tag{4.100}$$

$$\mathbf{A}_3 = \begin{bmatrix} \mathbf{0} & \dots & \dots & \dots & \mathbf{0} \\ \vdots & \vdots & \vdots & \vdots & \vdots \\ \vdots & \vdots & \vdots & \vdots & \vdots \\ \vdots & \vdots & \vdots & \vdots & \vdots \\ \mathbf{0} & \dots & \dots & \dots & \mathbf{0} \end{bmatrix}, \quad \mathbf{A}_4 = \begin{bmatrix} \mathbf{0} & \mathbf{0} & \dots & \dots & \mathbf{0} \\ \mathbf{I} & \mathbf{0} & \ddots & \ddots & \vdots \\ \mathbf{0} & \mathbf{I} & \ddots & \ddots & \vdots \\ \vdots & \ddots & \ddots & \ddots & \vdots \\ \mathbf{0} & \dots & \mathbf{0} & \mathbf{I} & \mathbf{0} \end{bmatrix} \tag{4.101}$$

$$\mathbf{B}_1 = [\mathbf{H}_1,\ \mathbf{0},\ \dots,\ \mathbf{0}]^T, \quad \mathbf{B}_2 = [\mathbf{I},\ \mathbf{0},\ \dots,\ \mathbf{0}]^T, \tag{4.102}$$

$$\mathbf{C}_1 = [\mathbf{I},\ \mathbf{0},\ \dots,\ \mathbf{0}], \quad \mathbf{C}_2 = [\mathbf{0},\ \dots,\ \mathbf{0}] \tag{4.103}$$

In the case of the plant model used in this research, the state variable of the discrete NMSS system is defined to be:

$$\mathbf{X}_\Omega(k)^T = [\mathbf{Y}_\Omega(k)^T, \dots, \mathbf{Y}_\Omega(k-5)^T, \mathbf{U}_\Omega(k-1)^T, \dots, \mathbf{U}_\Omega(k-6)^T] \tag{4.104}$$

where:

$$\mathbf{Y}_\Omega(k) = \begin{bmatrix} \Omega_{rev}(k) \\ T_g(k) \end{bmatrix}, \mathbf{U}_\Omega(k) = \begin{bmatrix} T_t(k) \\ \Omega_{rev_{SP}}(k) \end{bmatrix} \tag{4.105}$$

The non-augmented NMSS system is:

$$\begin{aligned} \mathbf{X}_\Omega(k+1) &= \mathbf{A}_\Omega \mathbf{X}_\Omega(k) + \mathbf{B}_\Omega \mathbf{U}_\Omega(k) \\ \mathbf{Y}_\Omega(k) &= \mathbf{C}_\Omega \mathbf{X}_\Omega(k) \end{aligned} \tag{4.106}$$

and the system matrices are constructed as:

$$\mathbf{A}_\Omega = \begin{bmatrix} -\mathbf{F}_1 & -\mathbf{F}_2 & -\mathbf{F}_3 & -\mathbf{F}_4 & -\mathbf{F}_5 & -\mathbf{F}_6 & \mathbf{H}_2 & \mathbf{H}_3 & \mathbf{H}_4 & \mathbf{H}_5 & \mathbf{H}_6 & \mathbf{H}_7 \\ \mathbf{I} & \mathbf{0} & \dots & \dots & \dots & \dots & \dots & \dots & \dots & \dots & \dots & \mathbf{0} \\ \mathbf{0} & \mathbf{I} & \ddots & \ddots & \ddots & \ddots & \ddots & \ddots & \ddots & \ddots & \ddots & \vdots \\ \vdots & \ddots & \mathbf{I} & \ddots & \ddots & \ddots & \ddots & \ddots & \ddots & \ddots & \ddots & \vdots \\ \vdots & \ddots & \ddots & \mathbf{I} & \ddots & \ddots & \ddots & \ddots & \ddots & \ddots & \ddots & \vdots \\ \vdots & \ddots & \ddots & \ddots & \mathbf{I} & \ddots & \ddots & \ddots & \ddots & \ddots & \ddots & \vdots \\ \vdots & \ddots & \ddots & \ddots & \ddots & \mathbf{0} & \ddots & \ddots & \ddots & \ddots & \ddots & \vdots \\ \vdots & \ddots & \ddots & \ddots & \ddots & \ddots & \mathbf{I} & \ddots & \ddots & \ddots & \ddots & \vdots \\ \vdots & \ddots & \ddots & \ddots & \ddots & \ddots & \ddots & \mathbf{I} & \ddots & \ddots & \ddots & \vdots \\ \vdots & \ddots & \ddots & \ddots & \ddots & \ddots & \ddots & \ddots & \mathbf{I} & \ddots & \ddots & \vdots \\ \vdots & \ddots & \ddots & \ddots & \ddots & \ddots & \ddots & \ddots & \ddots & \mathbf{I} & \ddots & \vdots \\ \mathbf{0} & \dots & \dots & \dots & \dots & \dots & \dots & \dots & \dots & \mathbf{0} & \mathbf{I} & \mathbf{0} \end{bmatrix} \tag{4.107}$$

$$\mathbf{B}_\Omega = \begin{bmatrix} \mathbf{H}_1 & \mathbf{0} & \dots & \dots & \dots & \mathbf{0} & \mathbf{I} & \mathbf{0} & \dots & \dots & \dots & \mathbf{0} \end{bmatrix}^T \tag{4.108}$$

$$\mathbf{C}_\Omega = \begin{bmatrix} \mathbf{I} & \mathbf{0} & \dots & \dots & \dots & \dots & \dots & \dots & \dots & \dots & \dots & \mathbf{0} \end{bmatrix} \tag{4.109}$$

As for traditional MPC, the augmented system is defined as:

$$\begin{aligned} \hat{\mathbf{X}}_\Omega(k+1) &= \hat{\mathbf{A}}_\Omega \hat{\mathbf{X}}_\Omega(k) + \hat{\mathbf{B}}_\Omega \boldsymbol{\Delta} \hat{\mathbf{U}}_\Omega(k) \\ \hat{\mathbf{Y}}_\Omega(k) &= \hat{\mathbf{C}}_\Omega \hat{\mathbf{X}}_\Omega(k) \end{aligned} \tag{4.110}$$

where:

$$\hat{\mathbf{A}}_\Omega = \begin{bmatrix} \mathbf{A}_\Omega & \mathbf{O}_\Omega^T \\ \mathbf{C}_\Omega \mathbf{A}_\Omega & \mathbf{I} \end{bmatrix}, \quad \hat{\mathbf{B}}_\Omega = \begin{bmatrix} \mathbf{B}_\Omega \\ \mathbf{C}_\Omega \mathbf{B}_\Omega \end{bmatrix}, \quad \hat{\mathbf{C}}_\Omega = \begin{bmatrix} \mathbf{O}_\Omega & \mathbf{I} \end{bmatrix}, \quad \mathbf{O}_\Omega = [\mathbf{0} \dots \mathbf{0}] \tag{4.111}$$

Note that, in this research, the definition of $\boldsymbol{\Delta}\hat{\mathbf{X}}_\Omega(k)$, used in the augmented system, is dependent on the choice of optimisation cost function used by the control algorithm. See Chapter 6 for specific details.

Chapter 5

WRAM Emulator

5.1 Concept

An emulation platform, shown in Figure 5.1, has been designed and built as part of this research for the purpose of testing real-time control algorithms for the WRAM, where the physical variable being emulated is the bidirectional air flow between the water column and the turbine. The air flow is produced using a linear hydraulic actuator that reciprocates a pivoting paddle within a sealed blast box. The emulator has been designed to be used within a real-time hybrid test loop, explained in Section 5.6, such that the control algorithm can be tested in response to the simulated dynamics of the WRAM's mechanical absorber. In addition to emulating the chamber's air flow, a realistic PTO consisting of a turbine-generator set and electrical drive converts the pneumatic energy into electromechanical energy. An embedded control system is installed to directly control the turbine's velocity, based on the commands of the advanced control algorithm.

5.2 Architecture

The block diagram in Figure 5.2 shows how the major components of the emulation platform link to the MTS hydraulic actuation and control system. Note that MTS is an abbreviation of MTS Systems Corporation who supply the hydraulic actuation system. The details are given in Section 5.6.2. The MTS system and the emulation platform are linked through a feedback loop, seen in Figure 5.2, where the main components include the MTS controller,

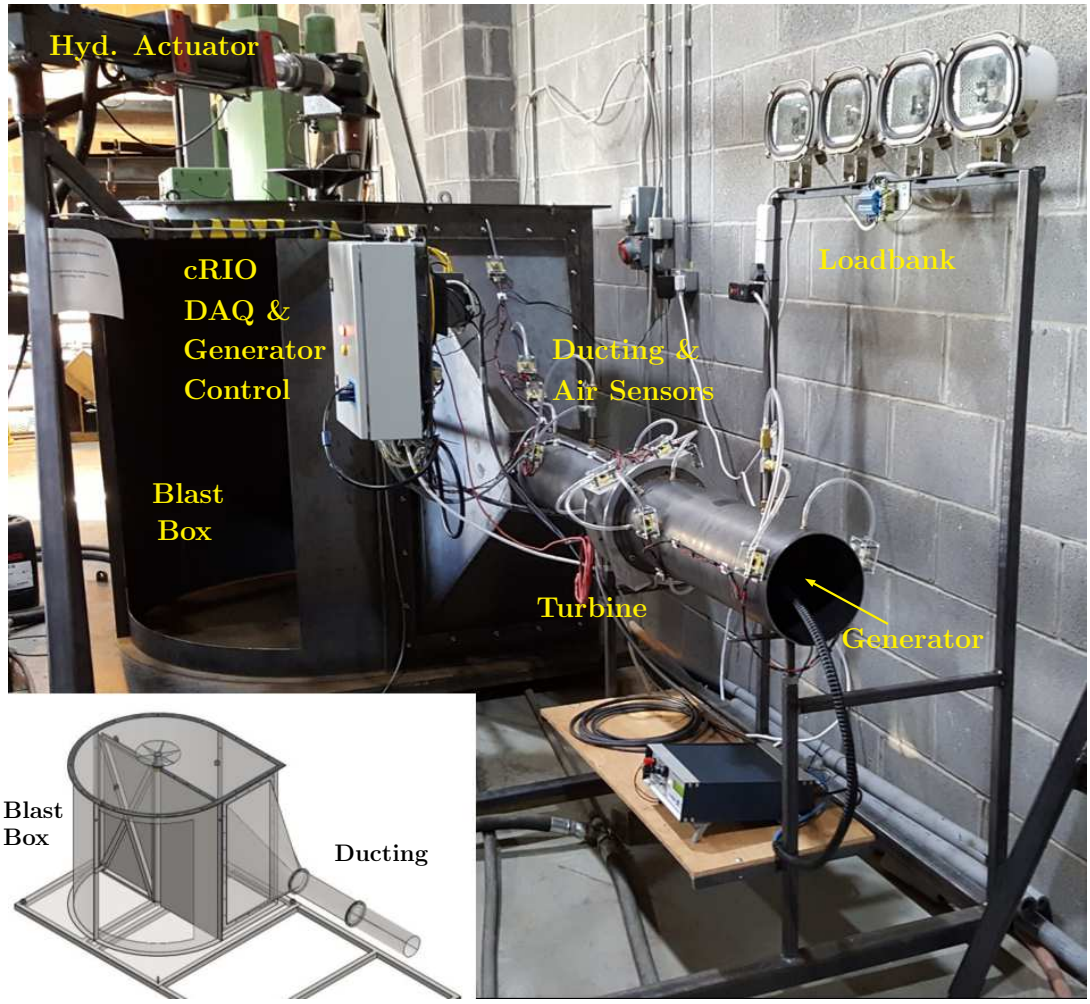

Figure 5.1: WRAM Emulation Platform.

hydraulic actuator, blast box, turbine, generator, generator drive and embedded control system, called the compact reconfigurable input-output (cRIO) controller. The PTO turbine is a small-scale replica of what has been previously used at sea on larger-scale WECs. The generator is also representative of what would be used at full-scale, as it provides four-quadrant motor-generation functionality that can be accurately controlled with setpoint tracking. The purpose of the loop is to facilitate real-time hybrid testing, discussed in Section 5.6.

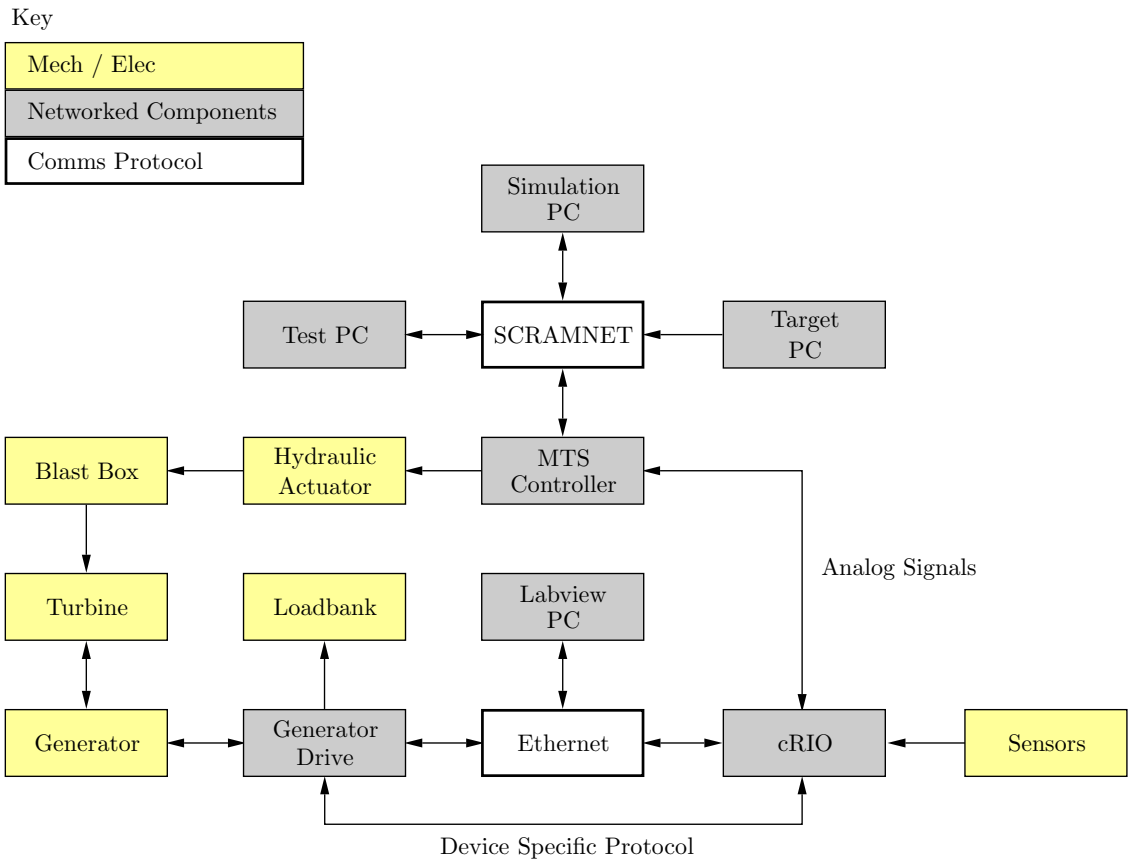

Figure 5.2: WRAM Emulator Platform Architecture.

5.3 Emulator Subsystems

5.3.1 Emulated OWC Air Flow

A blast box has been designed to force bidirectional air flow through a self-rectifying axial impulse turbine. The motivation of adopting this approach, rather than simply creating a unidirectional wind tunnel, was to produce air flow that closely mimics the behaviour of a real WEC. Implementing bidirectional flow facilitates the identification of unforeseen issues relating to process measurement and control performance. These lessons are missed in other approaches that use steady state or unidirectional air flow, especially in cases where the OWC is emulated with electrical machinery, such as in [66].

5.3.2 Paddle Actuation

The RT hybrid loop interface between the virtual and real worlds has been defined to be the volumetric flow resulting from the WRAM's relative velocity, $\dot{z}_9 - \dot{z}_3$. Inspiration has been drawn from researchers at Cranfield University who constructed a similar test rig called the 'Pneumatic Wave Generator' [67], where bidirectional air flow was generated by rotating a paddle within an enclosed chamber (or blast box). This concept has been adopted in the design of the WRAM emulation platform, however with a different actuation mechanism. The general arrangement can be seen in Figure 5.3.

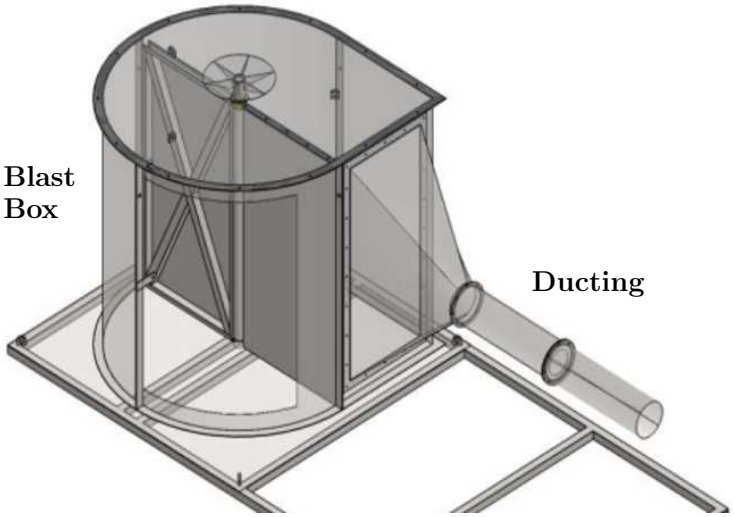

Figure 5.3: 3D Solid Model of Blast Box, showing Internal Paddle.

To utilise the WRAM emulation platform in the most efficient manner a cam system was designed to rotate the paddle using the existing hydraulic linear actuator on hand. Figure 5.4 provides a schematic top view of the concept. Rotation limits ensure the actuator can only follow a single arc path and avoid full rotation that would damage the rig.

The output from the WRAM model requires a conversion from relative body displacement to paddle rotation, derived as follows. The virtual-to-real world interface is defined as the volumetric flow swept by the paddle, and is equal to the volumetric flow from the numerical model. Therefore:

$$Q_{pad} = Q_{rel} = A_{wc}(\dot{z}_9 - \dot{z}_3) \tag{5.1}$$

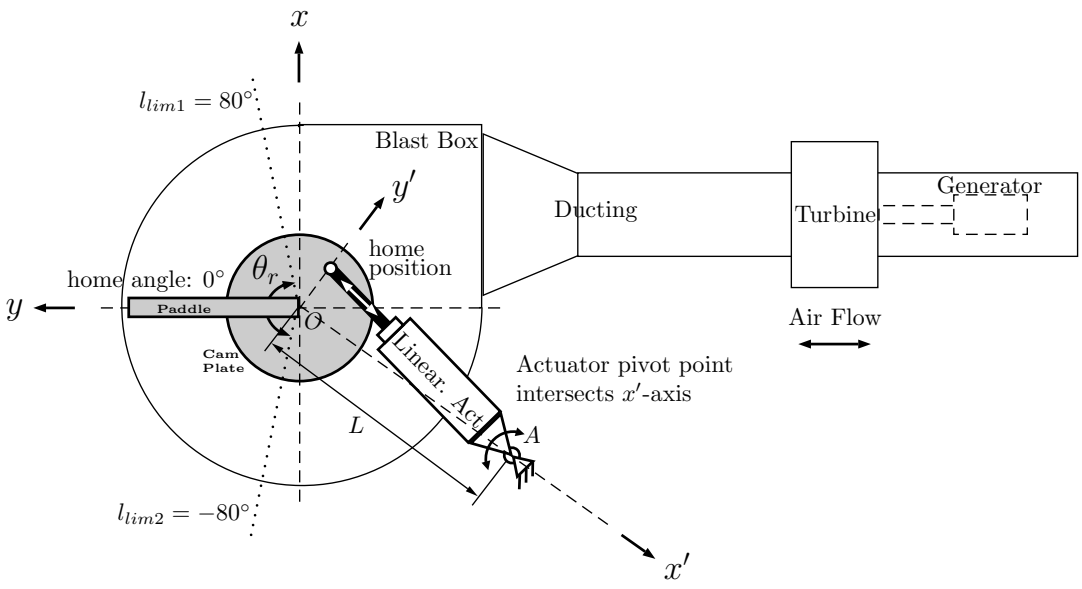

Figure 5.4: Paddle Actuation Arrangement using a Cam for Linear to Rotary Motion.

where:

Q_{pad} : Volumetric flow swept by paddle ($m^3\,s^{-1}$)

Q_{rel} : Volumetric flow from WRAM model ($m^3\,s^{-1}$)

The sign convention corresponds to positive flow out of the chamber. Considering the volume of a cylindrical sector swept by the paddle, V_{pad}, the angle of rotation, θ_r, in radians can be calculated from:

$$\theta_r = \frac{2V_{pad}}{r^2 H_p} = \frac{2}{r^2 H_p} \int Q_{pad} dt \tag{5.2}$$

where:

r : Paddle radial width (m)

H_p : Paddle height (m)

Substituting (5.1) into (5.2) leads to:

$$\theta_r = \frac{2A_{wc}}{r^2 H_p}(z_9 - z_3) \tag{5.3}$$

The relationship between the linear displacement of the hydraulic actuator and the paddle angle was found through characterisation tests conducted on the emulation platform. Details are provided in Section 5.4.2.

5.3.3 PTO Assembly

Figure 5.5 shows the bidirectional axial impulse turbine directly coupled to a permanent magnet servo-generator, designed to operate in both motoring and generating modes. Note, 'bidirectional' refers to the air flow, not the turbine's rotation which is unidirectional. An electrical servo-drive interfaces the generator with the control system, from which the velocity command is issued. As can be seen in Figure 5.5, the turbine-generator coupling assembly has an abrupt profile with regards to the air flow. To ensure smooth flow over the assembly, each side of the turbine has been fitted with 3D printed nacelles, seen in Figure 5.6.

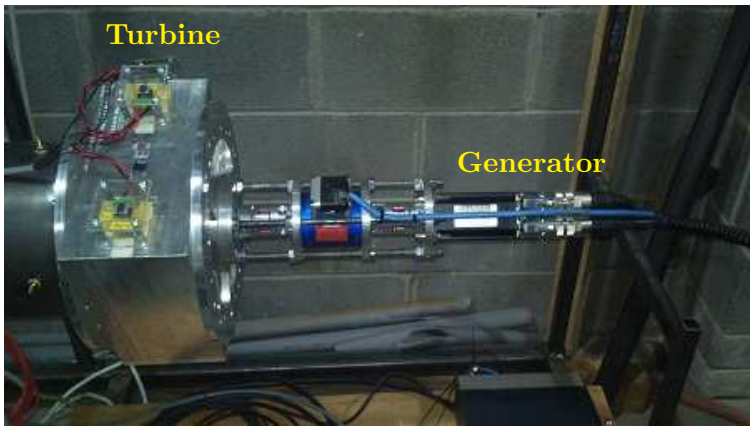

Figure 5.5: PTO Assembly showing the Generator-Turbine Coupling.

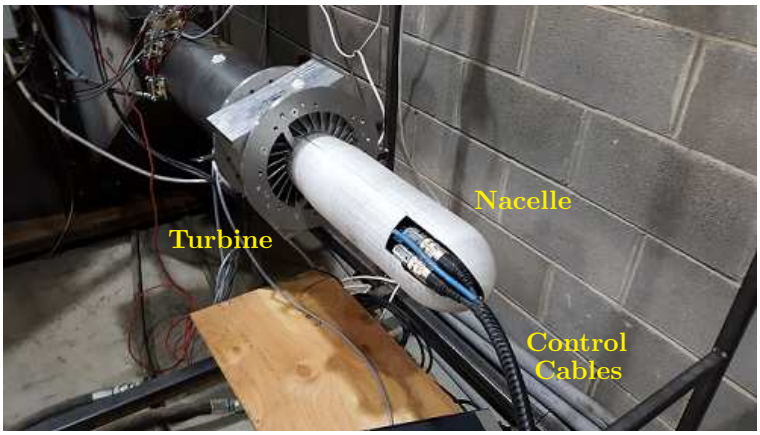

Figure 5.6: PTO Assembly covered by Nacelle to assist Streamlined Air Flow.

5.3.4 Instrumentation

The emulation platform has a variety of instrumentation for measuring process variables, controlling actuators and logging data. Figure 5.7 shows how the cRIO acts as the central hub for this instrumentation network.

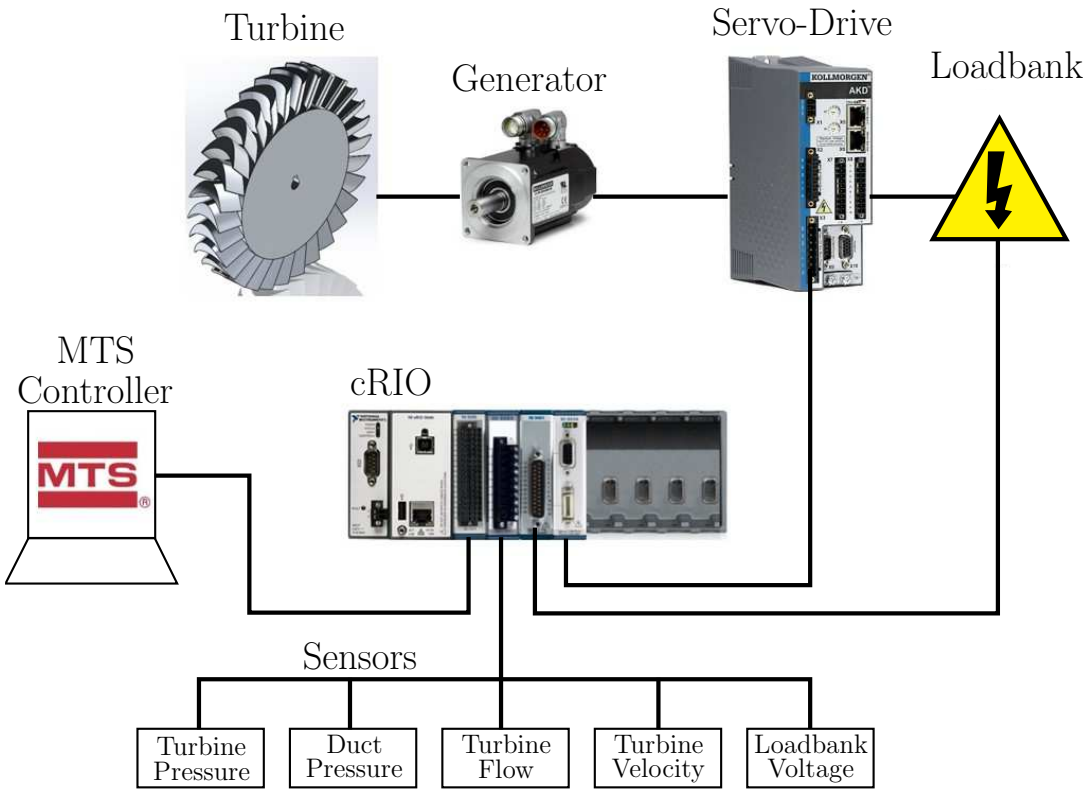

Figure 5.7: Instrumentation Network for the Emulation Platform.

The cRIO operates in parallel to the MTS system, communicating with it through analog IO. Various sensors are installed on the test rig for measuring air pressures and flows, generator velocity, torque, actuator feedback and other condition monitoring data. Figure 5.9 shows the location of some of the pneumatic sensors. All sensors feed into the cRIO's analog input module, and the turbine pressure signal is forwarded to the MTS system from the analog output module.

The measured turbine velocity is sent to the cRIO from the servo-drive which is calculated based on information obtained from a shaft encoder built into the generator. The generator torque is inferred from an internal control variable within the servo-drive. Both

signals are fed back to the cRIO through a multi-core cable that also contains the setpoint command and control handshaking signals.

All of the sensors are logged by a data acquisition (DAQ) loop on the cRIO, running in parallel to the control loop. The most important of these are the four differential pressure sensors, mounted across the turbine. These signals are averaged with each other before a single value feeds into the RT hybrid loop and control code, with minimal measurement error. Also, the RT hybrid loop is designed to use the pressure signal to calculate the PTO force, which is then fed into the WRAM equations of motion.

The loadbank is controlled by the cRIO through its digital output module in response to a hysteresis loop that monitors the servo-drive's DC bus voltage. Figure 5.8 shows the internal components of the instrumentation panel including the cRIO, signal conditioning circuitry and electrical power circuitry.

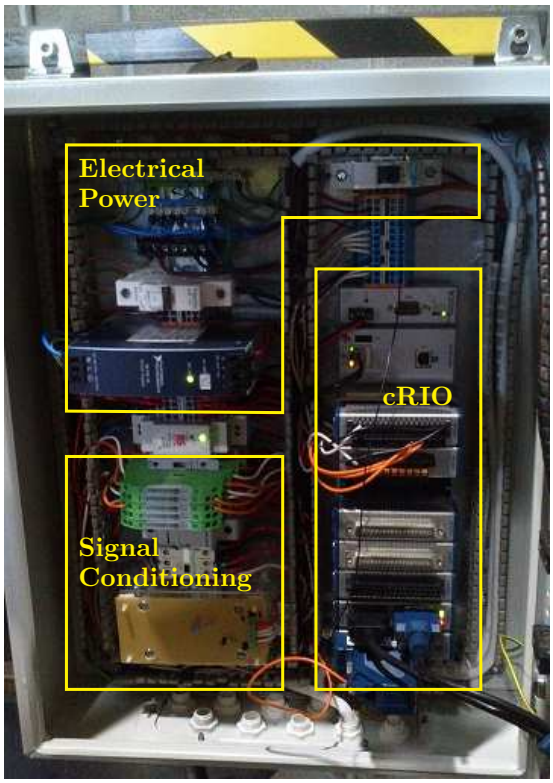

Figure 5.8: Control and Instrumentation Panel.

5.3.5 Communication

Referring to Figure 5.16, there are three main types of communication protocols within the emulation platform. During real-time execution the MTS Controller, Target PC and Test PC exchange data between the numerical model and real world. This data is shared over SCRAMNET (Shared Common Random Access Memory Network), a high-speed fibre-optic link designed to minimise signal latency. Ethernet is also used for communication between the Instrumentation PC, cRIO and servo-drive. Additionally, analog signals are used to interface the MTS Controller and cRIO.

5.3.6 Data Logging and Synchronisation

Data is logged, unsynchronised, on three separate computing nodes (cRIO, Simulation PC and Test PC). In order to synchronise the data for post-processing, one channel on each data logger is dedicated for receiving a 'synchronisation' signal with the same random content. The delay between each logger can then be detected and eliminated by calculating the cross-correlation of the signals. Even though each logger samples at different rates and starts logging at different times, the technique works very well. The results of the approach are shown in Section 5.4.4. This technique also ensures that normal process dynamics in the system, e.g. control response times, are preserved in the data.

5.3.7 Power Dissipation

The PTO's servo-drive has limited ability to internally dissipate regeneratively absorbed energy. To prevent the drive from shutting down and losing control of the turbine, the internal DC voltage bus is monitored by the cRIO to detect if the voltage approaches its maximum shutdown limit. Through the use of a hysteresis comparator the cRIO switches an external loadbank based on DC bus voltage fluctuations.

5.4 Calibration

The following section describes the calibration process of various systems on the WRAM emulation platform.

5.4.1 Pneumatic Sensors

Honeywell SSC Series differential pressure sensors are used to measure pressures and flows in the ducting and across the turbine, shown in Figure 5.9. The five ducting pressures are measured with respect to the atmosphere immediately outside the ducting. Four differential pressure measurements are taken across the turbine and then averaged by the control system for minimised measurement error.

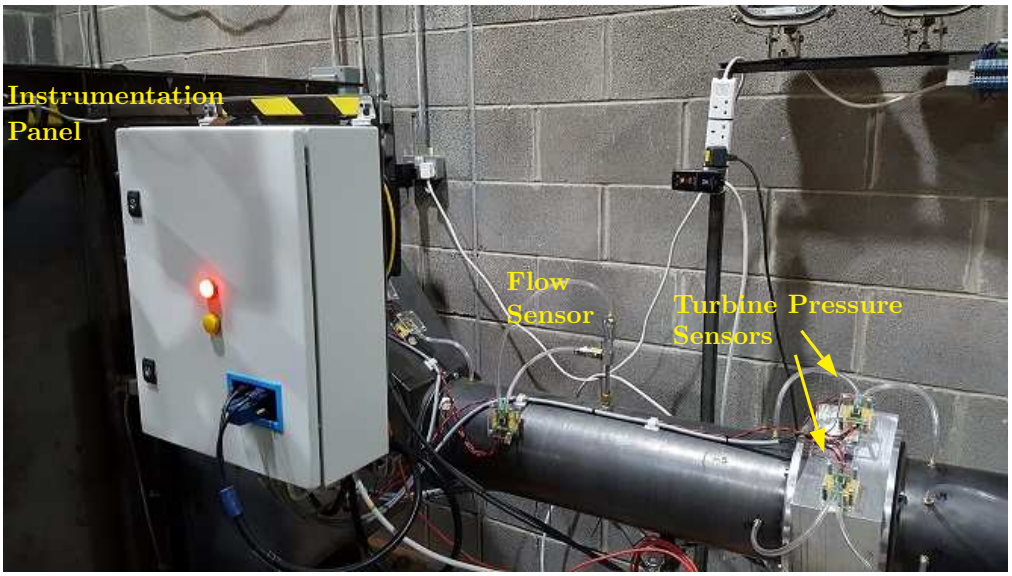

Figure 5.9: Sensors Installed on the Emulation Platform.

The sensors come fully calibrated and temperature compensated for offset, sensitivity, temperature effects and nonlinearity. The datasheet accuracy is quoted as ± 2 % total error band of full-scale span (FSS). The input range is ± 497.68 Pa with an output range of 0-5 Vdc. The sensor output voltage is scaled as per the datasheet without the need for further calibration, due to the factory pre-calibration and compensation. The measured pressure is then calculated as:

$$p_{out} = p_{min} + \frac{(V_{out} - 0.1V_s)(p_{max} - p_{min})}{0.8V_s} \tag{5.4}$$

where:

V_{out} :	Measured voltage	(V)
p_{out} :	Converted pressure	(Pa)
$V_s = 5$:	Supply voltage	(V)
$p_{min} = -497.68$	Lower range limit	(Pa)
$p_{max} = 497.68$	Upper range limit	(Pa)

For the flow measurements, Series DS-300 averaging Pitot tubes from Dwyer Instruments [68] measure the volumetric flow in the ducting upstream and downstream of the turbine. The total (high) pressure port and static (low) pressure port connect to the differential ports of the pressure sensor. The datasheet provides the equation for calculating volumetric flow in standard cubic feet per minute (SCFM) for any gas as:

$$Q_{scfm} = 128.8 K d_i^2 \sqrt{\frac{dP(P+B)}{S_s(T+460)}} \tag{5.5}$$

where:

Q_{scfm} :	Volumetric flow at Pitot tube	(SCFM)
K :	Pitot tube coefficient	(dimensionless)
d_i :	Internal duct diameter	(inches)
dP :	Differential pressure	(inches H_2O)
P :	Static line pressure	(psig)
B :	Barometric pressure	(psi)
S_s :	Specific gravity at 60 ^{o}F	(dimensionless)
T :	Temperature	(^{o}F)

SCFM refers to the worldwide standardised conditions of temperature and pressure. Converting Q_{scfm} to $\mathrm{m}^3.\mathrm{s}^{-1}$, assuming standard conditions for air, maintaining the sign of the oscillating pressure, scaling from p_{out} units to dP units and substituting the following datasheet values into (5.5) leads to:

$$Q_{pt} = 9.7297(10^{-3})\mathrm{sign}(p_{out})\sqrt{\mathrm{abs}(p_{out})} \tag{5.6}$$

where:

Q_{pt} : Volumetric flow at Pitot tube ($m^3\,s^{-1}$)

$K = 0.67$

$d_i = 7.87$ inches

$P = 0$

$B = 14.7$ psi

$S_s = 7.636$

$T = 60\ ^oF$

5.4.2 Paddle Rotation to Actuator Stroke

The characteristic that relates the paddle rotational angle and actuator stroke has been obtained experimentally, carried out through measurements of the paddle rotation in response to 1 mm stroke increments. To capture the effect of backlash the process was conducted in both clockwise (CW) and counter clockwise (CCW) directions. A look up table (LUT) was then created for determining the stroke from the specified angle in real-time simulations. Figure 5.10 shows the resulting characteristic.

To avoid the difficulty of automatically deciding which characterisation curve to use in real-time depending on the direction, while also avoiding abrupt switching, it was decided to use the average of the two curves. The paddle rotation limits have been chosen at the points where the CW and CCW curves begin to diverge significantly from the average, while still achieving sufficient rotation. The irregularity in the curves at approximately -45^o of rotation is caused by a tight spot in the chamber wall due to welding deformation, which the average curve smooths out well. The rotation limits imposed on the paddle are -60 deg and $+50$ deg.

5.4.3 Servo-Generator Tuning

The generator is controlled with a velocity control loop, partly implemented in the servo-drive and partly in the Labview code on the cRIO. The Labview configuration interface for the PID loop allows control for either the velocity or displacement, however for both control strategies, the PID gains are associated the displacement loop. This makes tuning

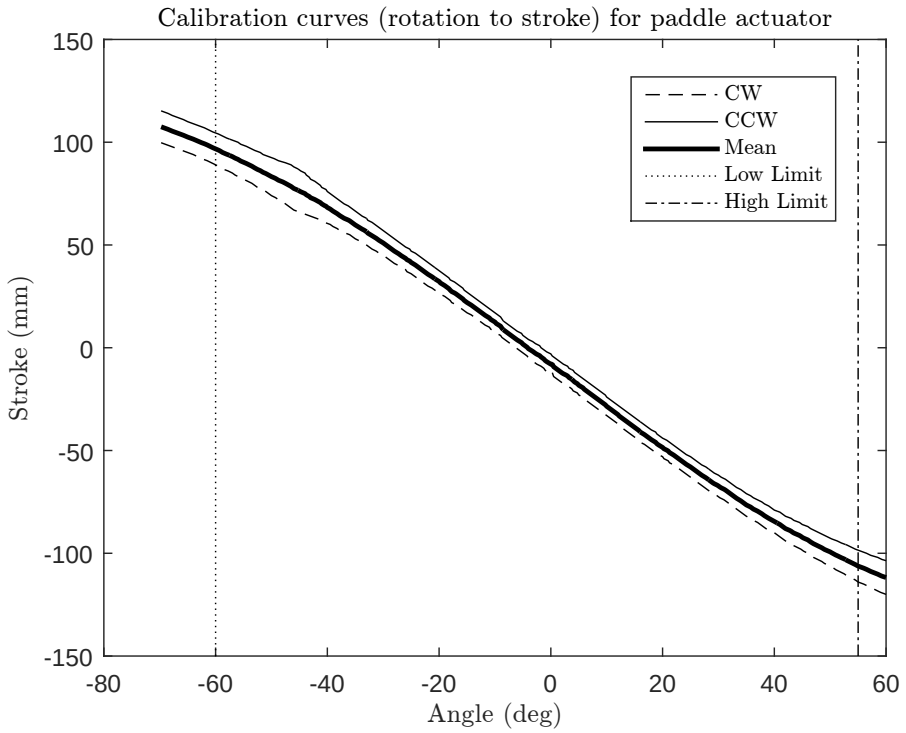

Figure 5.10: Paddle Calibration Curves with Limits Imposed.

the velocity loop very unintuitive when attempting to tune for critical damping and zero steady state error of the velocity. This tuning problem can be simplified by considering the generic PID control law, represented by the block diagram in Figure 5.11, being applied to two separate scenarios of controlling either a displacement or velocity loop.

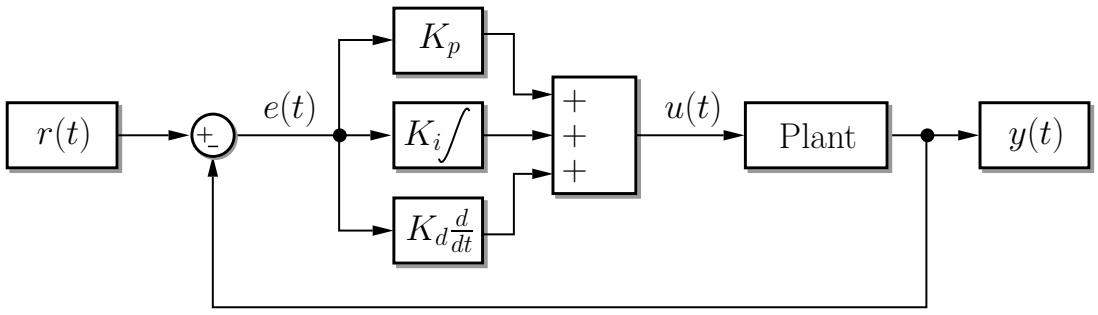

Figure 5.11: Generic PID Control Loop.

For the displacement loop, the control command, $u_\Delta(t)$ is

$$u_\Delta(t) = k_{p_\Delta} e_\Delta(t) + k_{i_\Delta} \int e_\Delta(t)dt + k_{d_\Delta} \frac{d}{dt} e_\Delta(t) \tag{5.7}$$

For the velocity loop, the control command, $u_v(t)$ is

$$u_v(t) = k_{p_v} e_v(t) + k_{i_v} \int e_v(t)dt + k_{d_v} \frac{d}{dt} e_v(t) \tag{5.8}$$

where:

$u_\Delta(t)$: Control output variable for displacement loop.

$e_\Delta(t)$: Error between displacement setpoint and output.

k_{p_Δ} : P-gain for displacement loop.

k_{i_Δ} : I-gain for displacement loop.

k_{d_Δ} : D-gain for displacement loop.

$u_v(t)$: Control output variable for velocity loop.

$e_v(t)$: Error between velocity setpoint and output.

k_{p_v} : P-gain for velocity loop.

k_{i_v} : I-gain for velocity loop.

k_{d_v} : D-gain for velocity loop.

It can been seen from equations (5.7) and (5.8) that $k_{p_v} \equiv k_{d_\Delta}$ and $k_{i_v} \equiv k_{p_\Delta}$, given that velocity is the first derivative of displacement. Therefore, when tuning the PID gains in Labview, the D- and P-gains for the displacement loop can be treated as P- and I-gains, respectively, for the velocity loop. Experimental tuning tests were conducted on that basis for the fully coupled PTO (generator and turbine). The final tuned gains were:

$$k_{d_\Delta} = 8000 \tag{5.9}$$

$$k_{p_\Delta} = 0.1 \tag{5.10}$$

$$k_{i_\Delta} = 0 \tag{5.11}$$

5.4.4 Data Synchronisation

The approach outlined in Section 5.3.6 using the random synchronisation signal has been tested with a measured pressure signal, logged on all of the individual data loggers. Figure 5.12 shows the cross-correlation between the signals from the Instrumentation PC and Test PC (using STS software). The peak, corresponding to the time offset between the signals, is shown to be 22.96 s. The same procedure was followed for the measured data between the Instrumentation PC and the Simulation PC. The offsets were then removed from the signals with the results shown in Figure 5.13.

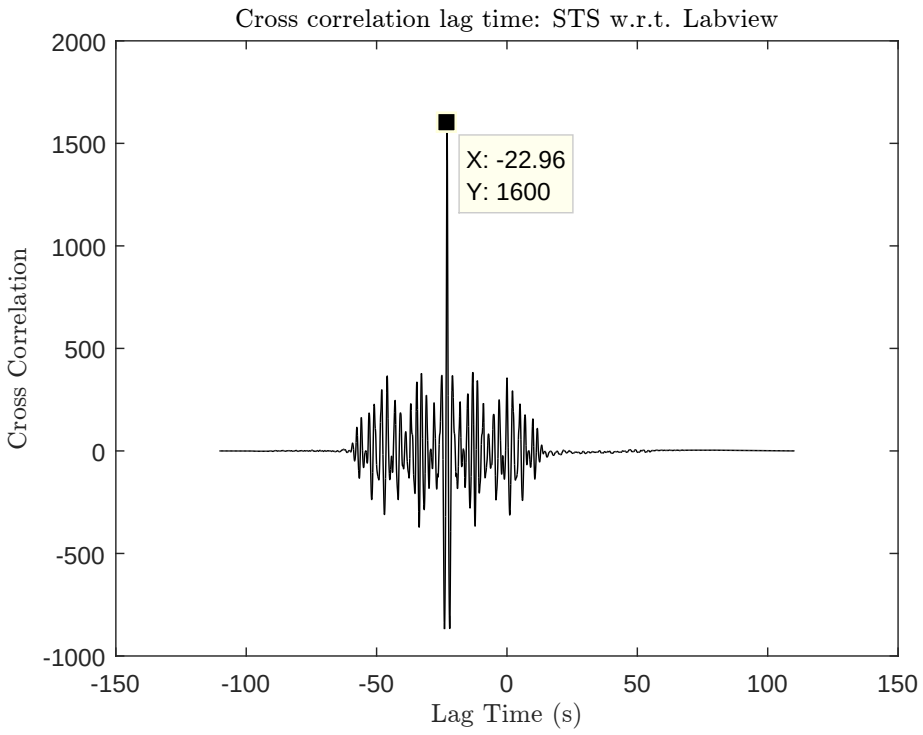

Figure 5.12: Cross Correlation Lag Time: STS w.r.t. Labview.

5.4.5 Open Loop Turbine Tests

Open-loop experiments were conducted where the blast box was used to drive irregular oscillating air flow through the turbine. The first intention was to qualitatively confirm a good

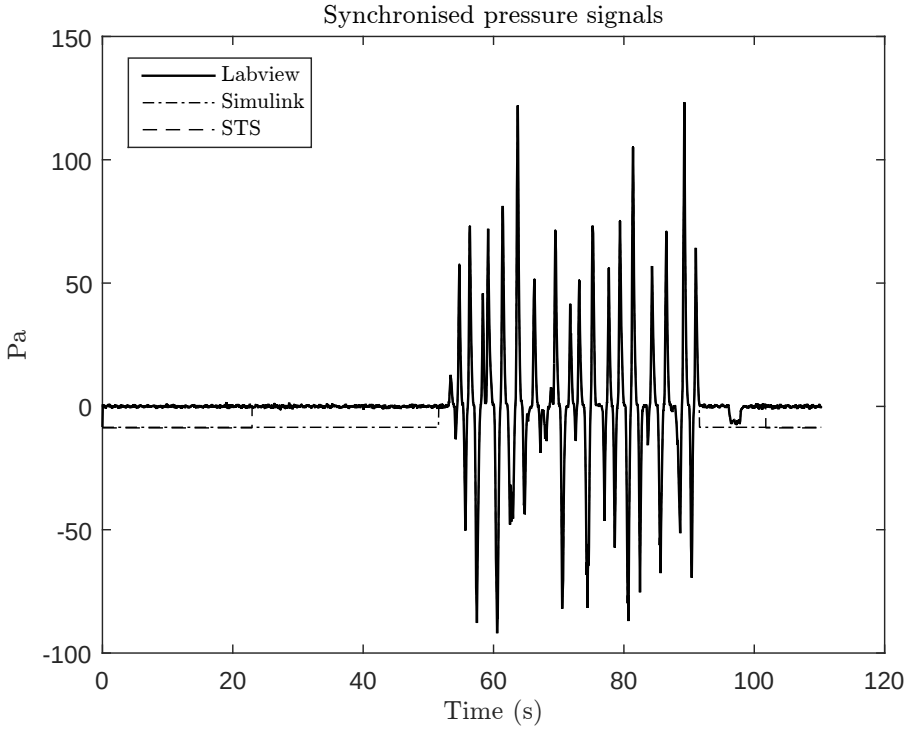

Figure 5.13: Synchronised Pressure Signals using Cross Correlation to Identify the Time Offset.

response of the turbine to the air flow, and confirm that the turbine was sized appropriately. Figure 5.14 shows the resulting turbine velocity in response to an uncontrolled generator. In this test, the generator was allowed to freewheel in order to witness the turbine's response to the irregular flow conditions. The turbine's self-rectification functionality can be seen clearly, since rotation is unidirectional. Also, the velocity slightly exceeds the maximum rating of 16.7 RPM, demonstrating a suitable match of the turbine to the air flow conditions. The irregular nature of the air flow is a well-known challenge for wave-by-wave control strategies. It is worth noting that the turbine inertia prevents the velocity from returning to zero, demonstrating a small amount of mechanical energy storage. While outside the scope of this research, the potential benefits of short-term storage are worth considering in the context of improving the power quality for grid connected WECs [69].

The second aim of these tests was to confirm that the generator was powerful enough to overcome the turbine torque generated by the air flow, important from a controllability point of view. To this end, a relatively low setpoint velocity of 4 rev.s^{-1} was given to the

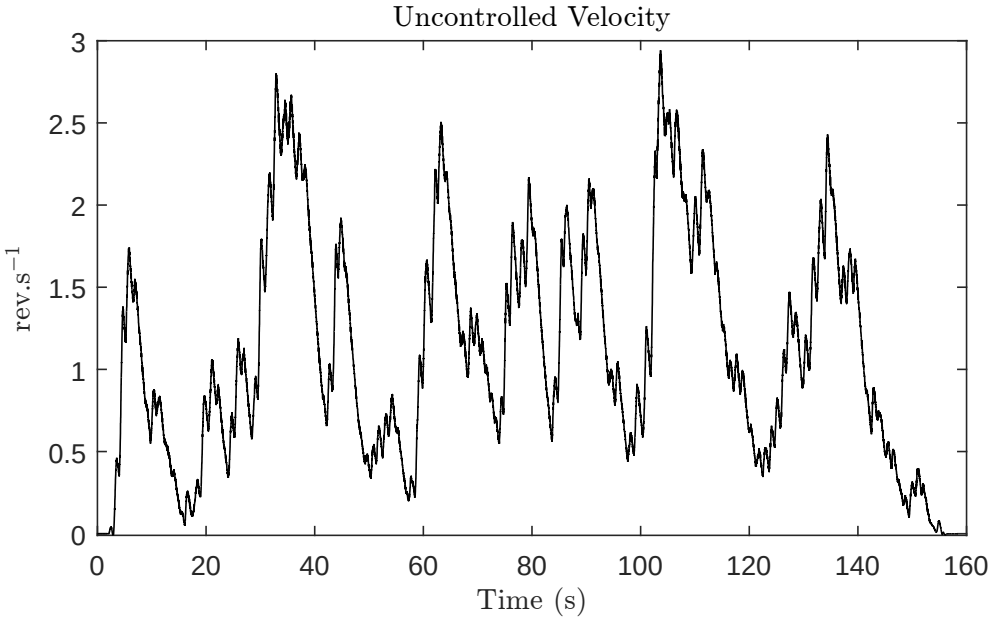

Figure 5.14: Uncontrolled Turbine Velocity due to Air Flow from the Blast Box.

cRIO's control loop while actuating the same air flow conditions of the previous test. Figure 5.15 shows the results, where the generator easily holds the constant setpoint velocity. Also, the irregular profile of the air flow is transferred to the torque.

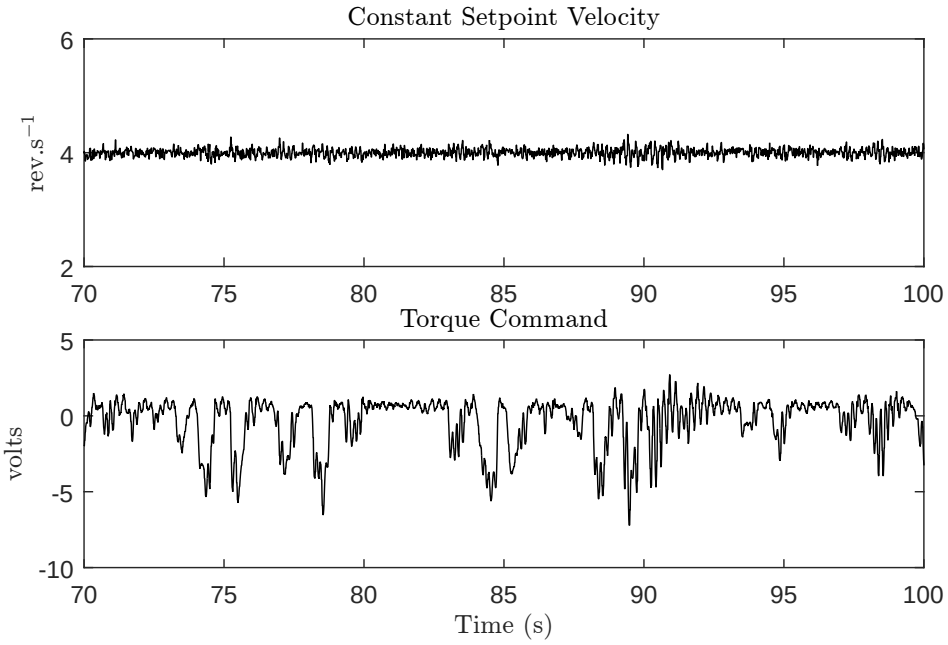

Figure 5.15: Controlled Turbine Velocity in the Presence of Air Flow.

5.5 RT Hybrid Testing Background

5.5.1 Concept

Hybrid testing is a technique used in civil and structural engineering, also known as Hardware -in-the-Loop (HIL) simulation in other engineering fields, that has been developing since the 1960's and 70's [70]. The term 'hybrid' refers to a feedback loop that is established between a physical system and numerical (or virtual) model [70]. The hybrid approach provides a cost-effective alternative for evaluating structures both analytically and experimentally [71]. Numerical models are often preferred where the underlying behaviour is well known or sufficiently represented by linear approximations [72]. It may also be the case that physical implementations are too dangerous or costly, for example with sea operations or other extreme and hostile environments [73]. Using physical components is highly advantageous where possible since most of the underlying assumptions are removed. Naturally, this leads to a more realistic test scenario, providing a higher degree of confidence in the proposed technology.

5.5.2 Historical Development

Development of hybrid testing began in Japan, and soon followed in the USA. First efforts in Japan [74], cited in [71], consisted of a single DoF system being subjected to seismic loading where an analog computer was used to solve the equations of motion. Subsequent efforts [75]–[77] then focussed on pseudo-dynamic investigations using digital computers. Some recent advances in hybrid testing, cited in [71] include distributed hybrid testing [78] and peer-to-peer (P2P) hybrid testing over the Internet [79]. Distributed hybrid testing allows different physical subsystems within the overall application to be located in different facilities. A P2P hybrid system additionally allows for parallel computations for different subsystems.

5.5.3 Applications

Hybrid (or HIL) testing has been widely used across several engineering fields. The following examples span across structural engineering, aerospace engineering, automotive engineering, control engineering, wind energy and wave energy. See [73], [80]–[83] for further details. In the wave energy sector HIL has been used in [84] to demonstrate the effectiveness of the testing approach in evaluating PTO systems for a two-body heaving WEC. And very recently HIL was used in [51] to characterise the dynamic behaviour of a PTO, suitable for a spar-buoy WEC, and validate the proposed control algorithms operating within safe limits.

5.6 RT Hybrid Test Rig

Trinity College Dublin (TCD) has a well-established RTHT system that can be adapted to many applications. Examples of previous work can be seen in [81], [82], [85], [86]. The existing rig can accurately provide fast linear actuation with feedback for force and displacement measurements.

5.6.1 Test Rig Architecture

The RTHT rig can be split into two main sections: the MTS control system; and the project specific WRAM emulation platform. Note, MTS is the supplier [87] of the hydraulic equipment and real-time computing nodes used to control and drive the linear actuator. A dedicated control room houses the RT hybrid computing nodes and also acts a safe operating station for the test rig operators. Figure 5.16 provides a high level network diagram of how the MTS computing nodes connect to the test platform nodes.

5.6.2 MTS Control System

The MTS subset of nodes can be considered to include the Simulation PC, Target PC, MTS Controller and Test PC. The Simulation PC serves as the development environment for the Simulink® numerical model and provides a user-friendly interface for cross-compilation of the real-time code. Following real-time simulation, the logged data is then captured for post processing analysis. Note, this is only possible if *host scopes* are included in the Simulink®

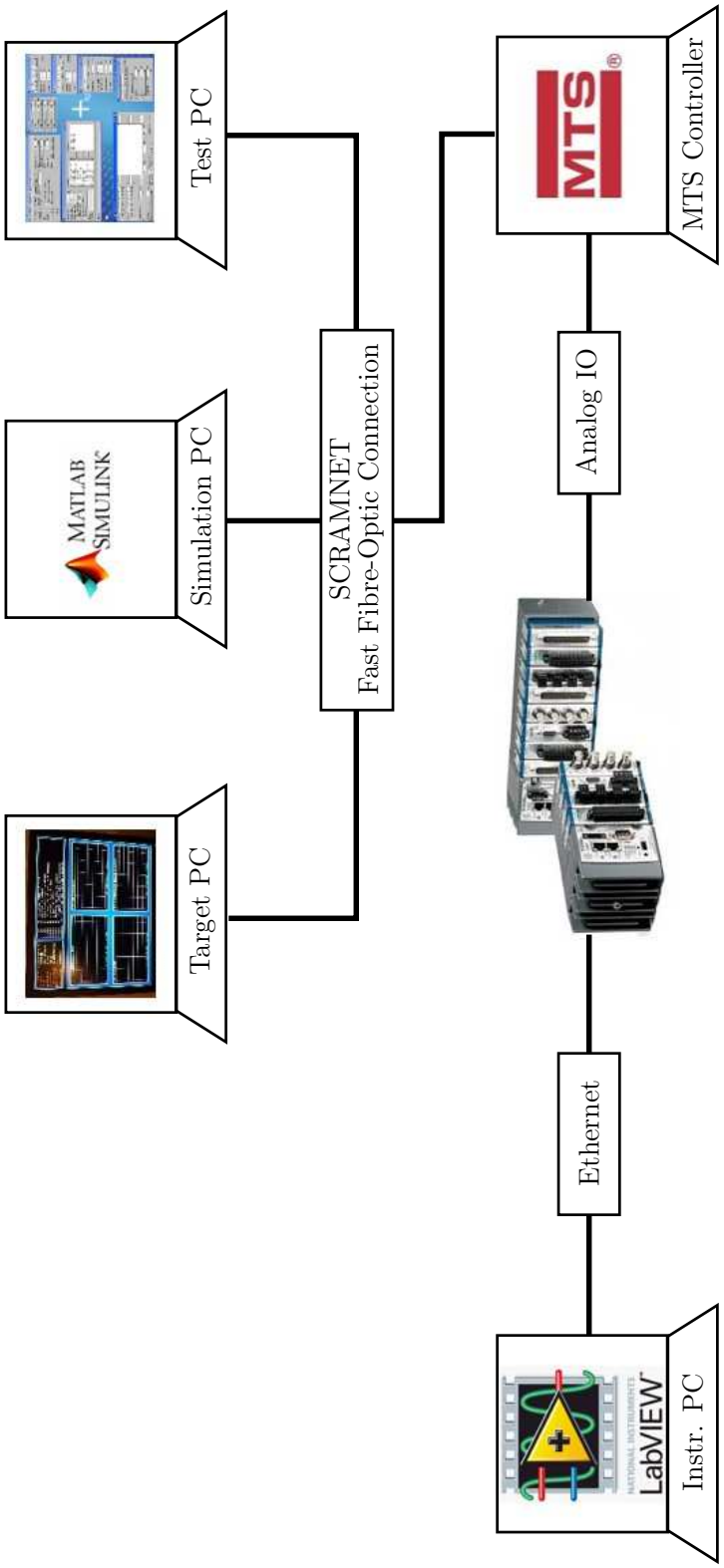

Figure 5.16: Computing Nodes on the RTHT Network.

model. The Target PC executes the real-time code that interacts with the SCRAMNET bus to exchange input and output signals. No user interaction is possible with the Target PC other than monitoring user-defined *target scopes* and execution parameters. One useful parameter provides an indication of whether the real-time code is executing within the prescribed sample rate of 1024 Hz.

The MTS Controller is the interface between SCRAMNET data and the linear actuator. Within its emergency override framework, it takes the SCRAMNET commands, converts them to analog signals and then feeds the signal to the linear actuator. In parallel, the MTS Controller reads the displacement and force measurements from the linear actuator and places them onto the SCRAMNET bus for the Target PC to read. The MTS controller also has a few spare analog inputs that can read a limited number of signals from the project specific platform.

The Test PC is used for configuring and controlling the linear actuator, and can be used in two ways. Following configuration and calibration, the first step one should take is to use the manual operation features, with the emergency safety limits set to low levels, ensuring appropriate interaction between the linear actuator and test platform. Later, during automatic real-time testing, the Test PC provides the user interface for enabling the linear actuator, and starting the data logging if desired. Once started, the MTS Controller is then enabled to use the Target PC commands for the linear actuator. An automatic supervisory routine continuously compares the measured feedback signals from the linear actuator within the configured limits. If exceeded, the MTS Controller stops the simulation and isolates the actuator, after which an emergency reset is required from the operator before the system can reset. Figure 5.17 shows an example screenshot of the Test PC user interface.

The Series 244 linear MTS actuator is a heavy duty, high powered hydraulic unit capable of fast dynamic performance through the use of servo-valve technology. It is typically used for loading and deflecting large structural specimens, and has force and stroke ratings of $\pm$ 150 kN and $\pm$ 125 mm respectively. The linear actuator is powered by a hydraulic power pack, designed for high duty cycle operation.

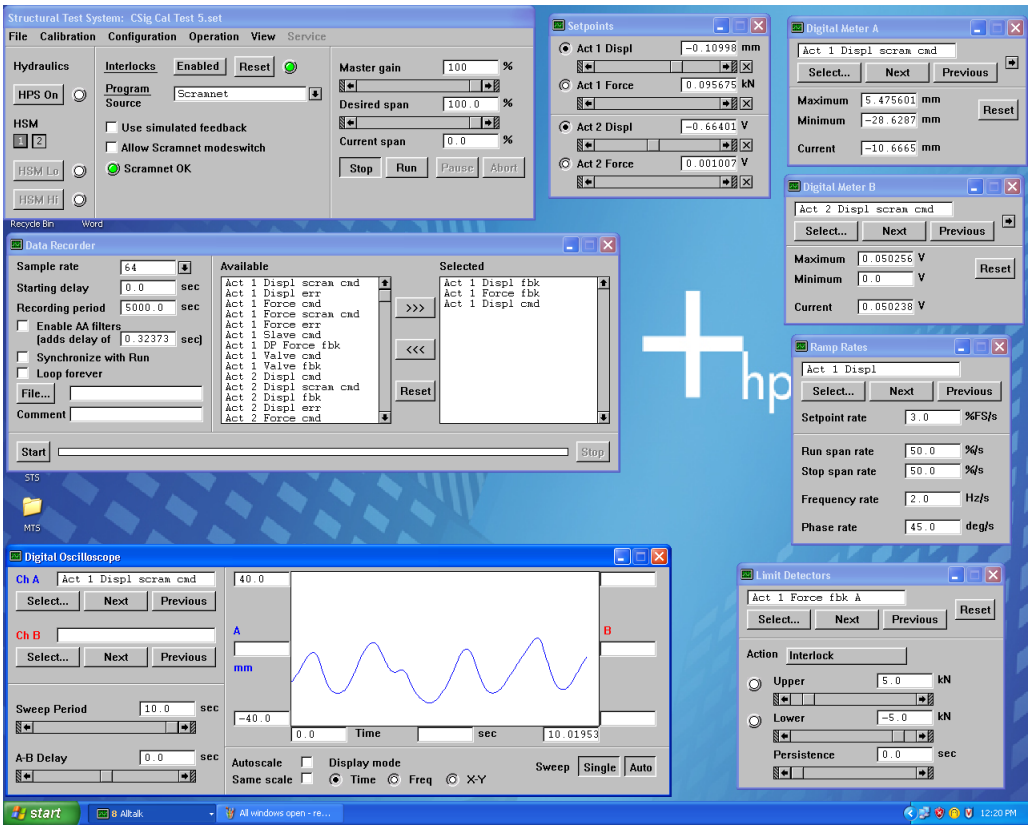

Figure 5.17: Test PC User Interface.

5.6.3 RT Hybrid Loop

Figure 5.18 shows the overall block diagram for the RT hybrid loop. The first thing to note is the distinction between virtual and and real parts. The virtual parts play the role of simulating the WEC's numerical model and emulating its output using the linear actuator. The real parts relate to the control algorithm and PTO (turbine and servo-generator). The emulated chamber air flow is directed through the PTO, fitted with pneumatic sensors. Data from these feed back into the equations of motion, thereby closing the RT hybrid loop. The control algorithm on the cRIO is designed to run in parallel to the WEC model and controls the generator in response to the turbine torque, induced by the air flow. There is an electrical servo-drive that interfaces the cRIO to the generator providing PID control for either velocity, torque or displacement, where the PID gains are configured through the cRIO. Any excess power generated in the servo-drive is dissipated in the loadbank using a hysteresis switching loop.

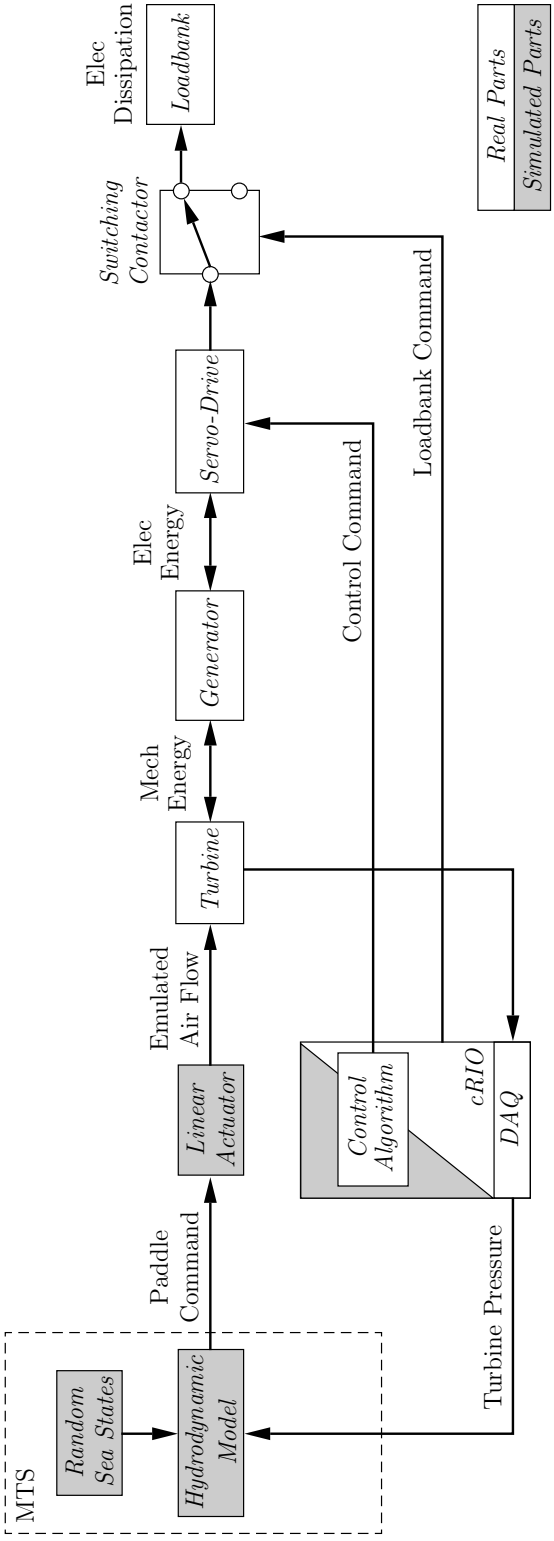

Figure 5.18: Real-Time Hybrid Loop Diagram.

Chapter 6

Control Implementation

6.1 Distinction between WRAM Absorber and PTO Control

Following an extensive literature review of WEC control strategies, the development approach for WRAM is now proposed with the fundamental aim being that the selected algorithms be fully implementable for assessment on a sea-going WRAM in the immediate future. In particular, focus has been placed on the benefits and pitfalls of prior strategies in the context of WRAM.

Also, during this research it has been noted that not all control approaches are suitable for devices with an OWC, which arises from the lack of a hard mechanical link between the wave energy absorber the PTO turbine. In direct contrast to devices that are mechanically linked, the lack of a hard mechanical link suggests that the WEC and PTO control problems can be dealt with relatively independently.

6.1.1 WRAM Absorber Control

Considering the WEC absorber control problem, several salient points emerge from the literature to guide the approach for WRAM. In practice, power capture for any WEC can only ever be suboptimal since true optimal control requires that the PTO can provide unrealistically high forces. Prediction of the hydrodynamic excitation and radiation damping forces would also be required. It has further been shown that model sensitivity drastically reduces the effectiveness of mathematically complex control algorithms, and the same is true for PTO constraints and non-ideal conversion efficiencies. Real-time capability is a must, and most of the advanced control techniques prove to be a significant challenge in this regard,

especially on CPU based computing. The literature demonstrates a growing acknowledgement of these issues with research trending towards simpler control algorithms. Therefore, extracting the key aspects of recent approaches leads to the following proposed design goals for WRAM:

- Phase control is worth pursuing given the well documented benefits. For WRAM this means bringing the volumetric flow into phase with the chamber pressure.
- Non-causal strategies should be avoided due to the high level of uncertainty for wave-by-wave prediction in real seas.
- Model sensitive methods should be avoided since the simplifications and assumptions typically applied in the WEC and sea state modelling are quite different to the conditions observed at sea.
- The control strategy should be insensitive to PTO imperfections.
- Constraints such as power, force and velocity should be included in the control implementation.

Combining these principles into a simple and effective first-stage algorithm is proposed as follows:

1. Use latching to implement phase control of the pressure and flow.
2. Latch the water column's volumetric flow at zero-crossing points of the chamber pressure.
3. Use the energy period, T_e, estimated from the last 30 mins of measured sea state data, to determine the unlatching instant.
4. Ensure the PTO constraints are adhered to in the PTO control algorithm.

This concludes the treatment of WEC absorber control for WRAM in this research. Attention is now shifted towards PTO control, equally important for the energy maximisation of sea-going WECs.

6.1.2 PTO Control

The first premise for the PTO control here is it can be treated in isolation from the WEC absorber control, where the air flow from the water column chamber effectively acts as a disturbance to the PTO. The control goal is to maximise the electrical power at the generator output which is coupled to an air turbine and controlled through an electrical drive. The control algorithm provides the optimal velocity command to the electrical drive in real-time.

In comparison to the WEC's hydrodynamic model all of the PTO's inputs and outputs are easily measurable, and changes to the model parameters vary by several orders of magnitude more slowly due to being more protected from the environment. PTO models are often quite straightforward to derive, and since the inputs and outputs can be measured the models can be easily validated. The PTO model is therefore inherently robust and well suited to advanced model based control algorithms. The PTO dynamics however are much faster than those of the WEC and this presents the practical challenge of real-time execution, for which these algorithms do not typically perform well. As discussed previously, constrained optimisation is highly important since the PTO must always operate within constraints for safe and reliable operation.

6.2 RT MPC of the Generator

A real-time MPC strategy has been formulated for the PTO generator, based on the principles presented in Chapter 3. This section provides the specific details of how the RT MPC algorithm has been formulated to facilitate simulation of the control approach on the PTO generator. Two different types of cost function are incorporated for comparison purposes, one for setpoint tracking of the turbine's velocity, and the other for directly maximising the generated power. Finally, the algorithm steps of the constrained closed-form method used in the simulations are tabulated.

6.2.1 Alternative Cost Functions

The principal objective of the RT MPC approach in this research is to optimise the power capture of WRAM's generator, defined by:

$$P_g = T_g \Omega_t \tag{6.1}$$

The RT MPC approach in [1] utilises setpoint feedback control where the cost function is formulated to minimise the error between the output and desired setpoint value. In wave energy, the goal is usually to maximise power capture and most MPC approaches in the literature formulate the cost function accordingly. Two approaches are adopted in this research. The first is to apply velocity setpoint control under the assumption that the optimal setpoint is reasonably obtainable. In this case, the cost function is the same as equation (3.58). The second approach is to reformulate the cost function to directly maximise P_g.

For the first case, the setpoint tracking cost function is used on the basis that the optimal turbine efficiency directly depends on its velocity. Using (4.37) and (4.47), the optimal setpoint velocity, in rev.s^{-1}, is defined as:

$$\Omega_{rev_{SP}} = \frac{\text{RMS}(\dot{m}_t)}{2\pi\rho_{in}\Phi_{t_{opt}}D_t^3} \tag{6.2}$$

Sea states do not vary greatly from one half hour to the next, so it is claimed reasonable to use the RMS mass flow rate from the previous half hour as the basis for the setpoint value held constant over the next half hour window. Note, the RT MPC algorithm has no problem dealing with a variable setpoint if required by the application. The augmented state variable for the setpoint tracking problem is defined as:

$$\mathbf{X}_{SP}(k)^T = [\Delta\mathbf{X}_\Omega(k)^T \quad (\mathbf{Y}(k) - \mathbf{R}_{SP})^T] \tag{6.3}$$

and the augmented NMSS MIMO model is:

$$\begin{aligned} \mathbf{X}_{SP}(k+1) &= \mathbf{A}\mathbf{X}_{SP}(k) + \mathbf{B}\boldsymbol{\Delta}\mathbf{U}(k) \\ \mathbf{Y}(k) &= \mathbf{C}\mathbf{X}_{SP}(k) \end{aligned} \tag{6.4}$$

where:

$$\mathbf{A} = \begin{bmatrix} \mathbf{A}_\Omega & \mathbf{O}_\Omega^T \\ \mathbf{C}_\Omega \mathbf{A}_\Omega & \mathbf{I} \end{bmatrix}, \quad \mathbf{B} = \begin{bmatrix} \mathbf{B}_\Omega \\ \mathbf{C}_\Omega \mathbf{B}_\Omega \end{bmatrix} \tag{6.5}$$

$$\mathbf{C} = \begin{bmatrix} \mathbf{O}_\Omega & \mathbf{I} \end{bmatrix}, \quad \mathbf{O}_\Omega = [\mathbf{0} \dots \mathbf{0}], \quad \mathbf{R}_{SP} = \begin{bmatrix} \Omega_{rev_{SP}} \\ 0 \end{bmatrix} \tag{6.6}$$

As described in Section 3.2.3, the cost function's quadratic matrix is defined as $\mathbf{Q}_{SP} = \mathbf{C}^T\mathbf{C}$, leading to:

$$\mathbf{Q}_{SP} = \begin{bmatrix} 0 & \dots & \dots & 0 \\ \vdots & \ddots & \ddots & \vdots \\ \vdots & \ddots & 1 & 0 \\ 0 & \dots & 0 & 1 \end{bmatrix} \in \mathbb{R}^{26x26} \tag{6.7}$$

containing zeros everywhere except where '1' is shown. The Laguerre cost function is:

$$J_{SP} = \boldsymbol{\eta}^T \boldsymbol{\Omega}_{SP} \boldsymbol{\eta} + 2\boldsymbol{\eta}^T \boldsymbol{\Psi}_{SP} \mathbf{X}_{SP}(k) \tag{6.8}$$

where $\boldsymbol{\Omega}_{SP}$ and $\boldsymbol{\Psi}_{SP}$ are calculated using (3.52) and (3.53). The optimal Laguerre coefficients are then calculated at each time step from:

$$\boldsymbol{\eta}_{opt_{SP}} = -\boldsymbol{\Omega}_{SP}^{-1} \boldsymbol{\Psi}_{SP} \mathbf{X}_{SP}(k) \tag{6.9}$$

The power maximisation cost function approach varies only very slightly to the setpoint tracking problem, where the cost matrix, $\mathbf{Q}$, and the state feedback vector output terms are modified. All else remains the same. The revised cost matrix now acts to multiply the two NMSS model outputs, namely the generator velocity, Ω_t, and generator torque, T_g, hence being equivalent to (6.1). The new cost matrix is:

$$\mathbf{Q}_P = \begin{bmatrix} 0 & \dots & \dots & 0 \\ \vdots & \ddots & \ddots & \vdots \\ \vdots & \ddots & 0 & 1 \\ 0 & \dots & 1 & 0 \end{bmatrix} \in \mathbb{R}^{26x26} \tag{6.10}$$

containing zeros everywhere except where '1' is shown. The revised state feedback variable is:

$$\mathbf{X}_P(k)^T = [\Delta\mathbf{X}_\Omega(k)^T \quad \mathbf{Y}(k)^T] \tag{6.11}$$

and the Laguerre cost function is:

$$J_P = \boldsymbol{\eta}^T \boldsymbol{\Omega}_P \boldsymbol{\eta} + 2\boldsymbol{\eta}^T \boldsymbol{\Psi}_P \mathbf{X}_P(k) \tag{6.12}$$

The matrices $\boldsymbol{\Omega}_P$ and $\boldsymbol{\Psi}_P$, and the optimal Laguerre coefficients are calculated in the same manner as for the setpoint tracking approach such that:

$$\boldsymbol{\eta}_{opt_P} = -\boldsymbol{\Omega}_P^{-1} \boldsymbol{\Psi}_P \mathbf{X}_P(k) \tag{6.13}$$

6.2.2 Implementation of Closed-Form Constrained Control

To maximise the real-time execution speed, the constrained control problem has been formulated using the closed-form solution described in Section 3.2.6. Once the augmented NMSS model is constructed, control is implemented as per the steps shown in table 6.1. Note that this algorithm is valid for both cost functions described in Section 6.2.1.

Table 6.1: Implementation Steps for Closed-Form Constrained Control.

Step	Task
1	Define the cost matrix, either $\mathbf{Q}_{SP}$ or $\mathbf{Q}_{P}$.
2	Define the tuning parameters, a, N, r_w and N_p.
3	Formulate the Laguerre network and obtain $\mathbf{L}(0)^T$.
4	Calculate ($\mathbf{\Omega}_{SP}$ and $\mathbf{\Psi}_{SP}$) or ($\mathbf{\Omega}_{P}$ and $\mathbf{\Psi}_{P}$).
5	Calculate the closed-loop poles from the state feedback matrix, $\mathbf{K}_{mpc}$.
6	Set the constraints for control amplitude, (u^{min}, u^{max}), and the rate of change of control, (Δu^{min}, Δu^{max}).
Real-Time Loop:	
7	Calculate unconstrained optimal Laguerre coefficients $\boldsymbol{\eta}$
8	Calculate the optimal rate of change of control using the Laguerre network.
9	Apply the constraints as per the closed-form method.
10	Simulate the plant's response to the uncontrollable turbine torque input and controlled setpoint velocity. Note, if the control is being applied to a real system, this step is replaced with reading and writing to the real-world IO.
11	Update the feedback matrix and repeat loop.

Chapter 7

Results and Discussion

7.1 WRAM Uncontrolled Simulations

Figure 7.1 shows the simulation results of the uncontrolled WRAM with a constant setpoint velocity of 15.9 rev.s^{-1}, or 100 rad.s^{-1}. It can be seen how the bidirectional relative velocity between the WEC and water column translate to a uni-directional turbine torque to be applied to the generator model. Figure 7.2(a) shows the PTO's nonlinear behaviour that occurs

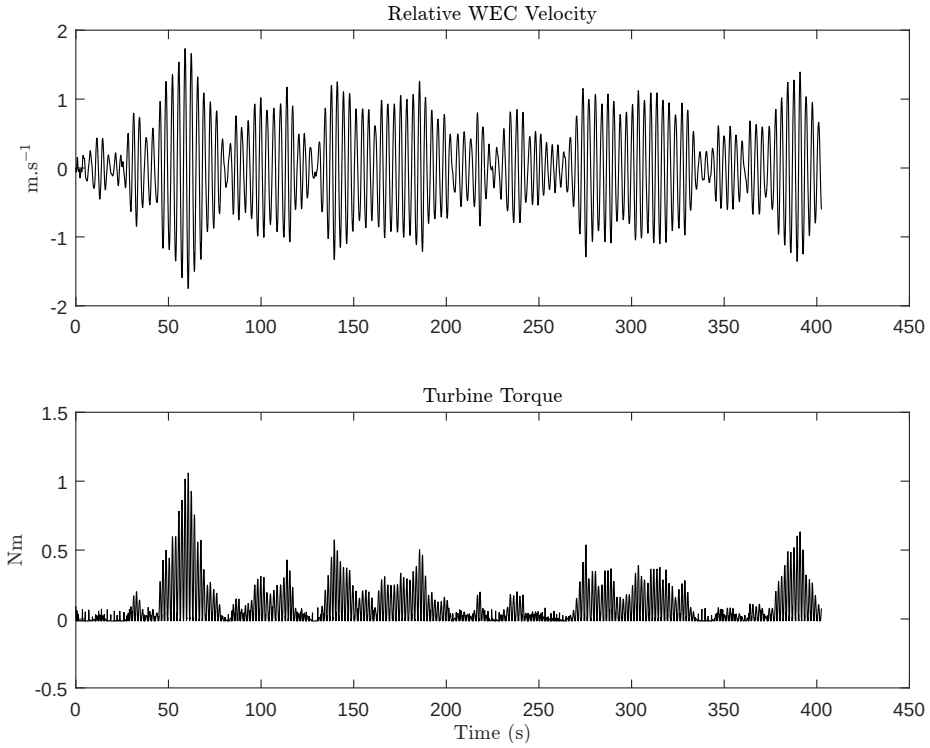

Figure 7.1: Simulation of Uncontrolled WRAM Relative Velocity and Turbine Torque.

around zero crossing regions due to the discrete switching of turbine's inlet density at the stagnation conditions. Figure 7.2(b) shows comparative results between a continuous model implemented in Simulink® and the MATLAB® discrete equivalent model. Simulink® is configured to use a Runge-Kutta 4th order solver with fixed time step and MATLAB® is programmed to use the same Runge-Kutta equations. The simulation responses agree everywhere except around these zero crossing points, however since the discrepancies occur at low torques and forces, the consequences are minimal, if not negligible. It can be seen from these figures that the disruptions occur for both the PTO force and turbine torque.

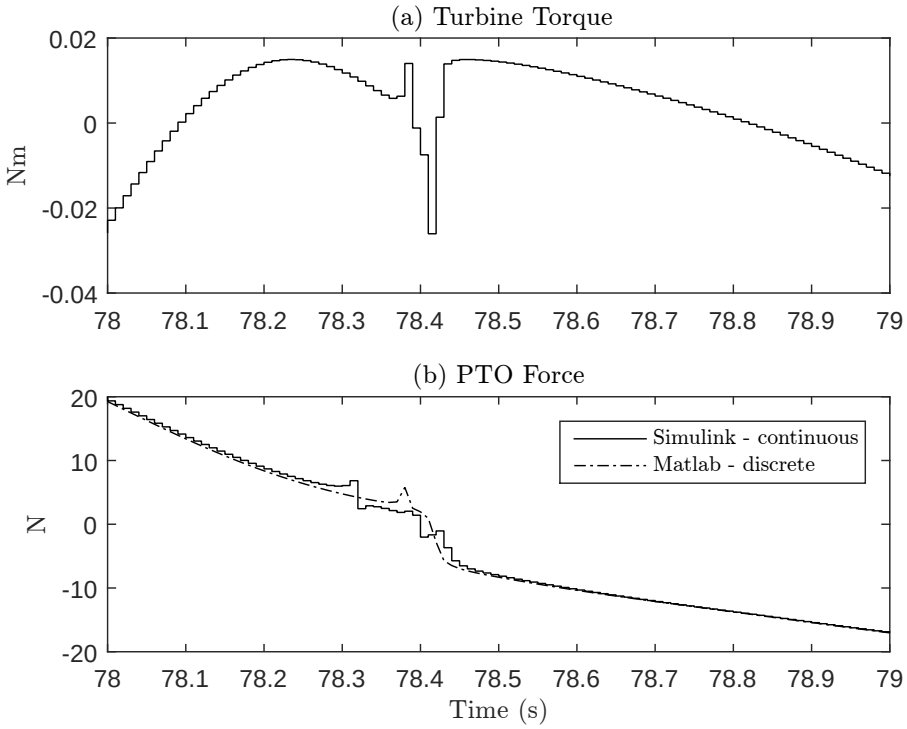

Figure 7.2: Nonlinear Behaviour around Zero Crossing Region.

7.2 Hydrodynamic Transfer Functions

Figures 7.3 to 7.6 show the transfer function approximations obtained during the frequency domain identification process described in Section 4.3.6. Figure 7.7 shows the transfer function approximations obtained for the excitation forces.

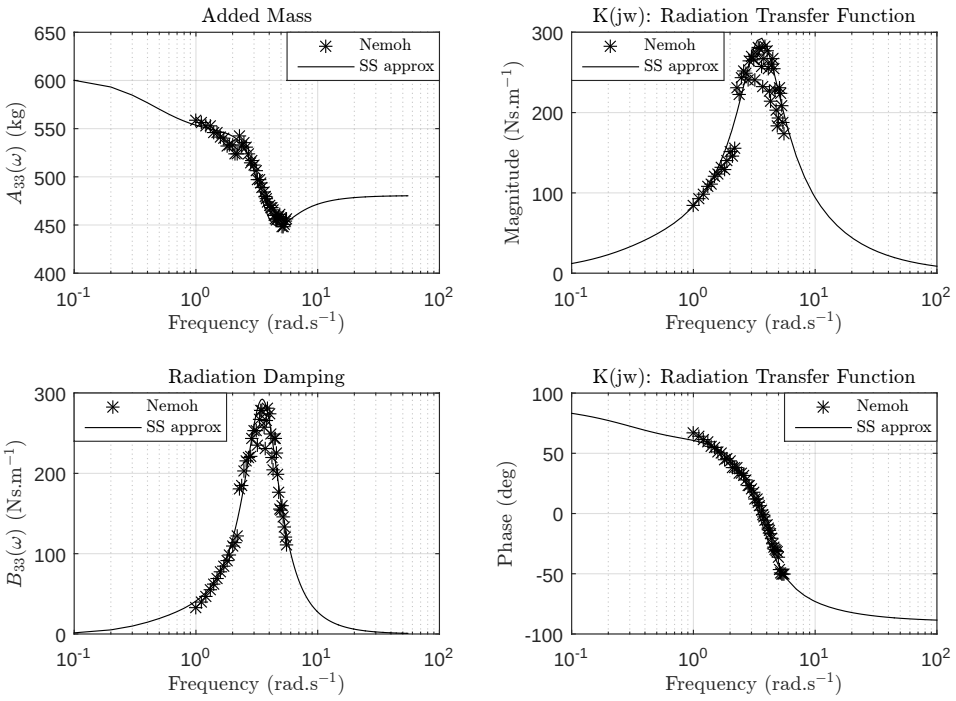

Figure 7.3: Hydrodynamic Radiation Transfer Function Approximation for Interaction 33.

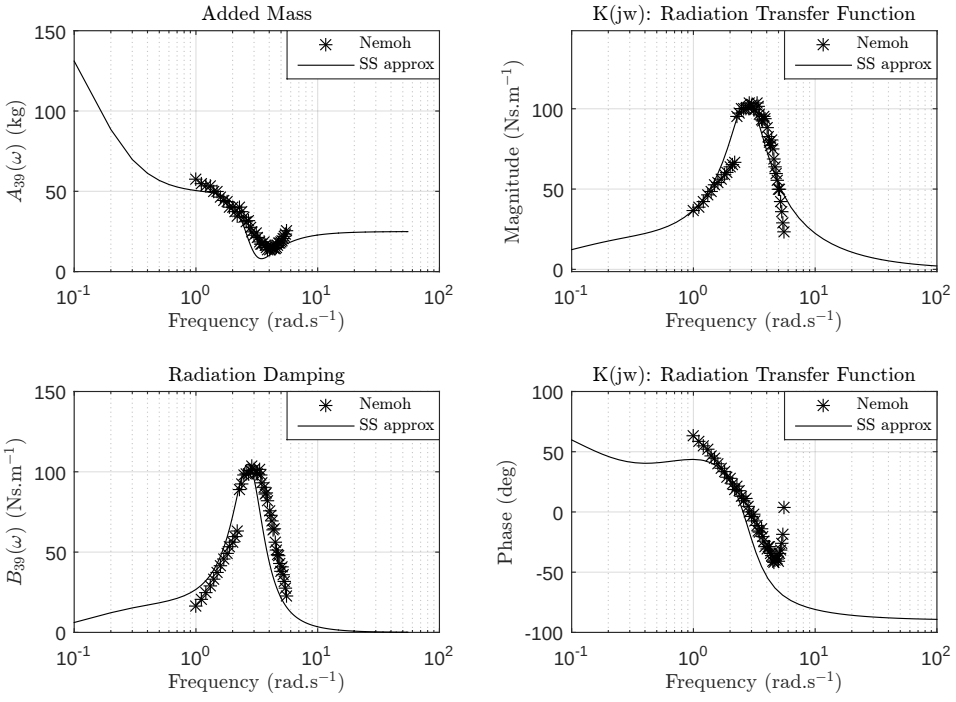

Figure 7.4: Hydrodynamic Radiation Transfer Function Approximation for Interaction 39.

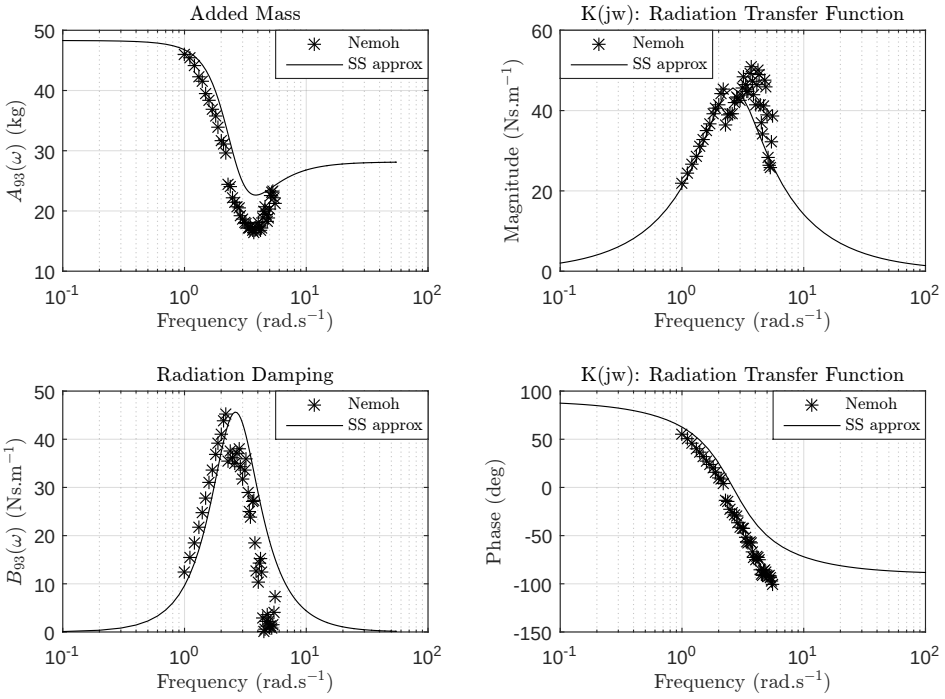

Figure 7.5: Hydrodynamic Radiation Transfer Function Approximation for Interaction 93.

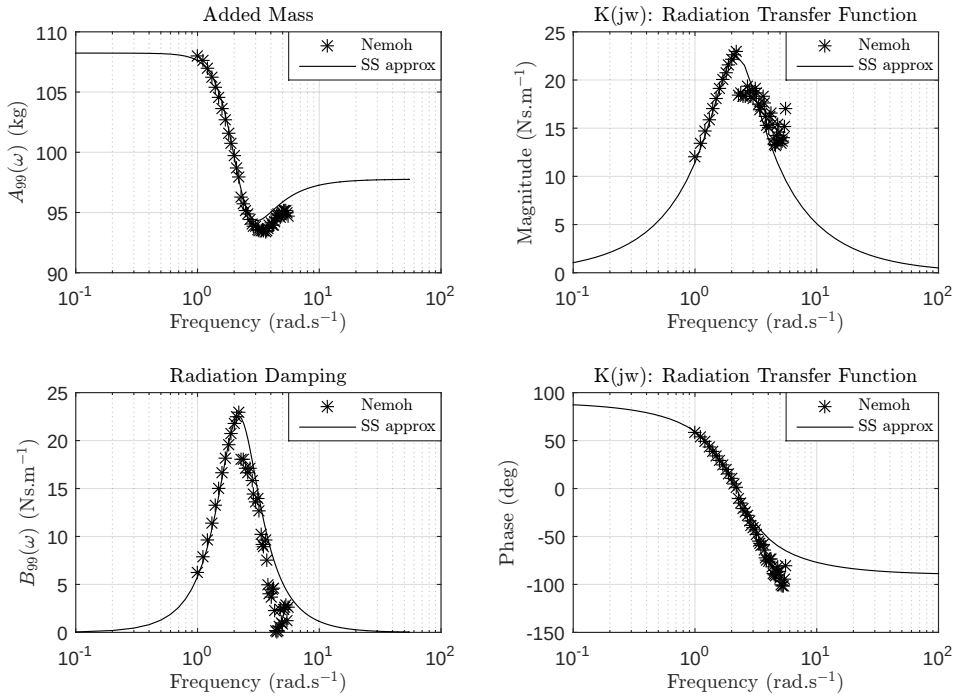

Figure 7.6: Hydrodynamic Radiation Transfer Function Approximation for Interaction 99.

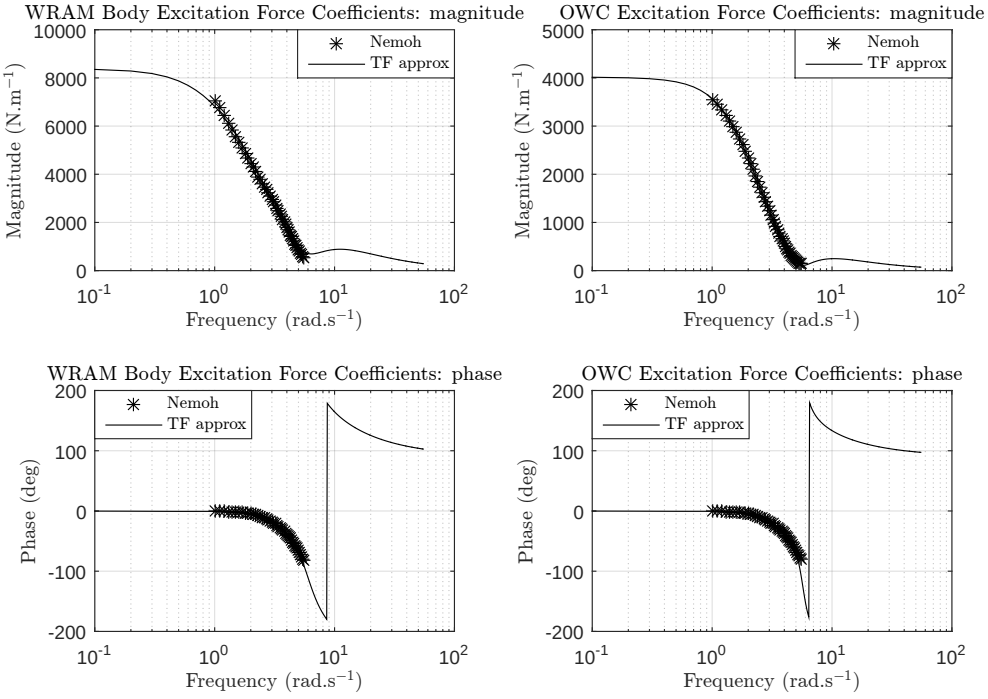

Figure 7.7: Excitation Force Transfer Function Approximations for both the WRAM Body and Water Column.

7.3 Generator Model

Figures 7.8 and 7.9 show the response of the MIMO generator model with the embedded PI-control loop. During the first half of the simulation a setpoint velocity is applied to the unloaded generator. Due to the embedded PI-control setpoint tracking is achieved and the generator torque experiences a brief positive transient before settling to zero as the velocity reaches the setpoint. When the turbine torque is applied at time $t = 5s$ the output velocity is briefly disturbed, at which point the generator applies a torque in the opposing direction to balance the input torque. The velocity again settles to its setpoint value.

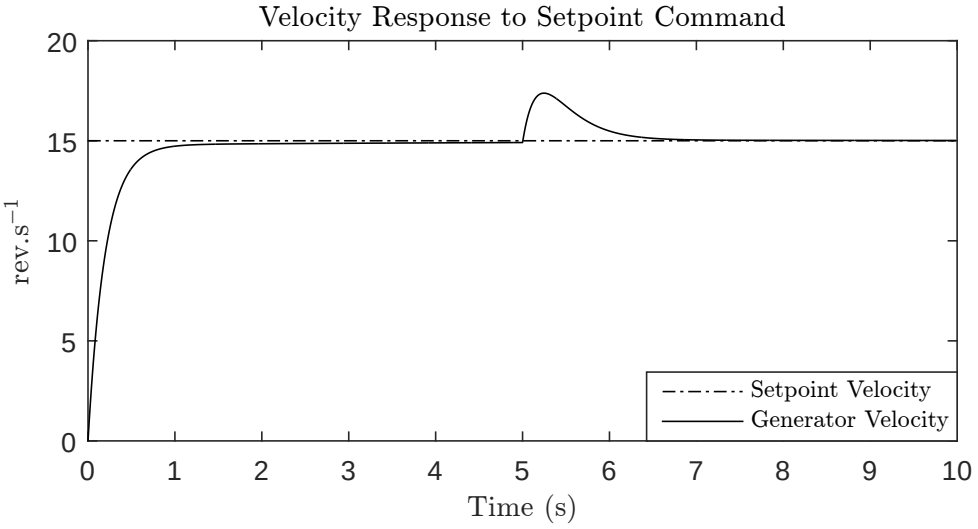

Figure 7.8: MIMO Generator Velocity Responses.

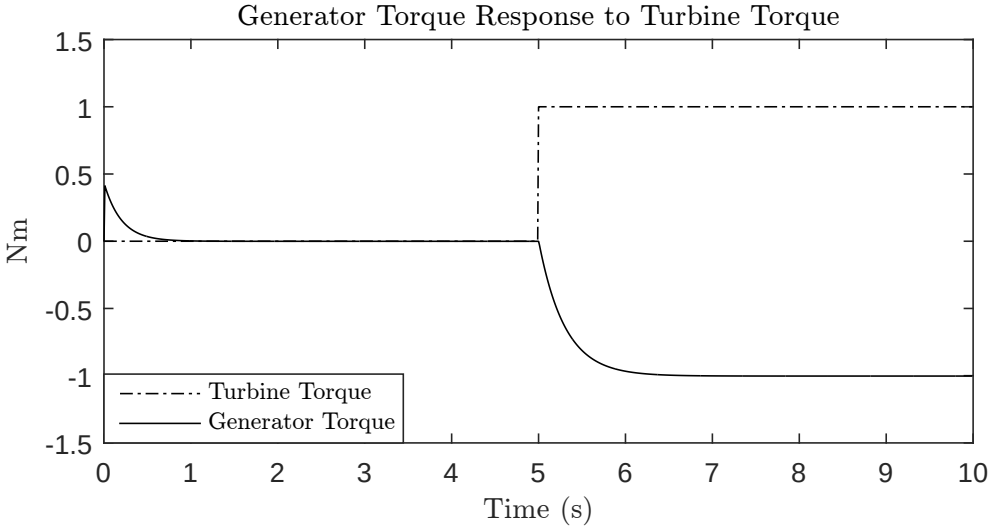

Figure 7.9: MIMO Generator Torque Responses.

7.4 Real-Time MPC

This section presents the results of the RT MPC simulations conducted in this research including analysis of Laguerre network tuning, general RT MPC performance, real-time execution and the comparison of two alternative cost functions.

7.4.1 Identification of Laguerre Parameters

As outlined in Section 3.2.5, the features of a well-tuned Laguerre network are orthonormality of the Laguerre basis functions, minimal network order, and a suitable response time for the application. In this research, the measure of orthonormality, O has been determined by taking the arithmetic mean of the diagonal elements of $\mathbf{L}(k)\mathbf{L}(k)^T$, since for true orthonormality, this matrix multiplication results in an identity matrix. To help narrow down the search for which parameter values of a, N and N_p result in good orthonormality of the Laguerre network, a sensitivity analysis was conducted using the parameter ranges:

$$\begin{aligned} a &= [0, 0.3, 0.6, 0.9] \\ N &= [1, 2, 5, 10] \\ N_p &= [2, 5, 10, 20] \end{aligned} \tag{7.1}$$

Table 7.1 shows the resulting correlation coefficients between all parameters. The results suggest that a and N are marginally more correlated to orthonormality than N_p. However, it is known that larger values of N_p lead to a higher orthonormality, and for values of $N_p = 20$, the orthonormality was predictably higher than for smaller values. Considering these results, the prediction window was arbitrarily set to $N_p = 30$, leaving the parameters a and N as the free search variables for a reasonable compromise in Laguerre network parameters.

For $N_p = 30$, the simulations were rerun with the ranges for a and N set as:

$$\begin{aligned} a &= [0, 0.3, 0.6, 0.9] \\ N &= [1, 2, 5, 10] \end{aligned} \tag{7.2}$$

Table 7.1: Correlation Coefficients for Laguerre Network Tuning Parameters.

	a	**N**	$\mathbf{N_p}$	**O**
a	1			
N	0	1		
$\mathbf{N_p}$	0	0	1	
O	-0.4927	-0.5150	0.4660	1

Figure 7.10 shows the results of the grid-search, providing insight into the correlation between the a, N and O. Strong orthonormality is achieved for small values of a and N. Keeping in mind that the speed of response is governed by a and the order by N, the parameters were initially chosen to lie somewhere mid-range, such that future tuning can be done in either direction for both variables if necessary, depending on the RT MPC performance. Accordingly, the parameters were chosen from Figure 7.10 to be:

$$\begin{aligned} a &= 0.6 \\ N &= 5 \end{aligned} \tag{7.3}$$

7.4.2 Sensitivity Analysis of Tuning Parameters

With a sense of the required region of a and N for achieving orthonormality, a sensitivity analysis was conducted by executing the RT MPC algorithm with setpoint tracking for various combinations of the four tuning parameters, a, N, r_w and N_p. The parameter ranges were:

$$\begin{aligned} a &= [0, 0.3, 0.6, 0.9] \\ N &= [1, 2, 5, 10] \\ r_w &= [0.1, 0.2, 0.5, 1] \\ N_p &= [2, 5, 10, 20, 30] \end{aligned} \tag{7.4}$$

At first, simulations were run for all permutations of a, N and r_w, holding $N_p = 30$. Table 7.2 shows the correlation coefficients between the tuning parameters and the performance measures of orthonormality, mean power and closed-loop pole statistics. All coefficients

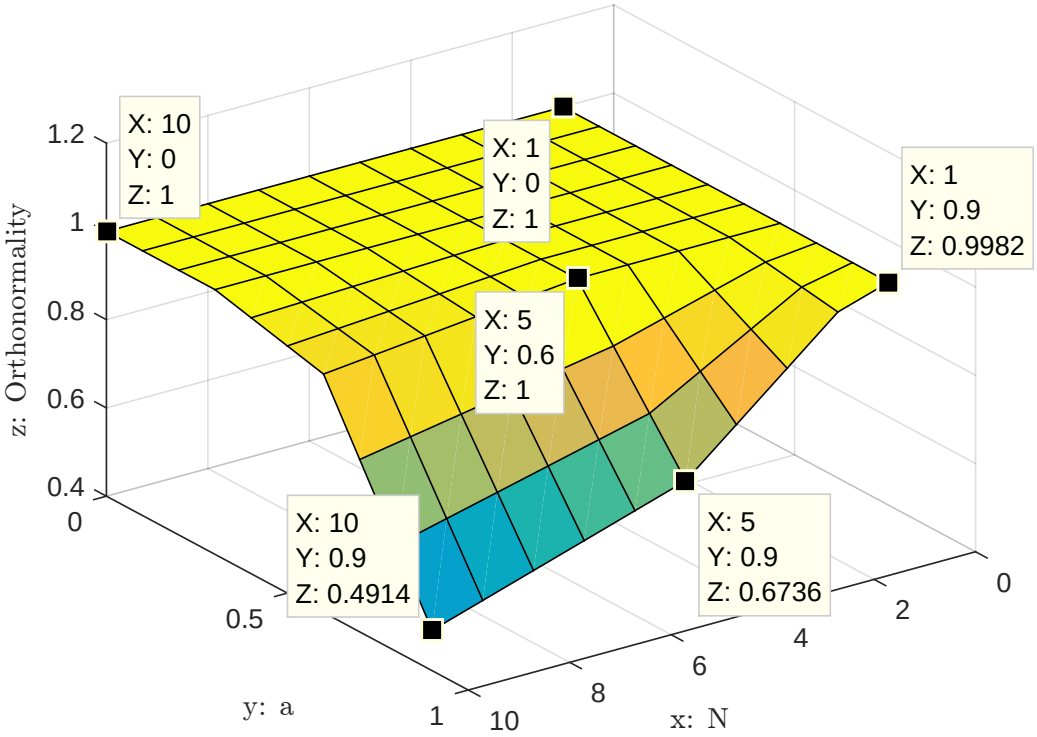

Figure 7.10: Orthonormality as a Function of a and N.

with a magnitude greater than 0.5 are highlighted, indicating relatively strong correlation. For this set of simulation results, the following observations have been made:

- The mean power is somewhat sensitive to N, and has very little influence from O, a and r_w.
- Orthonormality was again confirmed to be inversely influenced by a and N.
- The Laguerre pole, a, has a strong influence of the closed-loop pole locations.

To gain further insight, the mean power is plotted in Figure 7.11 as a function of a and N for the case where $r_w = 0.1$ and $N_p = 30$. For the most part, the mean power is insensitive to a except for a single Laguerre network order of $N = 2$. The relative dependence between a and N can also be seen here. For low values of N, the mean power is very sensitive, although it converges for large N.

Table 7.2: Correlation between Tuning Parameters and Performance with $N_p = 30$.

	a	**N**	$\mathbf{r_w}$	**O**	$\bar{\mathbf{P}}$	$\bar{\mathbf{X}}$	$\mathbf{X}_{max}$	$\mathbf{X}_{var}$
a	1							
N	0	1						
$\mathbf{r_w}$	0	0	1					
O	***-0.5340***	-0.4053	0	1				
$\bar{\mathbf{P}}$	0.1165	0.4817	-0.1184	-0.1578	1			
$\bar{\mathbf{X}}$	0.3058	***-0.5784***	0.4035	0.1934	-0.3281	1		
$\mathbf{X}_{max}$	-0.1627	-0.3113	-0.0806	0.1916	0.0364	0.0257	1	
$\mathbf{X}_{var}$	***0.6488***	0.3001	0.3237	-0.2166	0.1290	0.2844	-0.3787	1

O: Measure of orthonormality.

$\bar{\mathbf{P}}$: Mean power.

$\bar{\mathbf{X}}$: Mean pole magnitude.

$\mathbf{X_{max}}$: Max pole magnitude.

$\mathbf{X_{var}}$: Variance of pole magnitude.

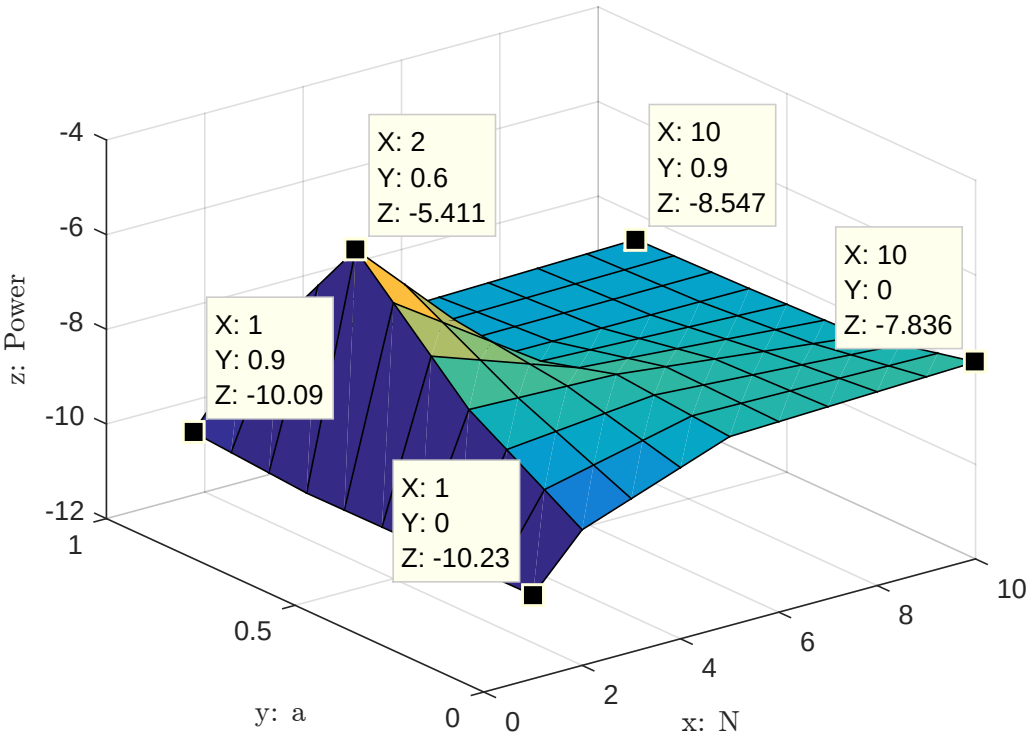

Figure 7.11: Power as a Function of a and N for $r_w = 0.1$, $N_p = 30$.

A second set of simulations was run with all permutations of a, N and $N_p = [2, 5, 10, 20]$. For this system, since the influence of r_w is small on the mean power it was set to the highest possible value of $r_w = 1$, signifying a fast response. A possible reason for r_w not being very influential could be due to the well tuned PI-controller, embedded within the NMSS model. If so, a higher influence of r_w might be expected if the PI-controller was removed from the system or detuned. Note, that removing it is not possible with the current generator and servo-drive. Table 7.3 shows the correlation coefficients, and Figures 7.12 and 7.13 show the mean power and pole magnitude variance as functions of N and N_p for $a = 0.6$ and $r_w = 1$.

The correlation coefficients show that the mean power is dependent on the prediction window, N_p, and the closed-loop pole variance. From the first set of simulations it was found that for $N = 1$, power is insensitive to a. Therefore in this case, the choice of $a = 0.6$ is inconsequential. Note, the theory says that for low N, a is very influential for achieving good orthonormality. However, the correlation coefficients show that the mean power for this

Table 7.3: Correlation between Tuning Parameters and Performance with $r_w = 1$.

	a	**N**	**N_p**	**O**	**$\bar{P}$**	**$\bar{X}$**	**X_{max}**	**X_{var}**
a	1							
N	0	1						
N_p	0	0	1					
O	-0.4927	***-0.5150***	0.4660	1				
$\bar{P}$	0.0566	0.3574	***-0.6100***	-0.4244	1			
$\bar{X}$	0.3770	-0.0286	-0.3565	-0.4382	0.3553	1		
X_{max}	0.0570	-0.1291	-0.4187	-0.3810	0.3311	***0.6222***	1	
X_{var}	0.2369	0.0067	***-0.7773***	***-0.5367***	***0.5074***	***0.7490***	***0.6519***	1

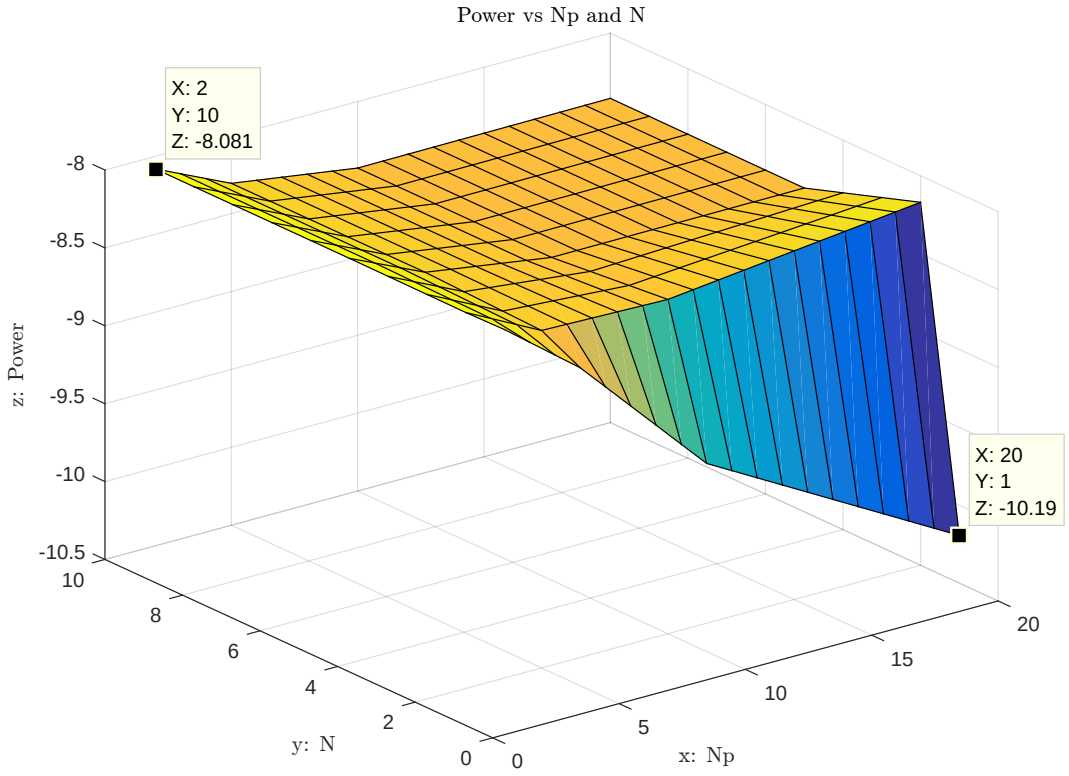

Figure 7.12: Power as a Function of N and N_p for $a = 0.6$, $r_w = 1$.

system is not greatly influenced by orthonormality. Therefore a can be tuned to satisfy the desired setpoint tracking behaviour without significantly affecting the power capture of the

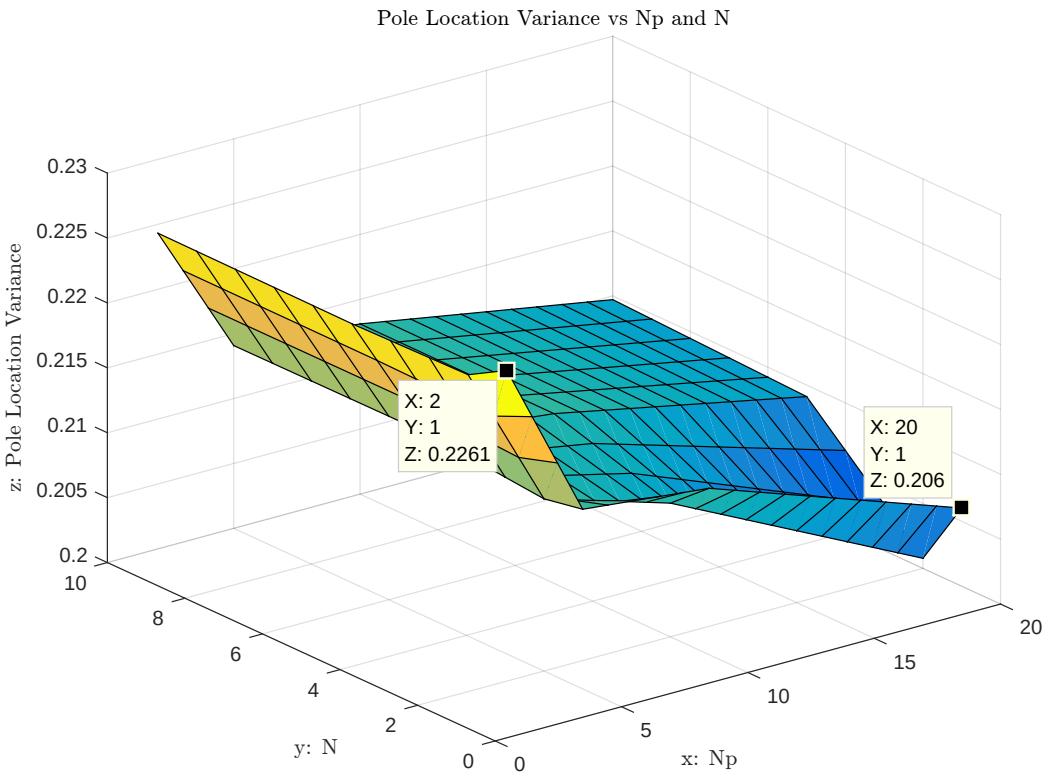

Figure 7.13: Variance of Closed-Loop Poles as a Function of N and N_p for $a = 0.6$, $r_w = 1$.

system. From Figure 7.12 the mean power appears largely insensitive for all combinations of N and N_p except when $N = 1$. In this case, it is very sensitive to N_p where the highest power occurs at $N_p = 20$. From Figure 7.13 it can be seen that the variance of the closed-loop poles is also very sensitive to N_p across the whole range of N values, where the variance decreases with N_p.

7.4.3 RT MPC Performance Assessment

From the sensitivity analysis the following two simulation cases are selected for further inspection:

$$\text{Case 1}: \quad a = 0.6 \quad N = 10 \quad r_w = 1 \quad N_p = 2$$

$$\text{Case 2}: \quad a = 0.6 \quad N = 1 \quad r_w = 1 \quad N_p = 20$$

Figure 7.14 shows the performance results of the RT MPC algorithm for case 1. Here, the

input turbine torque is created offline using equation (4.32) in an uncontrolled WRAM simulation, subject to a full-scale equivalent sea state of $H_s = 6.75$m and $T_e = 11.5$s. Note that in these simulations the controlled turbine is decoupled from the WRAM absorber, and therefore variations of turbine velocity are assumed to not affect the absorber's motion. The four

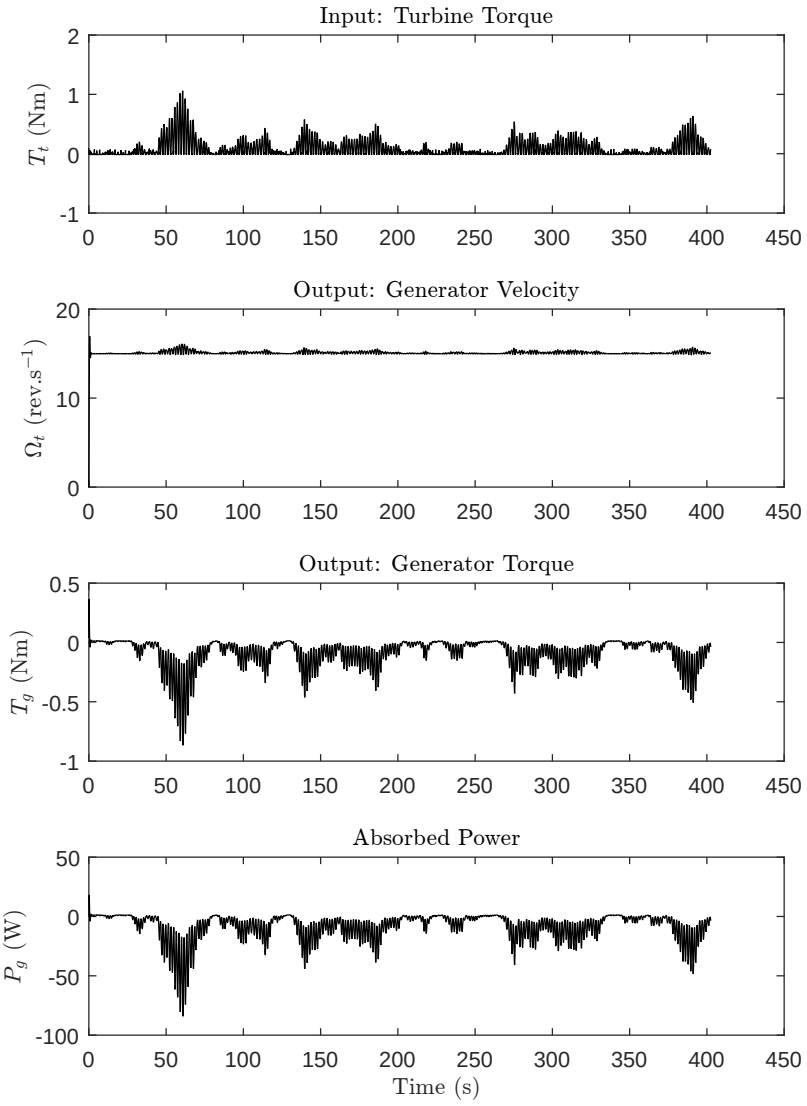

Figure 7.14: RT MPC Performance of Generator Control - Case 1.

subplots in Figure 7.14 show the time series data for turbine torque, T_t, generator velocity, Ω_t, generator torque, T_g, and absorbed generator power, P_g. The first thing to notice is that the generator velocity is being maintained at the setpoint value of 15.9 rev.s^{-1} in the presence of the input turbine torque which is attempting to speed up the generator. Disturbance

rejection can also be seen through small ripples in the velocity, coincident with energetic inputs. The generator can be seen to provide the necessary reaction for maintaining the output velocity and its inertial dynamic response can be observed through the slightly smoothed profile in comparison to that of the turbine torque. Given that the setpoint velocity is holding well, the power absorbed by the generator follows the same profile as the generator torque. It should also be noted that the frequency content appears to be mostly unmodified with the exception of the increase of some low frequency content due to the inertial storage of the turbine.

Figure 7.15 shows the main RT MPC variables including the generator velocity, Ω_t, control amplitude, $\Omega_{rev_{SP}}$, and rate of change in control, $\dot{\Omega}_{rev_{SP}}$. The point of interest here is that the optimal control goal is being satisfied without the constraints being activated, except in the first few samples when starting from rest. Figure 7.16 zooms into this region where $\Omega_{rev_{SP}}$ briefly saturates before settling to the setpoint within a few seconds.

Case 2 is now considered, with the generator and RT MPC performance results shown in Figures 7.17 and 7.18. The control response to the same input is particularly poor in the sense that firstly, the setpoint velocity is not being maintained, and secondly that there is significant high frequency content, appearing as sharp spikes. One redeeming feature is that the RT MPC is successfully limiting the damage of the poor control signal through activation of the constraints, which occurs much of the time for the control amplitude, and nearly all of the time for the rate of change of control. Even in the presence of active constraints, the generator never speeds out of control.

The closed-loop dynamics for both systems can be seen in Figures 7.19 and 7.20. It should be noted that while the closed-loop poles only have meaning when the constraints are inactive, the pole locations offer information about the speed of response of the system. It was also observed through the sensitivity analysis that the variance of the pole locations was reasonably well correlated to mean power and the tuning parameters N_p and O. Another observation, was that there seemed to be a qualitative correlation between the pole placement variability and the quality of control performance, for example, as seen in case 1 with respect to case 2.

Another interesting result is that the mean power for case 1 was approximately 20% less

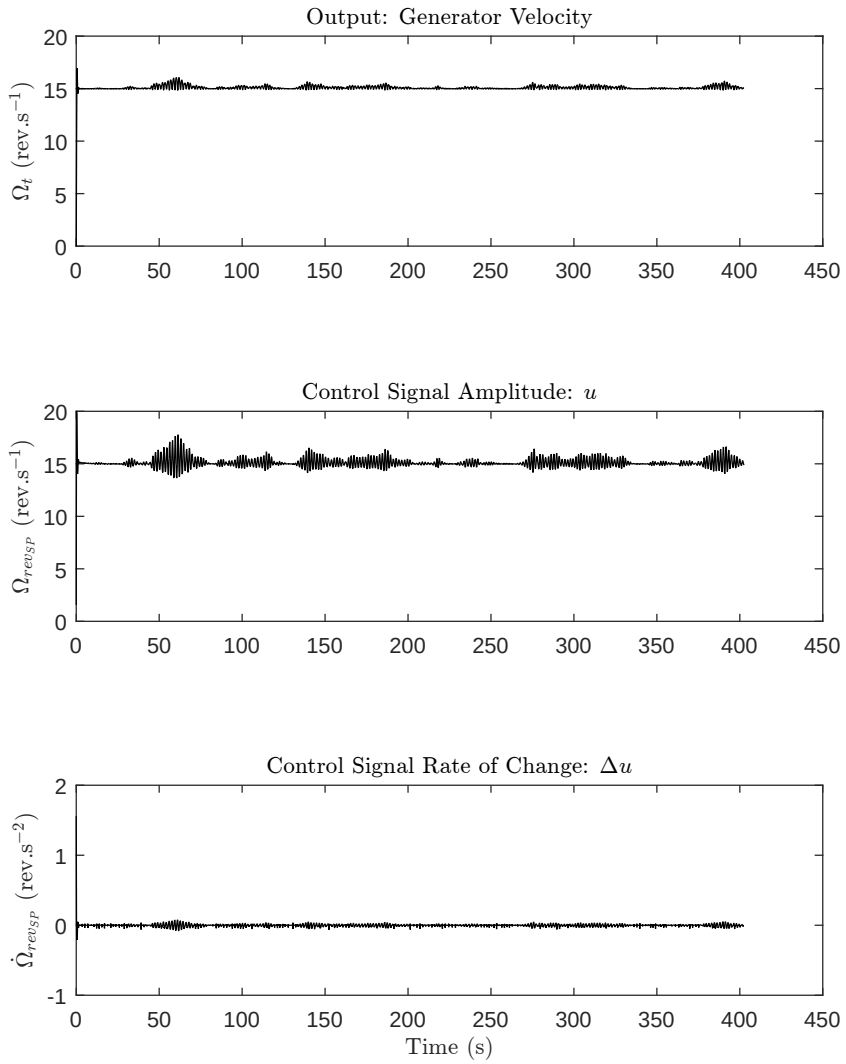

Figure 7.15: Performance of RT MPC Control Algorithm - Case 1.

than that of case 2, even though setpoint tracking appeared to be failing for the latter. One point to note here is that the turbine efficiency hasn't yet been included in the model which is heavily dependent on the turbine velocity. Incorporation of the dimensional efficiency characteristic into the simulation would mean that failing to keep the velocity close to the peak efficiency region would penalise the poor performance of case 2 more noticeably. Another strong argument for avoiding the system response in case 2, is that the harsh control signals experienced by the generator would quickly lead to high maintenance costs and the potential of device failure.

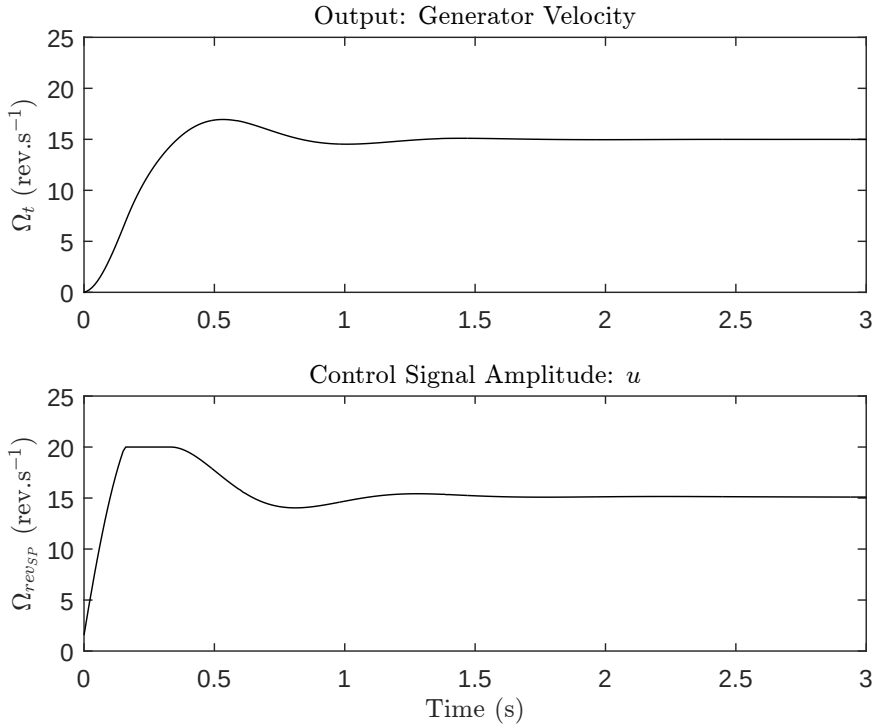

Figure 7.16: Performance of RT MPC Control with Initial Saturation - Case 1.

7.4.4 Real-Time Execution Speed

It is critical in this research to assess the execution speed of the RT MPC algorithm. Figures 7.21 and 7.22 show the benchmarked execution speed, measured at each time step of the simulation for case 1 and case 2. Values of the minimum, mean and maximum execution times are provided in Table 7.4. It should be noted that the algorithm was executed on a non-real-time Windows operating system in MATLAB®. Execution on a real-time target such as the cRIO could be expected to be faster and more deterministic.

7.4.5 Alternative Power Maximisation Cost Function

For most of the RT MPC simulations, optimisation of the power capture has been based on the principle of using velocity setpoint tracking to keep the turbine operating at its peak efficiency. The setpoint tracking approach is largely based on the assumption that the input torque is unidirectional. Note that in this research, the setpoint velocity is determined using equation (6.2). Given that the velocity setpoint is held constant for long periods of time, it is

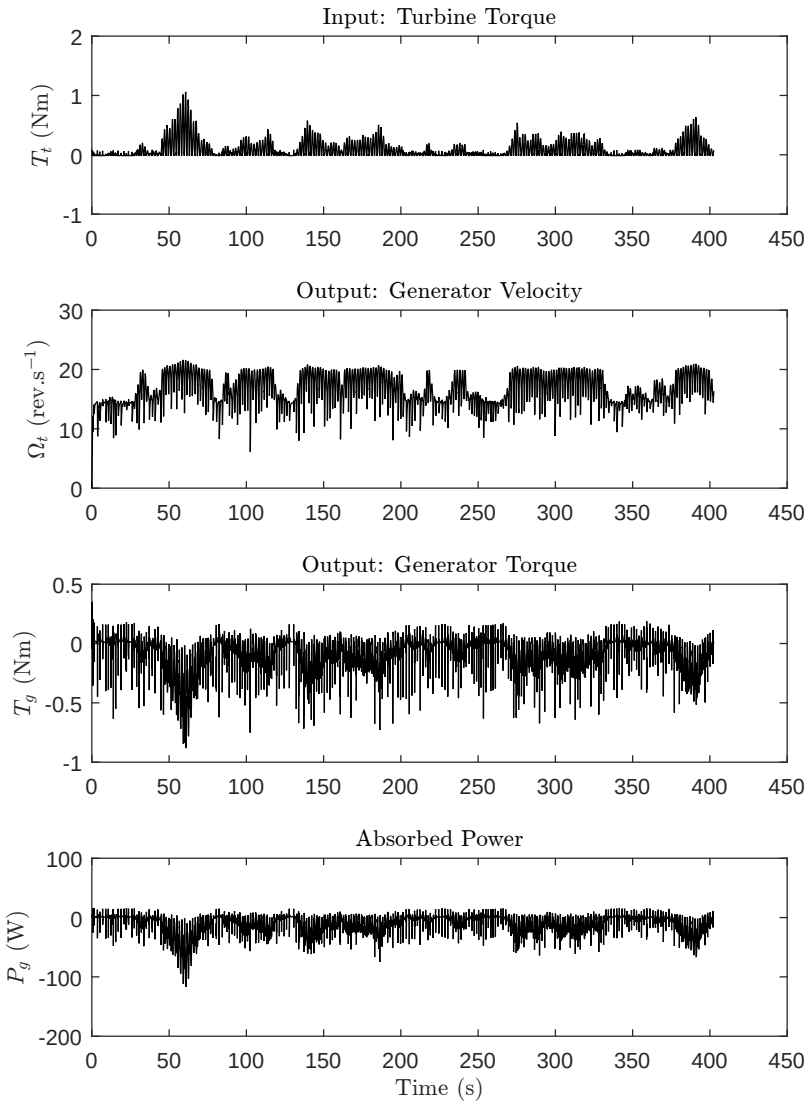

Figure 7.17: RT MPC Performance of Generator Control - Case 2.

reasonable to expect that the absorbed power will be proportional to the velocity within the velocity constraint limits. It should be noted that while the assumption of unidirectionality is valid for the self-rectifying axial impulse turbine, it doesn't hold true for other types of WEC PTO systems.

Alternatively, rather than using setpoint tracking the cost function can be formulated to directly maximise power, as described in Section 6.2.1. The results of each optimisation approach are now compared, where analysis is focused on the effect of using a bidirectional input torque profile on the power performance. To make the comparisons clearer the same

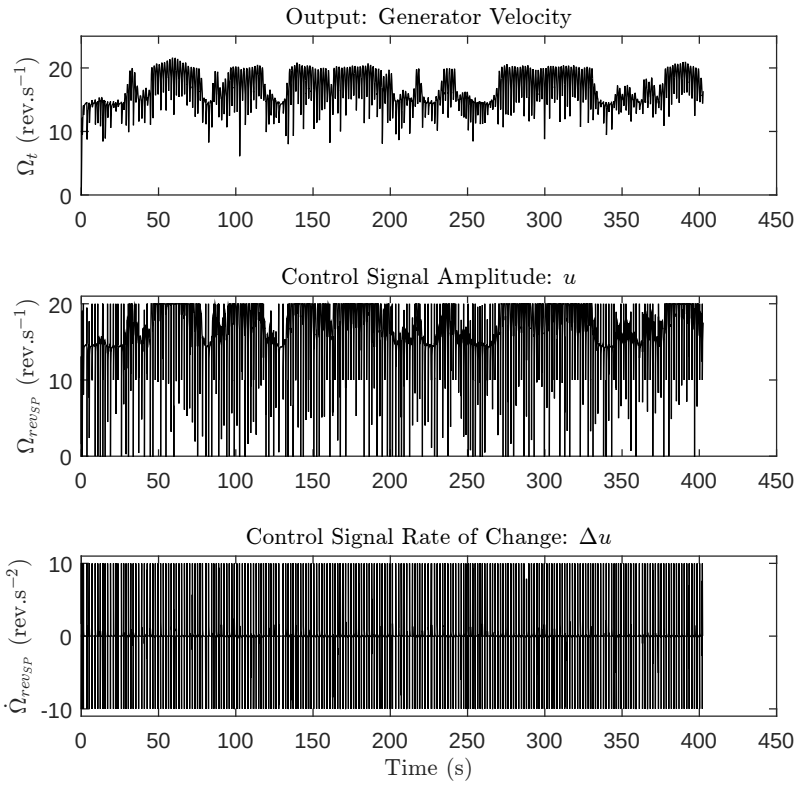

Figure 7.18: Performance of RT MPC Control Algorithm - Case 2.

torque profile was used for all test cases, except that in the bidirectional cases, the torque's mean value has been subtracted, resulting in a new profile with zero mean. Figures 7.23 to 7.25 show the generator performance curves for the new test cases, 3 to 5, using the parameters of test case 1. Table 7.5 shows these parameters and power absorbed in each case.

In cases 3 and 4, the power maximisation approach can be seen to autonomously implement phase control, where the generator velocity is directly out of phase with the torque. Also, the absorbed power is always unidirectional which is advantageous for minimising reactive power. The absorbed power was greatest with setpoint tracking when the torque was unidirectional, however setpoint tracking became the worst performer for bidirectional torque. In this scenario the power maximisation method performed more favourably since it autonomously ensured power was unidirectional, even though the input torque was not. Case 5 is particularly bad for setpoint tracking, considering that the power amplitudes are an order of magnitude larger than for the power maximisation method, and the absorbed

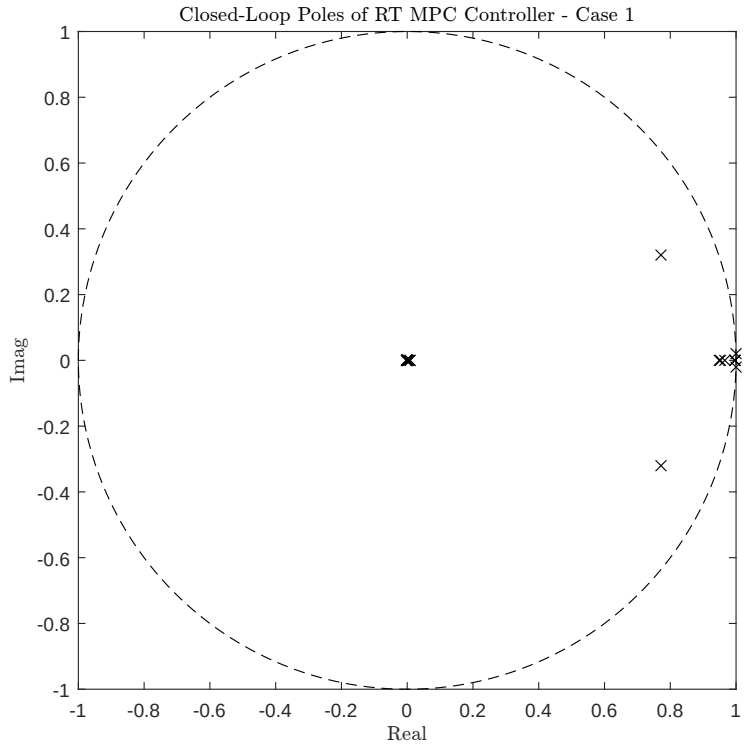

Figure 7.19: Closed-Loop Poles of Complete RT MPC Controller - Case 1.

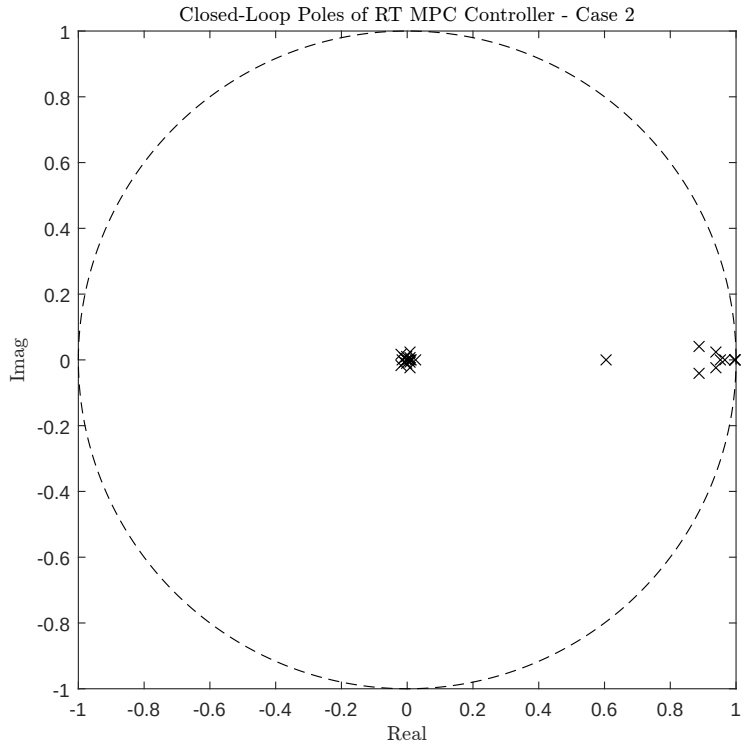

Figure 7.20: Closed-Loop Poles of Complete RT MPC Controller - Case 2.

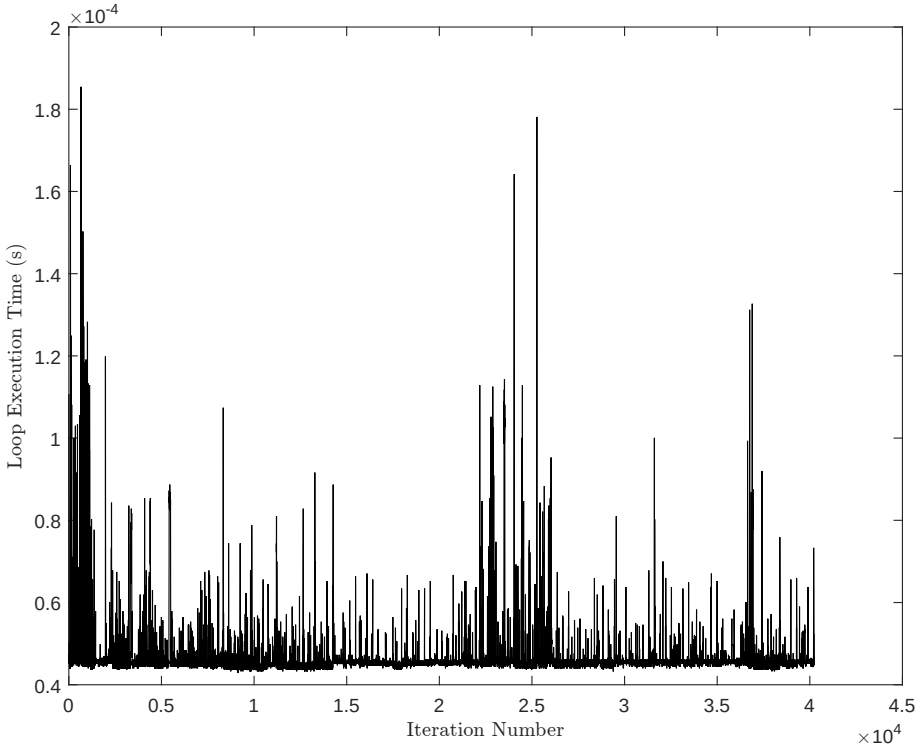

Figure 7.21: Real-Time Execution Speed (s) - Case 1.

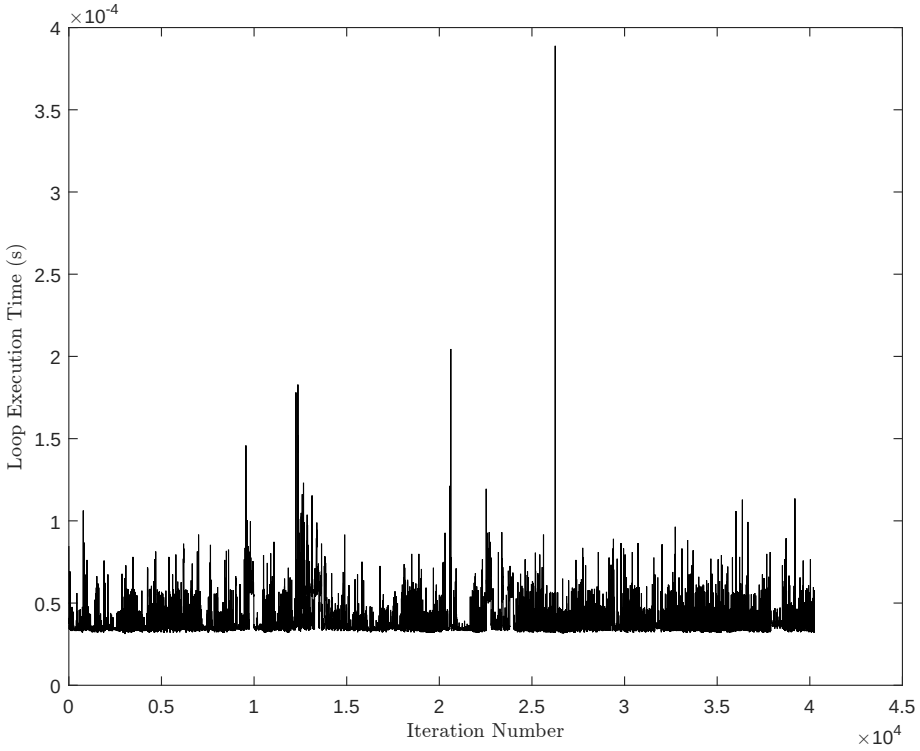

Figure 7.22: Real-Time Execution Speed (s) - Case 2.

Table 7.4: Real-Time MPC Execution Times (s) for Case 1 and Case 2.

	Case 1	**Case 2**
Minimum	$4.289(10)^{-5}$	$3.116(10)^{-5}$
Mean	$4.609(10)^{-5}$	$3.677(10)^{-5}$
Maximum	$1.855(10)^{-4}$	$3.889(10)^{-4}$

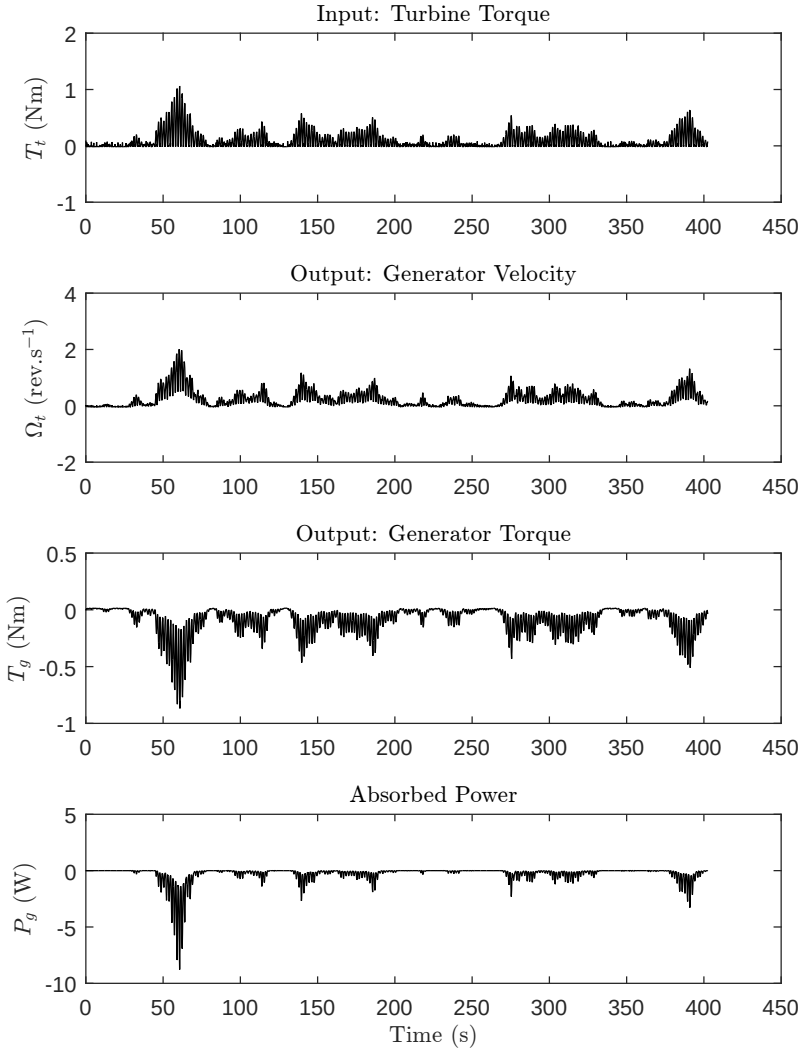

Figure 7.23: RT MPC Performance with 'Power Maximisation' - Case 3.

power is worse.

The poor performance of the power maximisation approach for unidirectional torque

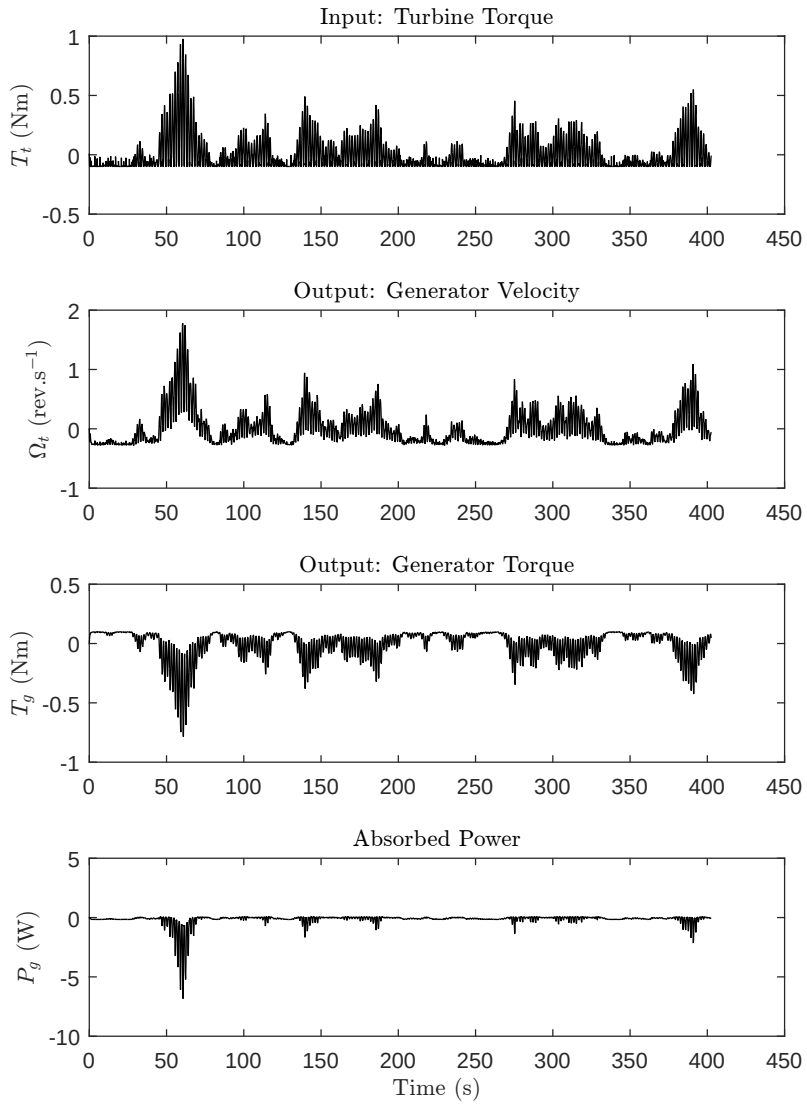

Figure 7.24: RT MPC Performance with 'Power Maximisation' - Case 4.

can be associated with the algorithm finding local, rather than global minima. This can be said, since the algorithm is not establishing the fact that a constant setpoint velocity provides higher power capture in this case. One reason for this may be due to the RT MPC algorithm being implemented with the closed-form solution. If so, then better power capture results may be obtained if the approach of solving the QP problem is reinstated. This hypothesis has not yet been investigated, however it is considered that using Hildreth's QP solver with the power maximisation approach could lead to improved power performance, while also maintaining relatively fast execution times.

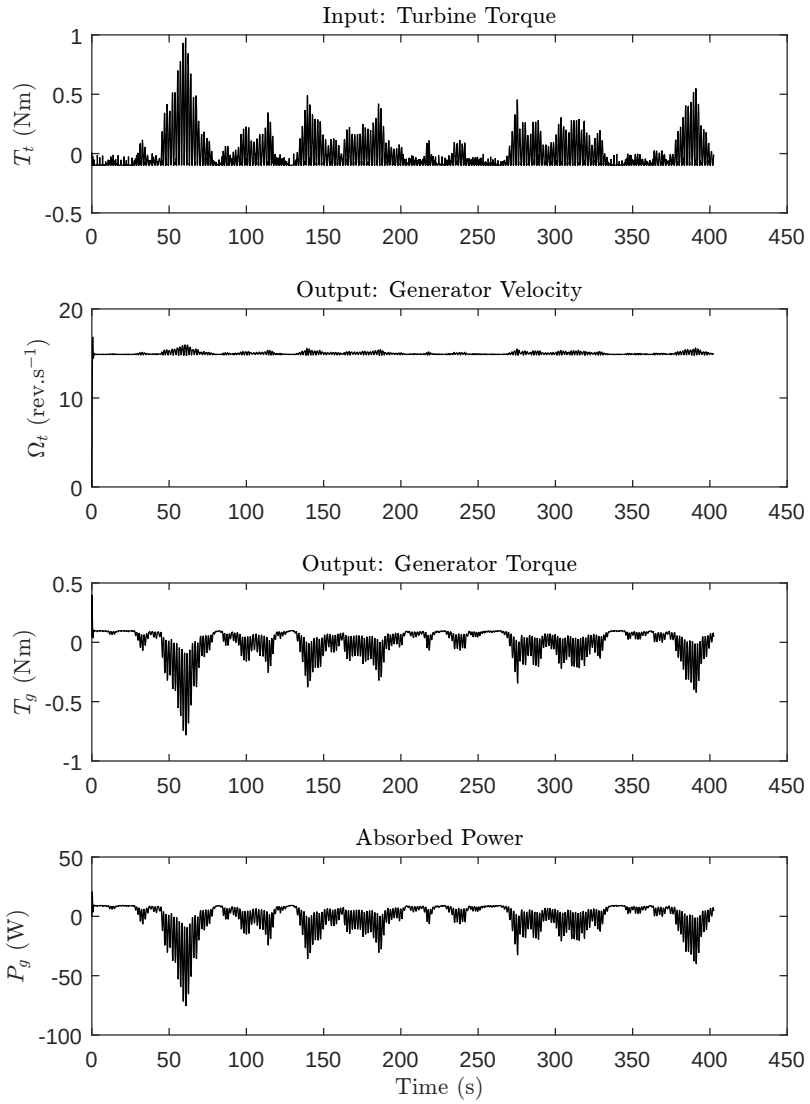

Figure 7.25: RT MPC Performance with 'Setpoint Tracking' - Case 5.

Table 7.5: Parameters used for Optimisation Method Comparison.

Case #	a	N	r_w	N_p	T_t	J	$\bar{P}(W)$
1	0.6	10	1	2	unidirectional	setpoint tracking	-8.0812
3	0.6	10	1	2	unidirectional	power maximisation	-0.2677
4	0.6	10	1	2	bidirectional	power maximisation	-0.1470
5	0.6	10	1	2	bidirectional	setpoint tracking	-0.0980

Chapter 8

Conclusions

8.1 Summary of the Research

The aims of this research have been to devise real-time control algorithms for the WRAM, intended for implementation on sea-going prototypes. In summary, the objectives set for achieving these aims have included: the construction of a new laboratory test facility; derivation of a wave-to-turbine model; development of a controllable PTO plant; formulation of control strategies; and performance assessment of the primary control approach through simulations.

The laboratory test facility is the WRAM emulation platform described in Chapter 5. The platform was designed by the author to be integrated into the existing real-time hybrid test (RTHT) framework at the School of Engineering, Trinity College Dublin. All aspects of the platform design including the mechanical, electrical, instrumentation and software were carried out by the author. The steel blast box, ducting and supporting frame were externally fabricated to the design specifications, with minor weldment adjustments being made on site by the technical team at Trinity College. The technical team also connected the RTHT hydraulic actuator to the blast box. Finally, the electrical and instrumentation subsystems were installed, tested and calibrated by the author.

Performance assessment of the primary control approach depends on a realistic numerical model of the WRAM. This model is also important for implementation of RTHT simulations on the WRAM emulation platform. Therefore the scale of the model was carefully chosen such that the PTO air flows and pressures would be compatible with the platform's driving capabilities. The suitable scale emerged as being twice that of a WRAM tank test model,

recently tested in 2015. The WRAM model used in the advanced control simulations has been decoupled into two broad categories: a wave-to-turbine model; and a turbine-to-wire model. The former includes the fundamental principles of linear wave theory, linear hydrodynamics, air compressibility, and turbomachinery principles. Given that this research is primarily aimed at control, the wave-to-turbine model has been derived from the standard fundamental principles in the literature for spar-buoys with oscillating water columns. The model has been decoupled in this way based on the assumption that variation in the turbine velocity does not significantly affect the WEC absorber's motion in the operating range close to peak turbine efficiency. Note however, that this assumption has not been rigorously investigated here, and should be researched further in the future.

The plant being controlled by the RT MPC algorithm is the turbine-to-wire model. Note that the complete WRAM model was decoupled such that the plant model could take the turbine torque as one of its inputs, thus simplifying the control formulation. As distinct from the wave-to-turbine model, the plant model has been developed as bespoke to include PTO subsystems installed on the WRAM emulator. Namely, these include the electrical generator, turbine dynamics, and low level velocity control loop within the servo-drive. Some of the plant's parameter values were not available at the design stage, which led to the need to estimate them through system identification. To facilitate this, system response experiments were conducted on the coupled turbine-generator, installed on the emulator platform. Once the parameter values were known, a non-minimal state space structure was used to create the final plant model used in the control formulation.

A review of the literature into various prior WEC control algorithms was conducted, specifically investigating: non-causal discrete control; causal reactive control; causal discrete control; model predictive control; and others. From this review, the RT MPC approach in [1] emerged as having potential for controlling the WRAM's PTO. It was an ideal choice since: it easily allows tracking the turbine's velocity, given the optimal setpoint; it naturally incorporates the PTO constraints for rotational velocity and acceleration; and it can execute in real-time. Furthermore, alternative cost functions can be formulated into the optimisation problem.

Once implemented, the RT MPC algorithm was simulated for several control tuning

parameter variations such that the algorithm's performance could be scrutinised. The key areas investigated were: real-time execution of the algorithm; searching for the best compromise of the Laguerre tuning parameters; a sensitivity analysis of the effects that the tuning parameters have on mean power output and closed-loop pole locations of the unconstrained plant; the relative control performance for alternative optimisation cost functions; and general algorithm performance.

8.2 Main Findings

From the literature review, salient points emerged regarding the challenges that need to be addressed for control algorithm implementation on sea-going WECs, with the most important considerations being: to ensure that the algorithm can execute in real-time on standard industrial control systems; to incorporate PTO constraints and efficiencies into the control formulation; and that the control algorithm is a good match for the WEC in question.

As mentioned in Section 8.1, it has been assumed that control of the PTO and the WRAM absorber can be treated independently, based on the operating conditions of the turbine around peak efficiency. While the focus in this research has been placed on controlling the PTO, some assertions have been made on the important features that should be incorporated into the WRAM's absorber control solution, including: phase control between the air flow and pressure should be adopted; non-causal strategies should be avoided; the control strategy should be insensitive to PTO imperfections; and PTO constraints should be included in the control approach. An example of possible implementation details is provided in Section 6.1.1.

A sensitivity study was conducted into the RT MPC algorithm's performance for a range of various control tuning parameters. Firstly, the orthonormality of the tuned Laguerre network was investigated. Of the three Laguerre network tuning parameters, and with the prediction window set to $N_p = 30$, orthonormality of the Laguerre network was found to be higher with small values of the network pole, a, and network order, N.

Next, further simulations were run to ascertain the sensitivity of a, N, the control action tuning parameter, r_w, and N_p, on the closed-loop pole variance and mean power. A strong correlation was found between a and the closed-loop pole variance. For the case where N_p

was held fixed at a high value, it was found that the mean power was somewhat sensitive to N, with very little influence from the other parameters. It is considered that a possible reason for the lack of sensitivity of r_w on the mean power could be due to the fine level of tuning within the internal PI-control loop of the generator's servo-drive. An alternative choice of generator, for example, such as a simple DC brushed motor, without the internal control loop, would possibly increase the influence of r_w on the mean power. However, this is the subject of future research. For the case where r_w was held fixed, and N_p allowed to vary, the mean power was found to be sensitive to N_p and the closed-loop pole variance. The change of mean power sensitivity in the study highlights the challenge in finding the optimal set of all tuning parameters. This is certainly an area where further research is warranted.

Following the sensitivity analysis, specific test cases were focussed on to comparatively assess the performance of the RT MPC control algorithm. The input to the controlled plant was a turbine torque time series simulated from the decoupled WRAM wave-to-turbine model. The inputs to that model were the excitation forces created from a scaled down Bretschneider sea state, representative of what could be expected at the AMETS wave energy test site in Ireland. The two main cases investigated were chosen specifically to demonstrate good (case 1) and bad (case 2) performances, depending on the choice of tuning parameters. Case 1 demonstrated the control algorithm successfully achieving its velocity setpoint tracking objective, rejecting large torque disturbances and staying within the constraint limits. Case 2 demonstrated how poorly chosen control tuning parameters can lead to severely deteriorated control performance. In this case setpoint tracking was not working well, and while the constraints were being satisfied, sharp spikes in the control signal were being introduced. This is particularly bad for higher maintenance costs and risk of device failure. It was found that the mean power in case 1 was about 20% less that in case 2. This reminds us that mean power capture should not be the sole criteria for judging the successful performance of WEC technology.

RT MPC performance was comparatively assessed with two alternative cost functions. The first was structured for applying velocity setpoint tracking to the generator, and the second was designed to directly maximise the generator output power. The setpoint tracking approach performed well at achieving quick minimisation of the error between the output

and setpoint, efficiently rejecting torque disturbance from the turbine. Due to the constant output velocity, the power profile mimicked that of the generator torque profile. Interestingly, the power maximisation approach autonomously established a form of phase control, bringing the generator velocity and torque into phase with each other. It was also noted that power was always unidirectional, which is an advantage for avoiding reactive power flow. In all test cases, the constraints on control amplitude signal and rate of change of control were satisfied without the control system becoming unstable.

Both alternative cost functions were further tested with a bidirectional turbine torque input, where the performance metric was the mean power. It was found that with unidirectional torque, the setpoint tracking approach far outperformed the power maximisation approach. In contrast to the power maximisation approach, setpoint tracking performed much worse with bidirectional torque, capturing near-zero mean power while still experiencing relatively high peak power. Naturally, this is the worst possible scenario, and although the power maximisation approach yielded higher mean power in this case, it still did not experience the large power swings. A significant conclusion from this is that mean power capture is very sensitive the choice of cost function. Therefore, the cost function needs to be selected specifically for each type of PTO, depending on the nature of the input conditions.

Perhaps one of the most striking findings in this research was the RT MPC algorithm's fast execution rates, which ran at a fraction of a millisecond. This finding is indeed a significant contribution to the wave energy community in the field of control engineering. The mean execution time for cases 1 and 2 were 46.09 μs and 36.77 μs respectively, with all other simulation cases having execution times consistently of this order. Note that these speeds were attained on a non-real-time PC running MATLAB®. It can therefore be assumed that the RT MPC algorithm will have no problem executing in real-time on standard industrial controllers, typically installed on sea-going WECs.

The contributions of the research to knowledge in the field can be summarised as follows. Firstly, a novel wave-to-wire model of the WRAM has been developed that encapsulates all of the fundamental physics surrounding the transfer of energy from the waves to the generator winding terminals. Secondly, a novel emulation platform has been designed and built for testing advanced control algorithms within a real-time hybrid test environment.

The entire RTHT rig is unique in the sense that it allows for both bidirectional and irregular air flow with real-time hybrid capabilities. Other similar facilities only contain a subset of these functionalities. Thirdly, the fast MPC approach in [1] has been applied for the first time to a wave energy application, and has performed at the speeds required for the real-time control of PTOs. Finally, sensitivity analysis has shown which RT MPC tuning parameters are most effective for maximising the WRAM's mean power capture.

8.3 Research Questions

As a final step, the research questions from Section 1.3 are addressed. Referring to the research question about what modelling approaches are best suited to the WRAM, it was decided to use reduced order models rather than other simulation methods, such as computational fluid dynamics models, for example. This ensured relative ease with coupling the wide variety of fundamental physics in the power conversion train. Also, the computation time is much quicker and compatibility with the control algorithm was ensured. Regarding the question of which subsystems should be based on established approaches in the literature, it was found that all subsystems in the wave-to-turbine model have been widely studied across a multitude of sources in the literature. While these systems incorporate several simplifying assumptions, the focus of this research was primarily on control, rather than devising new state-of-the-art modelling techniques for WECs. The turbine-to-wire model, on the other hand, has no prior formulations in the literature, since it represents a bespoke combination of industrial components installed on the WRAM emulation platform. Also, several of the parameter values were not available, analytically or from manufacturer data, and hence system identification was required to calculate them.

The literature review provided insight into the research question of what control features should be adopted for the WEC absorber. As presented in Section 8.2, key features include: implementation of phase control between the air flow and pressure; non-causal strategies should be avoided; the control strategy should be insensitive to PTO imperfections; and PTO constraints should be included in the control approach.

Next, the research question about the sea-going challenges for controlling the WRAM's

PTO, and hence what control algorithm to adopt in this research is addressed. The prominent findings were that the fast MPC approach [1] emerged as being an ideal choice for controlling WRAM's PTO due to: its ability to track the turbine's optimal velocity; its ability to handle the PTO constraints of rotational velocity and acceleration; its fast execution; and the ability to incorporate alternative cost functions into the optimisation problem.

With regards to the research question of reducing the financial risk for technology developers, the WRAM emulation platform contributes significantly to this. From a rudimentary point of view, this is achieved through the ability to simply implement and test control algorithms on standard industry equipment, in exactly the same manner as they would be on sea-going WECs. Financial risk is downgraded further, through incorporation of the RTHT system that allows the interaction of simulated WEC dynamics and scaled down PTO equipment, representative of their larger counterparts at sea. Additionally, the RT MPC simulation results in Section 7.4.3 show how poorly chosen tuning parameters can lead to sharp spikes in the control action, thereby increasing the risk of PTO failure. This can be addressed with an in-depth study at the design stage, where parameter tunings that lead to this behaviour could be avoided through careful design.

Lastly, the research question is addressed on how best to split the assignment of subsystems between the WRAM emulation platform and the RTHT simulator. The appropriate division essentially becomes a question of where subsystems are situated with respect to the air chamber's volumetric flow. Clearly, the large structures of the WRAM absorber are impractical to implement in the laboratory. Also, hydrodynamic excitation forces are necessarily implemented in software, unless there is a specific need to physically implement them. This would require wave tank testing, which suffers from large operational costs and difficulty of access due to high demand of the facilities. It can be seen then that real-time hybrid testing offers a cost-effective alternative to tank testing, provided the simplifying assumptions that come with the reduced-order model are acceptable. From Chapter 5, it can be seen that the components required to be simulated on the RTHT simulator include the excitation force generation, WRAM hydrodynamics, air chamber pneumatics and PTO force. The remaining components including the turbine, generator, servo-drive and load-bank, have been chosen for implementation on the emulation platform for two reasons.

Firstly, their nonlinear characteristics are not as easily modelled, and secondly, the laboratory scale PTO equipment can provide a closer match to their large-scale equivalents at sea. The feedback link from the emulation platform to the RTHT simulator is the pressure across the turbine, which is used to calculate the PTO force in the WRAM's equations of motion.

8.4 Recommendations for Further Work

Several opportunities for future research have arisen from the current body of work. The next logical research path with this research is to implement the RT MPC algorithm on the WRAM emulator platform's cRIO. Also, the part of the WRAM model that encapsulates conversion from the waves to the volumetric air flow would need to be implemented on the RTHT system. This work would validate that the RT MPC algorithm can work on industrial control systems. An extension to this would be implementing the RT MPC algorithm on industry standard programmable logic controllers, however additional control hardware would need to be procured.

From the bidirectional torque analysis, it is clear that the power maximisation optimisation method was converging to a local, rather than global optimal solution. The exact cause of this unknown at present, however one thought is that it may be related to the use of the closed-form control method in Section 3.2.6. As a starting point for future research, it may be beneficial to revert back to solving the QP problem. The rationale here is that including more future samples in the control horizon may lead to better convergence towards the global optimum. It is expected that using Hildreth's algorithm for solving the QP problem may give the desired real-time execution speed, however this needs to be investigated.

From the sensitivity analysis, it wasn't clear why the mean power was insensitive to the cost function's control action parameter, r_w. It is suspected that this is due to the fine tuning of the PI-control loop in the servo-drive. This PI-control loop turns out to be quite restrictive in the sense that generator is not fully controllable by the RT MPC algorithm alone. Unfortunately, the current servo-generator design does not allow the generator to be used without the servo-drive, nor can the PI-control loop be disabled. Further design and specification work is required to make this change possible, however if this is done, then

the increased freedom of RT MPC parameter variation may enable increased optimisation of the overall control system.

Another area that could benefit from future research with the emulator platform, is to replace the PTO generator with alternative types. This could be complemented with additional power electronics and artificial grids, such that control algorithms could be studied in the context of grid connection and power quality issues.

A key concept in this research has been to decouple the WRAM's absorber and PTO models. The reason for this was to facilitate the RT MPC algorithm being used to directly control the turbine's velocity. The approach was justified on the basis that variations in the velocity, close to the turbine's optimal efficiency, would not significantly affect the absorber's motion. This assumption could be eliminated if the absorber and PTO were fully coupled. The effect that the PTO has on the absorber would then be more accurately determined across the full range of the turbine's operating conditions.

Upon completion of the fully coupled absorber and PTO model, another interesting research area would be to investigate the potential of using robust MPC for the absorber control for the WRAM. When controlling the absorber, it is likely that the control variable would be the air chamber pressure, which is oscillatory in nature. As such, the Laguerre functions may not be the best choice for the orthonormal basis function set. Alternatives may include Kautz or half range Chebyshev functions, mentioned in Section 3.2.7, where the focus of the research could be to combine the alternative function sets with the principles outlined in [1].

The closed-form implementation of the RT MPC algorithm used in this research has the advantage of being very fast, however it is limited in the following ways: the number of constraints can be restrictively low; constraints can only be applied at the next instant within the control horizon; and only one variable can be controlled. These limitations can be alleviated by solving the QP problem, however this is where the heavy computational burden arises. Further research into speeding up the QP problem, through a combination of Hildreth's algorithm and implementation on field-programmable-gate-array (FPGA) technology could result in dramatic time savings. As an approximate guide, computation time steps of the RT MPC algorithm on the cRIO's FPGA unit might be expected to be in the order of hundreds of nanoseconds.

8.5 Concluding Remarks

The first aim of this thesis has been to address the issue of optimising the PTO efficiency of the WRAM wave energy converter, using real-time optimal predictive control. To adequately represent the WRAM numerically, a wave-to-wire model was developed such that a fast MPC algorithm, found in the literature, could be applied to the PTO. Investigation of the real-time MPC algorithm's performance and tunability showed that the algorithm could successfully perform its design goal, while executing at speeds suitable for real-time implementation at sea. In addition to development of the PTO control algorithm, broad suggestions have been established for controlling the WEC's absorber, taking into account findings from the literature on key challenges for sea-going WECs.

The second aim of the thesis has been to bridge the gap between theory and practice by the establishing a WRAM emulation platform, where control algorithms can be tested and evaluated in real-time before being implemented on sea-going prototypes. The emulation platform has been designed and commissioned, and is now ready for the implementation of newly developed control algorithms.

Through the above mentioned work the research objectives have been completed and new research avenues have been identified, both in the context of WRAM and otherwise. This research has successfully addressed some key issues related to controlling the WRAM, and contributed to knowledge in the field, however the achievements here only scratch the surface of the many challenges faced for wave energy generally. There is a wide gap in the research for the holistic optimisation of wave energy converters, that includes both technical and financial models. Future research in this regard would overwhelmingly benefit the wave energy community if, for example, optimisation cost functions were structured around technology and finance. Guideline business models and best practices could be established, potentially helping to curtail the reoccurring problem of startup wave energy companies hitting the commercial viability wall.

Appendix A

WRAM Emulation Platform Mechanical Design

The following diagrams show the mechanical assembly drawings for the WRAM emulation platform, designed for manufacture at a local steel fabricator, BA Steel Fabrication Ltd in Dublin 7. The individual part drawings are omitted. On completion, the technician team in the Department of Civil, Structural and Environmental Engineering, Trinity College Dublin provided additional assembly and fabrication services.

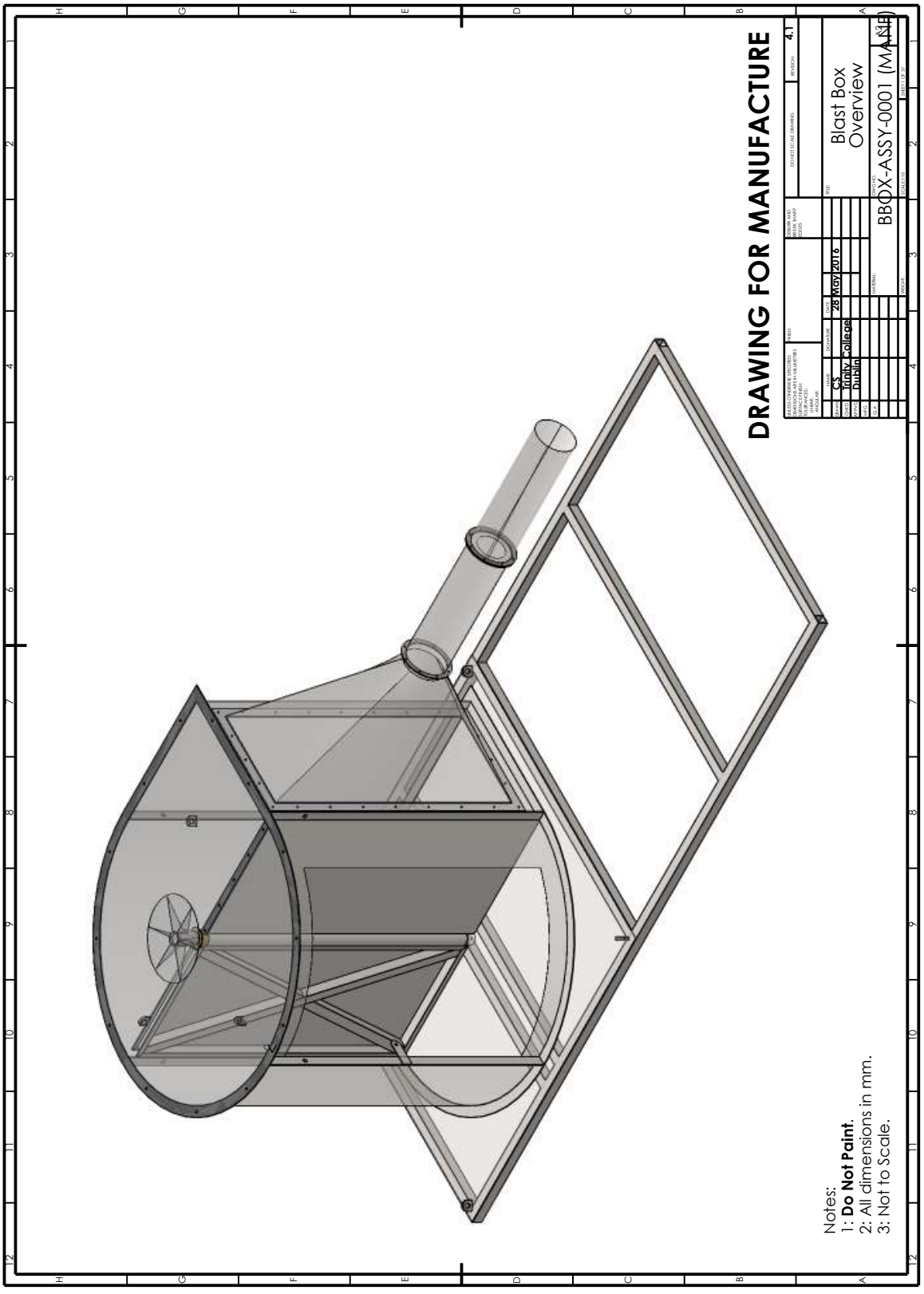
DRAWING FOR MANUFACTURE
Blast Box Overview
BBOX-ASSY-0001 (MAIN)
4.1
Notes:
1: **Do Not Paint**.
2: All dimensions in mm.
3: Not to Scale.

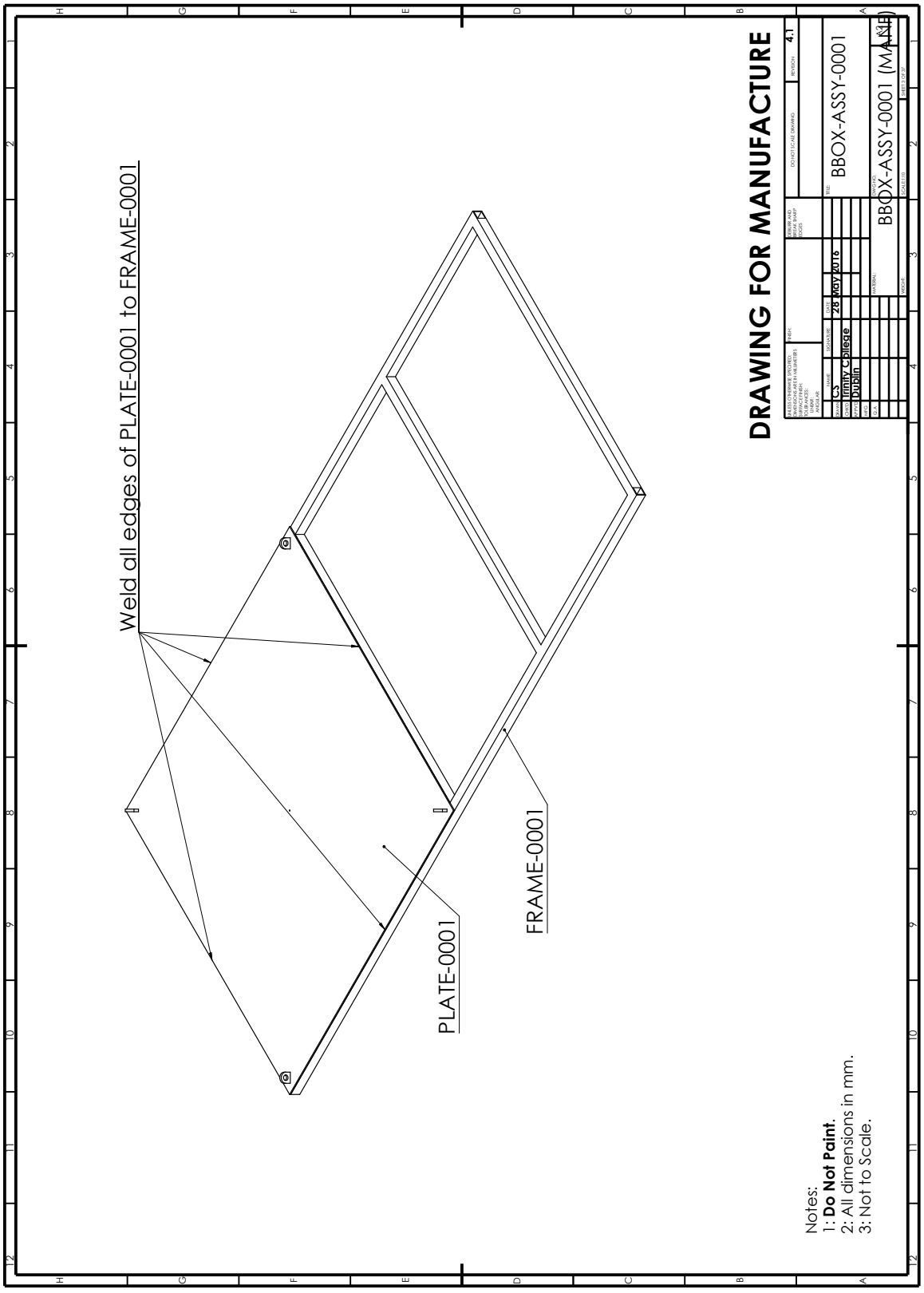
Weld all edges of PLATE-0001 to FRAME-0001
PLATE-0001
FRAME-0001
DRAWING FOR MANUFACTURE
4.1
BBOX-ASSY-0001
BBOX-ASSY-0001 (MAIN)
CS
Trinity College
Dublin
28 May 2016
Notes:
1: **Do Not Paint**.
2: All dimensions in mm.
3: Not to Scale.

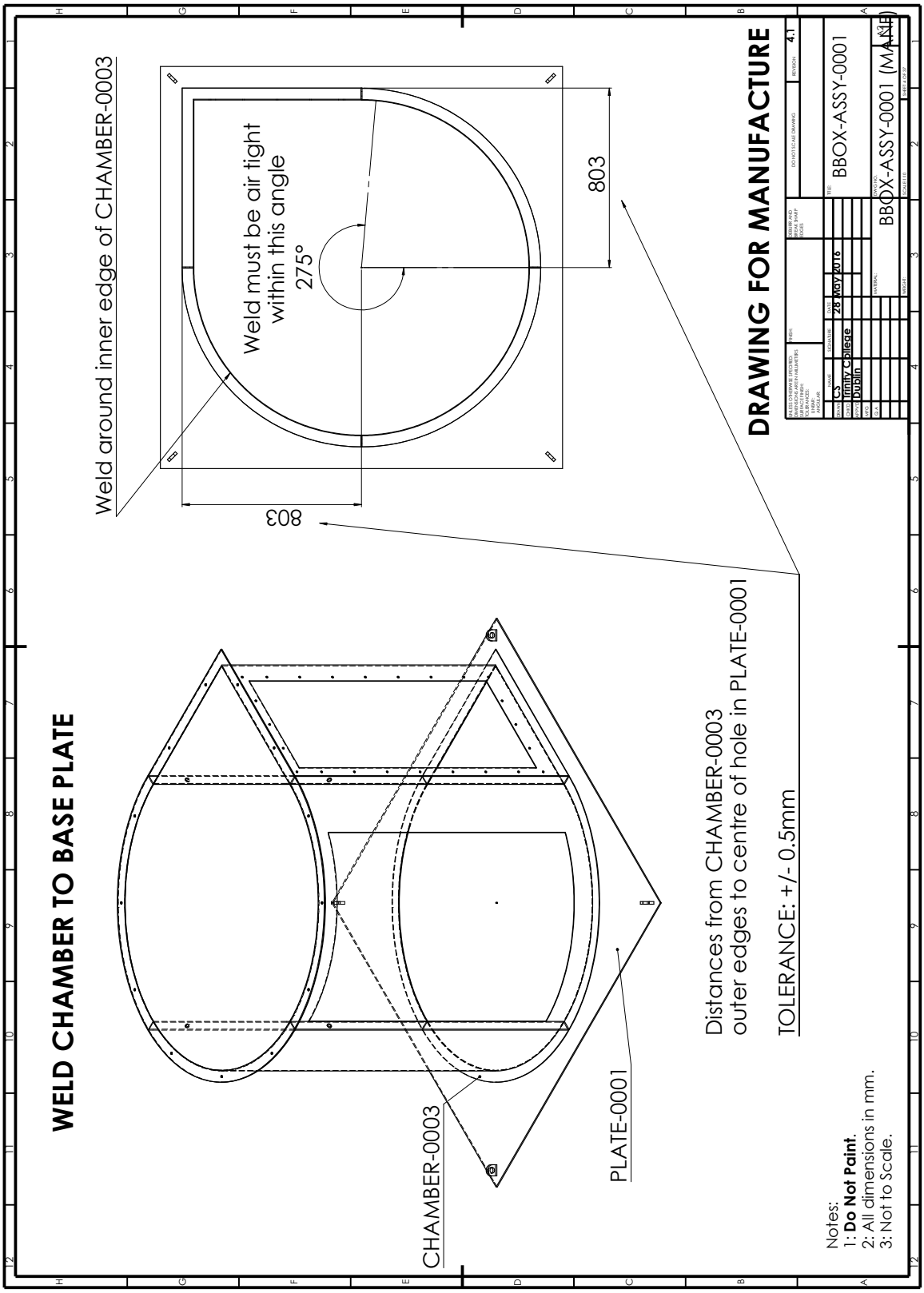
WELD CHAMBER TO BASE PLATE
DRAWING FOR MANUFACTURE
Weld around inner edge of CHAMBER-0003
Weld must be air tight
within this angle
275°
803
803
Distances from CHAMBER-0003
outer edges to centre of hole in PLATE-0001
TOLERANCE: +/- 0.5mm
CHAMBER-0003
PLATE-0001
Notes:
1: Do Not Paint.
2: All dimensions in mm.
3: Not to Scale.
DO NOT SCALE DRAWING
4.1
BBOX-ASSY-0001
BBOX-ASSY-0001 (MAIN)
CS
Trinity College
Dublin
28 May 2016

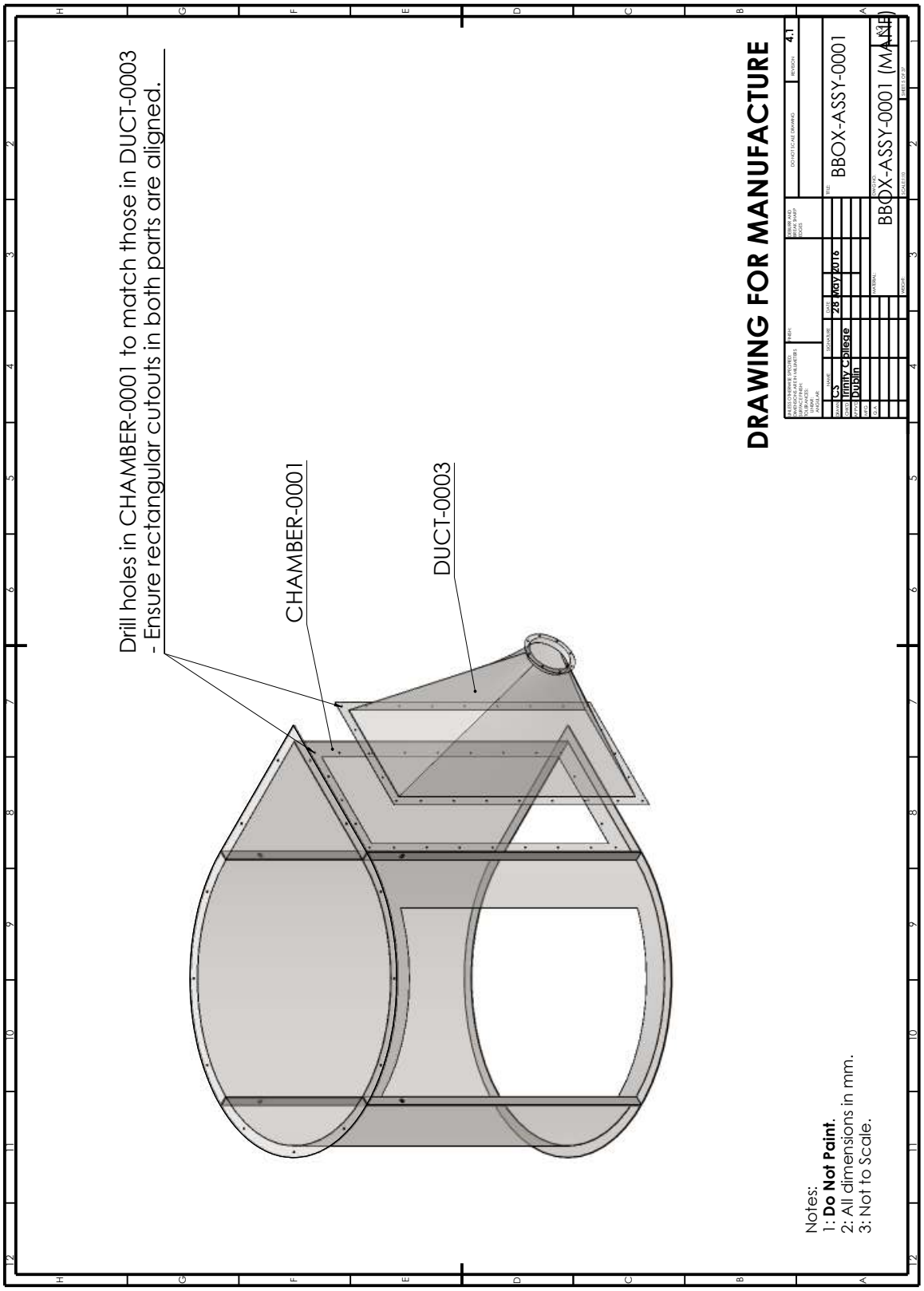
Drill holes in CHAMBER-0001 to match those in DUCT-0003
- Ensure rectangular cutouts in both parts are aligned.
CHAMBER-0001
DUCT-0003
DRAWING FOR MANUFACTURE
4.1
BBOX-ASSY-0001
BBOX-ASSY-0001 (MAIN)
CS
Trinity College
Dublin
28 May 2016
Notes:
1: Do Not Paint.
2: All dimensions in mm.
3: Not to Scale.

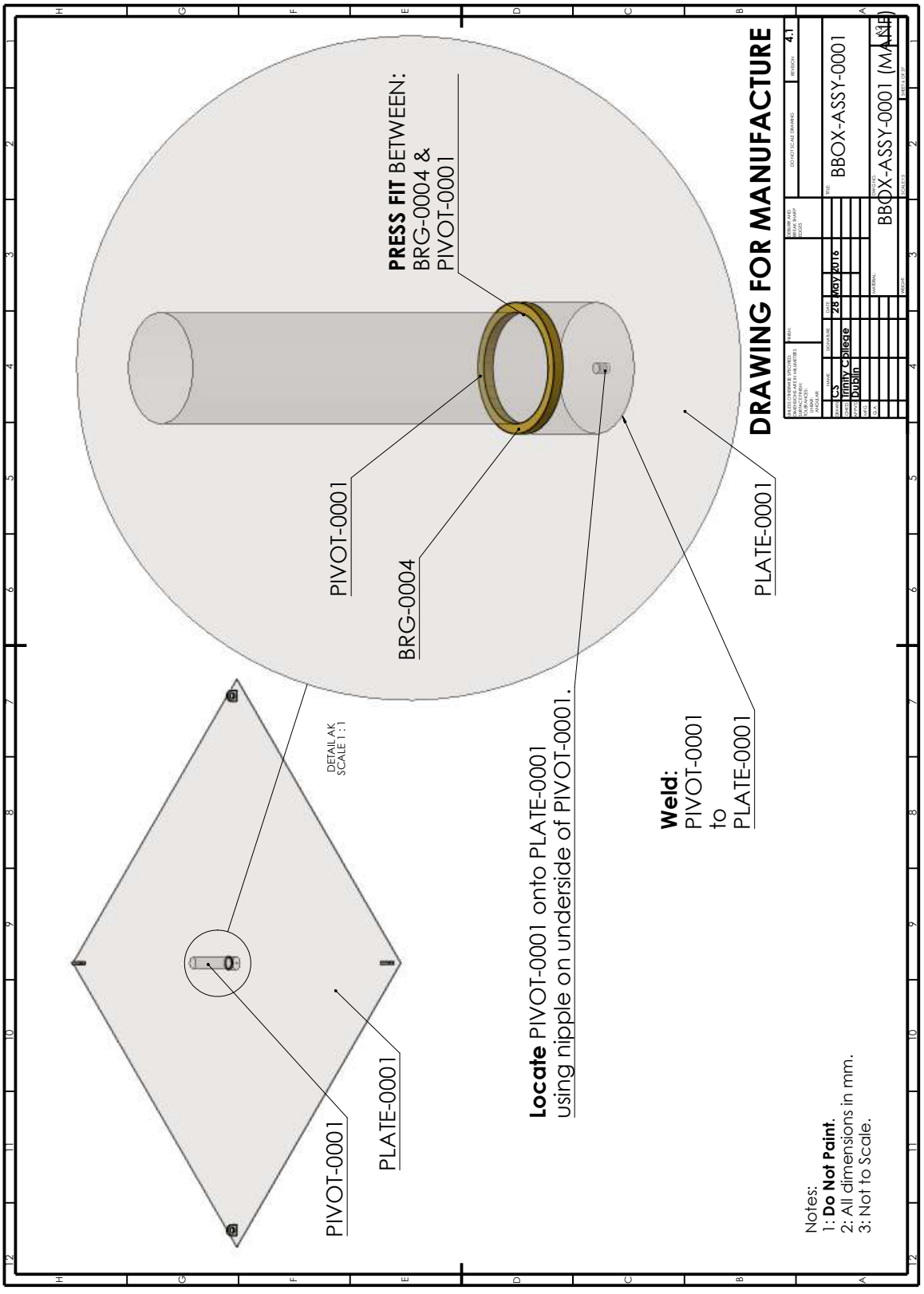
DRAWING FOR MANUFACTURE
PRESS FIT BETWEEN:
BRG-0004 &
PIVOT-0001
PIVOT-0001
BRG-0004
PLATE-0001
Locate PIVOT-0001 onto PLATE-0001
using nipple on underside of PIVOT-0001.
Weld:
PIVOT-0001
to
PLATE-0001
DETAIL AK
SCALE 1 : 1
PIVOT-0001
PLATE-0001
Notes:
1: Do Not Paint.
2: All dimensions in mm.
3: Not to Scale.
DO NOT SCALE DRAWING
BBOX-ASSY-0001
BBOX-ASSY-0001 (MAIN)
CS
Trinity College
Dublin
28 May 2016

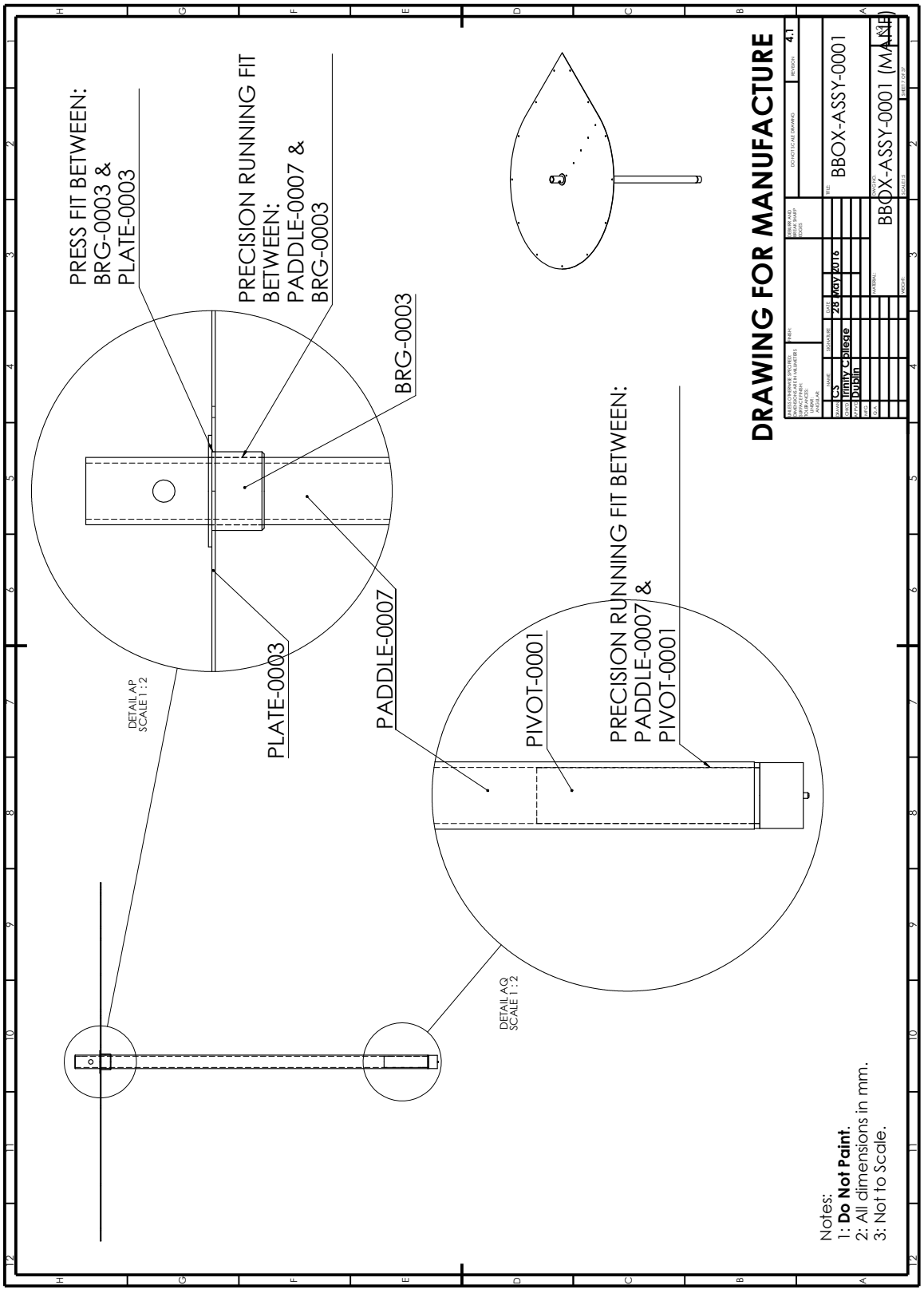
PRESS FIT BETWEEN:
BRG-0003 &
PLATE-0003
PRECISION RUNNING FIT
BETWEEN:
PADDLE-0007 &
BRG-0003
BRG-0003
PLATE-0003
PADDLE-0007
PIVOT-0001
PRECISION RUNNING FIT BETWEEN:
PADDLE-0007 &
PIVOT-0001
DETAIL AP
SCALE 1 : 2
DETAIL AQ
SCALE 1 : 2
DRAWING FOR MANUFACTURE
BBOX-ASSY-0001
BBOX-ASSY-0001 (MAIN)
Notes:
1: Do Not Paint.
2: All dimensions in mm.
3: Not to Scale.

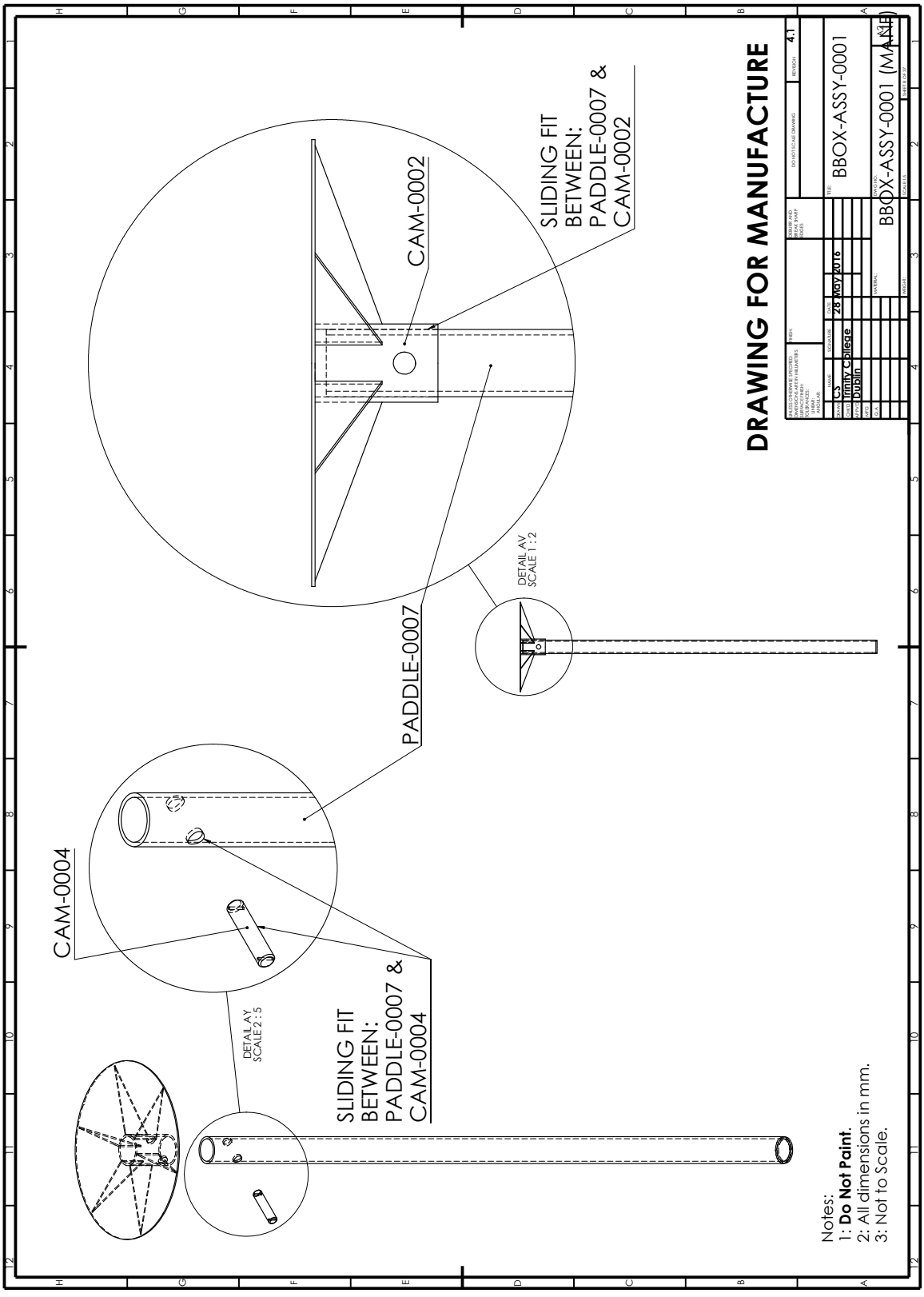
DRAWING FOR MANUFACTURE
BBOX-ASSY-0001
BBOX-ASSY-0001 (MAIN)
CAM-0002
SLIDING FIT BETWEEN: PADDLE-0007 & CAM-0002
PADDLE-0007
DETAIL A Y SCALE 1 : 2
CAM-0004
SLIDING FIT BETWEEN: PADDLE-0007 & CAM-0004
DETAIL A Y SCALE 2 : 5
Notes:
1: **Do Not Paint**.
2: All dimensions in mm.
3: Not to Scale.

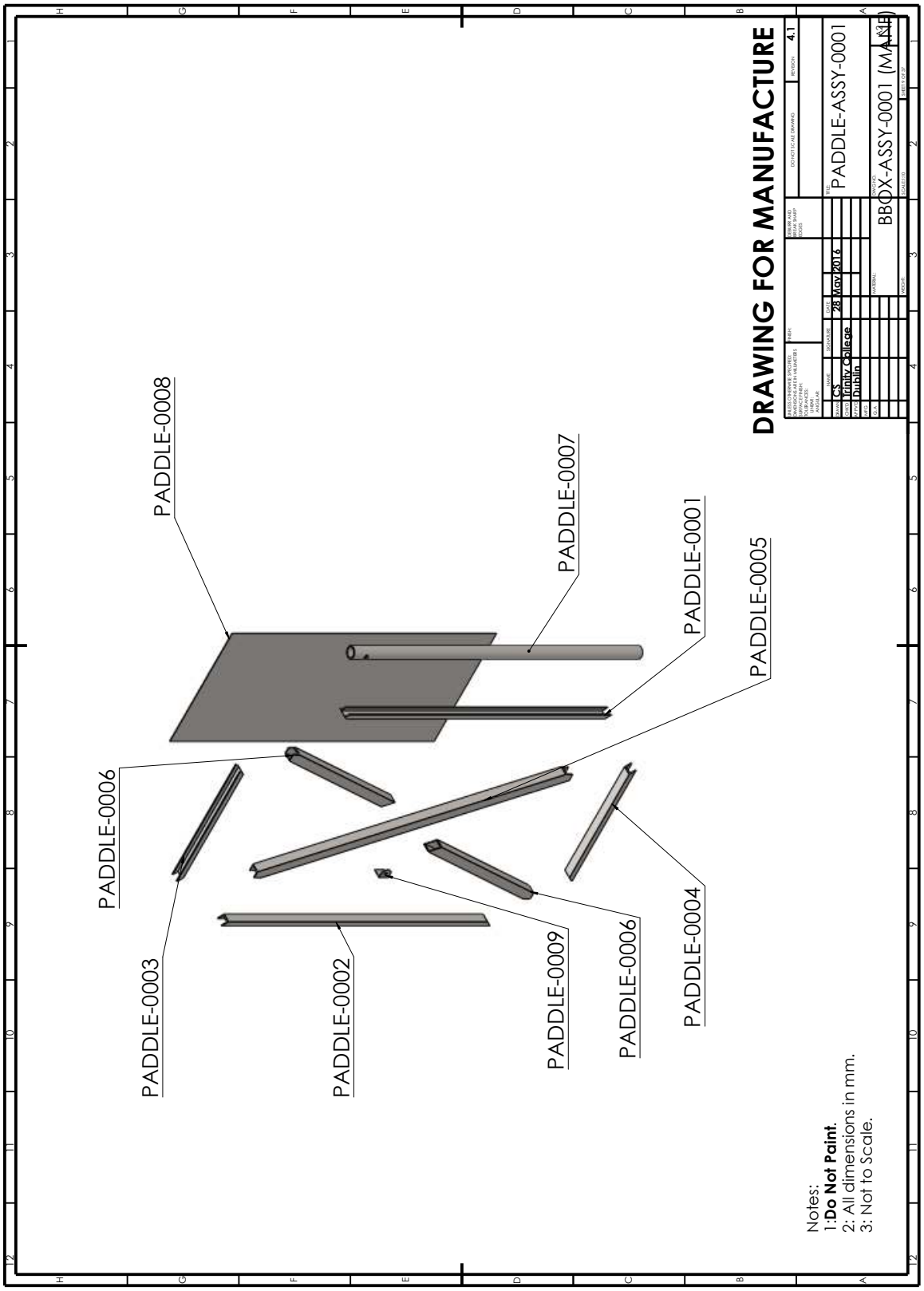
PADDLE-0008
PADDLE-0007
PADDLE-0001
PADDLE-0005
PADDLE-0006
PADDLE-0003
PADDLE-0002
PADDLE-0009
PADDLE-0006
PADDLE-0004
DRAWING FOR MANUFACTURE
4.1
PADDLE-ASSY-0001
BBOX-ASSY-0001 (MAIN)
CS
Trinity College
Dublin
28 May 2016
Notes:
1:**Do Not Paint**.
2: All dimensions in mm.
3: Not to Scale.

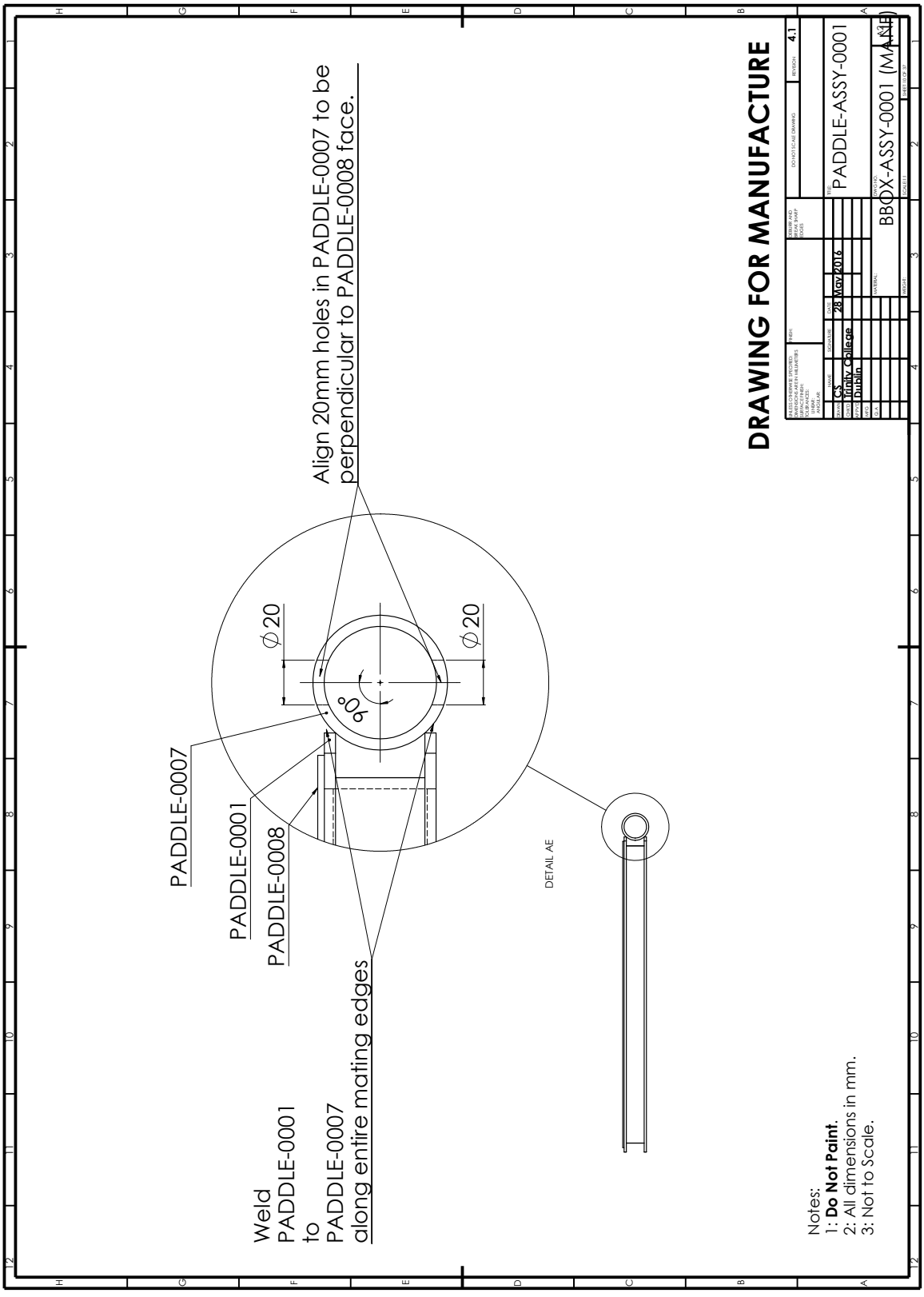
DRAWING FOR MANUFACTURE
DO NOT SCALE DRAWING
BBOX-ASSY-0001 (MAIN)
PADDLE-ASSY-0001
CS
Trinity College Dublin
28 May 2016
4.11
Align 20mm holes in PADDLE-0007 to be perpendicular to PADDLE-0008 face.
PADDLE-0007
PADDLE-0001
PADDLE-0008
Weld PADDLE-0001 to PADDLE-0007 along entire mating edges
Ø20
Ø20
90°
DETAIL AE
Notes:
1: **Do Not Paint**.
2: All dimensions in mm.
3: Not to Scale.

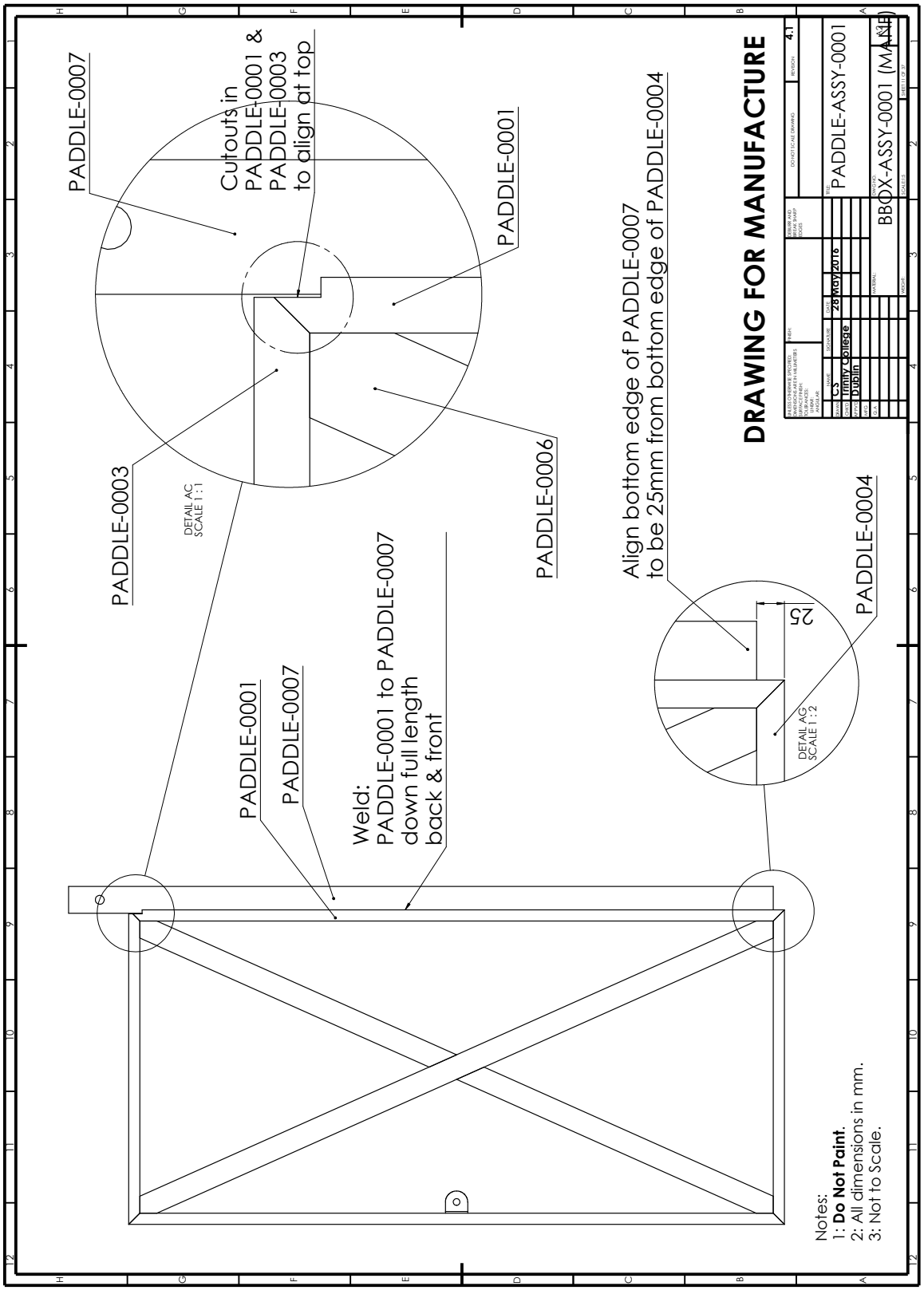
PADDLE-0007
Cutouts in PADDLE-0001 & PADDLE-0003 to align at top
PADDLE-0001
PADDLE-0003
DETAIL AC SCALE 1 : 1
PADDLE-0006
Align bottom edge of PADDLE-0007 to be 25mm from bottom edge of PADDLE-0004
PADDLE-0001
PADDLE-0007
Weld: PADDLE-0001 to PADDLE-0007 down full length back & front
25
PADDLE-0004
DETAIL AG SCALE 1 : 2
DRAWING FOR MANUFACTURE
4.1
PADDLE-ASSY-0001
BBOX-ASSY-0001 (MAIN)
Notes:
1: **Do Not Paint.**
2: All dimensions in mm.
3: Not to Scale.

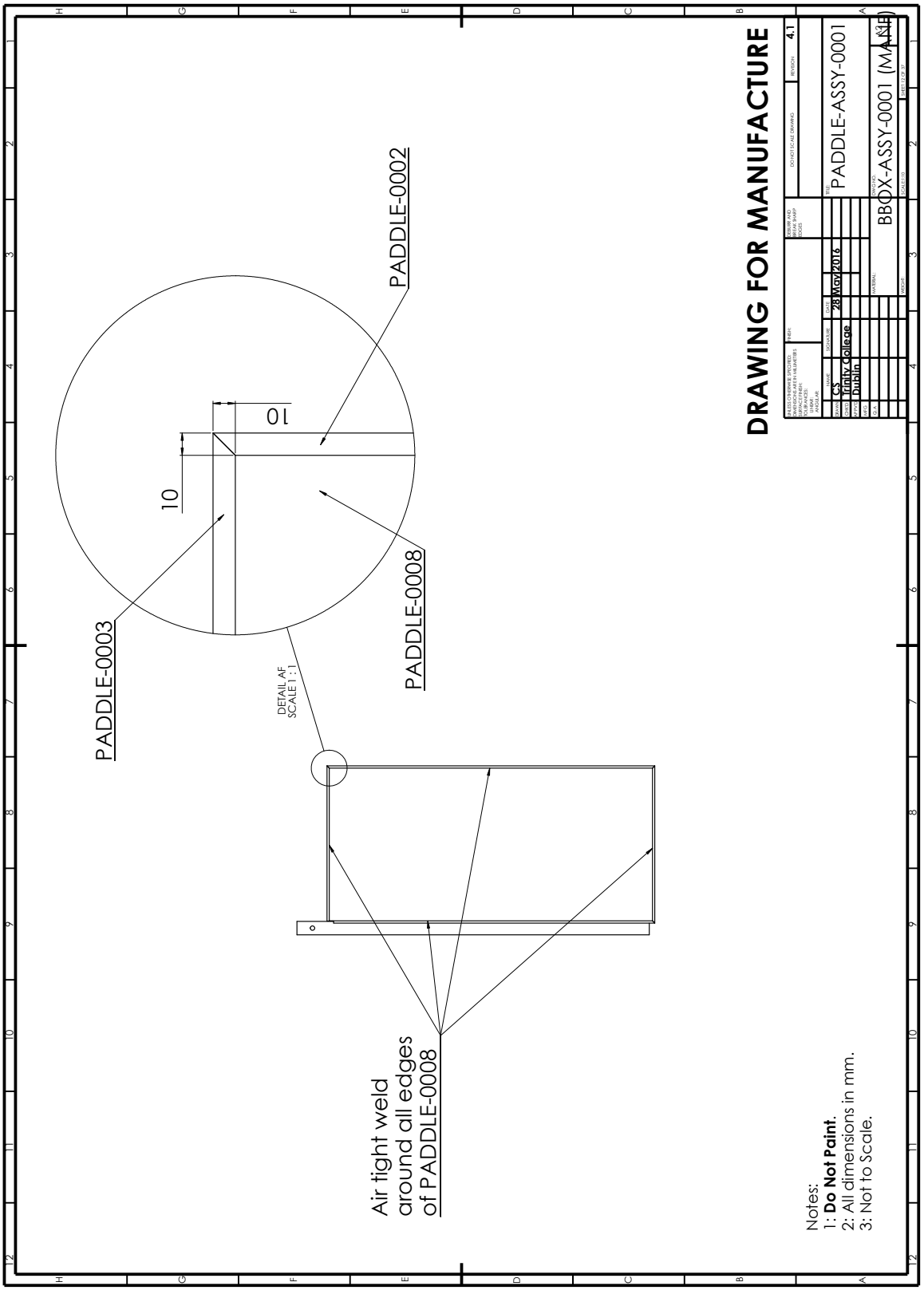
DRAWING FOR MANUFACTURE
PADDLE-0002
PADDLE-0003
PADDLE-0008
10
10
DETAIL AF
SCALE 1 : 1
Air tight weld
around all edges
of PADDLE-0008
Notes:
1: Do Not Paint.
2: All dimensions in mm.
3: Not to Scale.
PADDLE-ASSY-0001
BBOX-ASSY-0001 (MAIN)
CS
Trinity College
Dublin
28 May 2016

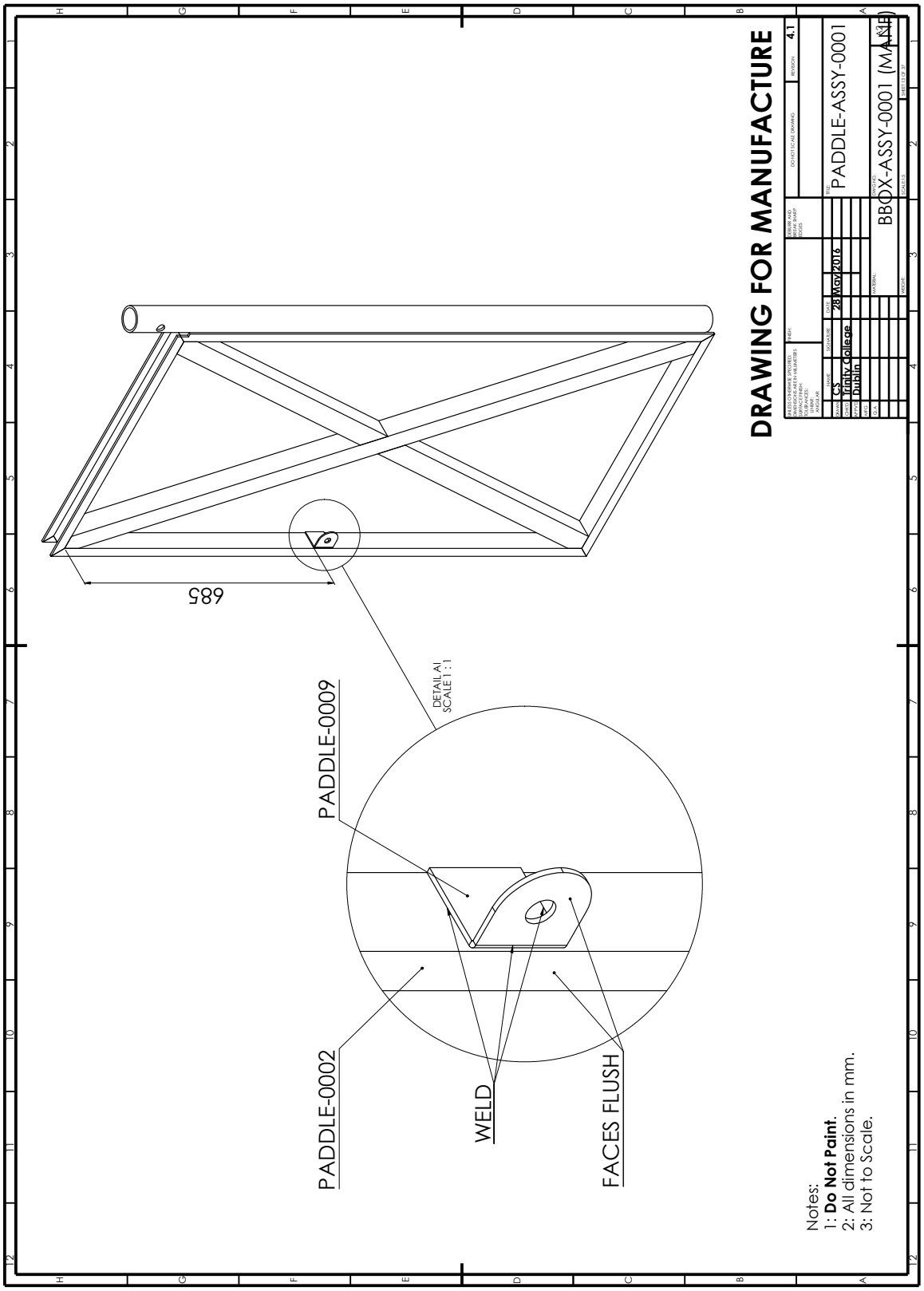
DRAWING FOR MANUFACTURE
4.1
PADDLE-ASSY-0001
BBOX-ASSY-0001 (MAIN)
CS
Trinity College
Dublin
28 May 2016
685
DETAIL A1
SCALE 1 : 1
PADDLE-0009
PADDLE-0002
WELD
FACES FLUSH
Notes:
1: Do Not Paint.
2: All dimensions in mm.
3: Not to Scale.

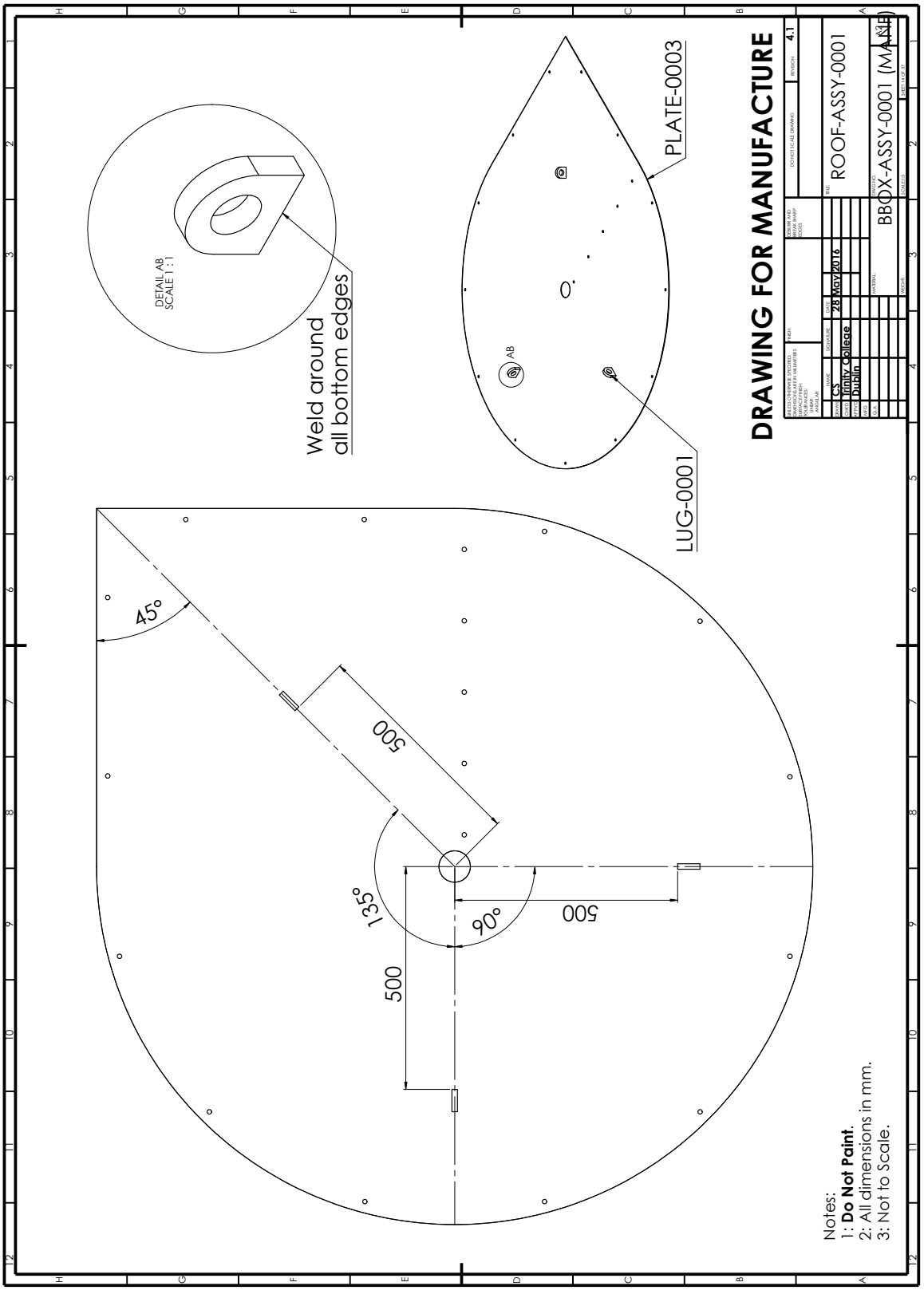
DRAWING FOR MANUFACTURE
DO NOT SCALE DRAWING
REMOVE ANY SHARP EDGES
ROOF-ASSY-0001
BBOX-ASSY-0001 (MAIN)
PLATE-0003
LUG-0001
Weld around all bottom edges
DETAIL AB SCALE 1 : 1
AB
45°
500
135°
90°
500
500
Notes:
1: Do Not Paint.
2: All dimensions in mm.
3: Not to Scale.

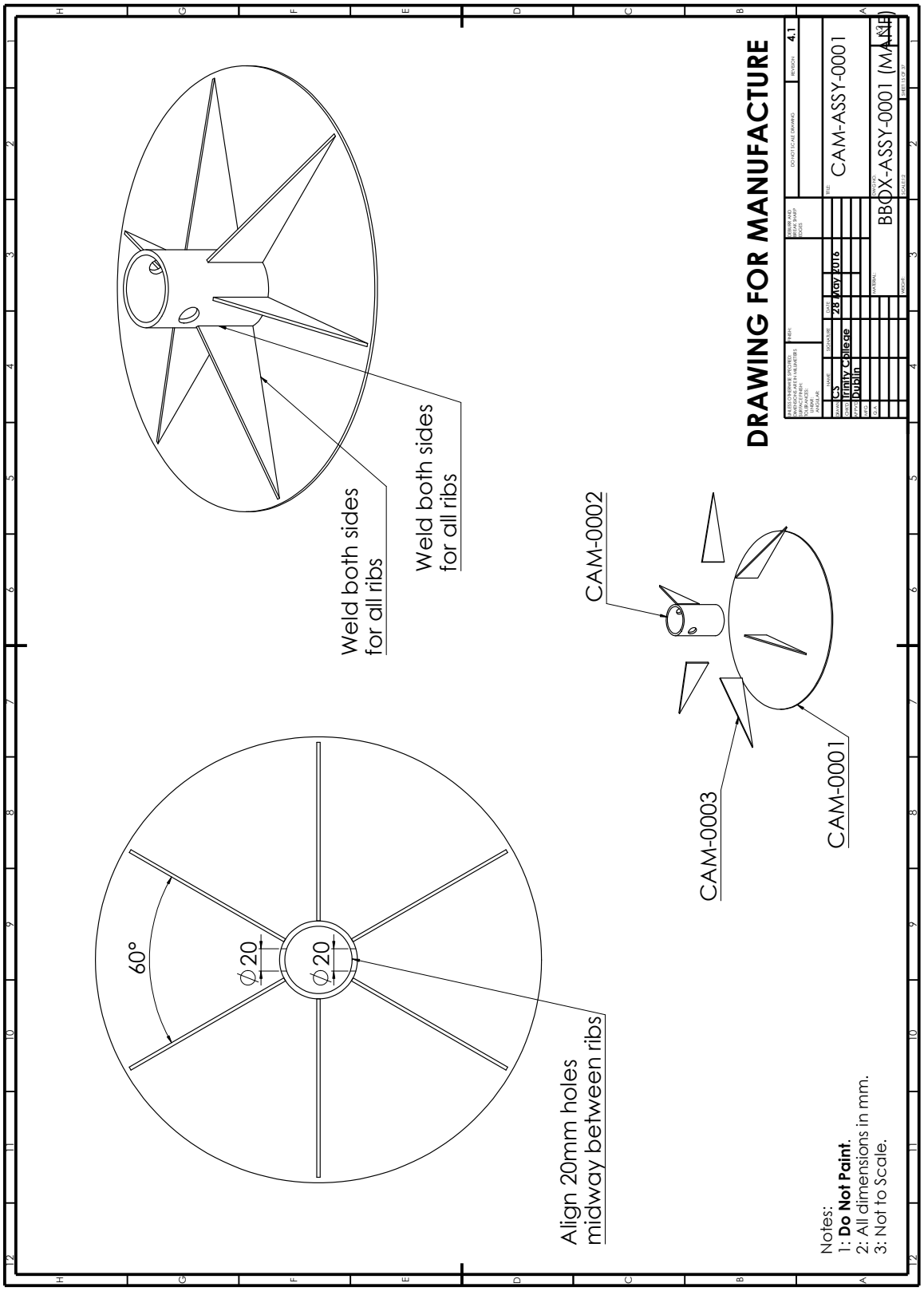
DRAWING FOR MANUFACTURE
Weld both sides for all ribs
Weld both sides for all ribs
CAM-0002
CAM-0003
CAM-0001
60°
⌀20
⌀20
Align 20mm holes midway between ribs
Notes:
1: **Do Not Paint**.
2: All dimensions in mm.
3: Not to Scale.
CAM-ASSY-0001
BBOX-ASSY-0001 (MAIN)
Trinity College
Dublin
28 May 2016
CS

Appendix B

WRAM Emulation Platform Electrical Design

The following diagrams show the electrical circuit schematics for the WRAM emulation platform, including the power distribution, generator and servo-drive, loadbank and instrumentation interfaces. All design, assembly and testing of the electrical systems were conducted by the author.

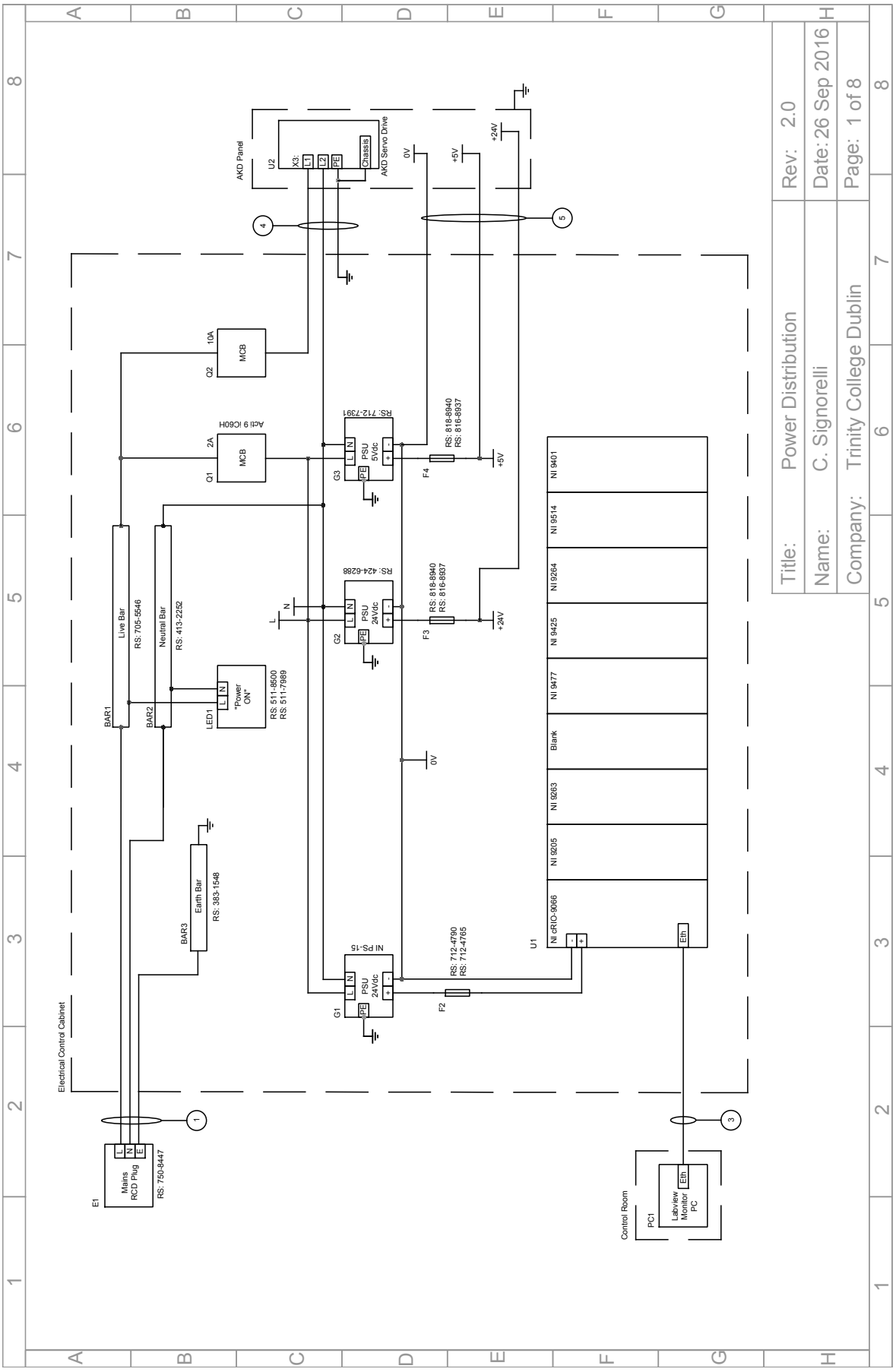
Title: Power Distribution
Name: C. Signorelli
Company: Trinity College Dublin
Rev: 2.0
Date: 26 Sep 2016
Page: 1 of 8
Electrical Control Cabinet
Control Room
AKD Panel
AKD Servo Drive
Chassis
PE
0V
+5V
+24V
Q2 MCB 10A
Q1 MCB 2A
Acti 9 iC60H
G3 PSU 5Vdc RS: 712-7391
G2 PSU 24Vdc RS: 424-6288
G1 PSU 24Vdc NI PS-15
RS: 818-8940
RS: 816-8937
F4
F3
F2
BAR1 Live Bar RS: 705-5546
BAR2 Neutral Bar RS: 413-2252
BAR3 Earth Bar RS: 383-1548
LED1 "Power ON" RS: 511-8500 RS: 511-7989
E1 Mains RCD Plug RS: 750-8447
U1 NI cRIO-9066
NI 9205
NI 9263
Blank
NI 9477
NI 9425
NI 9264
NI 9514
NI 9401
Eth
PC1 Labview Monitor PC

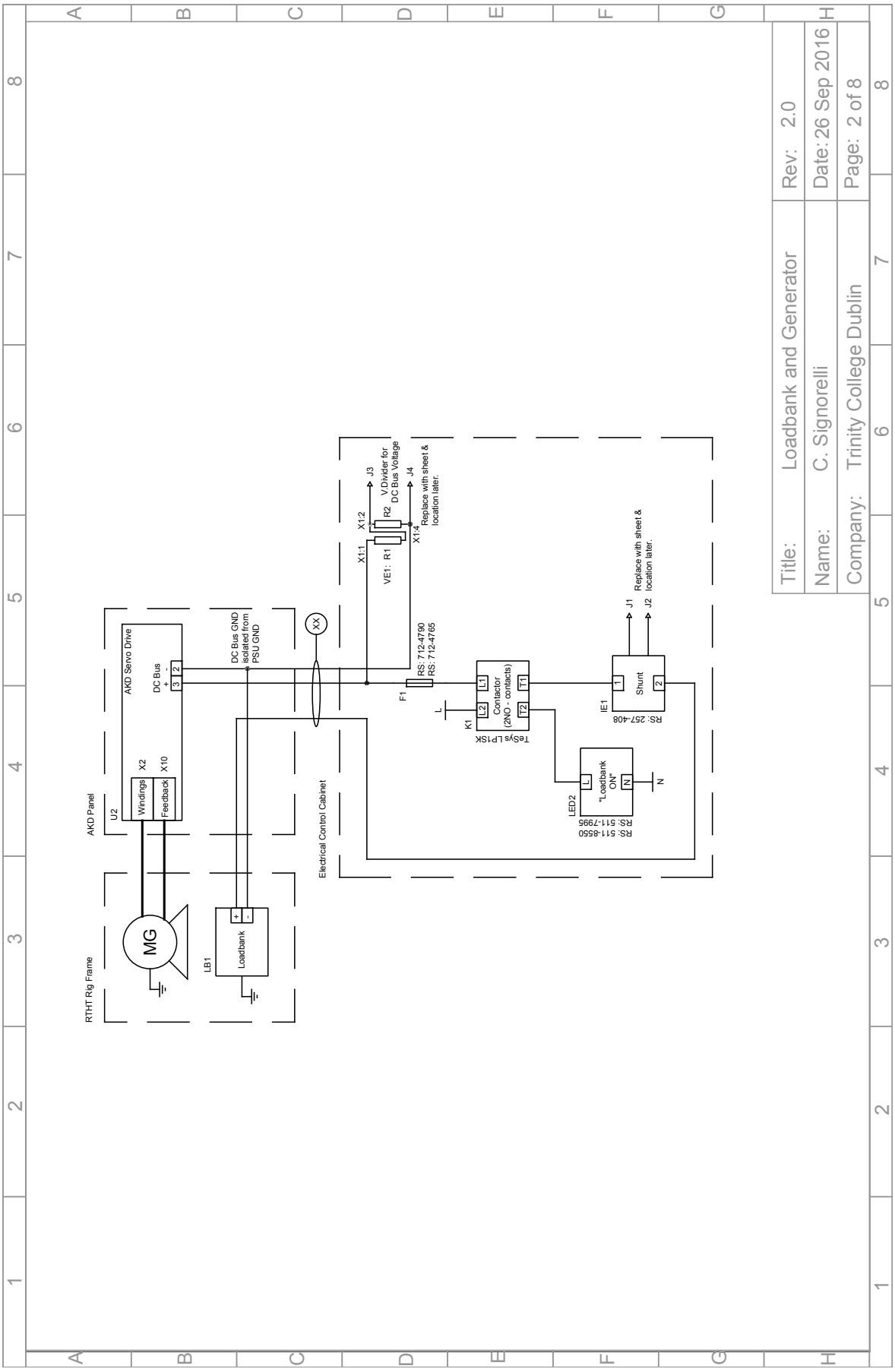
Title: Loadbank and Generator
Rev: 2.0
Name: C. Signorelli
Date: 26 Sep 2016
Company: Trinity College Dublin
Page: 2 of 8
RTHT Rig Frame
MG
AKD Panel
U2
AKD Servo Drive
Windings
X2
Feedback
X10
DC Bus
+
-
3
2
LB1
Loadbank
DC Bus GND isolated from PSU GND
XX
Electrical Control Cabinet
X1:1
X1:2
VE1: R1
J3
R2
V.Divider for DC Bus Voltage
J4
X1:4
Replace with sheet & location later.
RS: 712-4790
RS: 712-4765
F1
L
K1
L1
L2
T1
T2
Contactor (2NO - contacts)
TeSys LP1SK
LED2
"Loadbank ON"
RS: 511-8550
RS: 511-7995
N
IE1
1
Shunt
2
RS: 257-408
J1
J2
Replace with sheet & location later.

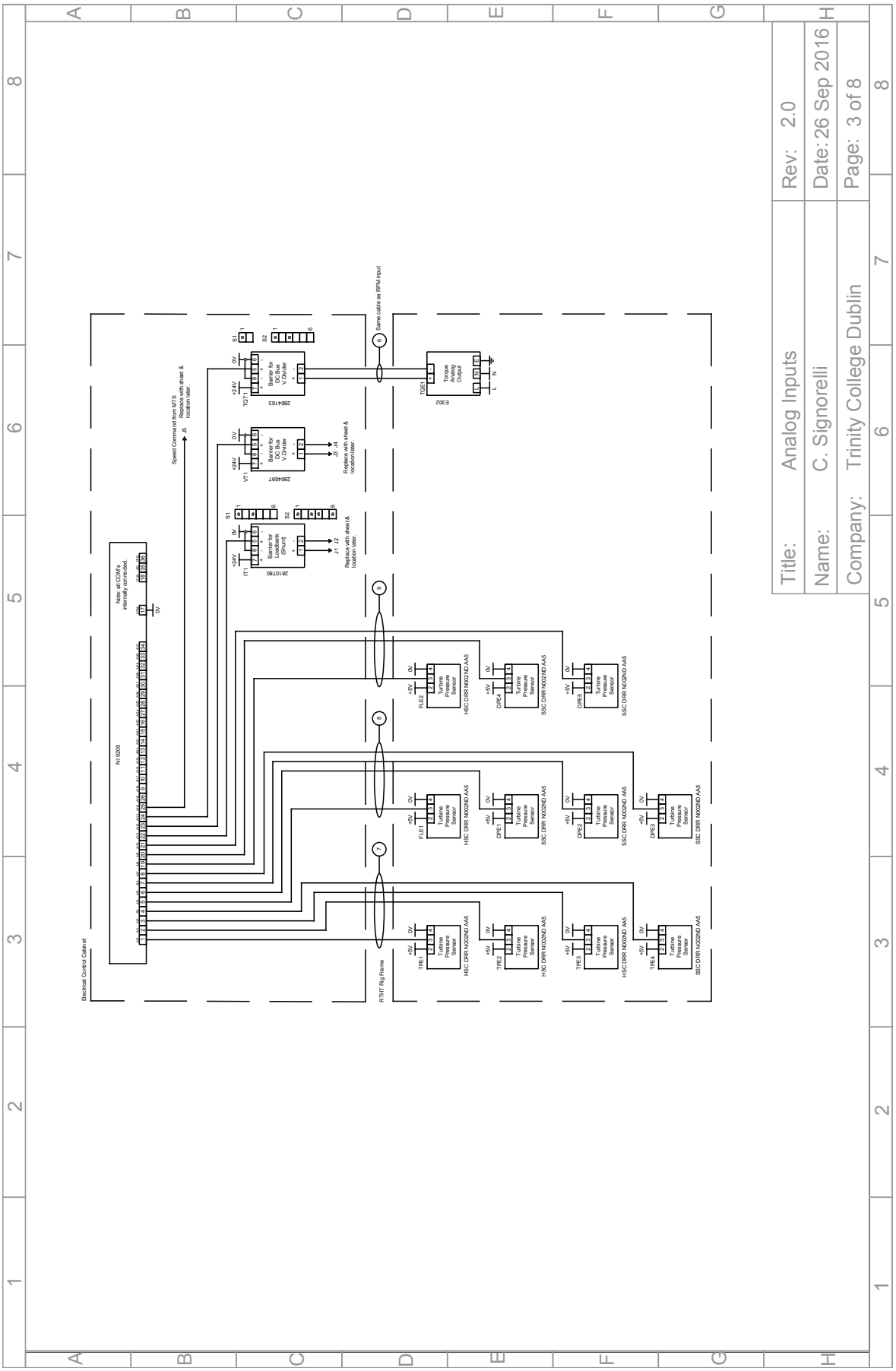
Title: Analog Inputs
Rev: 2.0
Name: C. Signorelli
Date: 26 Sep 2016
Company: Trinity College Dublin
Page: 3 of 8
Electrical Control Cabinet
R1hT Rig Frame
NI 9205
Note: all COM's internally connected.
Speed Command from MTS
Replace with sheet & location later.
Same cable as RPM input
Replace with sheet & location later.
Barrier Ex DC Bus V.Divider
Barrier Ex Loadbank (Shunt)
Torque Analog Output
Turbine Pressure Sensor
HSC DRR NX02ND AA5
SSC DRR NX02ND AA5

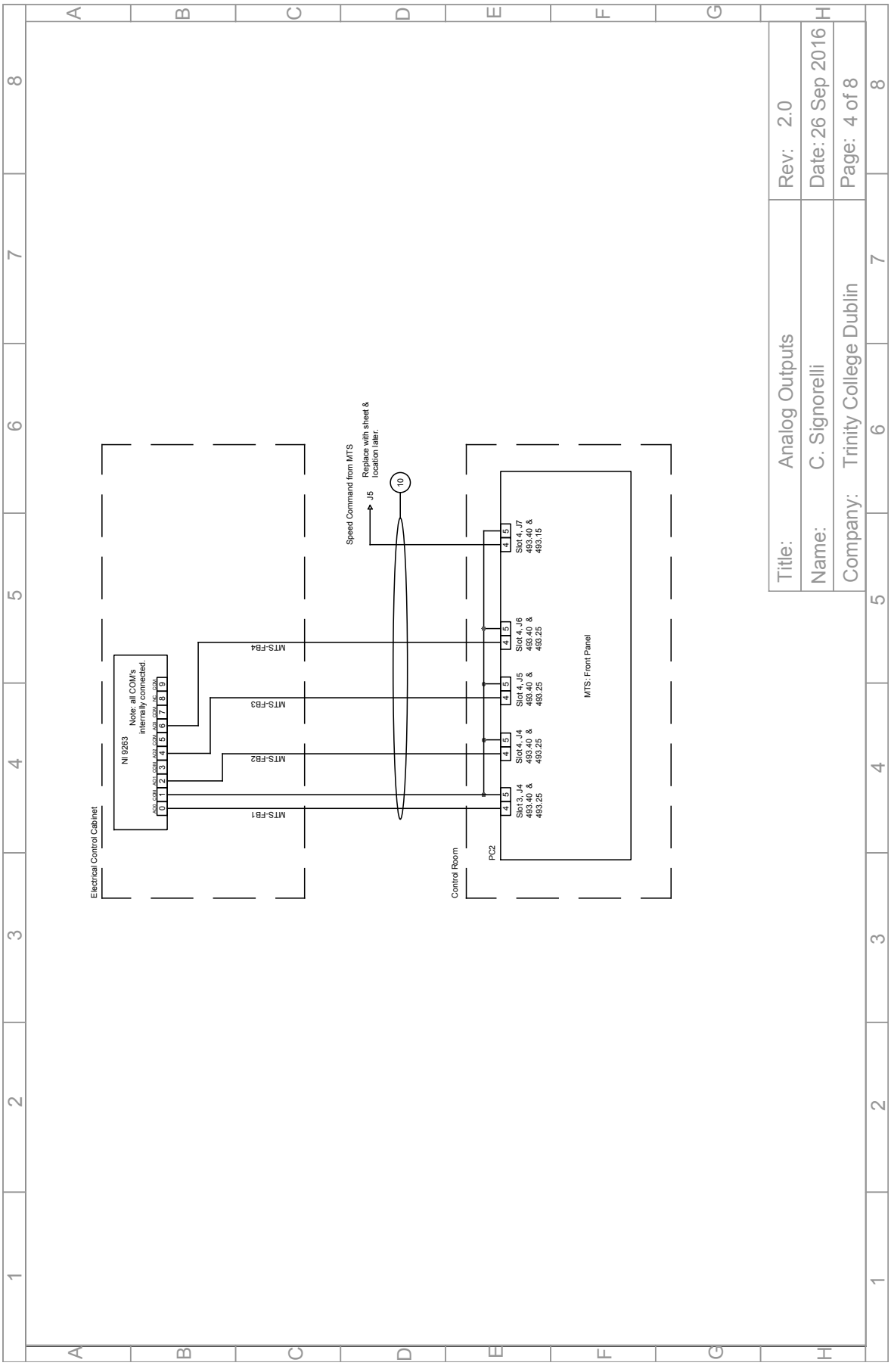
Electrical Control Cabinet
NI 9263
Note: all COM's internally connected.
AO0 +COM AO1 +COM AO2 +COM AO3 +COM
0 1 2 3 4 5 6 7 8 9
MTS-FB1
MTS-FB2
MTS-FB3
MTS-FB4
Speed Command from MTS
Replace with sheet & location later.
J5
10
Control Room
PC2
Slot3, J4 493.40 & 493.25
Slot 4, J4 493.40 & 493.25
Slot 4, J5 493.40 & 493.25
Slot 4, J6 493.40 & 493.25
Slot 4, J7 493.40 & 493.15
MTS: Front Panel
Title: Analog Outputs
Name: C. Signorelli
Company: Trinity College Dublin
Rev: 2.0
Date: 26 Sep 2016
Page: 4 of 8

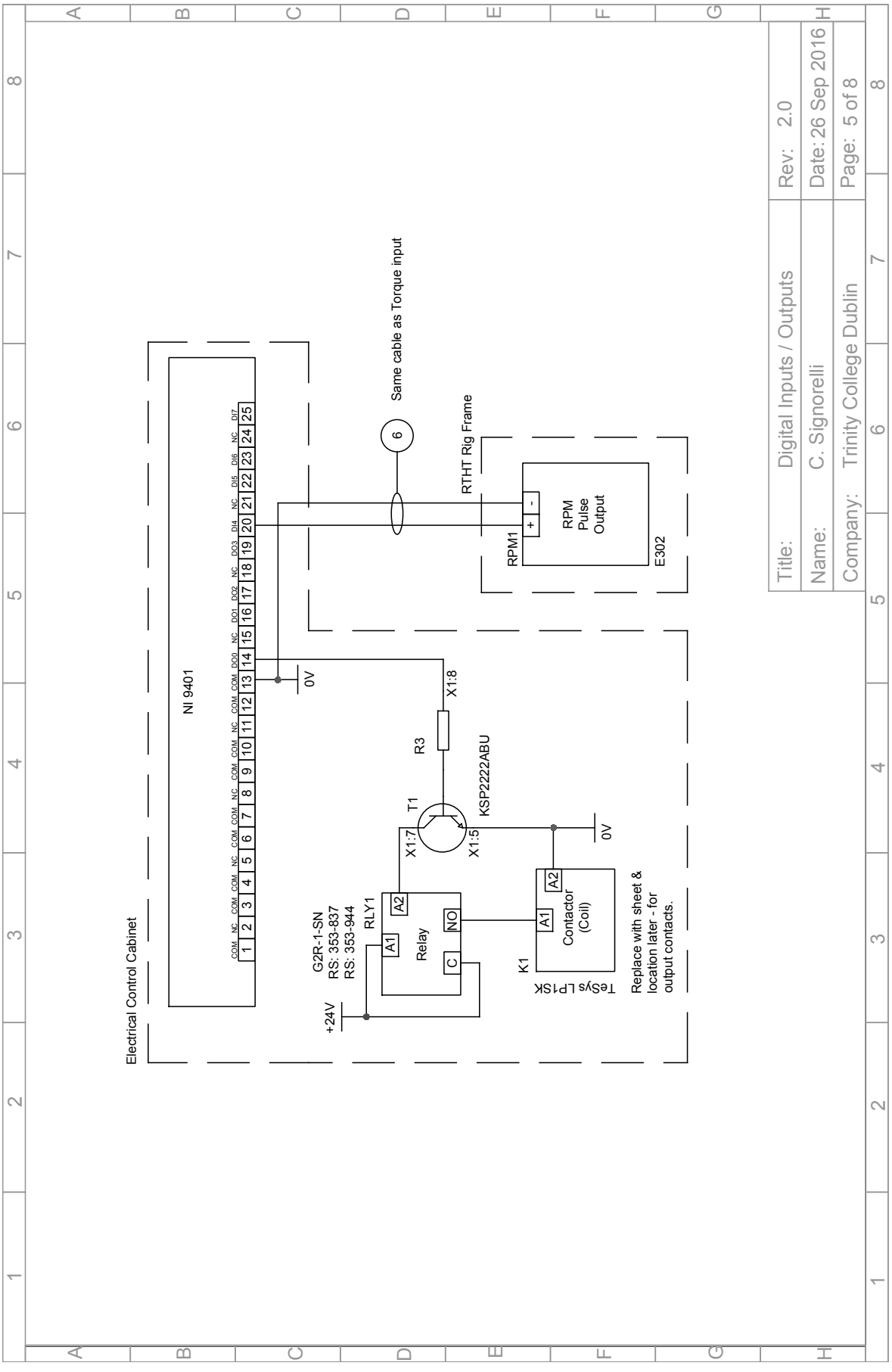
Electrical Control Cabinet
NI 9401
COM NC COM COM NC COM COM COM NC COM COM COM NC COM NC NC DO1 DO2 NC DO3 DI4 NC DI5 DI6 NC DI7
1 2 3 4 5 6 7 8 9 10 11 12 13 14 15 16 17 18 19 20 21 22 23 24 25
0V
X1:8
R3
KSP2222ABU
T1
X1:7
X1:5
0V
+24V
G2R-1-SN
RS: 353-837
RS: 353-944
RLY1
A1
A2
Relay
C
NO
K1
A1
A2
Contactor
(Coil)
TeSys LP1SK
Replace with sheet &
location later - for
output contacts.
Same cable as Torque input
6
RTHT Rig Frame
RPM1
+
-
RPM
Pulse
Output
E302
Title: Digital Inputs / Outputs
Rev: 2.0
Name: C. Signorelli
Date: 26 Sep 2016
Company: Trinity College Dublin
Page: 5 of 8

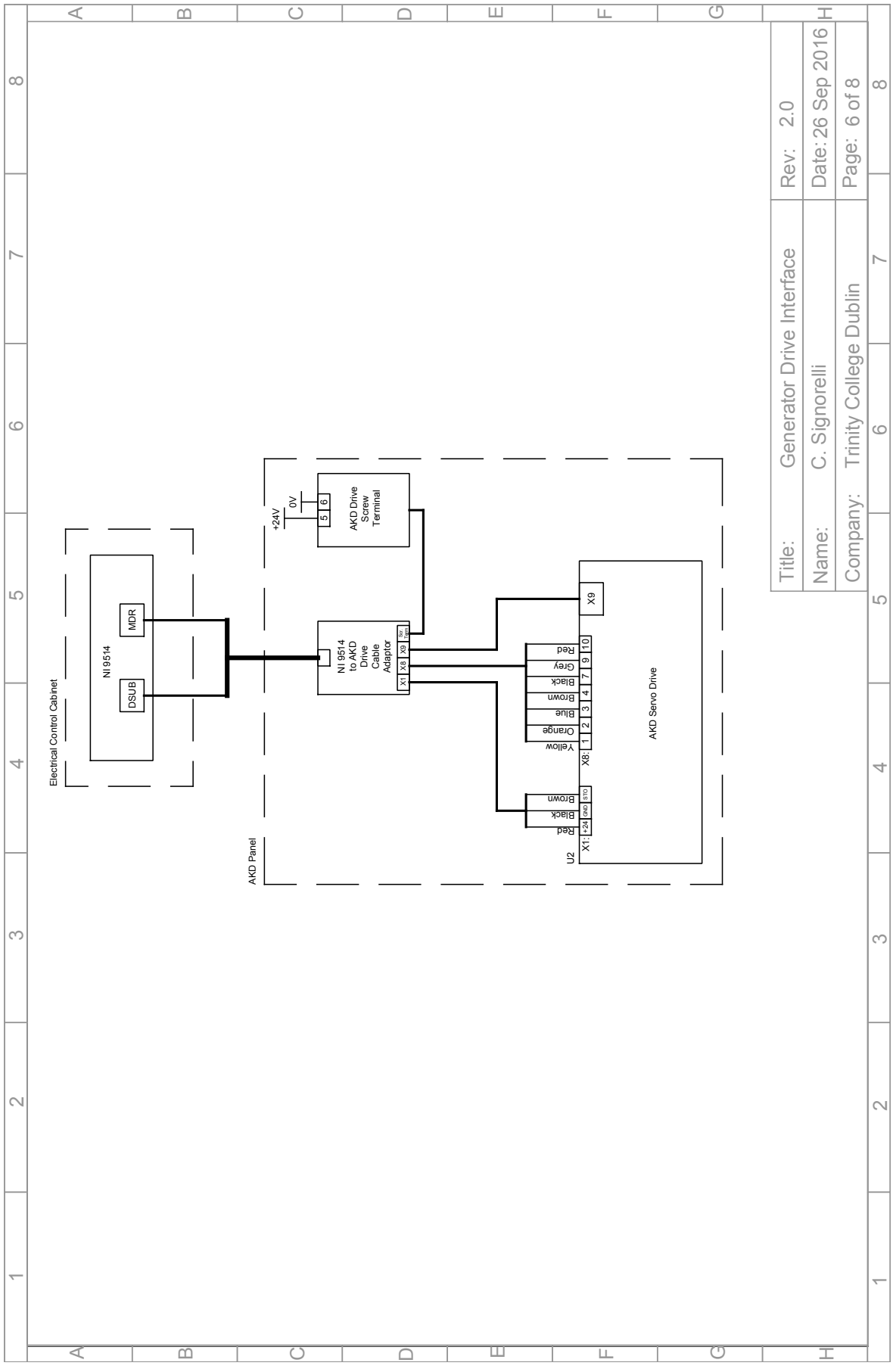
Title: Generator Drive Interface
Name: C. Signorelli
Company: Trinity College Dublin
Rev: 2.0
Date: 26 Sep 2016
Page: 6 of 8
Electrical Control Cabinet
NI 9514
MDR
DSUB
AKD Panel
+24V
0V
5
6
AKD Drive Screw Terminal
NI 9514 to AKD Drive Cable Adaptor
X1
X8
X9
X9
X8:
1
2
3
4
7
9
10
Yellow
Orange
Blue
Brown
Black
Grey
Red
X1:
+24
GND
STO
Red
Black
Brown
U2
AKD Servo Drive

Bibliography

[1] L. Wang, *Model predictive control system design and implementation using MATLAB®*. London, UK, Springer Science & Business Media, 2009.

[2] J. Falnes and P. Lillebekken, "Budal's latching-controlled-buoy type wave-power plant", in *Proc. of the 5th European Wave Energy Conf.*, Cork, Ireland, 2003.

[3] J. Falnes, "Optimum control of oscillation of wave-energy converters", *International Journal of Offshore and Polar Engineering*, vol. 12, no. 2, Jun. 2002.

[4] R. E. Hoskin, B. M. Count, N. K. Nichols, and D. A. C. Nicol, "Phase control for the oscillating water column", in *Hydrodynamics of Ocean Wave-Energy Utilization: Proc. of the IUTAM Symposium Lisbon/Portugal*, D. V. Evans and A. F. O. de Falcão, Eds. Berlin, Heidelberg: Springer Berlin Heidelberg, 1986, pp. 257–268.

[5] A. Babarit and A. H. Clément, "Optimal latching control of a wave energy device in regular and irregular waves", *Applied Ocean Research*, vol. 28, no. 2, pp. 77–91, Apr. 2006.

[6] A. Babarit, M. Guglielmi, and A. H. Clément, "Declutching control of a wave energy converter", *Ocean Engineering*, vol. 36, no. 12, pp. 1015–1024, Sep. 2009.

[7] J. C. C. Henriques, L. M. C. Gato, A. F. O. Falcão, E. Robles, and F. X. Faÿ, "Latching control of a floating oscillating-water-column wave energy converter", *Renewable Energy*, vol. 90, pp. 229–241, May 2016.

[8] A. Babarit and A. H. Clément, "Application of the optimal command method to the control of the SEAREV wave energy converter: A study on the influence of time constants on the efficiency of the latching control", in *Proc. of the 2009 European Control Conference, (ECC)*, Budapest, Hungary, Aug. 2009, pp. 3737–3742.

[9] S. R. Nielsen, Q. Zhou, M. M. Kramer, B. Basu, and Z. Zhang, "Optimal control of nonlinear wave energy point converters", *Ocean Engineering*, vol. 72, pp. 176–187, Nov. 2013.

[10] F. Fusco and J. V. Ringwood, "A simple and effective real-time controller for wave energy converters", *IEEE Transactions on Sustainable Energy*, vol. 4, no. 1, pp. 21–30, Jan. 2013.

[11] E. Tedeschi, M. Carraro, M. Molinas, and P. Mattavelli, "Effect of control strategies and power take-off efficiency on the power capture from sea waves", *IEEE Transactions on Energy Conversion*, vol. 26, no. 4, pp. 1088–1098, Dec. 2011.

[12] F. Fusco and J. Ringwood, "Suboptimal causal reactive control of wave energy converters using a second order system model", in *Proc. of the 21st (2011) International Offshore and Polar Engineering Conf.*, Maui, Hawaii, USA: International Society of Offshore and Polar Engineers (ISOPE), Jun. 2011, pp. 687–694.

[13] B. Guo, R. Patton, M. Abdelrahman, and J. Lan, "A continuous control approach to point absorber wave energy conversion", in *Proc. of the 2016 UKACC 11th International Conf. Control (CONTROL)*, Belfast, UK, Aug. 2016, pp. 1–6.

[14] A. F. O. Falcão and J. C. C. Henriques, "Effect of non-ideal power take-off efficiency on performance of single- and two-body reactively controlled wave energy converters", *Journal of Ocean Engineering and Marine Energy*, vol. 1, no. 3, pp. 273–286, Aug. 2015.

[15] R. Genest, F. Bonnefoy, A. H. Clément, and A. Babarit, "Effect of non-ideal power take-off on the energy absorption of a reactively controlled one degree of freedom wave energy converter", *Applied Ocean Research*, vol. 48, pp. 236–243, Oct. 2014.

[16] W. Sheng, R. Alcorn, and A. Lewis, "On improving wave energy conversion, part II: Development of latching control technologies", *Renewable Energy*, vol. 75, pp. 935–944, Mar. 2015.

[17] M. F. P. Lopes, J. Hals, R. P. F. Gomes, T. Moan, L. M. C. Gato, and A. F. d. O. Falcão, "Experimental and numerical investigation of non-predictive phase-control strategies for a point-absorbing wave energy converter", *Ocean Engineering*, vol. 36, no. 5, pp. 386–402, Apr. 2009.

[18] J. A. M. Cretel, G. Lightbody, G. P. Thomas, and A. W. Lewis, "Maximisation of energy capture by a wave-energy point absorber using model predictive control", *IFAC Proceedings Volumes*, vol. 44, no. 1, pp. 3714–3721, Jan. 2011.

[19] G. Bacelli, J. V. Ringwood, and J.-C. Gilloteaux, "A control system for a self-reacting point absorber wave energy converter subject to constraints", *IFAC Proceedings Volumes*, vol. 44, no. 1, pp. 11 387–11 392, Jan. 2011.

[20] E. Anderlini, D. I. M. Forehand, P. Stansell, Q. Xiao, and M. Abusara, "Control of a point absorber using reinforcement learning", *IEEE Transactions on Sustainable Energy*, vol. 7, no. 4, pp. 1681–1690, Oct. 2016.

[21] R. Patton, "Fault tolerant control in marine energy systems: A wave energy perspective", Presentation given at Maynooth Wave Energy Workshop 2017, School of Engineering & Computer Science, Jan. 2017.

[22] J. V. Ringwood, G. Bacelli, and F. Fusco, "Energy-maximizing control of wave-energy converters: The development of control system technology to optimize their operation", *IEEE Control Systems*, vol. 34, no. 5, pp. 30–55, Oct. 2014.

[23] K. Budal, J. Falnes, L. C. Iversen, P. M. Lillebekken, G. Oltedal, T. Hals, T. Onshus, and A. S. Høy, "The norwegian wave-power buoy project", in *Proc. of the 2nd International Symp. on Wave Energy Utilization*, H. Berge, Ed., Trondheim, Norway: Norges teknisk-naturvitenskapelige universitet, Fakultet for naturvitenskap og teknologi, Institutt for fysikk, 1982, pp. 323–344.

[24] A. Clément, A. Babarit, J. Gilloteaux, C. Josset, and G. Duclos, "The SEAREV wave energy converter", in *Proc. of the 6th European Wave and Tidal Energy Conf.*, Glasgow, UK, 2005.

[25] A. F. O. Falcão, "Phase control through load control of oscillating-body wave energy converters with hydraulic PTO system", *Ocean Engineering*, vol. 35, no. 3, pp. 358–366, Mar. 2008.

[26] J. Lan, R. J. Patton, and X. Zhu, "Fault-tolerant wind turbine pitch control using adaptive sliding mode estimation", *Renewable Energy*, vol. 116, pp. 219–231, Feb. 2018.

[27] R. Genest and J. V. Ringwood, "Receding horizon pseudospectral control for energy maximization with application to wave energy devices", *IEEE Transactions on Control Systems Technology*, vol. 25, no. 1, pp. 29–38, Jan. 2017.

[28] J. M. Maciejowski, *Predictive control: with constraints*. Harlow, UK, Pearson education, 2002.

[29] T. K. A. Brekken, "On model predictive control for a point absorber wave energy converter", in *Proc. of the 2011 IEEE Trondheim PowerTech*, Trondheim, Norway, Jun. 2011, pp. 1–8.

[30] A. O'Sullivan, "Power maximisation of a wave energy converter using predictive control: Robustness to system mismatch", in *Proc. of the Twelfth European Wave and Tidal Energy Conference*, A. Lewis, Ed., Cork, Ireland, 2017, pp. 1012-1 - 1012-10.

[31] R. Genest and J. V. Ringwood, "A critical comparison of model-predictive and pseudospectral control for wave energy devices", *Journal of Ocean Engineering and Marine Energy*, vol. 2, no. 4, pp. 485–499, Nov. 2016.

[32] S. Zhan and G. Li, "A reliable optimal controller design method for sea wave energy converters", in *Proc. of the Twelfth European Wave and Tidal Energy Conference*, A. Lewis, Ed., Cork, Ireland, 2017, pp. 1184-1 - 1184-7.

[33] P. Kracht, "Wave prediction and its implementation on control systems of wave-energy converters", Fraunhofer IWES, EU MaRINet Infrastructure Access Report, Tech. Rep. MARINET-TA1-Adaptive WEC Control, Sep. 2013.

[34] M. Richter, M. E. Magana, O. Sawodny, and T. K. Brekken, "Nonlinear model predictive control of a point absorber wave energy converter", *IEEE Transactions on Sustainable Energy*, vol. 4, no. 1, pp. 118–126, Jan. 2013.

[35] Y. Wang and S. Boyd, "Fast model predictive control using online optimization", *IEEE Transactions on control systems technology*, vol. 18, no. 2, pp. 267–278, Mar. 2010.

[36] F. Fusco and J. V. Ringwood, "Short-term wave forecasting for real-time control of wave energy converters", *IEEE Transactions on Sustainable Energy*, vol. 1, no. 2, pp. 99–106, Jul. 2010.

[37] L. Wang, "Discrete model predictive controller design using Laguerre functions", *Journal of Process Control*, vol. 14, no. 2, pp. 131–142, Mar. 2004.

[38] W. Kautz, "Transient synthesis in the time domain", *Transactions of the IRE Professional Group on Circuit Theory*, no. 3, pp. 29–39, Sep. 1954.

[39] B. Khan, J. A. Rossiter, and G. Valencia-Palomo, "Exploiting Kautz functions to improve feasibility in MPC", *IFAC Proceedings Volumes*, vol. 44, no. 1, pp. 6777–6782, Jan. 2011.

[40] D. Huybrechs, "On the Fourier extension of nonperiodic functions", *SIAM Journal on Numerical Analysis*, vol. 47, no. 6, pp. 4326–4355, Jan. 2010.

[41] R. P. F. Gomes, J. C. C. Henriques, L. M. C. Gato, and A. F. O. Falcão, "Hydrodynamic optimization of an axisymmetric floating oscillating water column for wave energy conversion", *Renewable Energy*, vol. 44, pp. 328–339, Aug. 2012.

[42] J. Falnes, *Ocean waves and oscillating systems: linear interactions including wave-energy extraction*. Cambridge, UK, Cambridge university press, 2002.

[43] A. Babarit and G. Delhommeau, "Theoretical and numerical aspects of the open source BEM solver NEMOH", in *Proc. 11th European Wave and Tidal Energy Conf. (EWTEC)*, Nantes, France, 2015.

[44] W. Sheng, R. Alcorn, and A. Lewis, "Hydrodynamics of OWC wave energy converters", in *Proc. of the RENEW 2014, 1st International Conference on Renewable Energies Offshore*, Lisbon, Portugal, 2014, Unpublished.

[45] C. H. Lee and J. N. Newman, *Wamit user manual*, Web Page, WAMIT, Inc., no date. [Online]. Available: `http://www.wamit.com/manual.htm`.

[46] Z. Yu and J. Falnes, "State-space modelling of a vertical cylinder in heave", *Applied Ocean Research*, vol. 17, no. 5, pp. 265–275, Oct. 1995.

[47] T. Perez and T. I. Fossen, "A Matlab toolbox for parametric identification of radiation-force models of ships and offshore structures", *Modeling, Identification and Control*, vol. 30, no. 1, p. 1, Jan. 2009.

[48] J. Dorsey, *Continuous and discrete control systems*. New York, USA, Publishing House of Electronics Industry, 2002.

[49] C. Josset and A. H. Clément, "A time-domain numerical simulator for oscillating water column wave power plants", *Renewable Energy*, vol. 32, no. 8, pp. 1379–1402, Jul. 2007.

[50] W. Sheng, R. Alcorn, and A. Lewis, "On thermodynamics in the primary power conversion of oscillating water column wave energy converters", *Journal of Renewable and Sustainable Energy*, vol. 5, no. 2, Mar. 2013.

[51] J. C. C. Henriques, R. P. F. Gomes, L. M. C. Gato, A. F. O. Falcão, E. Robles, and S. Ceballos, "Testing and control of a power take-off system for an oscillating-water-column wave energy converter", *Renewable Energy*, vol. 85, pp. 714–724, Jan. 2016.

[52] J. C. C. Henriques, L. M. C. Gato, J. M. Lemos, R. P. F. Gomes, and A. F. O. Falcão, "Peak-power control of a grid-integrated oscillating water column wave energy converter", *Energy*, vol. 109, pp. 378–390, Aug. 2016.

[53] R. Alcorn, A. Blavette, M. Healy, and A. Lewis, "FP7 EU funded CORES wave energy project: A coordinators' perspective on the galway bay sea trials", *Underwater Technology*, vol. 32, no. 1, pp. 51–59, Mar. 2014.

[54] T. Setoguchi, S. Santhakumar, H. Maeda, M. Takao, and K. Kaneko, "A review of impulse turbines for wave energy conversion", *Renewable energy*, vol. 23, no. 2, pp. 261–292, Jun. 2001.

[55] J. F. Kelly, W. M. D. Wright, W. Sheng, O. K, x, and Sullivan, "Implementation and verification of a wave-to-wire model of an oscillating water column with impulse turbine", *IEEE Transactions on Sustainable Energy*, vol. 7, no. 2, pp. 546–553, Apr. 2016.

[56] A. Thakker, J. Jarvis, and A. Sahed, "Design charts for impulse turbine wave energy extraction using experimental data", *Renewable Energy*, vol. 34, no. 10, pp. 2264–2270, Oct. 2009.

[57] H. Maeda, S. Santhakumar, T. Setoguchi, M. Takao, Y. Kinoue, and K. Kaneko, "Performance of an impulse turbine with fixed guide vanes for wave power conversion", *Renewable Energy*, vol. 17, no. 4, pp. 533–547, Aug. 1999.

[58] A. F. O. Falcão and J. C. C. Henriques, "Oscillating-water-column wave energy converters and air turbines: A review", *Renewable Energy*, vol. 30, pp. 1–34, Jan. 2015.

[59] J. Henriques, J. Lemos, L. Gato, and A. Falcão, "Latching and peak-power control of an oscillating water column based on a discontinuous galerkin method", in *Proc. of the Twelfth European Wave and Tidal Energy Conference*, A. Lewis, Ed., Cork, Ireland, 2017.

[60] U. M. Ascher and L. R. Petzold, "Computer methods for ordinary differential equations and differential-algebraic equations", *Society for Industrial and Applied Mathematics*, vol. 61, Dec. 1997.

[61] B. G. Cahill and T. Lewis, "Wave energy resource characterisation of the Atlantic marine energy test site", *International Journal of Marine Energy*, vol. 1, pp. 3–15, Apr. 2013.

[62] B. Cahill, "Characteristics of the wave energy resource at the Atlantic marine energy test site", Ph.D. dissertation, Dept. Civil and Env. Eng., National University of Ireland, Cork, 2013.

[63] P. A. Brodtkorb, P. Johannesson, G. Lindgren, I. Rychlik, J. Rydén, and E. Sjö, "WAFO-a Matlab toolbox for analysis of random waves and loads", in *Proc. of the Tenth International Offshore and Polar Engineering Conference*, Seattle, USA: International Society of Offshore and Polar Engineers, 2000, pp. 1–8.

[64] WAFOgroup, *WAFO-a matlab toolbox for analysis of random waves and loads - tutorial for WAFO version 2.5*, Lund University, Faculty of Engineering, Centre for Mathematical Sciences, Mathematical Statistics, Lund University, 2011. [Online]. Available: `http://www.maths.lth.se/matstat/wafo/documentation/`.

[65] Z. Lin, "On matrix fraction descriptions of multivariable linear nD systems", *IEEE transactions on circuits and systems*, vol. 35, no. 10, pp. 1317–1322, Oct. 1988.

[66] D. Ramirez, J. P. Bartolome, S. Martinez, L. C. Herrero, and M. Blanco, "Emulation of an OWC ocean energy plant with PMSG and irregular wave model", *Sustainable Energy, IEEE Transactions on*, vol. 6, no. 4, pp. 1515–1523, Oct. 2015.

[67] S. Herring, "Design and evaluation of turbines for use in OWC power plants", Ph.D. dissertation, School of Eng., Cranfield Univ., 2007.

[68] Dwyer Instruments Inc., *Home page*, Website, [Accessed: 1-Oct-2017]. [Online]. Available: `http://www.dwyer-inst.com`.

[69] D. O'Sullivan, F. Salcedo, A. Blavette, M. Santos, and A. Lewis, "Case studies on the benefits of energy storage for power quality enhancement: Oscillating water column arrays", in *Proc. of the 4th International Conference on Ocean Energy (ICOE2012)*, vol. 1719, Dublin, Ireland, 2012.

[70] V. Saouma and M. Sivaselvan, "Hybrid simulation: A historical perspective", in *Hybrid simulation: theory, implementation and applications*, V. Saouma and M. Sivaselvan, Eds. The Netherlands: Taylor & Francis, 2008, ch. Introduction.

[71] M. Nakashima, J. McCormick, and T. Wang, "Hybrid simulation: A historical perspective", in *Hybrid simulation: theory, implementation and applications*, V. Saouma and M. Sivaselvan, Eds. The Netherlands: Taylor & Francis, 2008, ch. 1.

[72] S. K. Lee, E. C. Park, K. W. Min, S. H. Lee, L. Chung, and J. H. Park, "Real-time hybrid shaking table testing method for the performance evaluation of a tuned liquid damper controlling seismic response of building structures", *Journal of Sound and Vibration*, vol. 302, no. 3, pp. 596–612, May 2007.

[73] R. Isermann, J. Schaffnit, and S. Sinsel, "Hardware-in-the-loop simulation for the design and testing of engine-control systems", *Control Engineering Practice*, vol. 7, no. 5, pp. 643–653, May 1999.

[74] M. Hakuno, M. Shidawara, and T. Hara, "Dynamic destructive test of a cantilever beam, controlled by an analog-computer", in *Proc. of the Japan Society of Civil Engineers*, Japan Society of Civil Engineers, 1969, pp. 1–9.

[75] K. Takanashi and M. Nakashima, "Japanese activities on on-line testing", *Journal of Engineering Mechanics*, vol. 113, no. 7, pp. 1014–1032, Jul. 1987.

[76] S. Mahin, P. Shing, C. Thewalt, and R. Hanson, "Pseudodynamic test method - current status and future directions", *Journal of Structural Engineering*, vol. 115, no. 8, pp. 2113–2128, Aug. 1989.

[77] P. B. Shing, M. Nakashima, and O. S. Bursi, "Application of pseudodynamic test method to structural research", *Earthquake Spectra*, vol. 12, no. 1, pp. 29–56, Feb. 1996.

[78] K. Tsai, S. Hsieh, Y. Yang, K. Wang, S. Wang, C. Yeh, W. Cheng, C. Hsu, and S. Huang, "Network platform for structural experiment and analysis (I)", *Report NCREE-03-021*, National Center for Research on Earthquake Engineering, Taiwan, 2003.

[79] P. Pan, H. Tomofuji, T. Wang, M. Nakashima, M. Ohsaki, and K. Mosalam, "Development of peer-to-peer (P2P) internet online hybrid test system", *Earthquake Engineering and Structural Dynamics*, vol. 35, no. 7, pp. 867–890, Jun. 2006.

[80] D. P. McCrum and B. M. Broderick, "An experimental and numerical investigation into the seismic performance of a multi-storey concentrically braced plan irregular structure", *Bulletin of Earthquake Engineering*, vol. 11, no. 6, pp. 2363–2385, Dec. 2013.

[81] A. Roy, A. Staino, A. Ghosh, B. Basu, and S. Chatterjee, "Seismic vibration control of elevated water tank by TLD and validation of full-scale TLD model through real-time-hybrid-testing", *Journal of Physics: Conference Series*, vol. 744, no. 1, Sep. 2016.

[82] A. Staino, "Vibration control of wind turbines with variable rotor speed and grid faults", Ph.D. dissertation, Dept. Civil, Struct. & Envir. Eng., Univ. of Dublin, Trinity College, 2014.

[83] J. De Carufel, E. Martin, and J.-C. Piedbœuf, "Control strategies for hardware-in-the-loop simulation of flexible space robots", *IEE Proceedings-Control Theory and Applications*, vol. 147, no. 6, pp. 569–579, Nov. 2000.

[84] C. Signorelli, C. Villegas, and J. Ringwood, "Hardware-in-the-loop simulation of a heaving wave energy converter", in *Proc. of the 9th European Wave and Tidal Energy Conf.*, Southhampton, UK, 2011.

[85] D. P. McCrum and B. M. Broderick, "Evaluation of a substructured soft-real time hybrid test for performing seismic analysis of complex structural systems", *Computers & Structures*, vol. 129, pp. 111–119, Dec. 2013.

[86] Z. Zhang, A. Staino, B. Basu, and S. R. K. Nielsen, "Performance evaluation of full-scale tuned liquid dampers (TLDs) for vibration control of large wind turbines using real-time hybrid testing", *Engineering Structures*, vol. 126, pp. 417–431, Nov. 2016.

[87] MTS Systems Corporation, *Actuators & hydraulic components*, Website, [Accessed: 1-Oct-2017], 2011. [Online]. Available: https://www.mts.com/en/products/producttype/test-components/actuators-hydraulic-components/index.htm.